A Theoretical Exploration of Compact Star, Black Holes and Wormholes

THESIS
submitted for the award of the degree
of

Doctor of Philosophy (Science)

by

SOMI AKTAR

under the guidance of

Prof. Farook Rahaman
Dr. Piyali Bhar

DEPARTMENT OF MATHEMATICS, FACULTY OF SCIENCE
JADAVPUR UNIVERSITY
KOLKATA-700032
INDIA
2024

Dedicated to
My beloved Parents

Md Abul Khayer Mondal

&
Tajmira Khatun

The architect of my dreams, whose love transcends dimensions and whose guidance shapes my universe.

যাদবপুর বিশ্ববিদ্যালয়

FACULTY OF SCIENCE
DEPARTMENT OF MATHEMATICS

JADAVPUR UNIVERSITY
Kolkata - 700 032, India
Telephone : 91 (33) 2457 2269

CERTIFICATE FROM THE SUPERVISORS

This is to certify that the thesis entitled **"A Theoretical Exploration of Compact Star, Black Holes and Wormholes."** submitted by **Somi Aktar**, who got her name registered on **12.10.2020** (Index No.: 37/20/Maths./27) for the award of **Ph.D. (Science)** degree of Jadavpur University, is absolutely based upon her own work under the supervision of **Prof. Farook Rahaman** and **Dr. Piyali Bhar** and that neither this thesis nor any part of it has been submitted for either any degree / diploma or any other academic award anywhere before.

Piyali Bhar
05/12/2024

Signature of the Supervisor
Date: 05.12.2024

DR. PIYALI BHAR
Assistant Professor
W.B.E.S. (Gr. 'A')
Department of Mathematics
Govt. General Degree College
Singur, Hooghly, WB-712409

Farook Rahaman
05.12.24

Signature of the Supervisor
Date: 05.12.2024

DR. FAROOK RAHAMAN
Professor
Department of Mathematics
JADAVPUR UNIVERSITY
Kolkata-700032, W.B., INDIA

DECLARATION

I, **Somi Aktar**, hereby declare that the thesis titled **"A Theoretical Exploration of Compact Star, Black Holes and Wormholes."** is based on my original research conducted at **Jadavpur University, Kolkata-700032, West Bengal, India** for the award of the degree of *Doctor of Philosophy (Science)*. I assert that the work is free from plagiarism and no part of this work has been previously submitted for any degree, diploma, or other qualification at any other institution.

Most of the figures presented in this thesis have been produced using Mathematica or Maple or Python software. The thesis has been diligently reviewed to rectify any discrepancies and typographical errors. Nevertheless, some inaccuracies or superfluous elements may persist, for which I alone bear responsibility.

Furthermore, I confirm that all contributions and references utilized in the preparation of this thesis have been duly cited and acknowledged.

Date: 05.12.2024
Place: Jadavpur

Somi Aktar
Index No.:37/20/Maths./27
Registration No.: SMATH1403720
Date of Registration:12.10.2020
Department of Mathematics
Jadavpur Univesity

ACKNOWLEDGEMENT

I, Somi Aktar, deeply grateful for the invaluable support, guidance and encouragement that have made this doctoral journey possible.

I must first express my deepest gratitude to my supervisor, Dr. Farook Rahaman. He has been the guiding star illuminating my path through the vast and enigmatic universe of astrophysics. From the inception of this research, his expertise and patience have been my gravitational force, anchoring me through the black holes of challenges and the nebulae of confusions. His skill in deciphering the universe's mysteries and his knack for guiding me through theoretical astrophysical quandaries have expanded my horizons beyond what I thought possible. He is not just an exceptional supervisor but an inspiring mentor and a steadfast ally. This voyage through the astrophysical universe would have been far less enriching without his mentorship and support.

I am grateful to Dr. Piyali Bhar, for her invaluable support throughout this journey. Her willingness to provide insights has enhanced the quality of this thesis.

I would like to extend special and profound thanks to Dr. Manjusha Majumder, without whom this journey would not have been possible. Her unwavering support, exceptional guidance and profound dedication have been fundamental to the completion of this research.

I would like to express my sincere gratitude to all the authority of Jadavpur University and all the eminent faculty members of Department of Mathematics, JU.

I am profoundly grateful to the Inter-University Centre for Astronomy and Astrophysics (IUCAA) for providing an exceptional research environment throughout the course.

I would like to extend my heartfelt thanks to my labmates and friends Anikul, Bidisha, Lipi Di, Tuhina Di, Antara Di, Tanmoy, Bikramarka, Aman, Asim, Tania, Shama, Shakina Di, Jyotirmoy and my seniors Amna Ali Di, Iftikar Da, Sayeedul Da, Payel Di, Monimala Di,

Nayeem Da, Nayan Da, Susmita Di, Hasan Da also my research Collaborators Dr. Safiqul Islam, Abdelghani Errehymy, Dr. Gholam Mustafa, Dr. Rajibul Islam for their invaluable contributions and support throughout this research journey and Special thanks to Dr. Ksh Newton Singh and Dr. Niyaz Uddin Molla for their comments and suggestions.

I am truly fortunate to have had the guidance and support of exceptional teachers Dr. Gopal Chandra Shit, Dr. Avishek Adhikary, Dr. Soma Mondal, Dr. Sunil Kumar Maity, Rabiul Islam, Suchanda Sen, Sumita Saha Roy, Lekha Mukhopadhyay, Dr. Shyam Das, Dr. Mehedi kalam, Dr. Prabir Rudra throughout my academic journey.

I am incredibly blessed to have the steadfast support and encouragement form our Joint family, my uncles, Md. Abdul Kader Mondal, Md Abdullah, Md. Motaleb Mondal, Mukul Mondal as well as my aunts, Sabina Bibi, Moni Khatun, Rajiya Sultana, Taslima Khatun and my brothers Hamidullah, Wasim Raihan and Sohel.

I am deeply blessed to have my sisters Dr. Selina Mostafi who is currently pursuing M.D. General Medicine in NRSMCH and Sania Aktar who is a grad student of JU the wellspring of strength and motivation, making this accomplishment possible.

At the heart of this achievement lies the unwavering support, boundless care and profound concern of my father, Md Abul Khayer Mondal and my mother Tajmira Khatun. Their indefatigable dedication, coupled with their unparalleled sacrifices and ceaseless encouragement has been the bedrock upon which this journey has been built. Their steadfast belief in my potential and relentless pursuit of my success have infused me with the fortitude and perseverance necessary to overcome the myriad challenges faced. This accomplishment stands as a tribute not only to my own efforts but also to the immeasurable depth of their unwavering love and support for which I am eternally grateful.

Somi Aktar
05.12.2024

(Somi Aktar)

LIST OF PUBLICATIONS

PUBLICATIONS INCLUDED IN THE THESIS

- "Possible existence of Bose–Einstein condensate compact stars."
  Somi Aktar, Ksh. Newton Singh, Piyali Bhar, Farook Rahaman and Pravin Bhandakkar.
  Chinese Journal of Physics , Vol. 89, Page-1188 (2024).
  https://doi.org/10.1016/j.cjph.2024.02.014

- "Anisotropic quintessence compact star in $f(T)$ gravity with Tolman-Kuchowicz metric potentials."
  Piyali Bhar, Farook Rahaman, Shyam Das, **Somi Aktar** and Abdelghani Errehymy.
  Communications in Theoretical Physics , Vol. 76, Page-015401, (2024).
  https://dx.doi.org/10.1088/1572-9494/ad08ad

- "Complexity characterization in modeling anisotropic compact stellar structures."
  Shyam Das, Megandhren Govender and **Somi Aktar.**
  The European Physical Journal C. Vol. 84 Page-1112, (2024).
  https://doi.org/10.1140/epjc/s10052-024-13439-5

- "A Reissner-Nordström+Λ black hole in the Friedman-Robertson-Walker universe."
  Safiqul Islam, Priti Mishra, **Somi Aktar** and Farook Rahaman.
  Journal of Applied Mathematics and Computation, Vol. 5, Page-283, (2021).
  https://dx.doi.org/10.26855/jamc.2021.12.007

- "Shadows and Strong Gravitational Lensing around black hole like solution in Quadratic gravity"
  Somi Aktar, Niyaz Uddin Molla, Farook Rahaman and G. Mustafa.

Communicated to journal.

- "Impact of Yukwa Potential on Wormhole Shadow."
  Somi Aktar, Niyaz Uddin Molla and Farook Rahaman.
  Communicated to journal.

- "Shadows of Lorentzian traversable Wormholes."
  Farook Rahaman, Ksh. Newton Singh, Rajibul Shaikh, Tuhina Manna and **Somi Aktar**.
  Classical and Quantum Gravity , Vol.38, Page-215007 (2021).
  https://dx.doi.org/10.1088/1361-6382/ac213b

PUBLICATIONS NOT INCLUDED IN THE THESIS

- "Thin accretion disks around traversable Wormholes."
  Farook Rahaman, Tuhina Manna, Rajibul Shaikh, **Somi Aktar**, Monimala Mondal, Bidisha Samanta. *Nucl. Phys. B*, Vol.972, Page-115548, (2021).

- "Finch-Skea dark energy star with anisotropy."
  Bibhash Das, **Somi Aktar**, Farook Rahaman and Bikash Chandra Paul. *Astrophysics and Space Science*, Vol.369, Page-76, (2024).

- "Quark stars in 4-dimensional Einstein–Gauss–Bonnet gravity."
  Ksh. Newton Singh, S. K. Maurya, Abhisek Dutta, Farook Rahaman and **Somi Aktar**. *The European Physical Journal C* , Vol.81, Page-909, (2021).

- "Dark matter supporting traversable Wormholes in the Galactic halo."
  Susmita Sarkar, Nayan Sarkar, **Somi Aktar**, Moumita Sarkar, Farook Rahaman and Anil Kumar Yadav. *New Astronomy* , Vol.109, Page-102183, (2024).

ARTICLE PRESENTED IN CONFERENCE

- **Somi Aktar**, *Wormhole's Shadow* , National conference on Relativistic Astrophysics and Cosmology (NCRAC), Malda College, 2024.

- **Somi Aktar**, *Thin accretion disks around traversable Wormholes* , ICMAAM 2023, 2nd International Conference on Mathematical Analysis and Applications in Modeling, JU, 2023.

- **Somi Aktar**, *Anisotropic quintessence Compact Star in $f(T)$ gravity with T-K metric potentials* , Indian Mathematical Society, an international meet (IMS 2023), BITS-PILANI, Hydrabad, 2023.

ABSTRACT

This thesis presents a comprehensive study on compact stars, black holes and wormholes, exploring their physical characteristics, formation processes and theoretical implications. By synthesizing current theoretical frameworks with observational constraints, this work aims to enhance understanding of these enigmatic cosmic entities and their roles in the broader structure of the universe. The thesis is embodied into the following chapters, each dedicated to explore different aspects and theoretical models related to these cosmic phenomena.

First chapter elucidates the transition from special to general relativity, explores modified gravity theories and discusses their impact on compact objects. It also covers the observational signatures of these objects, such as strong lensing and shadows and the role of Bose-Einstein condensation setting the stage for the detailed analysis in later chapters.

Second chapter constructs a compact star model incorporating Bose-Einstein Condensate (BEC) matter, governed by a polytropic equation of state with $\gamma = 2$ and a specific energy density. It evaluates the model's physical viability, stability and alignment with constraints from the GW 170817 event. Key findings include how the parameter κ affects central density, compactness and the likelihood of gravitational collapse, suggesting BEC stars could mimic neutron stars.

Third chapter explores relativistic quintessence anisotropic solutions within the $f(T)$ gravity framework, employing Tolman-Kuchowicz metric potentials. It analyzes how anisotropy and a quintessence field with parameter ω_q, along with $f(T)$ gravity parameter α, influence stellar characteristics. The study demonstrates that varying α from 0.5 to 2.5 affects density, pressure and compactness of the compact star Her X-1, with higher values of α yielding a more compact star. The chapter also evaluates the hydrostatic equilibrium and mass-radius relationship for the model emphasizing the impact of α on the star's structural and stability attributes.

Fourth chapter provides an exact solution to the Einstein field equations for a static, spherically symmetric, anisotropic stellar fluid sphere with non-zero complexity, using specific metric potentials and ensuring boundary continuity; stability is assessed through stan-

dard conditions and validated against pulsar data.

Fifth chapter explores a Reissner-Nordström+ Λ black Hole in a (2+1) dimensional Friedmann-Robertson-Walker universe. It presents new exact solutions and finds that the cosmological constant Λ is negative inside the black Hole. The chapter demonstrates that Λ depends on the black Hole's radius R, charge Q and the universe's scale factor $a(v)$. It shows that the black Hole's mass and charge increase with cosmic contraction and decrease with cosmic expansion.

Sixth chapter explores the astrophysical consequences of black holes in quadratic gravity. To evaluate the physical validity of black hole like solutions in quadratic gravity, their shadow and gravitational lensing properties are analyzed in the strong field regime.

Seventh chapter examines three new wormhole solutions with Yukawa gravitational potential, focusing on geometry, energy conditions, stability and shadow. Stability is assessed using the Tolman-Oppenheimer-Volkov equations, with parameters β, a and γ influencing wormhole properties.

Eighth chapter, investigates identifying wormholes through their shadows by analyzing the effects of rotating wormhole parameters on photon orbits, using Event Horizon Telescope (EHT) data to constrain shadow size and spin, aiming to potentially reveal wormholes in galactic regions.

Finally, **Ninth chapter** encapsulates the crux of the research, emphasizing the nuanced impacts of parameter variations on the attributes and detectability of cosmic entities. It outlines prospective research trajectories to further elucidate theoretical constructs and refine observational methodologies for these enigmatic phenomena.

Somi Akter
05.12.2024

Piyali Bhar
05/12/2024

DR. PIYALI BHAR
Assistant Professor
W.B.E.S. (Gr. 'A')
Department of Mathematics
Govt. General Degree College
Singur, Hooghly, [illegible]-712409

Farook Rahaman
05.12.24

DR. FAROOK RAHAMAN
Professor
Department of Mathematics
JADAVPUR UNIVERSITY
Kolkata-700032, W.B., INDIA

Contents

List of Figures

List of Tables

List of Abbreviations

3D 3 Dimensional

BEC Bose-Einstein Condensate

CMB Cosmic Microwave Background

DEC Dominant Energy Condition

EH Einstein-Hilbert

EHT Event Horizon Telescope

EoS Equation of State

FRW Friedmann-Robertson-Walker

K-N Kerr Newman

NEC Null Energy Condition

RN Reissner-Nordström

SEC Strong Energy Condition

TEC Trace Energy Condition

TOV Tolman-Oppenheimer-Volkov

TK Tolman-Kuchowicz

TEGR Teleparallel Equivalent of General Relativity

WEC Weak Energy Condition

Chapter 1

Introduction

Imagine a world at the turn of the 20th century where scientists believed space and time were unchanging, like the fixed stage upon which all of nature's events unfold. This was the world of Newtonian mechanics, where forces acted instantaneously across distances and time ticked uniformly for everyone. But as scientists peered deeper into the mysteries of light and motion, cracks began to appear in this comfortable view of reality. James Clerk Maxwell had shown that light moves at a constant speed, but how could that be? Shouldn't light slow down or speed up if you're moving towards or away from it, just like sound or a moving car? Then came the famous Michelson-Morley experiment in 1887, which sought to measure Earth's movement through a mysterious substance called "aether", thought to carry light waves. But no matter how hard they tried, they found no trace of this aether—light's speed remained bafflingly constant.

Enter Albert Einstein, a young patent clerk with a head full of revolutionary ideas. In 1905, Einstein tossed out the need for aether and flipped our understanding of the universe on its head. He declared that space and time weren't fixed after all they could stretch, bend and even slow down depending on how fast you were moving. According to his special theory of relativity, the faster you go, the more time slows down and distances shrink. And no matter how fast you chase it, the speed of light stays the same for everyone. But Einstein wasn't done yet. In 1915, he introduced the general theory of relativity, where gravity wasn't a force pulling objects together as Newton had thought, but a warping of the very fabric of space and time by massive objects. Imagine spacetime as a trampoline—place a heavy ball in the center and it bends, causing other smaller objects to roll toward it. This new view

of gravity explained everything from the strange wobble in Mercury's orbit to the bending of starlight around the Sun during an eclipse, even predicting exotic things like black holes and gravitational waves, which would not be confirmed until a century later.

1.1 Transition from Special to General Theory of Relativity

The transition from Special Theory of Relativity (STR) to General Theory of Relativity (GTR) marks a fundamental shift in the way one understands the universe. While STR revolutionized our understanding of space and time by unifying them into a single spacetime continuum, GTR goes a step further by explaining gravity as the curvature of this spacetime. This shift laid the groundwork for many modern advancements in astrophysics and cosmology, fundamentally altering our view of the universe.

1.1.1 Classical Physics to STR

Before Einstein's breakthrough in 1905, the world of physics was dominated by Newtonian mechanics. According to Newton's laws, space and time were fixed. Mass and energy were distinct, mass described the amount of "matter" in an object, while energy referred to its capacity to perform work, whether through motion (kinetic energy) or position (potential energy).

However, as scientists began exploring phenomena at higher velocities—close to the speed of light—anomalies started to emerge. The laws of physics, particularly those concerning electromagnetism and light, seemed to behave differently at these speeds. For example, James Clerk Maxwell's equations of electromagnetism implied that the speed of light remains constant, regardless of the observer's motion. This was puzzling because, according to classical mechanics, speeds should add up; if someone is moving toward or away from a light source, he or she should measure different speeds for light. But experiments showed otherwise.

This inconsistency hinted at the need for a new understanding of how space, time, mass and energy were connected.

1.1.2 STR Brief Overview

The journey from Newtonian mechanics to STR of Einstein marks one of the most transformative periods in the history of physics. In 1905, a 26-year-old Albert Einstein published a groundbreaking paper that would forever change the way one thinks about space and time. This was the STR and its foundation rested on two simple, yet revolutionary ideas

1.1.2.1 Foundation of STR

I **Laws of Physics**: The laws of physics are the same for everyone, no matter how fast they are moving—as long as they're not accelerating. In other words, the universe doesn't care if someone is zooming along in a spaceship or standing still on Earth; the rules are the same.

II **Speed of Light**: The speed of light is constant, regardless of the observer's motion or the light source's motion. Whether you're running toward a beam of light or away from it, one will always measure the same speed near about 300,000 kilometers per second.

1.1.2.2 Resultant of STR

These principles led to several groundbreaking conclusions

I **Time Dilation**: Moving clocks run slower compared to those at rest relative to an observer.

II **Length Contraction**: To a stationary observer, moving objects appear shortened along the direction of their motion.

III **Relativity of Simultaneity**: Events that are simultaneous in one reference frame may not be simultaneous in another frame that is in motion relative to the first.

1.1.2.3 Limitations of STR

STR was elegant and revolutionary, the main limitations of this arise from its assumptions and scope, but it had limitations,

I **Inapplicable to Accelerating Frames**: STR applies only to observers in constant motion (inertial frames). It doesn't work for accelerating reference frames, as it doesn't address forces like gravity or acceleration, which led to the development of GTR to include non-inertial frames and gravitational effects.

II **Applicable Only to Flat Spacetime**: STR is valid in the absence of curvature, i.e., in Minkowski spacetime. In curved spacetime, where gravity causes spacetime distortion, STR is no longer valid, necessitating GTR.

$$ds^2 = \eta_{\mu\nu} dx^\mu dx^\nu \tag{1.1.1}$$

where,

- $\eta_{\mu\nu} = diag(-1, -1, -1)$, for Minkowski Space.

1.1.3 GTR Brief Overview

GTR was necessary to bring together the concepts of spacetime and gravity in a consistent framework. Einstein realized that mass and energy influence the curvature of spacetime and that curved spacetime tells objects how to move. This replaced the concept of gravity as an instantaneous force with the idea that objects follow curved paths (geodesics) in spacetime.

1.1.3.1 Spacetime and the Metric Tensor

I **Spacetime**: In GTR, spacetime is described as a 4-dimensional manifold with a metric tensor $g_{\mu\nu}$, which specifies the separation between two nearby points in spacetime.

II **Line element**: The line element (infinitesimal distance between two points) is given by:

$$ds^2 = g_{\mu\nu} dx^\mu dx^\nu, \tag{1.1.2}$$

where,

- μ, ν = 0,1,2,3,
- x^μ = The spacetime coordinate,

- $$g_{\mu\nu} = \begin{bmatrix} g_{00} & g_{01} & g_{02} & g_{03} \\ g_{10} & g_{11} & g_{12} & g_{13} \\ g_{20} & g_{21} & g_{22} & g_{23} \\ g_{30} & g_{31} & g_{32} & g_{33} \end{bmatrix}$$

.

1.1.3.2 Lagrangian Derivation using Einstein-Hilbert Action

I **Einstein-Hilbert (EH) Action**: The EH action is given by

$$S_{\text{EH}} = \frac{1}{2\kappa} \int \sqrt{-g} R \; d^4x \tag{1.1.3}$$

where,

- $\kappa = \frac{8\pi G}{c^4}$ is a constant, G, gravitational constant,
- $g = |g_{\mu\nu}|$ is the determinant of $g_{\mu\nu}$,
- $R =$ Ricci scalar.

II **Total Action**: The total action in general relativity is

$$S_{\text{total}} = S_{\text{EH}} + S_m, \tag{1.1.4}$$

which expands to

$$S_{\text{total}} = \frac{1}{2\kappa} \int \sqrt{-g}\, R \; d^4x + \int \mathcal{L}_m \; d^4x \sqrt{-g}, \tag{1.1.5}$$

where,

- $\mathcal{L}_m =$ the Lagrangian density for the matter fields.

III **Variation of Action**: To derive the field equations, the total action is varied with respect to the metric $g_{\mu\nu}$

$$\delta S_{\text{EH}} = \frac{1}{2\kappa} \int \delta(\sqrt{-g}\, R) \; d^4x \tag{1.1.6}$$

This variation consists of two parts

a. The variation of $\sqrt{-g}$ is given by

$$\delta\sqrt{-g} = \frac{1}{2}\sqrt{-g}\, g^{\mu\nu}\delta g_{\mu\nu}. \tag{1.1.7}$$

b. The variation of the Ricci scalar R is

$$\delta R_{\mu\nu} = \nabla_\lambda(\delta\Gamma^\lambda_{\mu\nu}) - \nabla_\nu(\delta\Gamma^\lambda_{\lambda\mu}), \tag{1.1.8}$$

where,

- $R_{\mu\nu}$ = Ricci curvature tensor.

After integrating by parts and assuming the boundary terms vanish, the variation of the Ricci scalar leads to

$$\delta S_{\text{EH}} = \frac{1}{2\kappa}\int \sqrt{-g}\left(R_{\mu\nu} - \frac{1}{2}Rg_{\mu\nu}\right)\delta g^{\mu\nu}\; d^4x. \tag{1.1.9}$$

IV **Variation of the Matter Action** The variation of the matter action gives the energy-momentum tensor $T_{\mu\nu}$

$$\delta S_m = \int \sqrt{-g}\,\frac{1}{2}T_{\mu\nu}\,\delta g^{\mu\nu}\; d^4x. \tag{1.1.10}$$

By equating the variations to zero, the Einstein field equations are obtained.

1.1.3.3 Einstein Field Equations

The core of GTR is the Einstein field equations, which relate the geometry of spacetime (encoded in the Einstein tensor $G_{\mu\nu}$) to the energy and momentum of matter and radiation (encoded in the stress-energy tensor $T_{\mu\nu}$)

$$G_{\mu\nu} = \frac{8\pi G}{c^4}T_{\mu\nu}, \tag{1.1.11}$$

- $G_{\mu\nu} = R_{\mu\nu} - \frac{1}{2}g_{\mu\nu}R$, Einstein tensor.

1.1.3.4 Geodesics

Particles follow paths called geodesics in curved spacetime, which are the generalization

of straight lines in flat space. The geodesic equation is

$$\frac{d^2x^\lambda}{d\tau^2} + \Gamma^\lambda_{\mu\nu}\frac{dx^\mu}{d\tau}\frac{dx^\nu}{d\tau} = 0, \tag{1.1.12}$$

- τ: The proper time along the particle's worldline,
- $\Gamma^\lambda_{\mu\nu}$: The Christoffel symbols, which depend on the metric tensor.

1.1.3.5 Energy-Momentum Conservation

The Bianchi identity for the Riemann curvature tensor is given by

$$R_{\mu\nu;\rho} + R_{\nu\rho;\mu} + R_{\rho\mu;\nu} = 0. \tag{1.1.13}$$

GTR ensures the conservation of energy and momentum via the contracted Bianchi identity, which leads to the covariant divergence of the Einstein tensor being zero

$$\nabla^\mu G_{\mu\nu} = 0. \tag{1.1.14}$$

This leads to the conservation of the stress-energy tensor

$$\nabla^\mu T_{\mu\nu} = 0. \tag{1.1.15}$$

GTR offers a radically new, geometrical view of gravity, replaces Newtonian mechanics at cosmological scales and provides a more accurate description of the universe.

1.2 Cosmic Origins: The Big Bang and the Steady State Debate

Prior to GTR, the universe was thought of as static and unchanging. However, when Einstein's equations were applied to the large-scale structure of the universe, they revealed the possibility of a dynamic, evolving cosmos.

1.2.1 The Birth of the Big Bang Theory

One of the theories that explains universe's origin and evolution suggests it began in an incredibly hot and dense state, expanding rapidly from that initial condition, roughly 13.8 billion years ago. That extremely hot and dense state known as a singularity, marking the beginning of space and time and the expansion through the cosmic inflation and nucleosynthesis the cosmic structure is formed and still expanding and cooling.

I **Lemaître's Hypothesis**: In 1927, Belgian priest and physicist Georges Lemaître independently derived the idea of an expanding universe from Einstein's equations, before Hubble's observations.

II **Singularity**: The universe originated from a point where densities and temperatures are infinitely high. Lemaître proposed that the universe originated from a single point, which he called the "primeval atom" or cosmic egg, which exploded, leading to the expansion of the universe.

III **"Big Bang" Term**: The term "Big Bang" was coined by British astronomer Fred Hoyle in 1949 during a radio broadcast, though Hoyle intended it as a dismissive term because he supported the rival steady state theory. Ironically, the name stuck.

1.2.2 The Steady State Challenge

Not everyone was convinced by the idea of a universe with a singular beginning. The Steady State theory was introduced in 1948 by Fred Hoyle, Thomas Gold and Hermann Bondi. It was a bold cosmological model positing that the universe has no beginning or end, it is eternal and unchanging in its large-scale structure over time, relies on the Perfect Cosmological Principle, which extends the Cosmological Principle by asserting that the universe looks the same not only in space but also in time.

I **Infinite Universe**: The universe is infinite in time and has always existed in its current form, expanding forever.

II **Continuous Creation of Matter**: To account for the universe's expansion, the theory posits that new matter is continuously created from nothing at a rate just enough to keep the overall density constant as galaxies move apart.

III **Self-sustaining**: The theory implies a kind of "self-sustaining" universe, with no need for a beginning or end, unlike the Big Bang model, which requires a singularity.

IV **Observational Problems**: Observations show that galaxies evolve over time, there are more young galaxies at greater distances (looking further back in time), which contradicts the Steady State Theory's assertion that the universe remains unchanged in time.

Due to its failure to account for these observations, the Steady State Theory was largely rejected by the scientific community. Over time, the Big Bang theory became the dominant cosmological model due to key pieces of evidence.

1.2.3 Observational Evidence of Big Bang

The Big Bang theory emerged as the leading cosmological model by combining theoretical insights from general relativity with key observational evidence, such as Hubble's discovery of the expanding universe and the detection of the Cosmic Microwave Background (CMB).

I **Hubble's Discovery**: Edwin Hubble's observation in 1929 that galaxies are moving away from each other provided strong observational support for an expanding universe, a key prediction of the Big Bang model.

II **CMB**: The discovery of the CMB in 1965 provided crucial evidence for the Big Bang theory, as it represented the leftover radiation from the early, hot phase of the universe.

1.2.4 Challenges of Big Bang

While the Big Bang theory is now the dominant cosmological model, it doesn't explain everything,

I **Horizon Problem**: Why is the universe so uniform on large scales? The Big Bang theory doesn't fully explain how regions of the universe that were never in causal contact (due to the finite speed of light) appear so similar.

II **Flatness Problem**: The geometry of the universe is very close to being flat, but the Big Bang theory alone doesn't explain why.

III **Dark Matter and Dark Energy**: The Big Bang theory explains cosmic expansion, but the accelerated expansion observed today (attributed to dark energy) and the presence of dark matter (which doesn't emit or absorb light but interacts gravitationally) remain puzzles within the standard cosmological framework.

1.3 Modified Gravity

Since the inception of Big Bang, our universe has gone through various phases. Let's break down the evolution of the idea and how it comes about.

1.3.1 Cosmological Acceleration

It is interesting to note that the late time cosmological acceleration was discovered [Riess et al. (1998)] by the Supernova Cosmology Project and the High-Z Supernova Search Team in 1998, led by Saul Perlmutter, Brian P. Schnidh and Adam G. Riess. They observed distant Type la supernova and found that the universe expansion is accelerating. It is to be note that this acceleration phase is not only on the Big Bang but it also upper drive after the Big Bang which is called as Inflation. Although that is not an observational thing but that epoch was used to solve some fundamental problems of cosmology such as the Horizon, Flatness problems, the Fine Tuning problem and so on. After the inception of the observational evidence of acceleration of universe, the constituent universe are now following luminous matter 4.9%, Dark energy 68.3%, Dark matter 26.8%. It means that 95% of universe is still unknown to us. What causes this acceleration? The physics behind this acceleration has various motivation and various alternatives. The first alternatives is cosmological constant.

1.3.1.1 Cosmological Constant

Albert Einstein originally introduced the cosmological constant in 1917 as a term in his equations of general relativity to achieve a static universe model, which was the prevailing view at the time. It was added to counteract gravitational collapse in a static universe. After the discovery of the universe's expansion by Edwin Hubble, Einstein discarded Λ calling it his "biggest blunder". The modified field equation is

$$G_{\mu\nu} + \Lambda g_{\mu\nu} = \frac{8\pi G}{c^4} T_{\mu\nu}, \tag{1.3.1}$$

where,

- Λ = Cosmological constant and acts as a constant energy density filling space.

1.3.1.2 Problems of Cosmological Constant

From a quantum field theory perspective, empty space (the vacuum) is not truly empty but has fluctuations at the quantum level, leading to a non-zero vacuum energy. This energy should manifest as a cosmological constant in general relativity. The problem arises when comparing the theoretical predictions of the vacuum energy density from quantum mechanics to its observed value based on cosmological measurements. The vacuum energy density (or cosmological constant) should, according to quantum mechanics, be much larger on the order of 10^{-3} GeV^4 based on Quantum Chromodynamics phase transitions. However, the observed value today is around 10^{-3} eV^4, a huge discrepancy. The question is: Why is it so small today?

To elevate this problem, scientists thought about variable density cosmological constants which have variable equation of state and variable density. Alternative view is also floating, some scientists have alternate view that there is no exotic matter but there is a modification of gravity.

1.3.2 $f(R)$ Gravity

$f(R)$ gravity [Buchdahl (1970)] is a modification of general relativity that aims to explain cosmological phenomena such as the accelerated expansion of the universes without invoking dark energy or other exotic matter components. This class of theories extends the EH action by replacing the Ricci scalar R with a general function $f(R)$.

1.3.2.1 Action and Field Equation

In $f(R)$, this action is generalized to

$$S = \frac{1}{2\kappa^2} \int d^4x\sqrt{-g}\ f(R) + S_m, \tag{1.3.2}$$

where,

- $f(R)$ = Arbitrary function of the Ricci scalar R,

- S_m = The action for matter fields.

To derive the field equations, a variation of the action is performed with respect to the metric tensor $g_{\mu\nu}$,

$$\delta S = \frac{1}{2\kappa^2}\int \sqrt{-g}\left[f'(R)\delta R + f(R)\delta(\sqrt{-g})\right]\ d^4x + \delta S_m, \tag{1.3.3}$$

where, " $'$ " represent derivative with respect to R.

Using the variations,

$$\delta(\sqrt{-g}) = \frac{1}{2}\sqrt{-g}g_{\mu\nu}\delta g^{\mu\nu}, \tag{1.3.4}$$

$$\delta R = R_{\mu\nu}\delta g^{\mu\nu} + g_{\mu\nu}\Box\delta g^{\mu\nu} - \nabla_\mu\nabla_\nu - \delta g^{\mu\nu}, \tag{1.3.5}$$

it is obtained,

$$\delta S = \frac{1}{2\kappa^2}\int d^4x\sqrt{-g}\left[f'(R)\left(R_{\mu\nu}\delta g^{\mu\nu} + g_{\mu\nu}\Box\delta g^{\mu\nu} - \nabla_\mu\nabla_\nu\delta g^{\mu\nu}\right) + \frac{1}{2}g_{\mu\nu}f(R)\delta g^{\mu\nu}\right] + \delta S_m, \tag{1.3.6}$$

here, $\Box = \nabla^\mu\nabla_\mu$ is the d'Alembertian operator.

Integrating by parts and applying the variation, the field equations become

$$f'(R)R_{\mu\nu} - \frac{1}{2}f(R)g_{\mu\nu} + \left(g_{\mu\nu}\Box - \nabla_\mu\nabla_\nu\right)f'(R) = \kappa^2 T_{\mu\nu}, \tag{1.3.7}$$

where, $T_{\mu\nu}$ is the energy-momentum tensor of matter.

1.3.2.2 Stability and Viability Conditions

For $f(R)$ gravity to be physically viable, it must satisfy certain stability conditions.

I **No Tachyon:** The condition $f'(R) > 0$ ensures that the effective gravitational constant is positive as if then, it leads to a repulsive gravity effect and instability in the gravitational field equations avoid tachyon instabilities. Tachyonic instability arises when a field has an imaginary mass, leading to an unstable system where small perturbations grow exponentially.

II **No Ghosts:** The condition $f''(R) < 0$ prevents the presence of ghost fields, which lead to quantum instabilities. This condition ensures that the scalar degree

of freedom introduced by the modification of the gravity action does not have a wrong-sign kinetic term.

1.3.2.3 Significance of $f(R)$ Gravity

I **Generalized EH Action**: $f(R)$ gravity extends the EH action by substituting the Ricci scalar R with a general function $f(R)$. This allows the theory to describe a wide range of gravitational phenomena beyond general relativity, including the possibility of explaining cosmic acceleration without dark energy.

II **Late-Time Cosmic Acceleration**: $f(R)$ gravity has been studied extensively as a potential explanation for the observed late-time acceleration of the universe. By selecting appropriate forms of $f(R)$ models can mimic dark energy and provide a modified gravitational framework to explain cosmic expansion.

III **Higher-Order Field Equations**: Unlike general relativity, where the field equations are second-order, $f(R)$ gravity leads to fourth-order differential equations. This increases the complexity but also provides more flexibility in modeling gravitational interactions.

IV **Viable Models and Constraints**: Viable models of $f(R)$ gravity must pass stringent cosmological and astrophysical tests, such as consistency with the CMB, large-scale structure and solar system experiments. Some models have been found to be consistent with observations while offering new perspectives on gravitational theory.

1.3.3 Teleparallel Gravity

Following the successful introduction of general relativity, Einstein endeavored to unify it with electromagnetism through the use of affine connections. This led him to develop a pioneering theory in which gravity is mediated by torsion rather than curvature.

The metric signature $(-1,+1,+1,+1)$ is used for flat spacetime. The line element in Cartesian coordinates is chosen to be described by

$$ds^2 = \eta_{\mu\nu} dx^\mu dx^\nu = -dt^2 + dx^2 + dy^2 + dz^2. \tag{1.3.8}$$

- $\eta_{\mu\nu}$ = Minkowski metric.

All metric tensor line elements are produced by tetrads e^i_μ and inverse tetrads e^μ_i. e^i_μ are linear basis on the spacetime manifold, give us basis for vectors on tangent space. Where,

$$g_{\mu\nu} = \eta_{ij} e^i_\mu e^j_\nu, \tag{1.3.9}$$

$$g^{\mu\nu} = \eta^{ij} e^\mu_i e^\nu_j. \tag{1.3.10}$$

To calculate the curvature and torsion of a spacetime metric one must define a connection. Curvature and torsion are properties of connection, there are infinite choices of connection among their is a connection named Levi-Civita connection in which there is only curvature but torsion is zero, Einstein use this for general relativity

$$\hat{\Gamma}^\sigma_{\mu\nu} = \frac{1}{2}\eta^{\sigma\beta}\left(\eta_{\beta\mu,\nu} + \eta_{\beta\nu,\mu} - \eta_{\mu\nu,\beta}\right). \tag{1.3.11}$$

There is another connection named Weitzenböck connection in which there is only torsion where as curvature is 0. This is used for teleparallel gravity.

$$\Gamma^\sigma_{\nu\mu} = e^\sigma_i \left(\partial_\mu e^i_\nu + \omega^i_{j\mu} e^j_\nu\right), \tag{1.3.12}$$

where,

- $\omega^i_{j\mu}$ = The components of the teleparallel spin connection.

This is used to build torsion tensor, contorsion tensor, superpotential tensor as well as torsion scalar.

1.3.3.1 Compositions

I **Torsion Tensor**: The torsion tensor is defined as

$$T^i_{\mu\nu} = 2\Gamma^i_{[\nu\mu]} = e^i_{\nu,\mu} - e^i_{\mu,\nu} + \omega^i_{j\mu} e^j_\nu - \omega^i_{j\nu} e^j_\mu = -2\Gamma^i_{[\mu\nu]}, \tag{1.3.13}$$

where,

- $A_{[\mu\nu]} = \frac{1}{2}\left(A_{\mu\nu} - A_{\nu\mu}\right)$,

- $e_{,\mu} = \frac{\partial e}{\partial \mu}$.

II **Contortion Tensor**: The contortion tensor is basically the difference between the teleparallel connection and Levi-Civita connection defined as

$$K^{\sigma}_{\mu\nu} = \Gamma^{\sigma}_{\mu\nu} - \hat{\Gamma}^{\sigma}_{\mu\nu} = \frac{1}{2}\left(T_{\mu\ \nu}^{\ \sigma} + T_{\nu\ \mu}^{\ \sigma} - T^{\sigma}_{\mu\nu}\right). \tag{1.3.14}$$

III **Superpotential Tensor**: The superpotential tensor defined as

$$S^{\mu\nu}_{\sigma} = K^{\mu\nu}_{\sigma} - \delta^{\mu}_{\sigma}T^{\rho\nu}_{\rho} + \delta^{\nu}_{\sigma}T^{\rho\mu}_{\rho} = -S^{\nu\mu}_{\sigma}. \tag{1.3.15}$$

IV **Torsion Scalar**: The torsion scalar is defined as

$$T = \frac{1}{2}S^{\mu\nu}_{\sigma}T^{\sigma}_{\mu\nu}. \tag{1.3.16}$$

1.3.3.2 *f(T)* Gravity

The $f(T)$ theory of gravity is a relatively recent modification of the Teleparallel Equivalent of General Relativity (TEGR), introduced as an extension analogous to the $f(R)$ theory of gravity. It was proposed by [Ferraro and Fiorini (2007)] over a decade ago, also studied by so many authors [Linder (2010) and Yerzhanov et al. (2010)] and it generalizes the TEGR action in a similar way that $f(R)$ gravity generalizes the EH action of general relativity.

I **Action and Field Equations of $f(T)$ Gravity**: The action for the standard teleparallel gravity is given by

$$S = \frac{1}{2\kappa^2}\int d^4x\, e\, f(T) + S_m\ , \tag{1.3.17}$$

where,

- $e = \det(e^{\mu}_{A})$, the determinant of the tetrad field e^{μ}_{A},
- $f(T) =$ An arbitrary function of T,
- $S_m =$ The action of the matter fields.

II **Significance of $f(T)$ Gravity**:

(a) **Cosmological Implications:** $f(T)$ gravity has been widely explored in cosmology, as it offers possible explanations for the accelerated expansion of the universe without needing to invoke a cosmological constant or dark energy. By choosing appropriate forms for $f(T)$, researchers can model late-time cosmic acceleration or mimic inflationary dynamics.

(b) **Lower Order Equations:** Compared to $f(T)$ gravity, the field equations in $f(T)$ gravity are of second order, making them simpler to handle both analytically and numerically. This property is one of the main advantages of $f(T)$ gravity.

(c) **Breaking of Lorentz Invariance:** One of the main challenges of $f(T)$ gravity is the inherent breaking of local Lorentz symmetry due to the specific choice of tetrads. This issue has led to concerns about the physical viability of the theory, but it remains a subject of ongoing research.

III **Application**: The $f(T)$ theory of gravity provides a promising generalization of the teleparallel formulation of gravity, offering a new avenue to explore alternative models of gravity beyond general relativity. It has shown significant potential applications [Bamba et al. (2011), Boehmer et al. (2012), Cai et al. (2011), Dent et al. (2011), Iorio et al. (2015), and Ualikhanova and Hohmann (2019)], especially in explaining the accelerated expansion of the universe, while also presenting interesting theoretical challenges, such as the issue of Lorentz symmetry breaking and the behavior under conformal and disformal transformations.

In Chapter.3, I have elaborately discussed the construction of a compact star model within the framework of $f(T)$ gravity, where the modifications to the gravitational theory are used to explore the unique characteristics and structure of these celestial objects.

1.3.4 Einstein-Gauss-Bonnet Gravity

Among the myriad possibilities of modified gravity, the Einstein-Gauss-Bonnet (EGB) theory holds a particularly distinguished place. Originally proposed by [Lanczos (1932) and Lanczos (1938)], this theory was later generalized by [Lovelock (1970, 1971)]. EGB gravity is a higher-dimensional theory that extends general relativity by incorporating a specific

combination of higher-order curvature invariants, known as the Gauss-Bonnet term. This term appears naturally in the low-energy limit of string theory and provides corrections to Einstein's field equations.

1.3.4.1 Gauss-Bonnet term $\mathcal{L}_{GB}$

$\mathcal{L}_{GB}$ is a specific combination of the Ricci scalar R, the Ricci tensor $R_{\mu\nu}$ and the Riemann tensor $R_{\mu\nu\rho\sigma}$

$$\mathcal{L}_{GB} = R^2 - 4R_{\mu\nu}R^{\mu\nu} + R_{\mu\nu\rho\sigma}R^{\mu\nu\rho\sigma}. \tag{1.3.18}$$

This term is derived from the Euler characteristic in four dimensions but contributes to the dynamics in higher-dimensional spacetime. The Gauss-Bonnet term is topological in four dimensions (it does not contribute to the field equations in $D = 4$) but has dynamical effects in higher dimensions ($D > 4$).

1.3.4.2 Action and Field Equations

The EGB gravity action in D-dimensions is an extension of the EH action with the inclusion of the Gauss-Bonnet term.

The action for EGB gravity in D-dimensions is given by

$$S = \int \sqrt{-g} \left[\frac{1}{2\kappa} \left(R + \alpha \mathcal{L}_{GB} + \mathcal{L}_m \right) \right] d^D x, \tag{1.3.19}$$

where,

- κ = the gravitational constant in D-dimensions,
- α = The EGB Lagrangian coupling constant.

To derive the field equation, the action is varied with respect to the metric tensor $g_\mu\nu$

$$\delta S = \int \sqrt{-g} \left[\frac{1}{2\kappa} \left(\delta \left(R + \alpha \mathcal{L}_{\mathrm{GB}} \right) + \delta \left(\sqrt{-g} \mathcal{L}_m \right) \right) \right] d^D x. \tag{1.3.20}$$

The modified field equations are

$$G_{\mu\nu} + \alpha H_{\mu\nu} = \kappa T_{\mu\nu}, \tag{1.3.21}$$

where,

- $H_{\mu\nu}$ = The contribution from the Gauss-Bonnet term,

$H_{\mu\nu}$ is of the form

$$H_{\mu\nu} = 2\left(RR_{\mu\nu} - 2R_{\mu\alpha\nu\beta}R^{\alpha\beta} - 2R_{\mu\alpha}R^{\alpha}_{\nu} + R_{\mu\alpha\beta\gamma}R^{\alpha\beta\gamma}_{\nu}\right) - \frac{1}{2}g_{\mu\nu}\mathcal{L}_{GB}. \tag{1.3.22}$$

1.4 Compact Object

The term compact emphasizes the unusual combination of small physical size and enormous mass that is a small volume relative to mass. The compactness leads to extreme physical conditions such as high density, intense gravity and strong magnetic fields which are not found in less dense objects like regular stars.

- **Formation of Compact Objects**:

  Compact objects are formed when stars undergo gravitational collapse after burning out their nuclear fuel. Gravitational collapse is the process by which an astronomical object, such as a star or cloud of gas, contracts under its own gravity, leading to a significant increase in density. It occurs when the internal pressure of an astronomical object is no longer sufficient to counteract the force of gravity pulling its mass inward. Stars begin in a state of hydrostatic equilibrium, where the force of gravity pulling inward is counteracted by the outward pressure generated by nuclear fusion within the star's core. For most stars, this internal pressure is provided by nuclear fusion reactions occurring in their cores, which produce energy and heat that generate an outward pressure. However, once a star exhausts its nuclear fuel, it loses this source of pressure and gravity takes over, causing the star to collapse. Let's discuss the physics behind gravitational collapse. As the star collapses, fermions, electrons, neutrons within the star obey the Pauli exclusion principle (no two fermions can occupy the same quantum state, simultaneously within a given system) creating a degeneracy pressure that can temporarily halt the collapse.

The final fate of a compact object is determined by the primary parameter, that is its mass at birth.

1.4.1 Compact Star

I have classified compact stars into two types white dwarfs and neutron stars. These objects represent the end stages of stellar evolution and each type has distinct characteristics determined by the mass and internal processes that govern their structure and stability.

1.4.1.1 White Dwarf

A white dwarf is the remnant core of a star with low to medium mass, which has depleted its nuclear fuel.

I **Formation**: Each of these stages represents a critical step in the transformation of a star into a white dwarf, from main sequence burning through to the eventual cooling and dimming phases.

(a) **Main Sequence Star**: During its life cycle it goes through the longest and most stable phase called main sequence stage. In a star's life, during this stage, the star fuses hydrogen into helium in its core through nuclear fusion, producing vast amounts of energy that counterbalances the gravitational forces trying to collapse the star. This energy is radiated out into space, causing the star to shine.

A star's position on the main sequence is primarily determined by its mass. More massive stars burn their fuel quickly and are hotter, while less massive stars burn fuel slowly and are cooler. Stars can spend millions to billions of years in this stage, depending on their mass. For example, massive stars might remain on the main sequence for only a few million years, while stars like our Sun can stay in this phase for about 10 billion years.

(b) **Red Giant Phase**: Then it goes through the red giant stage, when a star exhausts the hydrogen in its core, it can no longer maintain the pressure needed to support itself against gravity. The core contracts and heats up, while the outer layers expand dramatically, causing the star to enter the red

giant stage. As the star's outer envelope swells, its temperature drops, giving it a reddish hue.

The red giant phase is relatively short lived compared to the main sequence, typically lasting a few hundred million years. For stars like the Sun, this stage marks the final phase of active fusion before the star sheds its outer layers and involves into a white dwarf.

(c) **Planetary Nebula Formation**: After the star goes through its life cycle, including the main sequence and red giant phases, it sheds its outer layers. Meanwhile, in the core, helium begins to fuse into heavier elements like carbon and oxygen if the star is massive enough, in a process called the helium flash. The star's outer layers may become unstable contributing to the formation of planetary nebulae.

(d) **Final Stage**: This core is no longer undergoing nuclear fusion, slowly cools and contracts under the influence of gravity. The resulting object is incredibly dense, with a mass similar to that of the Sun but compressed into a volume comparable to that of Earth. The electrons within the White dwarfs are degenerate, meaning they are packed so closely together that quantum mechanical effects dominate preventing further collapse. Over billions of years, the white dwarf will continue to radiate its residual heat into space gradually cooling and fading, eventually becoming a cold, dark, "black dwarf " though the universe is not old enough for any black dwarf to exist yet. White dwarfs are key to understanding stellar evolution and most stars including our Sun will end their lives in this state.

II **Discovery**: The discovery and understanding of white dwarfs began in the early 20th century, marking a significant departure from the study of ordinary stars, the realization that a new class of stars, which were small, faint and incredibly dense existed, came about in 1910. Henry Norris Russell played a key role in identifying this new class through his studies of the Hertzsprung - Russell diagram.[Russell (1977)] He noticed that while most faint stars were red, a star now known as 40 Eridani B, part of a triple system, was both faint and white, this was a key observation leading to the identification of white dwarfs as a distinct class of stars.

[Van Maanen (1917)] also puzzled astronomers. There spectral type suggested it was too hot for its faint luminosity, again hitting at the existence of these unusual objects. Sirius B the companion to the bright star Sirius was detected visually in 1861 by Alvan Clark[Warner (1968)]. In 1910, its mass was determined and further studies revealed its effective temperature and density which were strikingly high, leading to the realization of its compact nature[Koester (1990)].

III **Types**: Initially, only 3 types of white dwarfs were known by 1920, as observational techniques improved more white dwarfs were discovered. Systematic surveys in the 20th century [Greenstein (1986) and Luyten (1970)] such as the Bruce Proper Motion survey, led to the discovery of many more white dwarfs by capitalizing on their intrinsic faintness and proper motion. Surveys focusing on the blue color and faintness of white dwarfs, such as the Polomar - Green Survey further expanded the catalogue of known white dwarfs By 1980s, catalogues such as that by [Green et al. (1986)] listed over a thousand spectroscopically identified white dwarfs.

IV **Physical Characteristic**: Early estimates of the density of white dwarfs, such as Sirius B, yielded values around $5 \times 10^4 g/cm^3$, which [Eddington (1925)] initially found " absurd ". However, more accurate measurements later [Thejll and Shipman (1986)] confirmed densities as high as $3 \times 10^6 g/cm^3$.

Chandrasekhar (1931) on the structure of white dwarfs, conducted while he was still a student, led to the discovery of the Chandrasekhar limit. His calculations showed that white dwarfs, supported by electron degeneracy pressure, have a maximum mass $1.4 M_\odot$ beyond which they can't remain stable.

V **Ultimate Fate**: However, unsolved issues remain such as the precise composition of the hydrogen and helium layers, the behavior of carbon / oxygen mixtures in the crystalline phase and the relationship between different spectral types of white dwarfs. Despite being less exotic than neutrons stars or black hole, white dwarfs remain crucial to understanding many aspects of physics and astronomy.

1.4.1.2 Neutron Star

white dwarfs and neutron stars are closely related in the evolutionary paths of stars

but represent different endpoints based on the mass of the progenitor star.

- **Progenitor Star**: A progenitor star refers to the original star from which compact star eventually forms after it has exhausted its nuclear fuel and undergo stellar evolution.

I **Formation**: Neutron stars are formed from the remnants of massive stars that have undergone a supernova explosion. When a progenitor star with an initial mass between approximately 8 to 25 times solar mass, exhausts its nuclear fuel, it can no longer support itself against gravitational collapse.

During the supernova, the core of the star collapses under gravity and the outer layers are expelled. The collapse is so extreme that protons and electrons combine to form neutrons, resulting in a dense object primarily composed of neutrons as it becomes a star nearly in between $1.4M_{\odot} - 2.9M_{\odot}$ but is only about $10 - 12km$ in radius, that is around $10^{17}kg/m^3$.

II **Discovery**: The search for neutron stars and their eventual Discovery is a fascinating story that spans several decades, beginning in the 1960s with the advent of the practical X-ray astronomy.

- It was initially expected that neutron stars could be discovered by detecting thermal radiative from the surfaces, as cooling isolated neutron stars with surface temperatures around 10^6K would emit primarily soft X-rays, which are not detectable by ground- based observations. This led to the launch of the first X-ray detectors on rockets and balloons.
- The first significant breakthrough came when [Giacconi et al. (1962)] discovered the first Cosmic X-ray source, Sco x-1, in the Scorpius constellation. This discovery was a pivotal moment in the X-ray astronomy and garnered significant interest in neutron stars. However, early attempts to link neutron stars with these newly discovered X-ray sources were unsuccessful. For example, [Bowyer et al. (1964)] measured the size of the X-ray source in the Crab Nebula, finding it to be much larger than a neutron star should be, which initially cast doubt on the presence of a neutron star there.
- Ironically the Crab Nebula Fig.1.1 indeed contained a neutron star, the fa-

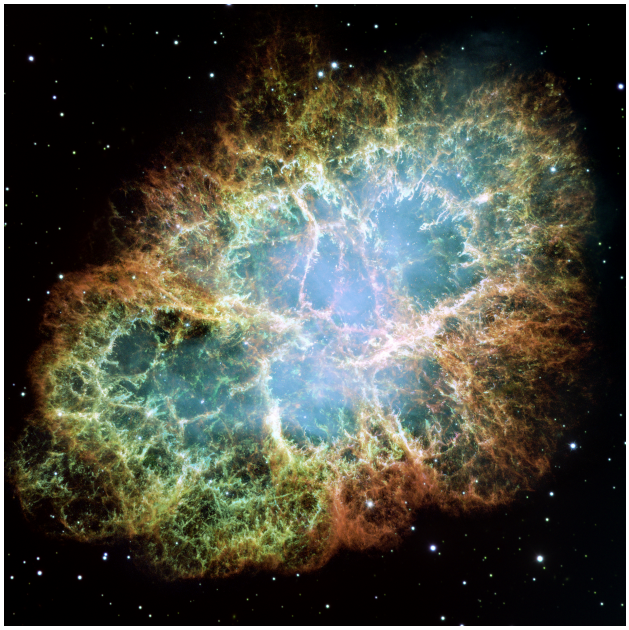

Fig. 1.1. The Beautiful Crab Nebula.(NASA (2000))

mous Crab Pulsar, but it was concealed within a compact pulsar nebula. The detection of the Crab Pulsar provided crucial evidence supporting this model, cementing the connection between pulsars and neutron stars. While Hewish received the Nobel Prize in 1974 for this discovery, [Hewish (1975)] controversy remains over the exclusion of Jocelyn Bell in the award, despite her crucial role in the discovery.

III **Types**: There are various types of neutron Star, such as

- **Radio Pulsars**: Emit regular pulses of radio waves due to their rapid rotation and strong magnetic fields.
- **X-ray Pulsars**: Emit X-rays due to accretion of material from a companion star. Often found in binary systems.
- **Magnetars**: Neutron Star with extremely strong magnetic fields, emit bursts of high-energy gamma rays and X-rays and so on.

IV **Physical Characteristics**: In the period following World War II and leading up to the discovery of neutron stars, theoretical progress advanced significantly in understanding these enigmatic objects. Initially researchers focused on constructing models for the equation of state of dense stellar matter with key contributions from [Harrison et al. (1958)] who explored how nuclear forces and interactions

between various particles could affect neutron star structure and stability.

[Bahcall and Wolf (1965)] who identified key neutrino processes and their role in the thermal evolution of neutron stars. Additionally, research into neutron star thermal evolution, including early estimates of cooling rates and models of thermal emissions, laid the groundwork for interpreting observations of these stars, setting the stage for their eventual Discovery and detailed study.

The layers of Neutron Stars are,

- The outermost layer of a neutron star is the crust, which is composed of a lattice of atomic nuclei and a sea of electrons.
- As if one moves deeper into the crust, the density increases and the nuclei become more neutron rich.
- Below the crust lies the outer core, which contains a superfluid of neutrons along with a smaller fraction of protons and electrons.
- The composition of the inner core is less certain and is the subject of active research. It may contain exotic states of matter such as hyperons, pion condensates, or even deconfined quark matter, Bose-Einstein condensates (BEC). This will be discussed in the next part of this chapter.

V **Ultimate Fate**: The ultimate fate of a neutron star depends on various factors including its mass and environment such as if the neutron star gains enough mass, it can collapse into a black hole or as neutron star lose rotational energy and their magnetic fields decay, they may eventually cease to emit significant radiation, becoming invisible as “dead” neutron stars.

1.4.2 Black Hole

A black hole is a region of space where the gravitational pull is so intense that nothing, not even light, can escape from it. The classical explanation is that the escape velocity in a black hole exceeds the speed of light. However, this explanation, rooted in Newtonian physics, does not fully capture the predictions of general relativity.

1.4.2.1 Formation

Black holes are typically formed from the remnants of massive stars that have ended their life cycles. When such a star exhausts its nuclear fuel, it can undergo a supernova explosion and if the remaining core is massive enough, it will collapse under its own gravity to form a black hole.

According to general relativity, a black hole is a region where space itself is falling faster than the speed of light. Inside the event horizon (the boundary of black hole) space is pulled inward at a rate faster than light can more outward, making escape impossible.

1.4.2.2 Types According to Mass

According to the mass there are mainly four types of black holes.[Frolov and Zelnikov (2011)]

I **Primordial Black Holes**: Can range from very small , mass upto $1M_{\odot}$.

II **Stellar-Mass Black Holes**: They are commonly found throughout galaxies, including the Milky Way, mass range upto $3M_{\odot}$.

III **Intermediate-Mass Black Holes**: They are hypothesized to exist in star clusters or dwarf galaxies, though observational evidence is limited, mass range upto $10^3 M_{\odot}$.

IV **Supermassive Black Holes**: Supermassive black holes are found at the centers of most large galaxies, including the Milky Way (e.g. Sagittarius A*), mass range upto $10^5 M_{\odot} - 10^9 M_{\odot}$.

1.4.2.3 Eminent Black Holes

I **Schwarzschild Black Hole [Non Rotating, Non Charged Black Hole]**: The Schwarzschild metric was discovered by [Schwarzschild (1916)] in 1915, shortly after Einstein formulated his GTR. Unfortunately, Schwarzschild passed away in 1916, shortly after his discovery. The Schwarzschild metric describes the spacetime around spherically symmetric, non-rotating mass like a black hole. In the co-ordinate system (t, r, θ, ϕ), where t and r represents time, radial distance

respectively and θ, ϕ are angular co-ordinates, the metric is

$$ds^2 = -\left(1 - \frac{2M}{r}\right) dt^2 + \left(1 - \frac{2M}{r}\right)^{-1} dr^2 + r^2 d\Omega^2, \tag{1.4.1}$$

where, $d\Omega^2 = d\theta^2 + sin^2\theta d\phi^2$ is the metric on a unit 2-sphere, M is the mass of the black hole.

Features:

- The Schwarzschild geometry is asymptotically flat, meaning it approaches the flat spacetime of special relatively at large distances from the mass.
- This spacetime is stationary, meaning there exists a time like co-ordinate t such that the metric does not change over time.
- This spacetime is also static, meaning that the time co-ordinate t is orthogonal to the spatial coordinates. In a static spacetime, observers who are at rest with respect to these co-ordinates will not observe any movement among themselves over time.
- This geometry is spherically symmetric, meaning that the space time looks the same in all directions around the central mass.
- The Schwarzschild radius $r_s = \frac{2GM}{c^2}$ defines the event horizon of a black hole.

II **Reissner-Nordström (RN)[Non Rotating but Charged Black Hole]**: RN geometry describes a black hole that possesses both mass M and electric charge q, was independently discovered by [Nordström (1918), Reissner (1916), and Weyl (1917)]. It is a solution to Einstein's field equations that generalizes the Schwarzschild solution by including the effects of electric charge. The RN metric is

$$ds^2 = -\left(1 - \frac{2M}{r} + \frac{q^2}{r^2}\right) dt^2 + \left(1 - \frac{2M}{r} + \frac{q^2}{r^2}\right)^{-1} dr^2 + r^2 d\Omega^2, \tag{1.4.2}$$

where, $d\Omega^2 = d\theta^2 + sin^2\theta d\phi^2$.

Features

- The R-N black hole is stationary.
- The R-N black hole is also static.

- Horizons are important because they mark boundaries in spacetime where different physical behaviors occur. The horizons are located from the following Eq.(1.4.3),

$$\left(1 - \frac{2M}{r} + \frac{q^2}{r^2}\right) = 0. \tag{1.4.3}$$

From this, it is obtained,

$$r_{\pm} = M \pm \sqrt{M^2 - q^2}. \tag{1.4.4}$$

Where,

- r_+ is called the outer event horizon.
- r_- is called the inner Cauchy horizon.

- The Einstein tensor for the RN is diagonal: $G^{\mu}_{\nu} = 8\pi T^{\mu}_{\nu}$ where the energy-momentum tensor T^{μ}_{ν} describes a radial electric field $E_1 = \frac{q}{r^2}$.
  The tension associated with the radial electric field causes a gravitational repulsion that counteracts the usual gravitational attraction near the black hole, leading to unique behaviors, particularly near the inner horizon.
  The Weyl scalar for R-N geometry is $C_1 = -\frac{M}{r^3} + \frac{q^2}{r^4}$ as r the Weyl scalar diverges, indicating a singularity where the curvature of spacetime become infinite.

III **Kerr Black Hole[Rotating, Non Charged Black Hole]**: [Kerr (1963)] provided the exact solution of Einstein field equations, it describes an axially symmetric, rotating, stationary black hole, the metric is

$$\begin{aligned} ds^2 = &-\left(1 - \frac{2Mr}{\rho^2}\right) dt^2 - \frac{4Mrasin^2\theta}{\rho^2} d\phi dt + \frac{\rho^2}{\Delta} dr^2 \\ &+ \rho^2 d\theta^2 + \left(r^2 + a^2 + \frac{2Mra^2 sin^2\theta}{\rho^2}\right) sin^2\theta d\phi^2 \end{aligned} \tag{1.4.5}$$

where,

- a = angular momentum per unit mass,
- $\rho^2 = r^2 + a^2 cos^2\theta$,
- $\Delta = r^2 - 2Mr + a^2$,

- when $a \to 0$ it becomes Schwarzschild black hole.

IV **Kerr Newman Black Hole[Rotating,Charged black hole]**: Shortly after kerr's work [Kerr (1963), Newman et al. (1965)] extended the solution to include electrically charged black holes, resulting in what is now known as the Kerr Newman (K-N) metric. The K-N metric is expressed using Boyer - Lindquist coordinates,

$$ds^2 = -\frac{\Delta}{\rho^2}\big(dt - asin^2\theta d\phi\big)^2 + \frac{\rho^2}{\Delta}dr^2 + \rho^2 d\theta^2 + \frac{sin^2\theta}{\rho^2}\big((r^2+a^2)d\phi - adt\big)^2 \quad (1.4.6)$$

where,

- $\Delta = 1 - \frac{2Mr}{R^2} + \frac{e^2}{R^2}$
- $\rho = \sqrt{r^2 + a^2 cos^2\theta}$
- a : angular momentum per unit mass.

when both $a = 0$ and $e = 0$, this metric reduces to Schwarzschild black hole metric.

The K-N geometry exhibits time translation symmetry and rotational symmetry around its axis, which are reflected in the killing vectors corresponding to the time and azimuthal coordinates.

There are various types of black holes. Black holes are widespread in the universe. While they cannot be observed directly, they reveal their presence through the effects they have on their surroundings. Black holes are observed in X-ray binary systems, in active galactic nuclei at the centers of galaxies, including our own. The first direct detection of gravitational waves occurred on September 14, 2015, by LIGO, [Abbott et al. (2016)] consistent with the merger of two black holes.

1.5 Wormhole

Wormholes, theoretical constructs speculated to exist within spacetime, have been a source of intrigue and investigation in the fields of theoretical physics and astrophysics. These traversable routes through spacetime, largely theoretical, still intrigue the scientific community because of their potential significance in comprehending the fundamental laws of the

universe, particularly within the context of Einstein's theory of general relativity. The theoretical framework for wormholes was first developed by Flamm in 1916 [Flamm (1916)]. Later on, a comprehensive exploration of wormholes was undertaken by Albert Einstein and Nathan Rosen in their seminal paper in 1935 [Einstein and Rosen (1935)] , commonly known as the Einstein-Rosen bridge. In the 20th century, the exploration of black holes and wormholes intersected as physicists delved deeper into the mathematical and physical principles governing these extraordinary phenomena. One of the most notable papers that advanced our comprehension of wormholes was published in 1988. This paper delved into the theoretical aspects of traversable wormholes and their possible applications in interstellar travel [Morris and Thorne (1988)]. This research propelled wormholes into the forefront of astrophysical inquiry and introduced the notion of "exotic matter" as a crucial element for stabilizing these theoretical pathways through spacetime. In the literature, numerous authors have extensively examined various aspects of traversable wormhole (TW) geometries, as evidenced in References[Almheiri et al. (2020), Bronnikov and Kim (2003), Hawking (1988), Lemos et al. (2003), Penington et al. (2022), and Visser (1989)]. The line element for a static, spherically symmetric traversable wormhole is given by

$$ds^2 = -e^{2\Phi(r)}dt^2 + \frac{dr^2}{1-\frac{S(r)}{r}} + r^2\left(d\theta^2 + \sin^2\theta\, d\phi^2\right), \tag{1.5.1}$$

where,

- $\Phi(r)$ is the redshift function, which determines the gravitational time dilation,
- $S(r)$ is the shape function, which determines the spatial shape of the wormhole,
- r is the radial coordinate with a minimum value at the throat of the wormhole, i.e., at $r = r_{th}$, $S(r_{th}) = r_{th}$.

1.5.1 Einstein Rosen Bridge

The Einstein-Rosen bridge essentially connects two asymptotically flat regions [Einstein and Rosen (1935)], effectively linking two distinct universes or different parts of the same universe. This bridge appears as a non-traversable wormhole, meaning that an object cannot pass through it from one side to the other. The idea was rooted in an attempt to understand

singularities and elementary particles within the framework of general relativity, without the singularities that plagued classical theories of particles.

In modern physics, the Einstein-Rosen bridge is interpreted as part of the maximally extended Schwarzschild geometry, which describes the structure of black holes.

They took the metric Eq.(1.4.1) and give the coordinate change

$$u^2 = r - 2M, \tag{1.5.2}$$

get the Einstein-Rosen form

$$ds^2 = -\frac{u^2}{u^2 + 2M} dt^2 + 4\left(u^2 + 2M\right) du^2 + (u^2 + 2M)^2 d\Omega^2. \tag{1.5.3}$$

Where, $-\infty < u < +\infty$.

The "bridge" refers to the non-traversable connection between two regions that arise from a coordinate transformation removing the singularity at the Schwarzschild radius. The The narrowest region of the geometry is referred to as the "throat" where as the nearby region is called "bridge". [Einstein and Rosen (1935)], here, they discuss two particular types of "bridges", "neutral" and "quasicharged". Later, [Visser (1995)] using those two concept of "bridges" formulated a generalized bridge.

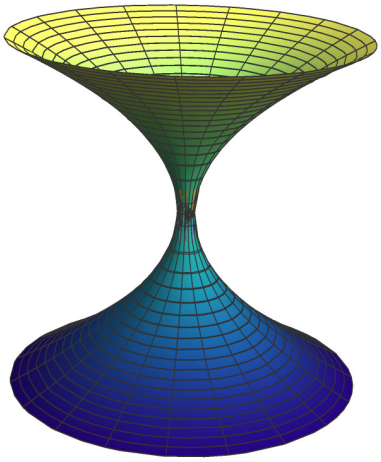

Fig. 1.2. A 3D surface of wormhole.

In Fig.1.2, a 3D surface of a traversable wormhole is depicted, produced in Mathematica, using specific parameters outlined in Chapter.7 of this thesis. The figure offers a captivating visual representation of a traversable wormhole, capturing its essence as an accessible structure that can be explored. This visualization embodies the concept of a wormhole that not only exists in theory but can also be conceptualized as a conduit for travel across vast cosmic distances.

1.5.2 Taxonomy of Wormholes

The taxonomy of wormholes, as described in [Visser (1995)], categorizes different types of wormholes based on their geometric and topological properties. Here's an overview of the taxonomy presented below

1.5.2.1 Basic Distinction: Lorentzian vs. Euclidean Wormholes

The basic distinction between Lorentzian and Euclidean wormholes lies in the type of manifold in which they exist.

I **Lorentzian Wormholes**: These wormholes are embedded in Lorentzian (pseudo-Riemannian) manifolds, which are associated with spacetime in general relativity. These are the kinds of wormholes often studied in connection with traversability and exotic matter.

II **Euclidean Wormholes**: These are based on Riemannian manifolds with Euclidean signature metrics, typically arising in quantum gravity theories. However, experimentally, real physics happens in Lorentzian signatures, so the status of Euclidean wormholes is considered more theoretical.

1.5.2.2 Variations of Lorentzian Wormholes

Within Lorentzian wormholes, the classification is further broken down into,

I **Permanent Wormholes**: These do not violate classical topology change theorems and exist without significant changes in spacetime structure.

II **Quasipermanent Wormholes**: These exist for a finite duration, violating classical topology change theorems. They may require exotic physics like quantum gravity or violations of causality to explain their creation and destruction.

III **Transient Wormholes**: These are temporary structures in spacetime, popping in and out of existence. The topology of these involves higher-dimensional spaces that violate the classical topology change theorems. They also require more extreme manipulations of classical general relativity to exist.

1.5.2.3 Macroscopic vs. Microscopic Wormholes

I **Macroscopic Wormholes**: These are large-scale structures that could, in theory, connect different regions of the universe and allow for traversability. Their "active" regions are large enough to have physical meaning within general relativity.

II **Microscopic Wormholes**: These are tiny structures, possibly at the quantum scale, where their size is close to the Planck length. Quantum gravity effects would dominate in these wormholes and their existence would likely be short-lived.

Galaxies, compact stars, black holes and wormholes are all interconnected through the dynamics of spacetime and gravity. In essence, gravitational lensing serves as a bridge connecting our understanding of these objects, revealing the influence of massive bodies on the fabric of spacetime. In the next section this gravitational lensing is discussed elaborately.

1.6 Gravitational Lensing and Shadow

The concept of gravitational lensing was first proposed by Albert Einstein in the early 20th century, based on his theory of General Relativity. In 1915, Einstein predicted that light from a distant star would bend as it passed near a massive object due to the curvature of spacetime caused by gravity. Although he initially considered the effect to be too small to observe, he later published a more detailed paper in 1936 discussing the concept of gravitational lensing, though he did not actively seek observational confirmation [Einstein (1936)]. The first observational confirmation of gravitational lensing occurred in 1919, led by the British astronomer Sir Arthur Eddington. During a solar eclipse on May 29, 1919, Eddington's expedition measured the apparent shift in the position of stars near the Sun's edge. The observed bending of starlight matched Einstein's predictions, providing

strong evidence for General Relativity and indirectly confirming the idea of gravitational lensing. Over the years, gravitational lensing has been classified into weak, strong and microlensing, with strong-gravitational lensing offering the best opportunity to study the curved spacetime.

1.6.1 Gravitational lensing by Black Hole

The study of strong gravitational lensing around black holes has evolved significantly since Darwin's early exploration of photon orbits around Schwarzschild black holes [Darwin (1959)]. These studies reveal that dark matter can significantly impact the observables of strong lensing, such as the size of the black hole shadow, the positions of relativistic images and time delays.

To investigate the strong gravitational lensing phenomena, here, a static, spherically symmetric metric is considered as

$$ds^2 = -f(r)dt^2 + \frac{1}{h(r)}dr^2 + r^2(d\theta^2 + \sin^2\theta d\phi^2). \tag{1.6.1}$$

The analysis is simplified by confining the photon's trajectory around the black hole to the equatorial plane ($\theta = \frac{\pi}{2}$). The Lagrangian equation is used to express the equation governing the motion of photons around a black hole Eq.(1.6.1)

$$\begin{aligned}\mathcal{L} &= -\frac{1}{2}g_{\mu\nu}\dot{x}^\mu\dot{x}^\nu \\ &= \frac{1}{2}(f(r)dt^2 - \frac{1}{h(r)}dr^2 - r^2(d\theta^2 + \sin^2\theta d\phi^2)) = \epsilon.\end{aligned} \tag{1.6.2}$$

Here, $\dot{x}^\mu$ indicates the four-velocity of a light ray, with the dot indicates derivative w.r.t. the affine parameter τ. The parameter ϵ can take values of 1, 0 or -1 which correspond to timelike, null or spacelike geodesics, respectively. The metric coefficients in Eq.(1.6.1), result in the inability to explicitly solve for the coordinates t and θ, leading to the emergence of two conserved quantities the energy E of the particle and its angular momentum L, respectively which are defined as follows [Tsukamoto (2017)]

$$E = -g_{\mu\nu}t^\mu\dot{x}^\nu = f(r)\dot{t},$$

$$L = g_{\mu\nu}\phi^{\mu}\dot{x}^{\nu} = r^2\dot{\phi}.$$

The photon follows null geodesics around the black hole, indicating $\epsilon = 0$. The null geodesics derived from Eq.(1.6.2) are as follows

$$\dot{t} = \frac{dt}{d\tau} = \frac{E}{f(r)}, \tag{1.6.3}$$

$$\dot{\phi} = \frac{d\phi}{d\tau} = \frac{L}{r^2}, \tag{1.6.4}$$

$$\dot{r} = \frac{dr}{d\tau} = \pm\sqrt{h(r)\left(\frac{E^2}{f(r)} - \frac{L^2}{r^2}\right)}. \tag{1.6.5}$$

The symbol $\pm$ in $\dot{r}$ indicates the direction of radial motion, for ingoing and outgoing trajectories, respectively. Eq.(1.6.5) can be written as

$$\left(\frac{dr}{d\tau}\right)^2 + V_{eff} = 0. \tag{1.6.6}$$

Without loss of generality, it can be proceed by setting $E = 1$. Thus, the effective potential function can be obtained as

$$V_{eff} = h(r)\left(\frac{L^2}{r^2} - \frac{1}{f(r)}\right). \tag{1.6.7}$$

where as the function $V_{\text{eff}}(r)$ satisfies specific conditions

$$V_{\text{eff}}(r) = \frac{dV_{\text{eff}}(r)}{dr} = 0, \tag{1.6.8}$$

$$\frac{d^2V_{\text{eff}}(r)}{dr^2} > 0, \tag{1.6.9}$$

$$\frac{d^2V_{\text{eff}}}{dr^2} < 0. \tag{1.6.10}$$

Eq.(1.6.9) stands for stable and Eq.(1.6.10) for unstable circular orbit. Consequently, photon rays approaching the black hole from infinity, reaching the closest distance r_0 with a minimum impact parameter, trace unstable circular orbits near the black hole and form a photon sphere at radius r_{ph}. Therefore, the photon sphere radius r_{ph} is given by the largest real solution of the following equation

$$2f(r_{ph}) - r_{ph}f'(r_{ph}) = 0. \tag{1.6.11}$$

1.6.2 Strong Gravitational Lensing by Black Holes

To determine the strong deflection angle of a light ray traveling in the equatorial plane ($\theta = \frac{\pi}{2}$) around a static, spherically symmetric black hole, the metric from Eq.(1.6.1) was reformulated using dimensionless variables, scaling quantities in terms of the radius $2M$. This helps to deepen our understanding of how these parameters affect the strong gravitational lensing phenomena in the vicinity of a black hole. By expressing the metric in dimensionless form, Eq.(1.6.1) can be rewritten as

$$d\bar{s}^2 = -A(r)dt^2 + B(r)dr^2 + C(r)d\phi^2. \tag{1.6.12}$$

When particles approach their nearest distance, $r = r_0$ to the black hole, where $\frac{dr}{d\tau} = 0$, the quantity u_0 can be defined as the minimum impact parameter, corresponding to the closest distance r_0 [Bozza (2002)].

$$u_0 = \frac{r_0}{\sqrt{A(r_0)}}. \tag{1.6.13}$$

The strong deflection angle in a static, spherically symmetric spacetime, expressed as a function of the closest approach distance r_0, can be read as [Claudel et al. (2001), Virbhadra and Ellis (2002), and Zhao and Xie (2017)]

$$\alpha_D(r_0) = I(r_0) - \pi = 2\int_{r_0}^{\infty} \frac{\sqrt{B(r)}dr}{\sqrt{C(r)}\sqrt{\frac{A(r_0)C(r)}{A(r)C(r_0)} - 1}}dr - \pi. \tag{1.6.14}$$

The strong deflection angle $\alpha_D(r_0)$ depends on r_0 and r_{ph} while $r_0 \approx r_{ph}$, it increases. To simplify the analysis, a new variable is introduced, z as

$$z = 1 - \frac{r_0}{r}. \tag{1.6.15}$$

For, $r_0 \approx r_{ph}$, the strong deflection angle becomes

$$\alpha_D(u) = -\bar{a}\ log\left(\frac{u}{u_{ph}} - 1\right) + \bar{b} + \mathcal{O}((u - u_{ph})log(u - u_{ph})), \tag{1.6.16}$$

where,

$$\bar{a} = \sqrt{\frac{2A(r_{ph})B(r_{ph})}{A(r_{ph})C''(r_{ph}) - A''(r_{ph})C(r_{ph})}}, \tag{1.6.17}$$

$$\bar{b} = -\pi + I_R(r_{ph}) + \bar{a}\ log\left[r_{ph}^2\left(\frac{C''(r_{ph})}{C(r_{ph})} - \frac{A''(r_{ph})}{A(r_{ph})}\right)\right]. \tag{1.6.18}$$

Here,

$$I_R(r_{ph}) = 2\int_0^1 \left(r_{ph}\left[\sqrt{\frac{B(z)}{C(z)}}\left(\frac{A(r_{ph})}{C(r_{ph})}\frac{C(z)}{A(z)} - 1\right)\frac{1}{(1-z)^2}\right] - \frac{\bar{a}}{z\ r_{ph}}\right)dz, \tag{1.6.19}$$

which is evaluated numerically.

1.6.3 Lensing Observables

Next, the observable characteristics of strong gravitational lensing effects by a black hole is studied. It is to be considered that both the source and the observer to be nearly aligned along the optical axis, situated within a flat spacetime framework. Furthermore, it is assumed that the curvature influences the strong deflection angle only near the black hole (lens), as outlined in [Bozza (2010)]. The source is assumed to be located behind the lens and the corresponding lens equation is provided in Fig.1.3 [Bozza (2008), Bozza et al. (2001), and Islam et al. (2020)]

$$\beta = \theta - \frac{D_{ls}}{D_{os}}\Delta\alpha_n. \tag{1.6.20}$$

Here, the offset deflection angle, denoted as $\Delta\alpha_n$ is the difference between the primary deflection angle $\alpha_D(\theta)$ and $2n\pi$ where, n represents the number of photon revolutions around the black hole.

The angle β is the angular position of source w.r.t. the optical axis and θ is the angular position of the image as seen by the observer without the gravitational lens. This is the true angle from the observer to the source in the absence of any lensing effects, depicted in Fig.1.3.

The distances D_{ol} is the distance between the observer and the lens, D_{ls} is the distance between the lens and the source and D_{os} represents the distance between the observer and

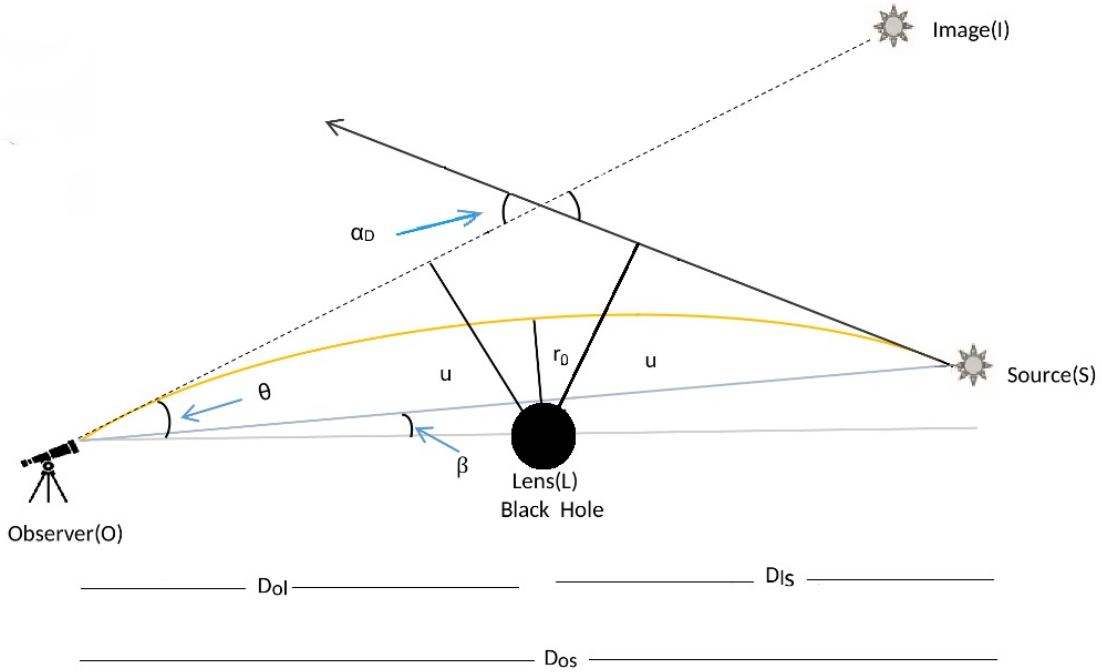

Fig. 1.3. A schematic diagram illustrating gravitational lensing, where a light ray with impact parameter u, originates from a source positioned at an angle β. As the ray passes through the gravitational lens, it is deflected by an angle α_D. The observer detects the deflected ray at an angle θ.

the source, with,

$$D_{os} = D_{ol} + D_{ls}.$$

Using Eqs. (1.6.16) and (1.6.20), the angular position of the n^{th} relativistic image can be expressed as

$$\theta_n = \theta_n^0 - \frac{u_{ph} e_n (\theta_n^0 - \beta) D_{os}}{\bar{a} D_{ol} D_{ls}}, \tag{1.6.21}$$

where,

$$e_n = e^{\frac{\bar{b} - 2n\pi}{\bar{a}}},$$

$$\theta_n^0 = \frac{u_{ph}(1 + e_n)}{D_{ol}},$$

.

Here, θ_n^0 represents the angular position of the image at $\theta = 2n\pi$.

The magnification for the n-th relativistic image is given by[Bozza (2002)]

$$\mu_n = \left(\frac{\beta}{\theta}\frac{d\beta}{d\theta}\right)^{-1}\Big|_{\theta_0} = \frac{u_{ph}^2(1+e_n)e_n D_{os}}{\beta \bar{a} D_{ls} D_{ol}^2}. \tag{1.6.22}$$

The Eq.(1.6.22) indicates that the first relativistic image exhibits the highest brightness, with the magnification is exponentially decreasing as the winding number n increases. Consequently, the brightness of the first image exceeds that of the following relativistic images. Notably, Eq.(1.6.22) becomes diverges as $\beta \to 0$, indicating that perfect alignment maximizes the probability of detecting relativistic images.

In this scenario, focus on the brightest image, namely the outermost image θ_1, which appears as a single resolved image. On the other hand, the remaining inner set images are tightly clustered together at θ_∞ (i.e., $\theta_n|_{n\to\infty} = \theta_\infty$). By using the deflection angle Eq.(1.6.16) and the lens equation Eq.(1.6.20), strong lensing observables can be calculated, including the angular position θ_∞, Einstein's ring θ_n^E, the angular separation S and the relative magnification r_{mag} of the relativistic images. These three quantities can be precisely defined based on the formulations presented in Bozza (2002) and Kumar et al. (2022b).

$$\theta_\infty = \frac{u_{ph}}{D_{ol}}, \tag{1.6.23}$$

$$S_a = \theta_1 - \theta_\infty \approx \theta_\infty e^{\frac{(\bar{b}-2\pi)}{\bar{a}}}, \tag{1.6.24}$$

$$r_{mag} = \frac{\mu_1}{\Sigma_{n=2}^{\infty}\mu_n} \approx \frac{5\pi}{\bar{a}\ log(10)}. \tag{1.6.25}$$

If the observables θ_∞, S and $r_{\rm mag}$ are measured through observations, the lensing coefficients $\bar{a}$, $\bar{b}$ and the critical impact parameter $u_{\rm ph}$ can be determined by solving Eqs. (1.6.23), (1.6.24) and (1.6.25) in reverse, respectively. This allows for a direct comparison between the observed data and the theoretically derived values.

1.6.4 Shadow of Black hole and Wormhole

The shadow of a compact object is one of the most significant observables in gravitational lensing. The study of black hole shadows has garnered significant attention, particularly following the groundbreaking achievement of the EHT, which captured the first-ever image of a black hole shadow in the galaxy $M87$. This shadow arises due to the bending of light caused by the strong gravitational field near the event horizon, creating a dark region

bordered by bright photon rings. Shadows have been widely investigated for black holes [Afrin and Ghosh (2023) and Molla and Debnath (2023b)]. I have shown a schematic diagram giving an idea how the shadow of a non rotating axially symmetric black hole looks like in Fig.1.4, where r_s is the Schwarzschild radius. In Chapter.6, Sec.6.3 shadow of a non rotating black hole is depicted through strong gravitational lensing.

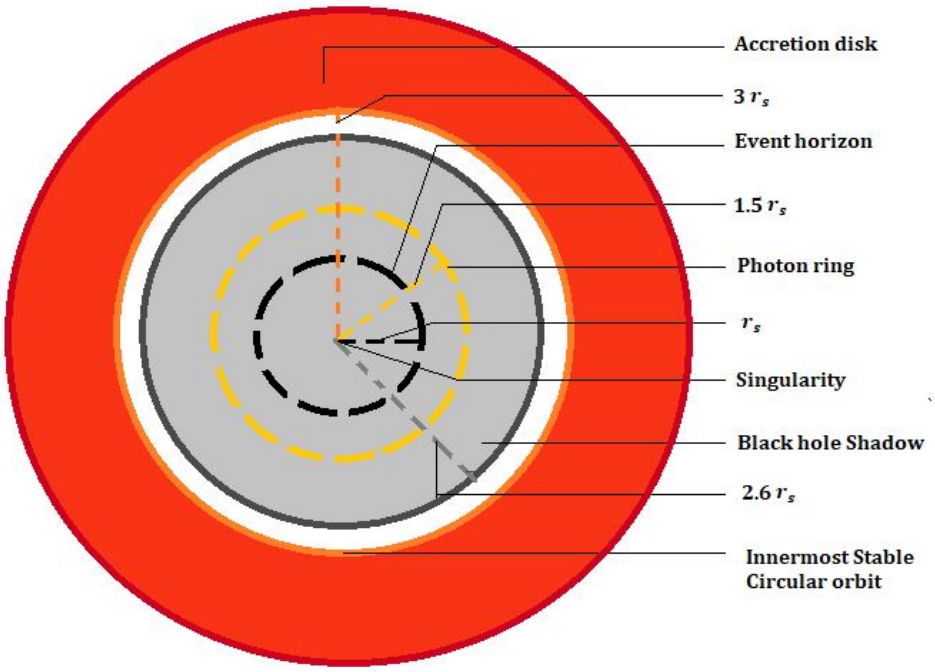

Fig. 1.4. A schematic diagram of the structure of Shadow of a non rotating axially symmetric black hole is shown here.

While black hole shadows have been the focus of extensive research, similar principles can be extended to wormholes, leading to the intriguing concept of a wormhole shadow. In this scenario, light would bend around the throat of the wormhole, potentially creating a detectable dark region.

Among the fascinating aspects of wormholes, the investigation of their shadows and associated gravitational lensing effects provides a unique opportunity to probe their properties. In astrophysics, a shadow refers to the apparent outline of an object as seen by a distant observer. This concept is tightly linked to gravitational lensing, where light bends around massive objects. A wormhole's gravitational field can bend light in such a way that it creates multiple images or a bright ring around its shadow. Unlike black holes, which have a distinct photon sphere shaping their shadow, wormholes can produce a more intricate shadow pattern due to light that traverses or loops around the wormhole's throat. In Chapter.7,

Sec.7.6 shadow cast by a non rotating wormhole has been analyzed. This section offers an deep analysis of the non rotating wormhole, providing both its mathematical framework and physical interpretation. Physical analysis for rotating wormhole also shown in Chapter.8 The study of shadows in wormholes [Alloqulov et al. (2024) and Shaikh (2022)] is an emerging field with its own unique challenges and opportunities. The shadows cast by wormholes offer vital information regarding their size, structure and the nature of the exotic matter inside them. These investigations not only deepen our understanding of wormholes' theoretical viability but also explore the possibility of traversable wormholes and their observable signatures, potentially revolutionizing our understanding of spacetime. The recent image of the shadow of the supermassive black hole shown in Fig.1.5 at the centre of $M87$ galaxy captured by the Event Horizon Telescope, provided strong evidence for the existence of black holes [Akiyama et al. (2019)].

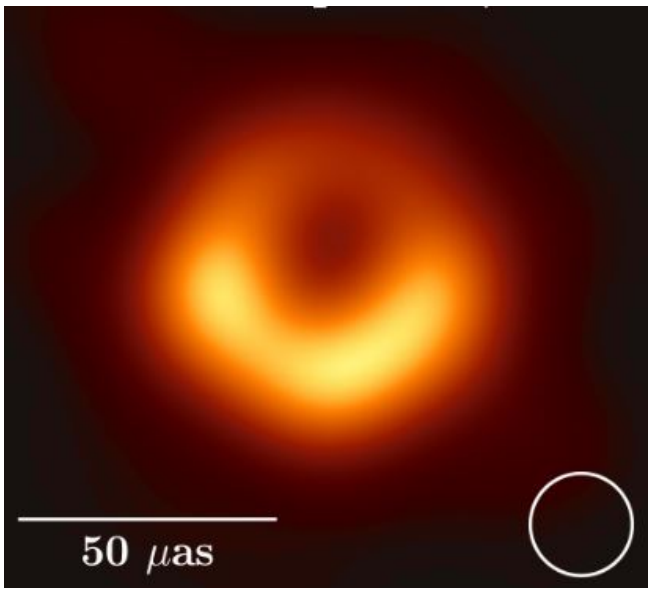

Fig. 1.5. Shadow of the supermassive black hole $M87^*$ captured by EHT in April, 2017 [Akiyama et al. (2019)].

1.7 Bose Einstein Condensate

In the labyrinthine interplay of quantum statistical paradigms, the germination of Bose–Einstein Condensation (BEC) can be traced to the alchemical musings of 1924, wherein [Wali (2006)] the Bengali Scientist Satyendra Nath Bose transmuted the etheric quanta of light into a statistical tableau, subsequently extrapolated by the illustrious Albert Einstein into a specula-

tive condensate of noninteracting atomic entities. This cryptic phase transition, enigmatic in its quantum statistical essence, envisaged a coagulation of atoms into a primordial ground state, cocooned within the spectral confines of low-temperature realms. For epochs, these theoretical reveries meandered in the arcane recesses of academic curiosity, bereft of empirical resonance, until the epochal synthesis of 1995 [Anderson et al. (1995) and Davis et al. (1995)], when the experiment orchestrated a tangible manifestation of this elusive quantum phenomenon, the first successful observation of BEC at MIT. They achieved BEC in vapours of Rubidium-87 (^{87}Rb) [Anderson et al. (1995)] and Sodium-23 (^{23}Na) [Davis et al. (1995)], marking a significant milestone in quantum physics.

A vivid historical background on theory as well as experiment can be created based on the source material from the book [Pitaevskii and Stringari (2016)], as this wasn't still just the theoretical conga line.

1.7.1 Historical Background

- During 1925 Albert Einstein, inspired by S. N. Bose's work on the statistical description of photons, predicted a phase transition in a gas of noninteracting atoms, leading to the formation of a Bose-Einstein Condensate (BEC).
- The discovery of superfluidity in helium to BEC was linked [London (1938)].
- Landau developed a theory of superfluidity in 1941, introducing the two-fluid model of helium.
- The first microscopic rendition of BEC in interacting Bose gases, bringing in a deeper understanding of BEC in relation to superfluidity was concocted [Bogoliubov (1947)].
- In 1950s the relationship between BEC and superfluidity was further explored by [Penrose (1951)], Onsager and others, focusing on the concept of nondiagonal long-range order. This work led to the prediction and discovery of quantized vertices, key features of superfluid behavior.

1.7.2 Advancements in Experimentation

- In the 1970s, experimental efforts shifted to study BEC in dilute atomic gases, initially focusing on hydrogen.
- Later, in the 1980s, with the development of laser cooling and magneto-optical trapping, it became possible to cool and trap alkali atoms at temperatures close to absolute zero.
- These advances were crucial in the final realization of BEC in 1995, as they enabled scientists to further cool trapped atoms using evaporative cooling, eventually leading to the observation of Bose-Einstein condensation.

1.7.3 Physical Phenomena

- **Relation with de-Broglie Wavelength:** BEC is a pure quantum phenomenon, at the heart of this phenomenon is wave-particle duality, which states that every quantum particle exhibits both particle-like and wave-like properties. The wavelength associated with a particle, known as the de-Broglie wavelength in the Eq.(1.7.1) plays a crucial role in determining whether quantum mechanical effects become significant. As the temperature of a gas decreases, the de-Broglie wavelength of its atoms increases [Jochim et al. (2003)]. The formula for the de-Broglie wavelength is

$$\lambda_{dB} = \sqrt{\frac{2\pi\hbar^2}{mk_BT}} \tag{1.7.1}$$

  where,

  - T: Temperature,
  - m: The mass of the atom
  - $\hbar$: The reduced Planck's constant
  - k_B: Boltzmann's constant

  As the temperature drops, the de-Broglie wavelength increases and when it becomes comparable to the average distance between atoms, significant quantum effects emerge. Under these conditions, the atomic wave packets overlap, leading to the BEC phase

transition. This phase transition occurs at a critical temperature T_c, where atoms collectively enter the ground state, forming a BEC and behave as a single macroscopic quantum entity, describable by a single wave function.

- **Critical Temperature:**

  When a gas of bosons is cooled down to the point where the de-Broglie Wavelength of the particles becomes comparable to the inter-particle distance, they begin to occupy the same quantum state, leading to Bose - Einstein Condensation [Jochim et al. (2003)]. The critical temperature T_c for this to occur in a harmonic trap is given by

$$T_c = \frac{\hbar_\omega}{k_B} \left(\frac{N}{\zeta(3)} \right)^{\frac{1}{3}}, \tag{1.7.2}$$

  where,

  - ω: Trap frequency,
  - N: Number of particles,
  - $\zeta(3)$ ≈1.202, The Riemann zeta function.

  In the context of quantum statistics, the Fig.1.6 likely demonstrates how, below a critical temperature, a macroscopic number of particles occupy the lowest energy level, which corresponds to the onset of BEC. The figure emphasizes the quantum mechanical nature of the transition and the statistical distribution of particles, distinguishing the condensed fraction from the thermal cloud above the transition.

  The diagram could also potentially contrast Bose-Einstein statistics with classical Maxwell-Boltzmann distributions, showing the buildup of particles in the ground state that does not occur in classical systems.

- **Wider Existence of BECs:** BECs are found not only in ultracold gases but also in materials at higher temperatures that host bosonic quasiparticles and excitons.

- **BEC Matter:** A detailed physical and mathematical description is given in Chapter.2, Sec.2.3.

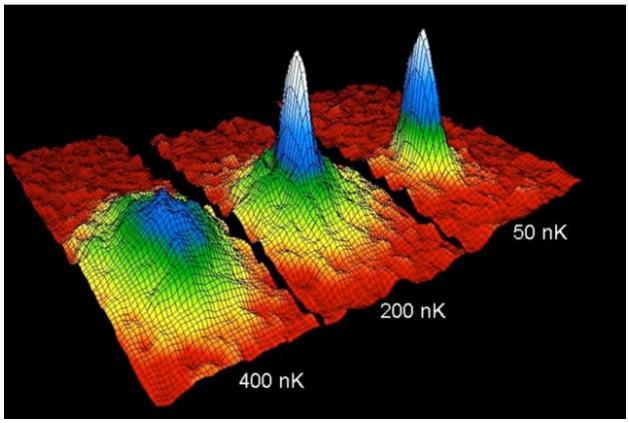

Fig. 1.6. The leftmost image depicts a gas nearing condensation; the central image shows the state right after the condensate emerges; and the rightmost image represents a sample with nearly pure condensate following additional evaporation.(Image credit: NIST/JILA/CU-Boulder - NIST Image)

1.7.4 BEC's Application

- **Atomic Clock:** BEC's can enhance the precision of cesium atomic clocks, potentially improving time measurement accuracy by 100 times. Using BECs in the clock mechanism provides sharper resonance signals for more precise frequency measurements.

- **Simulation of Black Hole Radiation:** BEC's simulate black hole radiation (Hawking radiation) by mimicking the event horizon with different flow speeds in a BEC. Sound waves represent quantum particles, providing a model for studying black hole phenomena in a controlled lab environment.

- **Atom Laser:** An atom laser emits coherent matter waves similar to a regular laser's light waves. Recent advances in creating continuous BEC's open the door for atom lasers, which could improve precision in atomic clocks, quantum computing and nanotechnology.

1.7.5 Epilogue of BEC

Continued BEC research promises deeper insights into quantum behavior and advancements in precision measurement, quantum information and quantum phase transitions. BEC, by bridging quantum theory and experimental physics, continues to be a pivotal area of research with the potential to transform various scientific and technological domains.

Chapter 2

Possible Existence of Bose-Einstein Condensate Compact Stars

2.1 Introduction

Universe is a cosmic theatre where stars take center stage. From the grandeur of their birth in the depths of interstellar clouds to their dramatic climax, stars go through a marvelous journey that shapes the cosmos. This journey, called stellar evolution, the remarkable tale of stars is a saga of immense power, cosmic choreography and wondrous transformation. The endpoint of stellar evolution is the final stage in the celestial saga of stars, a captivating narrative where stars leave their mark on the universe in diverse and profound ways. It is believed that this endpoint of stellar evolution reveals the beauty and complexity of the universe by forming compact stars. The formation of compact stars is a cosmic symphony where the universe's most remarkable structures emerge from the depths of nebulae. Compact stars are the cosmic remnants that bridge the gap between the luminous lives of stars and the profound mysteries of the universe.

Compact stars are frequently believed to be isotropic, which means that their pressure and density profile are exactly the same in every direction. This over simplification is often made for the sake of mathematical tractability because it provides a good first approximation for understanding the behavior of many compact stars. In the context of highly compact objects, Ruderman (1972) first raised the idea of pressure anisotropy of the stellar object. The traditional notion of compact objects as being spherically symmetric and

isotropic may be challenged under certain conditions. The work of Bowers and Liang (1974), Canuto (1974) likely refers to deviations from perfect symmetry and isotropy in certain astrophysical scenarios as in high density, radial pressure and transverse pressure differ from each other. Ideally, compact objects are assumed to be isotropic, but pressure variations cause deviations from this assumption [Canuto (1974) and Herrera and Santos (1997)], electric field, magnetic field [Cardall et al. (2001) and Frieben and Rezzolla (2012)], fluid interaction [Di Prisco et al. (2007)], the presence of type 3A superfluid [Kippenhahn et al. (1990) and Sokolov (1980)], pion condensation [Sawyer (1972)] sometimes it becomes anisotropic. Anisotropy is generally calculated or demonstrated by dividing the pressure into two different parts, radial and transverse directions which are orthogonal to each other. The difference between them is called anisotropic factor which is denoted by $\Delta = p_t - p_r$. Recently some authors [Estrada et al. (2023), Jasim et al. (2023), and Maurya et al. (2023)] have worked on anisotropic strange star model.

Quantum principles describe compact objects in the quantum scales. The most popular theory argues that they are made of degenerate gases of fermions, with the collapse being counteracted by their Fermi pressure, which results from the Pauli Exclusion Principle. However, a degenerated boson gas can also balance gravity because of Heisenberg's uncertainty principle, even though its pressure is relatively low because of Bose-Einstein condensation. A BEC star is made entirely of interacting bosons, formed when two neutrons team up and spin parallel. The pressure created by these particles' interactions counteract gravity and the intensity of these interactions determines the maximum mass of the compact object which can reach up to two solar masses [Chavanis and Harko (2012) and Latifah et al. (2014)]. Quintero Angulo et al. (2019) examined how the boundary conditions affected the γ-structure equation solutions for magnetized Bose–Einstein condensate stars (BECs). They looked at two scenarios, one with pure BECs and the other with BECs embedded in a magnetic field. They found that the magnetized BECs are smaller and less massive than the non-magnetic ones and that these effects are more significant at low densities. The link between pressure and density inside a star model is yet unknown. A quadratic EoS was employed by a number of researchers to model compact objects. Gedela et al. (2019a) investigated a new exact solution for the anisotropic matter distribution. The author used the quadratic EoS in conjunction with the Einstein field equations to analyze the overall struc-

ture of space-time within the star configuration. The core-envelope model of an isotropic, spherically symmetric superdense star with a quadratic EoS for the envelope section has been studied [Gedela et al. (2019b), Pant et al. (2019), and Takisa et al. (2019)]. A three layered model of neutron stars with quarks at the core, super-fluid (BEC) matter at the middle and a normal matter shell was also constructed [Bisht et al. (2021) and Lighuda et al. (2021)]. In the framework of the general theory of relativity, Rahaman et al. (2011a) proposed spherically symmetric charged perfect fluid distribution of matter by assuming a matter source that is characterized by quadratic EoS. Maharaj and Mafa Takisa (2012) used a quadratic EoS to relate the radial pressure to the energy density, leading to novel exact solutions to the Einstein-Maxwell system of equations that are physically plausible. Sharma and Ratanpal (2013) report a class of solutions using the Finch and Skea *ansatz* for the metric potential g_{rr} to describe the interior of a static spherically symmetric compact anisotropic star. It has been demonstrated by the authors that the model accepts a quadratic EoS. Further studies on the quadratic EoS are available [Aygün et al. (2019), Ngubelanga et al. (2015), Rahaman et al. (2019), Singh et al. (2018), and Singh et al. (2020)]. Bose–Einstein condensate (BEC) EoS is one type of quadratic EoS $p \propto \rho^2$ [Chavanis (2017)]. Colpi et al. (1986) first presented the BEC EoS model, which has since been suggested as the most likely candidate for the EoS of matter in the interior of neutron star. A BEC can be formed by neutrons bound in Cooper pairs. Depending on the high binding energy between each pair, they can be viewed as a composite boson with an effective mass almost equivalent to twice the mass of a neutron or less.

In this chapter, a class of relativistic solutions is provided to describe the inner structure of the compact star with the assistance of BEC EoS by assuming BEC matter. The structure of this chapter is as follows: In the section 2.2 Einstein field equations are recapitulated describing a spherically symmetric static anisotropic configuration. In the section 2.3, BEC EoS are described and the compact star stellar interior solution is speculated in the section 2.4. The unknown parameters of the generalized solutions are fixed using boundary conditions in section 2.5. The behavior of density, radial and transverse pressure at $r = 0$, energy conditions, surface redshift and causality are discussed in section 2.6. In section 2.7 the stability of the stellar model is pursued, 2.8 is dedicated to $M - R$ relationship and effect of k and finally the discussion remarks in section 2.9.

In what follows, natural units with $G = c = 1$ are used and a signature convention of $\{+ - - -\}$ is adopted.

2.2 Interior Spacetime and the Einstein Field Equations

The interior of the super-dense star is assumed to be described by the line element of spherically symmetric in standard coordinates $x^\mu = (t, r, \theta, \phi)$ as

$$ds^2 = e^{\nu(r)}dt^2 - e^{\lambda(r)}dr^2 - r^2(d\theta^2 + \sin^2\theta\, d\phi^2), \tag{2.2.1}$$

where,

- ν and λ: Functions of the radial coordinate 'r' only.
- $e^{\lambda(r)}$ and $e^{\nu(r)}$: The gravitational potentials.

The gravitational potentials will be determined in the next part.

The field equations that connect the matter sector and the associated geometry in the framework Einstein's gravity, is given by

$$8\pi\, T_{\mu\nu} = G_{\mu\nu} = \mathcal{R}_{\mu\nu} - \frac{1}{2}\,\mathcal{R}\, g_{\mu\nu}, \tag{2.2.2}$$

where,

- $T_{\mu\nu}$: The energy-momentum tensor,
- $\mathcal{R}_{\mu\nu}$: The Ricci tensor,
- $\mathcal{R}$: The Ricci scalar,
- $g_{\mu\nu}$: The metric tensor.

It is assumed that the matter within the stellar interior is anisotropic in nature, the corresponding energy-momentum tensor can be described by

$$T^\mu_\nu = (\rho + p_r)u^\mu u_\nu - p_t g^\mu_\nu + (p_r - p_t)\eta^\mu \eta_\nu, \tag{2.2.3}$$

with,

- $u^\mu u_\nu = -\eta^\mu \eta_\nu = 1$ and $u^\mu \eta_\nu = 0$,
- u^μ : The fluid 4-velocity vector,
- η_ν : Spacelike vector, orthogonal to u^μ,
- ρ : Matter density,
- p_r : Radial pressure,
- p_t : Transverse pressure of the fluid in the orthogonal direction to p_r.

The components of T^μ_ν are

$$T^0_0 = \rho, \quad T^1_1 = -p_r, \quad T^2_2 = T^3_3 = -p_t, \quad T^j_i = 0; \quad \forall \ \ i \neq j. \tag{2.2.4}$$

Using Eq.(2.2.4) and the matter distribution Eq.(2.2.3), the Einstein field equations reduce to

$$8\pi\rho = \frac{1-e^{-\lambda}}{r^2} + \frac{\lambda' e^{-\lambda}}{r}, \tag{2.2.5}$$

$$8\pi p_r = \frac{\nu' e^{-\lambda}}{r} - \frac{1-e^{-\lambda}}{r^2}, \tag{2.2.6}$$

$$8\pi p_t = \frac{e^{-\lambda}}{4}\left(2\nu'' + \nu'^2 - \nu'\lambda' + \frac{2\nu'}{r} - \frac{2\lambda'}{r}\right), \tag{2.2.7}$$

where, primes ($'$) represent differentiation with respect to the radial coordinate r. Using Eq.(2.2.6) and Eq.(2.2.7) it is obtained

$$\begin{aligned} 8\pi\Delta &= 8\pi(p_t - p_r) \\ &= e^{-\lambda}\left[\frac{\nu''}{2} - \frac{\lambda'\nu'}{4} + \frac{\nu'^2}{4} - \frac{\nu'+\lambda'}{2r} + \frac{e^\lambda - 1}{r^2}\right]. \end{aligned} \tag{2.2.8}$$

2.3 Bose-Einstein Condensate (BEC) Matter

Diluted Bose gas can be accommodated in a same quantum ground state at very low temperature, which can be observed as a sharp peak in momentum and coordinates space. This

phenomenon is termed as BEC. In the realm of condensed matter physics, BEC condensation can be obtained via several techniques such as laser and evaporative cooling, magnetic traps etc. Using the Gross-Pitaevskii equation one can model a diluted BEC gas at near absolute zero temperature [Dalfovo et al. (1999)].

The concepts of dark matter as BEC of very light scalar particles ($m \approx 10^{-22}\ eV$) was presented by Barkana and Gruzinov [Hu et al. (2000)] and later by Khlebnikov (2002). It was also suggested that dark energy was formed by gradual condensation of bosonic dark matter [Nishiyama et al. (2004)]. The equation of motion of gravitationally trapped rotating BEC is given by the generalized Gross–Pitaevskii equation [Boehmer and Harko (2007)]

$$i\hbar\,\frac{\partial\psi(\vec{r},t)}{\partial t} \;=\; \Big[-\frac{\hbar^2}{2m}\nabla^2 + V_{rot}(\vec{r}) + V_{ext}(\vec{r}) + g'(|\psi(\vec{r},t)|^2)\Big]\,\psi(\vec{r},t), \tag{2.3.1}$$

where,

- $g' = dg/d\tilde{\rho}$, [Barcelo et al. (2001)]
- $\tilde{\rho} = |\psi(\vec{r},t)|^2$,
- N : Normalized probability density with $\int \tilde{\rho}\, d^3\vec{r} = N$.

The V_{rot} is defined as,

$$V_{rot}(\vec{r}) = \zeta_{rot}(t)\ \frac{m\omega^2}{2}\ \vec{r}^{\,2}, \tag{2.3.2}$$

with,

- ω : Angular velocity of the condensate,
- $\zeta_{rot}(t)$: A possible time variation in the potential function.

The external gravitational potential $V_{ext}(\vec{r}) = V$ holds the Poisson equation

$$\nabla^2 V = 4\pi\rho. \tag{2.3.3}$$

with $\rho = m\tilde{\rho}$, the mass density of the BEC. By adopting the Madelung method of wave

function [Barcelo et al. (2001) and Madelung (1927)] separation through

$$\psi(\vec{r},t) = \sqrt{\tilde{\rho}(\vec{r},t)}\ \exp\left(\frac{i}{\hbar}\ S(\vec{r},t)\right), \tag{2.3.4}$$

where,

$$S(\vec{r},t) = -i\,\frac{\hbar}{2}\,\ln\left(\frac{\psi}{\psi^*}\right). \tag{2.3.5}$$

Eq.(2.3.1) under the slowly rotating Newtonian approximation [$V_{rot}(\vec{r}) = 0$] reduces to

$$\vec{\nabla}p\left(\frac{\rho}{m}\right) = -\rho\ \vec{\nabla}\left(\frac{V}{m}\right) \quad \text{and} \quad \nabla^2 V = 4\pi\rho, \tag{2.3.6}$$

where,

$$p\left(\frac{\rho}{m}\right) = g'\left(\frac{\rho}{m}\right)\ \frac{\rho}{m} - g\left(\frac{\rho}{m}\right), \tag{2.3.7}$$

which is the EoS $p = p(\rho)$ of the system. Assuming the non-linear term in the Gross–Pitaevskii equation in the form of $g(\tilde{\rho}) = w\tilde{\rho}^{\,\gamma}$, Eq.(2.3.7) reduces to the polytropic form $p = \alpha\rho^{\gamma}$.

In general, the non-linearity term g in BEC is chosen as $g(\tilde{\rho}) = w\tilde{\rho}^2$ [Dalfovo et al. (1999)] which eventually leads to the EoS $p(\rho) = \alpha\rho^2$ [Boehmer and Harko (2007)] i.e. a polytropic EoS of $\gamma = 2$. This EoS and the boundary condition force the matter density to obey the form [Boehmer and Harko (2007)]

$$\rho = a\ \frac{\sin(kr)}{kr}, \tag{2.3.8}$$

where,

- a and k : arbitrary constant to be determined.

However, if the BEC to form a compact star, its pressure at the boundary/surface must be vanishing while the surface density remains non-vanishing. Hence, the BEC EoS has been modified as

$$p_r = \alpha\rho^2 - \beta, \tag{2.3.9}$$

where,

- α and β : arbitrary constant to be determined later.

2.4 BEC Compact Star

Recently, Sarkar et al. (2023) have presented a compact star model using the same density profile, however they couldn't include the EoS and therefore the claim of BEC compact star is incomplete. The mass function takes the form,

$$m(r) = \int 4\pi\, r^2 \rho(r)\, dr = \frac{4\pi a[\sin(kr) - kr\cos(kr)]}{k^3}. \tag{2.4.1}$$

On using Eq.(2.4.1) one can determine g_{rr} metric function as

$$e^{-\lambda} = 1 - \frac{2m(r)}{r} = 1 + \frac{8\pi a\,[kr\cos(kr) - \sin(kr)]}{k^3\, r}. \tag{2.4.2}$$

Using the metric potential Eq.(2.2.6) and Eq.(2.4.2) in Eq.(2.3.9), ν can be obtained as

$$\nu(r) \;=\; \int \frac{8\pi\Big[a\sin(kr)\Big\{\alpha\, a\, k\, r\, \sin(kr) + 1\Big\} - a\, k\, r\cos(kr) - \beta\, k^3 r^3\Big]}{r[k^3 r - 8\pi a\, \sin(kr) + 8\pi a\, k\, r\cos(kr)]} dr \tag{2.4.3}$$

which can be integrated only by numerical technique.

Now, using Eq.(2.4.2) and Eq.(2.4.3), the expression of matter density ρ, radial pressure p_r, transverse pressure p_t and anisotropic factor Δ are obtained as

$$\rho \;=\; \frac{a\, \sin(kr)}{kr}, \tag{2.4.4}$$

$$p_r \;=\; \alpha\,\rho^2 - \beta = \frac{\alpha\, a^2\, \sin^2(kr)}{(kr)^2} - \beta, \tag{2.4.5}$$

$$\begin{aligned} p_t \;=\; & \frac{1}{2k^2r^2\Big[k^3 r - 8\pi a\sin(kr) + 8\pi a\, k\, r\cos(kr)\Big]}\Bigg[2\beta\, k^5 r^3(2\pi\beta r^2 - 1) \\ & + a\Bigg\{ - 12k^3\pi r^3\beta\cos(kr) + 2\pi\sin(kr)\Bigg(k^2r^2(5\alpha a^2 + 6\beta - 2\beta k^2 r^2) + 2a \\ & \sin(kr)\{a\alpha\sin(kr) + kr - 2k^3r^3\alpha\beta\}\{a\alpha\, kr\sin(kr) + 1\} + 3a^2\alpha k^2 r^2 \\ & \cos(2kr)\Bigg) + ak\, r\sin(2k\, r)\left[\alpha k^3 r - 10\pi\, a\,\alpha\sin(kr) - 2\pi k\, r\right]\Bigg\}\Bigg] \end{aligned} \tag{2.4.6}$$

$$\Delta = \frac{1}{2k^2r^2\Big(k^3r - 8\pi a\sin(kr) + 8\pi akr\cos(kr)\Big)}\Bigg[4\beta^2k^5r^5 + a\Bigg\{4k^3 \pi r^3\beta\cos(kr) + 2\pi\sin(kr)\Bigg(k^2\pi r^2\Big\{5\alpha a^2 - 2\beta(1+k^2r^2)\Big\} + a\sin(kr) \Big\{-kr(-2\pi + k^2\alpha + 4k^2\pi r^2\alpha\beta) + 2a\pi\,\alpha\sin(kr)\big[5 + a\alpha kr\sin(kr)\big]\Big\} + 3\pi a^2\,\alpha k^2r^2\cos(2kr)\Bigg) + akr\sin(2kr)\,(\alpha k^3r - 18\pi a\,\alpha\sin(kr) - 2\pi k\,r)\Bigg\}\Bigg]. \quad (2.4.7)$$

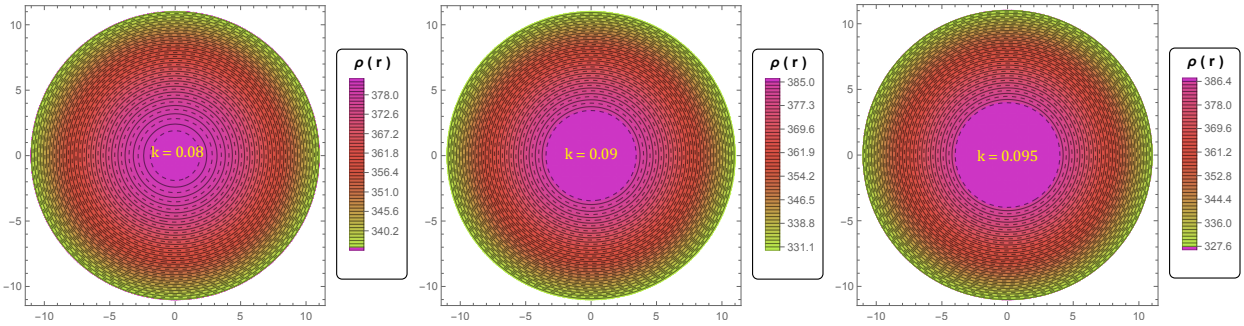

Fig. 2.1. Variations of density with r for different values of k in MeV/fm^3 unit with $M = 1.77M_\odot$, $\beta = 0.86 \times 10^{-4}/km^2$ and $R = 11km$.

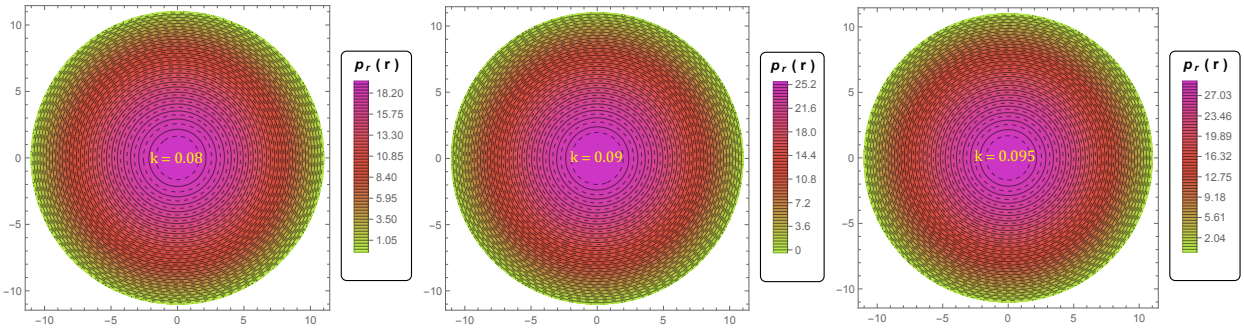

Fig. 2.2. Variations of radial pressure with r for different values of k in MeV/fm^3 unit with $M = 1.77M_\odot$, $\beta = 0.86 \times 10^{-4}/km^2$ and $R = 11km$..

The behavior of the pressure, density and anisotropy at the interior are shown in Figs.2.1, 2.2 and 2.3 for different values of k. Examining the relative changes in isolines for $\rho(r)$, radial pressure and anisotropy as depicted in Figs.2.1-2.3, It is observed that the energy density parameter k rises, both the energy density and radial pressure show an upward trend towards the center, while anisotropy decreases, causing a reduction in confining radii at the same density, radial pressure and anisotropy, as depicted by concentric contours. This increase in

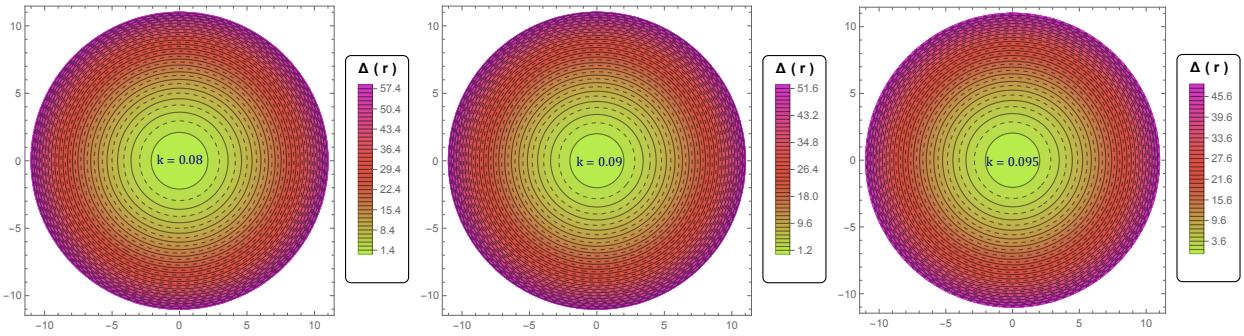

Fig. 2.3. Variations of anisotropy with r for different values of k in MeV/fm^3 unit with $M = 1.77M_{\odot}$, $\beta = 0.86 \times 10^{-4}/km^2$ and $R = 11km$..

energy density can play a role in establishing a stable dense core at a lower stellar radius, mitigating the risk of disastrous collapse. The variations of the central density, central radial pressure, central adiabatic index and surface anisotropy with respect to the k parameter are given in Table.2.1.

Table 2.1: Central density, central pressure, surface anisotropy and central adiabatic index.

k	$p_{rc} \times 10^{-5}/km^2$	$\rho_c \times 10^{-4}/km^2$	$\Delta_s \times 10^{-5}/km^2$	Γ_c
0.080	2.610	3.435	1.224	9.23
0.085	3.019	3.469	1.085	8.39
0.090	3.453	3.506	0.502	7.70
0.095	3.954	3.547	0.101	7.01

2.5 Matching of Interior and Exterior Spacetime

Assuming the exterior spacetime to be the Schwarzschild exterior solution which is matching smoothly with the interior solution is given by

$$ds^2 = \left(1 - \frac{2M}{r}\right) dt^2 - \left(1 - \frac{2M}{r}\right)^{-1} dr^2 - r^2(d\theta^2 + \sin^2\theta\, d\phi^2). \tag{2.5.1}$$

Now, the interior solution Eq.(2.2.1) and exterior solution Eq.(2.5.1) is matched at the boundary $r = R$,

$$e^{-\lambda(R)} = 1 - \frac{2M}{R} = e^{\nu(R)}. \tag{2.5.2}$$

Also, the vanishing value of the radial pressure at the boundary of the matter configuration

implies

$$p_r(R) = 0. \tag{2.5.3}$$

Using the boundary conditions Eq.(2.5.2) & Eq.(2.5.3), a and α are obtained as

$$a = -\frac{k^3 M}{4\pi kR\cos(kR) - 4\pi\sin(kR)}, \tag{2.5.4}$$

$$\alpha = \frac{\beta k^2 R^2 \mathrm{cosec}^2(kR)}{a^2}. \tag{2.5.5}$$

The remaining parameters will be chosen freely for well-behaved solution.

2.6 Physical Analysis of the Model

This new solution comprising a compact star composed of BEC matter has to be tested under certain physical criteria which are to be satisfied by any physical model.

2.6.1 Non-Singularity of the Central Pressure and Density

For a solution to be considered physically meaningful, the energy density, along with the radial and transverse pressures, should be finite and positive. This implies that their values at the center must also remain finite and positive. Now, the central values of density and pressures for the solution are obtained as,

$$\rho_c(r=0) = a > 0. \tag{2.6.1}$$

This leads to Zeldovich's condition at the interior, $p_{rc}/\rho_c \leq 1$,

$$\frac{a^2\alpha - \beta}{a} \leq 1 \quad \text{or} \quad a \leq \frac{1}{2\alpha} + \frac{\sqrt{1+4\alpha\beta}}{2\alpha} \quad . \tag{2.6.2}$$

Using Eq.(2.6.1) and Eq.(2.6.2) it is obtained that a constraint on a given as,

$$0 < a \leq \frac{1}{2\alpha} + \frac{\sqrt{1+4\alpha\beta}}{2\alpha}, \quad \text{provided} \quad 1+4\alpha\beta > 0. \tag{2.6.3}$$

2.6.2 Energy Conditions

Physically acceptable models of compact star should fulfill the null energy condition (NEC), weak energy condition (WEC), strong energy condition (SEC) and dominant energy condition (DEC) i.e.

$$\text{NEC} \quad : \quad \rho(r) + p_r \geq 0, \tag{2.6.4}$$

$$\text{WEC} \quad : \quad \rho(r) + p_r(r) \geq 0 \quad \text{and} \quad \rho \geq 0, \tag{2.6.5}$$

$$\text{SEC} \quad : \quad \rho + p_r(r) + 2p_t(r) \geq 0, \tag{2.6.6}$$

$$\text{DEC} \quad : \quad \rho \geq |p_r|. \tag{2.6.7}$$

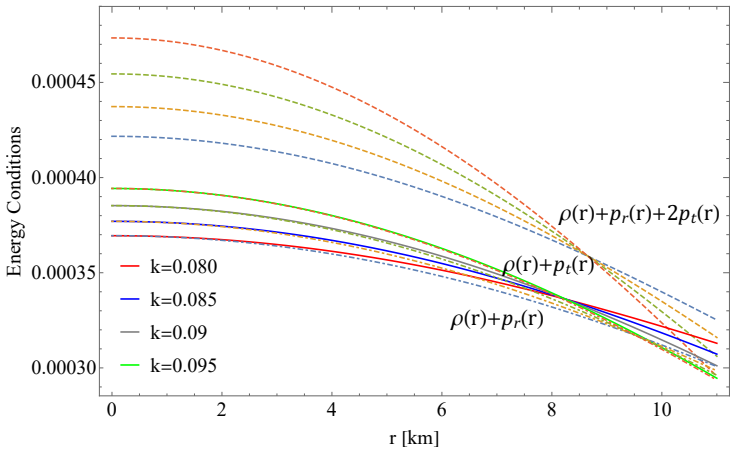

Fig. 2.4. Variations of the Energy Conditions against the radial coordinate r for $M = 1.77M_{\odot}$, $\beta = 0.86 \times 10^{-4}/km^2$ and $R = 11km$.

Fig.2.4 confirms that solution satisfy the above energy conditions. The dominant condition can also be easily verified from the Figs.2.1 and 2.2. Satisfying energy conditions is essential for ensuring that compact stars are physically realistic and stable, behave in ways that respect the laws of general relativity and maintain the causal structure of spacetime.

2.6.3 Surface Redshift

Surface redshift refers to the gravitational redshift experienced by light emitted from the surface of a massive object, such as a star or a compact object like a neutron star or black hole. Due to the strong gravitational field near the surface, the light loses energy while escaping, causing its wavelength to stretch and shift toward the red end of the spectrum.

The surface red-shift can be determine by

$$\begin{aligned} z_s &= e^{\lambda(R)/2} - 1 \\ &= \left[\frac{8\pi a\{kR\cos(kR) - \sin(kR)\}}{k^3 R} + 1\right]^{-1/2} - 1. \end{aligned} \tag{2.6.8}$$

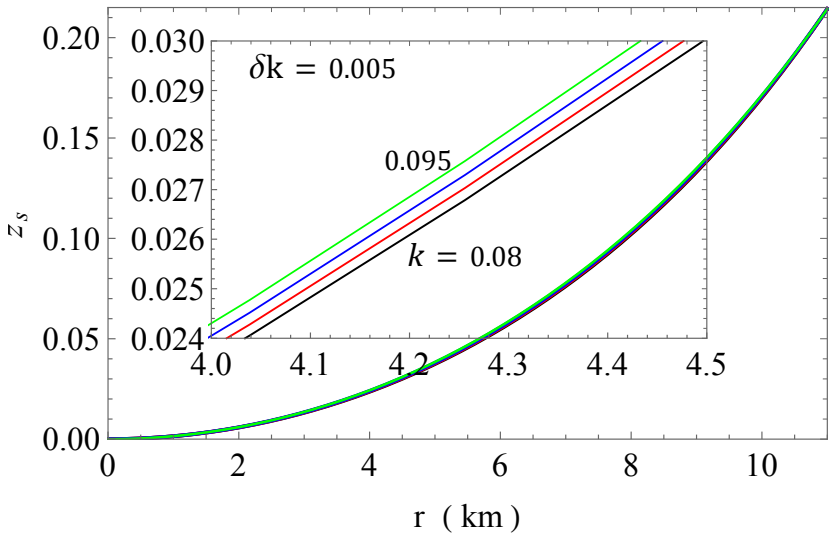

Fig. 2.5. Variations of surface redshift against the radial coordinate r for $M = 1.77M_{\odot}$, $\beta = 0.86 \times 10^{-4}/km^2$ and $R = 11km$.

The profile of the surface red-shift has also been drawn, as shown in Fig.2.5 which is far within the acceptable limit i.e. $z_s \leq 2$.

2.6.4 Causality Condition

The causality condition in the context of general relativity refers to the requirement that cause-and-effect relationships are preserved in spacetime. Specifically, it ensures that no information or influence can propagate faster than the speed of light, so in any general relativistic model of compact stars, the causality condition where the speed of the sound inside the stellar interior should be less than that of light. The radial velocity (v_r) and transverse velocity (v_t) of sound can be obtained as

$$v_r = \frac{dp_r}{d\rho}, \quad v_t = \frac{dp_t}{d\rho}. \tag{2.6.9}$$

The profile of radial and transverse velocity of sound are shown in Fig.2.6.

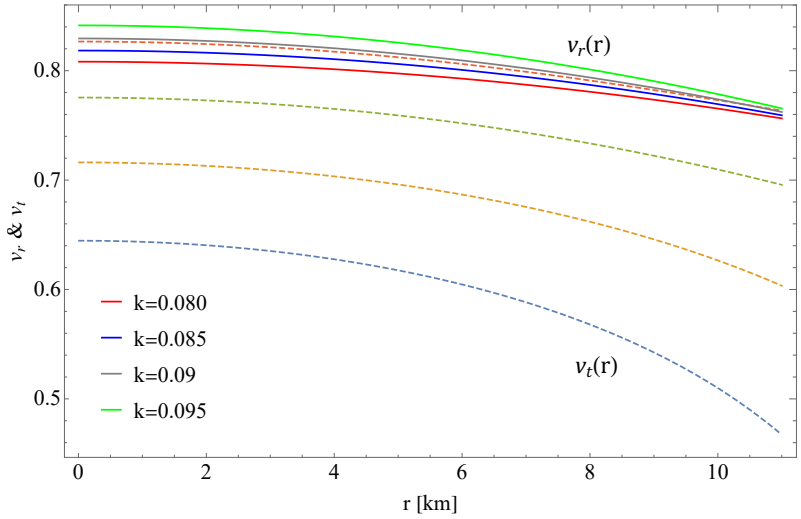

Fig. 2.6. Variations of speed of sound against the radial coordinate r for $M = 1.77M_{\odot}$, $\beta = 0.86 \times 10^{-4}/km^2$ and $R = 11km$.

2.7 Stability and Equilibrium Analysis

Once the model satisfies all the physical acceptability conditions, it is further required to investigate the equilibrium and stability under radial perturbations.

2.7.1 Equilibrium Condition

The interior of stellar static objects contain three different forces *viz* gravitational force, hydrostatics force and anisotropic force which governs through the equation of hydrostatic equilibrium i.e.

$$-\frac{\nu'}{2}(\rho + p_r) - \frac{dp_r}{dr} + \frac{2}{r}(p_t - p_r) = 0, \tag{2.7.1}$$

proposed by Tolman-Oppenheimer-Volkov (TOV). The above equation may also be written as

$$F_g + F_h + F_a = 0, \tag{2.7.2}$$

with

$$F_g = -\frac{\nu'}{2}(\rho + p_r)\ , \quad F_h = -\frac{dp_r}{dr}\ ; \quad F_a = \frac{2\Delta}{r}. \tag{2.7.3}$$

The three different forces acting on the system are shown in Fig.2.7 and is balanced indicating that the system is under equilibrium.

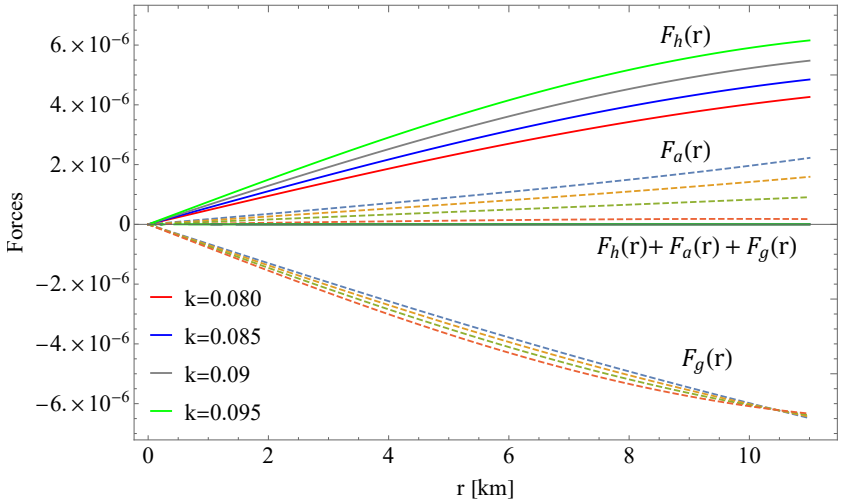

Fig. 2.7. Variations of different forces in TOV-equation against the radial coordinate r for $M = 1.77M_{\odot}$, $\beta = 0.86 \times 10^{-4}/km^2$ and $R = 11km$.

2.7.2 Adiabatic Index

The relativistic adiabatic index Γ is defined as

$$\Gamma = \frac{\rho + p_r}{p_r} \frac{dp_r}{d\rho} = \gamma + 2\alpha\rho = 2 + 2\alpha\rho > 2. \tag{2.7.4}$$

Here $\gamma = \frac{\rho}{p_r} \frac{dp_r}{d\rho} = 2$ for non-relativistic BEC EoS that follows $p_r = \alpha\rho^2$. However, at high density regime due to the relativistic quantum interactions the relativistic adiabatic index modifies as Γ. Hence, the fulfillment of Bondi criterion [Bondi (1964)] i.e. $\Gamma > 4/3$ for a stable star is achieved. Further, due to the regenerative effect of pressure it requires more stiffer EoS to achieve an equilibrium [Bondi (1964)]. For an anisotropic general relativistic sphere the situation becomes more complicated, because the stability will depend on the type of anisotropy. For an anisotropic relativistic sphere the stability condition is given by [Chan et al. (1993)],

$$\Gamma > \frac{4}{3} + \left[\frac{4}{3}\frac{\Delta_i}{|p'_{ri}|r} + \frac{8\pi}{3}\frac{r\,\rho_0 p_{ri}}{|p'_{ri}|}\right], \tag{2.7.5}$$

where,

- Δ_i : initial anisotropy,
- p_{ri} : initial radial pressure,
- ρ_i : initial energy density.

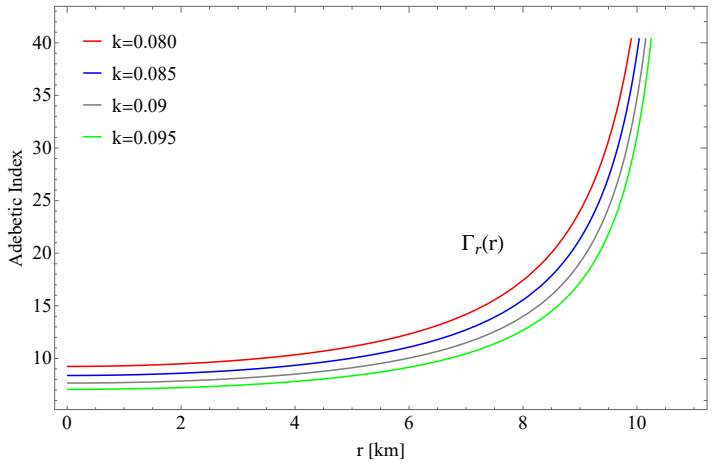

Fig. 2.8. Adiabatic index r for $M = 1.77M_{\odot}$, $\beta = 0.86 \times 10^{-4}/km^2$ and $R = 11km$.

Initial anisotropy, initial radial pressure and initial energy density in static equilibrium satisfying Eq.(2.7.1). The profile of Γ is shown in Fig. 2.8 showing that $\Gamma > 4/3$ everywhere within the BEC sphere.

2.7.3 Static Stability Criterion

Investigating the stability of a compact stellar system is a crucial aspect of astrophysics. This criterion plays a key role in understanding the stability of compact stellar objects under external perturbations. Considering a radial perturbation, Chandrasekhar (1964) first analysed the stability of compact stars through pulsation equation. Further development and simplification of the Chandrasekhar's stability method were envisioned by Harrison-Zel'dovich-Novikov. It states that the gravitational mass (M) must increase with the increase in central density (ρ_c). Thus, one implies a stable structure if $(dM(\rho_c)/d\rho_c > 0)$ and unstable if $(dM(\rho_c)/d\rho_c < 0)$. The Fig. 2.9 satisfies stable stellar configuration under Harrison-Zel'dovich-Novikov criterion under radial pulsation. The mass of the BEC compact star as a function of its central density is given by

$$M(\rho_c) = \frac{4\pi\rho_c[\sin(kR) - kR\cos(kR)]}{k^3}, \tag{2.7.6}$$

and its graphical representation is given in Fig. 2.9. As the interactions of the BEC particles increases (i.e. k increases), the mass that hold by the system decreases as well as the stability under radial density oscillation.

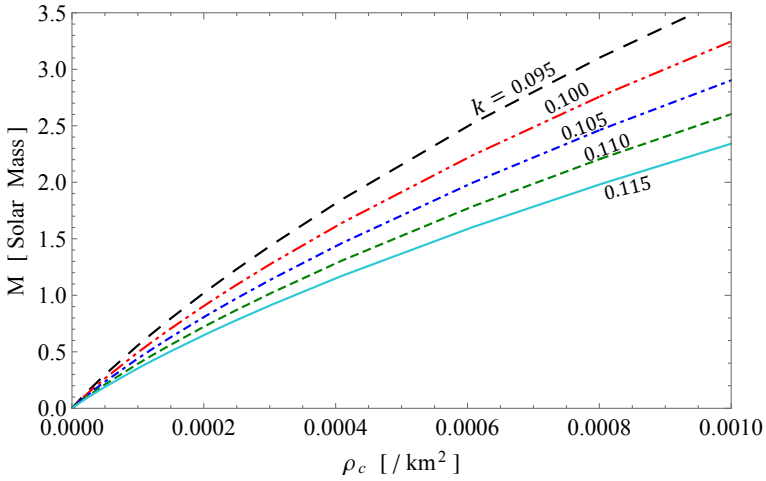

Fig. 2.9. The $M - \rho_c$ curve of the Bose-Einstein condensate star with r for $M = 1.77M_\odot$, $\beta = 0.86 \times 10^{-4}/km^2$ and $R = 11km$.

2.8 Mass-Radius Relationship

For the BEC compact star, the $M - R$ curve has been plotted to observe the effect of k on it (Fig.2.10). Here one can observe that the mass and radius decrease with increase in k. This is because as the $k-$parameter increases the density of the BEC star also increases, leading to more mass and therefore more compactness (or smaller radii). The effect on mass due to the $k-$parameter is not seen significantly at lower mass below $\approx 1M_\odot$. Due to this characteristic, some massive compact stars have been fitted to predict their radii if they were BEC compact candidates. Using uncertainties from observations, the radii have been predicted and are given in Table.2.2.

Table 2.2: Prediction of radii for few well known compact star as BEC stars.

Compact star	$M/M_\odot$	R (km)				
		k				
		0.095	0.0975	0.100	0.105	0.115
PSR J1614−2230	1.97 ± 0.04	$13.09^{+0.06}_{-0.08}$	$13.01^{+0.05}_{-0.06}$	$12.92^{+0.05}_{-0.06}$	$12.71^{+0.05}_{-0.05}$	$11.93^{+0.03}_{-0.03}$
PSR J0952−0607	2.35 ± 0.17	$13.66^{+0.20}_{-0.23}$	$13.55^{+0.16}_{-0.22}$	$13.40^{+0.13}_{-0.19}$	$13.01^{+0.08}_{-0.08}$	-
GW190814	2.5-2.67	$13.94^{+0.08}_{-0.10}$	$13.77^{+0.06}_{-0.09}$	$13.57^{+0.02}_{-0.05}$	$12.77^{+0.19}_{-0.09}$	-

In the Table.2.2, it can be seen that for the same mass the radius decreases with increase in $k-$parameter thereby increasing the compactness M/R and bringing closer to the Buchdahl limit. This leads the BEC compact star more unstable with when k increases. It is also highlighted that the GW 170817 observations the constraints on mass and ra-

dius i.e. (a) for $M = 1.6M_{\odot}, R > 10.68^{+0.15}_{-0.04}km$ [Bauswein et al. (2017)] and (b) for $M = 1.4M_{\odot}, R > 11.0^{+0.9}_{-0.6}km$ [Capano et al. (2020)] are also fulfilled by the $M - R$ curve in Fig. 2.10. In the $M - R$ curve, for $1.6M_{\odot}$ compact star the expected radius is above $12km$ while for $1.4M_{\odot}$ compact star the radius is just below $12km$, which are in agreement with the above constraints.

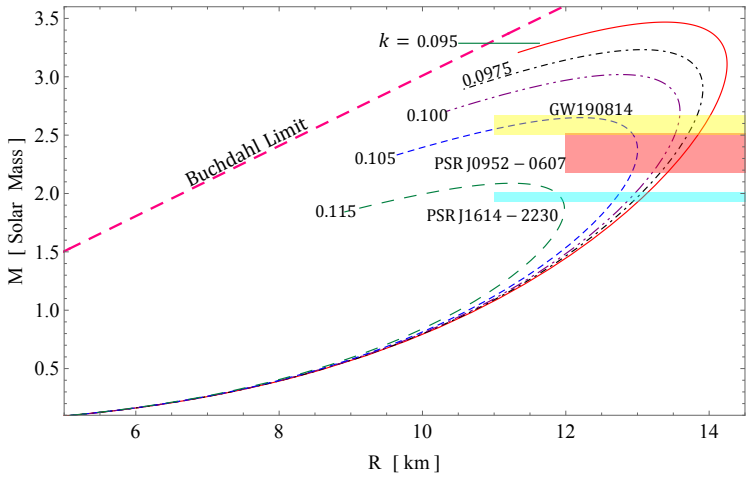

Fig. 2.10. $M - R$ relationship for the BEC compact star.

2.9 Discussion and Conclusion

In this chapter, compact stars formed by BEC matter have been modeled where the physical properties of the star depend on a single $k-$parameter. When the generalized Gross–Pitaevskii equation is solved using the Medelung method of wave function separation under non-relativistic approximation one can get a density profile of $\sim \sin(kr)/kr$ and an EoS $p_r \sim \rho^2$. A slight modification has been made by adding an extra constant term β so that the pressure vanishes at the boundary while the density remains non-zero. On using the density profile and the EoS, Einstein's field equations have been solved exactly to determine the physical properties of the general relativistic BEC compact star. The pressure and density increases with increase in the $k-$parameter while the anisotropy decreases (hence the solution is isotropic asymptotically i.e. $k \to \infty$). Due to the increase in compactness with k, the surface redshift also increases. The stiffness of the BEC matter also depends on the single $k-$parameter and as k increases the speed of sound also increases indicating the increase in stiffness of the EoS. The BEC matter has adiabatic index 2 in the non-relativistic realm

although due to the relativistic effect its adiabatic index drastically increases above 5. When k increases the central values of adiabatic index decreases thereby coming closer to 4/3 limit. On the other hand when k increases the compactness get closer to the Buchdahl limit. Therefore, $k-$parameter alter the stability of the BEC compact star. The static stability criterion also supports this claim, if there is a radial perturbation that cause to oscillation/increase in the central density, the BEC matter can hold less mass star if $k-$parameter increases. The GW 170817 event provides very narrow windows of possible radii for specific masses, which also holds good by the new BEC compact matter. At the end it was desired to highlight that BEC matter might also be able to form compact objects that mimic neutron/quark stars.

Chapter 3

Anisotropic Quintessence Compact Star in $f(T)$ Gravity with Tolman-Kuchowicz Metric Potentials

3.1 Introduction

The construction of gravitational modifications, namely extended gravity theories with general relativity as a specific constraint but with generally richer structures [Akrami et al. (2021)], is motivated by both theoretical and observational implications. The initial proposal depends on the concept that, due to the fact that general relativity does not seem renormalizable, it might be presumed that its more intricate extensions would have better renormalizability attributes [Stelle (1977)]. The necessity to characterize the universe's two accelerated phases—one in the early universe (inflation) and one in the late universe (the dark energy era)—is the second motive. It is tied to the observable characteristics of the universe. Starting with the Einstein-Hilbert action and extending it in different ways [Capozziello and De Laurentis (2011)] is the typical method for constructing gravitational modifications. However, starting with the Teleparallel Equivalent of General Relativity (TEGR) [Maluf (2013), Shirafuji and Nashed (1997), and Unzicker and Case (2005)], which is the analogous torsional formulation for gravity, it can be manipulated to arrive at $f(T)$ gravity [Bengochea and Ferraro (2009) and Cai and Capozziello (2016)], $f(T, \mathcal{T}_G)$ gravity [Kofinas and Saridakis (2014)], $f(T, \mathcal{B})$ gravity [Bahamonde et al. (2015) and Böhmer and

Jensko (2021)], scalar-torsion theories [Bahamonde et al. (2019), Geng et al. (2011), and Hohmann et al. (2018)] etc.

An alternative geometrical theory of gravity known as TEGR was developed by Albert Einstein using absolute parallelism and the tangent space as a frame of reference [Hayashi and Shirafuji (1979)]. At every point in tangent space, an orthogonal tetrad is generated in TEGR and can therefore be employed as a dynamical variable [Aldrovandi and Pereira (2009)]. The torsion in space-time, which may be determined using a torsion tensor, defines the gravitational influence in TEGR. A torsion scalar is used to describe the effect of gravity and the tetrad field is used as one of the theory's dynamical variables to generate the field equation for TEGR. The action of TEGR may now be modified for generating $f(T)$ gravity by employing a more general function of torsion scalar [Bahamonde et al. (2023)]. The $f(T)$ gravity has recently been shown to be incredibly effective in interpreting a variety of celestial observations [El Hanafy and Nashed (2016) and Jamil et al. (2012a, 2012b, 2013, 2015)]. It has been established that the galactic dynamics and cosmic expansions can both be explained quite well by the $f(T)$ gravity theory. In Ref. [Li et al. (2018)], the effective field theory is put forward in a systematic approach to explain torsion gravity. Moreover, the gravitational wave propagation bound from GW170817 and GRB170817A are two examples of how this approach of effective field theory description and application of specific operators, including torsional terms, by observational constraints has already demonstrated its effectiveness in interpreting stellar phenomena. The combined interpretation of H_0 and σ_8 tensions has recently also been investigated by Yan and colleagues [Yan et al. (2020)].

Significant attempts are underway to describe compact stellar configurations using modified theories of gravity in order to shed light on some remarkable observations of them [Astashenok et al. (2020, 2021)]. Moreover, the study of anisotropic compact stellar structures with diagonal and off-diagonal tetrads in $f(T)$ gravity has been extensively explored [Daouda et al. (2012), Ditta et al. (2021), and Zubair and Abbas (2016)]. Besides that, an analysis of spherically symmetric stellar structures in $f(T)$ gravity based on diagonal tetrad yields necessities on $f(T)$ for being a linear function of T, thereby making the theory fundamentally TEGR [Bahamonde et al. (2023)].

Studying the physical attributes of compact stellar objects using teleparallel gravity is also useful for understanding their nature. Typically, compact stars are modeled using the

isotropic stellar configuration. Anisotropy pertains to the directional dependence of properties such as pressure. Naturally, the pressures inside a star characterized differently along radial and transverse directions respectively leading to generate anisotropy measured as the difference of the radial (p_r) and tangential (p_t) pressures. This difference can significantly influence the internal structure, stability, and observable characteristics of the object. The anisotropy factor Δ is often defined as $\Delta = p_r - p_t$. If $\Delta > 0$, the tangential pressure dominates, leading to a more oblate structure. Conversely, if $\Delta < 0$, the radial pressure dominates, leading to a more prolate structure. The presence of anisotropy can have a stabilizing effect on compact objects. In particular, a positive anisotropy (where $p_t > p_r$) can support a higher maximum mass for neutron stars, making them less prone to collapse. Thus anisotropy not only affects the stability and structure of stars but also has implications for observable phenomena, making it a vital factor in modern astrophysical models. Ruderman (1972) first analyzed this deviation from isotropy in the context of stellar structure and dynamics. In the study of relativistic anisotropic compact stars, Bowers and Liang have shown that anisotropy could have significant influence on mass and surface redshift [Bowers and Liang (1974)]. Over the years various factors have been recognized to contribute to the anisotropy, such as extremely high densities in the core [Canuto (1974)], the presence of pion and meson condensate states [Sawyer (1972)], mixtures of different fluids, slow rotational motion [Herrera and Santos (1995)], mixture of perfect and a null fluid [Letelier (1980)], strong magnetic fields [Weber (1999)], the presence of strong electromagnetic field [Usov (2004)] etc. On the other hand, Ivanov (2010) highlighted that the effects of shear and electromagnetic fields on stellar systems can be accommodated by considering them to be anisotropic. It was found that boson stars composed of scalar fields are anisotropy exhibit in naturally [Schunck and Mielke (2003)]. Additionally, structures like wormholes [Morris and Thorne (1988)] and gravastars [Cattoen et al. (2005)] are also characterized as anisotropic objects. A complete review on the origin and impact of anisotropy on stellar structure can be found in the seminal work of Herrera and Santos (1997). In modeling compact objects, there is a wide plethora of arguments in favor of the presence of anisotropy within stellar interiors. The instability of the pressure isotropy condition was demonstrated by Herrera (2020). They showed that an initially isotropic pressure profile will evolve into an anisotropic state as the star loses hydrostatic equilibrium. The study of anisotropy and its impact in

modeling compact stars has been studied by many researchers [Deb et al. (2017), Ivanov (2002), Kalam et al. (2012), Mak and Harko (2003), Maurya et al. (2016), Maurya et al. (2019), Rahaman et al. (2010, 2011b), and Schunck and Mielke (2003)].

In this chapter, an analytical relativistic anisotropic quintessence spherical model has been developed within the framework of $f(T)$ gravity theory, driven by all of the preceding arguments. A quintessence star is a hypothetical astrophysical object where the primary source of internal pressure counteracting gravitational collapse is provided by a form of dark energy known as quintessence. Regarding this, some ingredients have been imposed by considering the pressure anisotropy condition and the metric potential of the Tolman-Kuchowicz (TK) type, which serve as the main pillars of the resulting paradigm. Along with the anisotropic matter distribution, it is also assumed that the current model includes a quintessence field, defined by a parameter ω and then study the stability of motion and thermodynamic properties.

This chapter is organized in the following way: In section 3.2, the interior spacetime and Einstein's equations in the $f(T)$ theory are briefly described. In section 3.3, relativistic quintessence anisotropic spherical solutions are addressed analytically in the context of $f(T)$ gravity. In section 3.4, the interior and exterior Schwarzschild solutions at the boundary of stellar surfaces is matched. In section 3.5 physical analysis of this model has been discussed and in section 3.6 the analysis of motion stability and thermodynamic characteristics are investigated. Using the $M-R$ curve the predicted mass and radius of stars that may exist in nature are listed in section 3.7. The overall summary and a few final concluding remarks on the investigation are addressed in section 3.8.

3.2 Interior Spacetime and Einstein Equation in $f(T)$ Theory

When considering static geometry for stellar formations with spherically symmetric matter distribution, spacetime is described by the following line element,

$$\mathrm{d}s^2 = \mathrm{e}^{\nu(r)}dt^2 - \mathrm{e}^{\lambda(r)}dr^2 - r^2(d\theta^2 + \sin^2\theta d\phi^2). \tag{3.2.1}$$

Here, the metric coefficients $e^{\nu(r)}$ and $e^{\lambda(r)}$ are pure radial functions of r.
With the help of the matrix transformation known as the tetrad, the line element Eq.(3.2.1) can be transformed into a Minkowskian space as follows

$$ds^2 = g_{\mu\nu}dx^\mu dx^\nu = \eta_{ij}\theta^i\theta^j, \tag{3.2.2}$$

$$dx^\mu = e^\mu_i\theta^i,\ \theta^i = e^i_\mu dx^\mu. \tag{3.2.3}$$

where,

- $\eta_{ij} = \text{diag}(1,-1,-1,-1)$,
- $e^\mu_i e^i_\nu = \delta^\mu_\nu$,
- $e = \sqrt{-g} = det(e^i_\mu)$.

The action of the $f(T)$ theory is given as the starting point [Bengochea and Ferraro (2009) and Li et al. (2011)]

$$S[e^i_\mu, \phi_A] = \int d^4x\ e\ \left[\frac{1}{16\pi}f(T) + \mathcal{L}_{\text{matter}}(\phi_A)\right]. \tag{3.2.4}$$

Here, ϕ_A represents matter fields and $f(T)$ is an arbitrary analytic function of the torsion scalar T. Here the expression of the torsion scalar is given as follows

$$T = S_\sigma{}^{\mu\nu}T_{\mu\nu}{}^\sigma, \tag{3.2.5}$$

where the tensor $S^{\mu\nu}_\sigma$ is described as [Nashed and Bamba (2022)],

$$S_\sigma{}^{\mu\nu} = \frac{1}{2}\left(K^{\mu\nu}{}_\sigma + \delta^\mu_\sigma T^{\beta\nu}{}_\beta - \delta^\nu_\sigma T^{\beta\mu}{}_\beta\right). \tag{3.2.6}$$

In which,

$$T^\sigma{}_{\mu\nu} = \Gamma^\sigma{}_{\nu\mu} - \Gamma^\sigma{}_{\mu\nu} = e_i{}^\sigma\left(\partial_\mu e^i{}_\nu - \partial_\nu e^i{}_\mu\right), \tag{3.2.7}$$

$$K^{\mu\nu}{}_\sigma = -\frac{1}{2}\left(T^{\mu\nu}{}_\sigma - T^{\nu\mu}{}_\sigma - T_\sigma{}^{\mu\nu}\right). \tag{3.2.8}$$

By varying the action with respect to the tetrads, the field equations of $f(T)$ gravity can

be obtained as [Li et al. (2011)]

$$S_{\mu}{}^{\nu\rho}\partial_{\rho}T f_{TT} + \left[\mathrm{e}^{-1}\mathrm{e}^{\mathrm{i}}_{\mu}\partial_{\rho}(e\mathrm{e}_{\mathrm{i}}{}^{\alpha}S_{\alpha}{}^{\nu\rho})\right] f_T + \frac{1}{4}\delta^{\nu}_{\mu} f = 4\pi T^{\nu}_{\mu}, \tag{3.2.9}$$

where,

$$f_T = \frac{\partial f}{\partial T} \quad f_{TT} = \frac{\partial^2 f}{\partial T^2}, \tag{3.2.10}$$

here, ∂_{μ} stands for partial derivative with respect to four coordinates x_{μ}, (x_{μ} stands for t, r, θ, ϕ) and $e = det(\mathrm{e}^{\mathrm{i}}_{\mu}) = \mathrm{e}^{\frac{\lambda+\nu}{2}} r^2 \sin\theta$. Now the expression of the torsion scalar becomes,

$$T(r) \;=\; \frac{2\mathrm{e}^{-\lambda}}{r}\left(\nu' + \frac{1}{r}\right). \tag{3.2.11}$$

Here, T^{ν}_{μ} is the energy-momentum tensor of the underlying fluid. Let us assume that this model includes an anisotropic fluid that represents regular baryonic matter and a quintessence field.

The energy-momentum tensor for normal baryonic matter is given by

$$\mathcal{T}^{\nu}_{\mu} = \mathrm{diag}(\rho,\, -p_r,\, -p_t,\, -p_t), \tag{3.2.12}$$

where, ρ, p_r and p_t respectively, represent the energy density, radial pressure and transverse pressure of normal matter.

Furthermore, let us assume that τ^{ν}_{μ} represents the energy-momentum tensor for the quintessence field and its non-zero components are given by

$$\begin{aligned} \tau^{r}_{r} = \tau^{t}_{t} &= -\rho_q, \\ \tau^{\theta}_{\theta} = \tau^{\phi}_{\phi} &= \frac{(3\omega+1)\rho_q}{2}, \end{aligned}$$

here ρ_q represents the energy density for the quintessence field characterized by the parameter ω, with $(-1 < \omega < -\frac{1}{3})$ and

$$T^{\nu}_{\mu} = \mathcal{T}^{\nu}_{\mu} + \tau^{\nu}_{\mu}. \tag{3.2.13}$$

The field equations in $f(T)$ gravity for the underlying fluid are given by

$$4\pi\left(\rho+\rho_q\right) = \frac{f}{4}-\left[T-\frac{1}{r^2}-\frac{\mathrm{e}^{-\lambda}}{r}(\lambda'+\nu')\right]\frac{f_T}{2}-\frac{\mathrm{e}^{-\lambda}}{r}T'f_{TT}, \quad (3.2.14)$$

$$4\pi\left(p_r-\rho_q\right) = \left[T-\frac{1}{r^2}\right]\frac{f_T}{2}-\frac{f}{4}, \quad (3.2.15)$$

$$4\pi\left(p_t+\frac{3\omega+1}{2}\rho_q\right) = \left[\frac{T}{2}+\mathrm{e}^{-\lambda}\left\{\frac{\nu''}{2}+\left(\frac{\nu'}{4}+\frac{1}{2r}\right)(\nu'-\lambda')\right\}\right]\frac{f_T}{2} - \frac{f}{4}+\frac{\mathrm{e}^{-\lambda}}{2}\left(\frac{\nu'}{2}+\frac{1}{r}\right)T'f_{TT}, \quad (3.2.16)$$

$$\text{and} \quad \mathrm{e}^{-\frac{\lambda}{2}}\frac{\cot\theta}{2r^2}T'f_{TT} = 0. \quad (3.2.17)$$

Here, $(')$ denotes differentiation with respect to the radial coordinate 'r'.

For the choice of $f(T)=T$, the aforementioned field equations in Eqs.(3.2.14)-(3.2.16) lead to the corresponding field equations in general relativity.

Now the Eq.(3.2.17) gives two choices: (i) $T'=0$ or (ii) $f_{TT}=0$. In the second case, one obtains a linear form of the $f(T)$ function as

$$f(T)=\alpha T+\beta, \quad (3.2.18)$$

where α and β are constants of integration.

If $T'=0$ is chosen instead of $f_{TT}=0$, it gives a constant torsion scalar, $T=T_0$. With the choice of $T=T_0$, the right side of the Eq.(3.2.15) blows up as $r\to 0$. This implies that the pressure of the substance is not finite; therefore, this case is excluded.

3.3 Present Model

With the choice of $f(T)$ function given in Eq.(3.2.18), from the Eqs.(3.2.14)-(3.2.15), the following equation can be arrived as

$$\rho+p_r = \frac{\alpha}{8\pi r}\mathrm{e}^{-\lambda}(\lambda'+\nu'). \quad (3.3.1)$$

At this stage, let us assume that the metric potentials $e^{\nu(r)}$ and $e^{\lambda(r)}$ are of TK type, i.e.,

$$\nu(r) = Br^2 + 2\ln D \qquad \text{and} \qquad \lambda(r) = \ln(1 + ar^2 + br^4), \tag{3.3.2}$$

here, a, b, B, D, are all arbitrary constants and their value can be obtained by a smooth matching of interior and exterior spacetime at the boundary.

Using Eqs.(3.3.1) and (3.3.2) the following form is obtained

$$\rho + p_r = \frac{\alpha}{4\pi}\left[\frac{a + 2br^2}{1 + ar^2 + br^4} + B\right]. \tag{3.3.3}$$

Let us further suppose that the energy density ρ and the radial pressure p_r maintain a linear relationship given as

$$p_r = \gamma\rho - \delta, \tag{3.3.4}$$

where γ and δ are arbitrary positive constants with $0 < \gamma < 1$.

Now, using the above relationship, the field equations are solved and the expressions of the parameters are obtained as follows,

$$\rho = \frac{1}{4(1+\gamma)}\left[\frac{(a + B + (2b + aB)r^2 + bBr^4)\alpha}{\pi(1 + ar^2 + br^4)^2} + 4\delta\right], \tag{3.3.5}$$

$$\rho_q = \frac{1}{16\pi(1+\gamma)}\Bigg[(1+\gamma)\beta \tag{3.3.6}$$

$$+2\Bigg\{\frac{\alpha\Big((a - 2B + br^2)(1 + ar^2 + br^4) + \Big(3a + (a^2 + b)r^2 + 2abr^4 + b^2r^6\Big)\gamma\Big)}{(1 + ar^2 + br^4)^2} - 8\pi\delta\Bigg\}\Bigg], \tag{3.3.7}$$

$$p_r = \frac{1}{4(1+\gamma)}\left[\frac{\Big(a + B + (2b + aB)r^2 + bBr^4\Big)\alpha\gamma}{\pi(1 + ar^2 + br^4)^2} - 4\delta\right], \tag{3.3.8}$$

$$p_t = \frac{1 + 3\omega}{32\pi(1 + ar^2 + br^4)^2}\Big[-\beta(1 + ar^2br^4)^2 - 2\Big\{a^2r^2\alpha + 2abr^4\alpha$$

$$+\frac{\alpha\Big(a(1 - 2Br^2 + 3\gamma) - 2B(1 + br^4) + br^2(1 + 5\gamma + br^4(1 + \gamma))\Big) - 8\pi(1 + ar^2 + br^4)^2\delta}{1 + \gamma}$$

$$-\frac{2\Big(2B - a + (-2b + B(a + B))r^2 + aB^2r^4 + bB^2r^6\Big)\alpha - (1 + ar^2 + br^4)^2\beta}{1 + 3\omega}\Big\}\Big]. \tag{3.3.9}$$

For the current model, the central density and central pressure are obtained as follows,

$$\rho(r=0) = \ \rho_c \ = \frac{a\alpha + B\alpha + 4\pi\delta}{4(1+\gamma)}, \tag{3.3.10}$$

$$p_r(r=0) = \ p_{rc} \ = \frac{(a+B)\alpha\gamma - 4\pi\delta}{4(1+\gamma)}, \tag{3.3.11}$$

$$p_t(r=0) = \frac{4\alpha B(3+2\gamma+3\omega) - 2a\alpha(3+5\gamma+3\omega+9\gamma\omega) + 16\delta\pi - 3(\beta(1+\gamma)(1+\omega) - 16\delta\omega\pi)}{32(1+\gamma)\pi}, \tag{3.3.12}$$

therefore the anisotropic factor Δ at the origin is obtained as

$$\Delta(r=0) = -\frac{3(1+\omega)(-4\alpha B + \beta + \beta\gamma + 2a(\alpha+3\alpha\gamma) - 16\delta\pi)}{32(1+\gamma)\pi} \tag{3.3.13}$$

For a physically acceptable model, the anisotropic factor should vanish at the center of the star, which gives

$$-4\alpha B + \beta + \beta\gamma + 2a(\alpha+3\alpha\gamma) - 16\delta\pi = 0. \tag{3.3.14}$$

In the next sections, the boundary condition and the physical viability of the present model will be checked via different tests.

3.4 Boundary Matching Condition

In this section, the interior spacetime is matched to the exterior geometry and for the model, it is determined by the Schwarzschild line element given by

$$\mathrm{d}s^2 \ = \ \left(1 - \frac{2M}{r}\right)\mathrm{d}t^2 - \left(1 - \frac{2M}{r}\right)^{-1}\mathrm{d}r^2 - r^2(\mathrm{d}\theta^2 + \sin^2\theta\mathrm{d}\phi^2), \tag{3.4.1}$$

Now at the boundary $r = R$ the metric coefficients g_{rr}, g_{tt} and $\frac{\partial}{\partial r}(g_{tt})$ are all continuous,

Table 3.1: The numerical values of a, B and D for some well known compact objects by assuming $b = 0.1 \times 10^{-4}$ km^{-4}.

Star	Observed mass $M_\odot$	Observed radius km.	Estimated mass ($M_\odot$)	Estimated radius (km.)	a km^{-2}	B km^{-2}	D
Her X-1 Abubekerov et al. (2008)	0.85 ± 0.15	8.1 ± 0.41	0.85	8.5	0.00543030	0.00289578	0.756246
SMC X-4 Rawls et al. (2011)	1.29 ± 0.05	8.831 ± 0.09	1.29	8.8	0.00945188	0.00491954	0.622699
4U 1538-52 Rawls et al. (2011)	0.87 ± 0.07	7.866 ± 0.21	0.87	7.8	0.00775626	0.00403023	0.724610
Vela X-1 Rawls et al. (2011)	1.77 ± 0.08	9.56 ± 0.08	1.77	9.5	0.01307120	0.00676124	0.494630
Cen X-3 Rawls et al. (2011)	1.49 ± 0.08	9.178 ± 0.13	1.49	9.2	0.01038580	0.00540449	0.574909
LMC X-4 Rawls et al. (2011)	1.04 ± 0.09	8.301 ± 0.2	1.04	8.3	0.00816755	0.00425600	0.685691
EXO 1785-248 Ozel et al. (2009)	1.3 ± 0.2	8.849 ± 0.4	1.4	8.85	0.01078010	0.00558588	0.586810

which gives the following set of equations

$$\text{Continuity of } g_{tt} \quad : \quad 1-\frac{2M}{R}=\mathrm{e}^{BR^2}D^2, \tag{3.4.2}$$

$$\text{Continuity of } g_{rr} \quad : \quad \left(1-\frac{2M}{R}\right)^{-1}=1+aR^2+bR^4, \tag{3.4.3}$$

$$\text{Continuity of } \frac{\partial}{\partial r}(g_{tt}) \quad : \quad \frac{2M}{R^2}=2BR\mathrm{e}^{BR^2}D^2. \tag{3.4.4}$$

Again, the radial pressure p_r vanishes at the boundary, i.e.,

$$p_r(r=R)=0. \tag{3.4.5}$$

Solving the Eqs.(3.4.2)-(3.4.4), with the help of Eq.(3.3.14) and Eq.(3.4.5), one can obtain,

$$\begin{aligned}
a &= \frac{1}{R^2}\left[\left(1-2\frac{M}{R}\right)^{-1}-1-bR^4\right],\\
B &= \frac{M}{R^3}\left(1-2\frac{M}{R}\right)^{-1},\\
D &= \mathrm{e}^{\frac{-BR^2}{2}}\sqrt{1-2\frac{M}{R}},\\
\beta &= \frac{-2(a-2B)(1+aR^2+bR^4)^2\alpha-2(a-2B+2(3a^2-2b-aB)R^2}{(1+aR^2+bR^4)^2(1+\gamma)}\\
&\quad+\frac{(3a^3+6ab-2bB)R^4+6a^2bR^6+3ab^2R^8)\alpha\gamma}{(1+aR^2+bR^4)^2(1+\gamma)},\\
\delta &= \frac{(a+B+(2b+aB)R^2+bBR^4)\alpha\gamma}{4\pi(1+aR^2+bR^4)^2}.
\end{aligned}$$

3.5 Physical Analysis of the Model

In this section, the physical features of the developed model shall be discussed. A model corresponding to a stellar structure has been developed by assuming TK-type metric potentials and a linear pressure density relation for the matter distribution. The physical quantities are presented in a simple, elementary functional form to analyze the physical behavior of the model. To examine the physical acceptability of the model, recently observed values corresponding to the mass and radius of known pulsar Her X-1 have been used as input parameters. For the given mass and radius ($M=0.85\pm0.15M_{\odot}$ and $R=8.1\pm0.41\ km$), the values of the model parameters have been determined from the condition of the vanish-

ing radial pressure and the smooth matching of two metrics at the boundary. Using this value the numerical values of a, B and D have been calculated for different stars shown in Table.3.1. To figure out the behavior of the physically relevant quantities, the graphical method was used and analyzed the model graphically under $f(T)$ gravity with different α values. The nature of the plots shows the regular and well-behaved basic features of all the physical quantities within the stellar interior. Based on the graphical analysis, some salient features are discussed in the developed model.

3.5.1 Metric Coefficients

The profiles of the metric potential for the present model are shown in Fig.3.1 and it shows that the metric potentials are positive and continuous within the stellar interior, which is the requirement for a physically viable model presenting stellar structure. Also, it is finite and regular at the center.

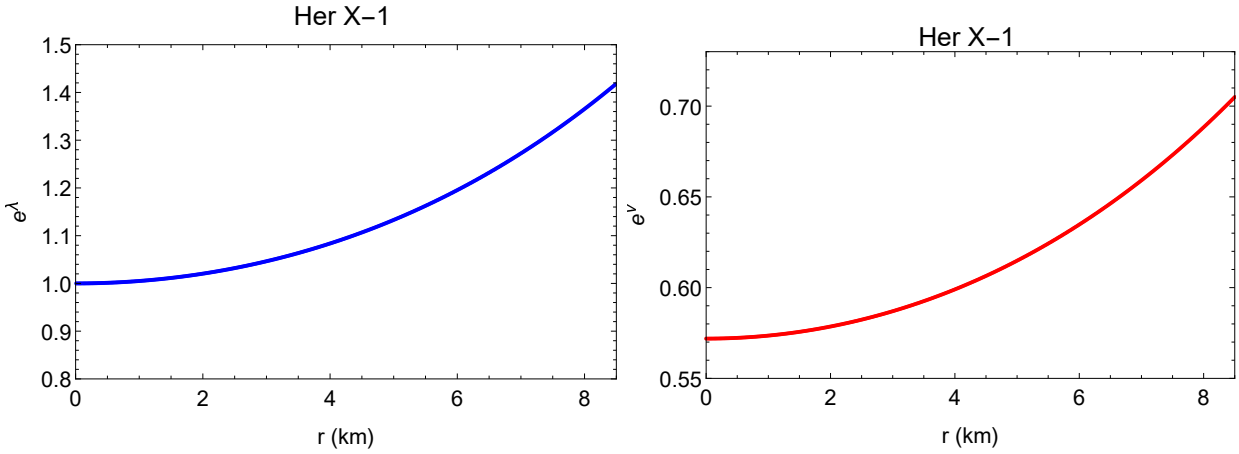

Fig. 3.1. The metric potentials are shown against 'r' for different values of α.

3.5.2 Density Profiles

Fig.3.2 shows variations of the energy density and quintessence density respectively, for the α values ranging from 0.5 to 2.5. The plots depicted a monotonically decreasing nature from their maximum values at the center towards the boundary.ρ_q decreases with radial parameter and takes more negative as α increases. Also, it is inferred that for higher values of α, density pick up higher values.

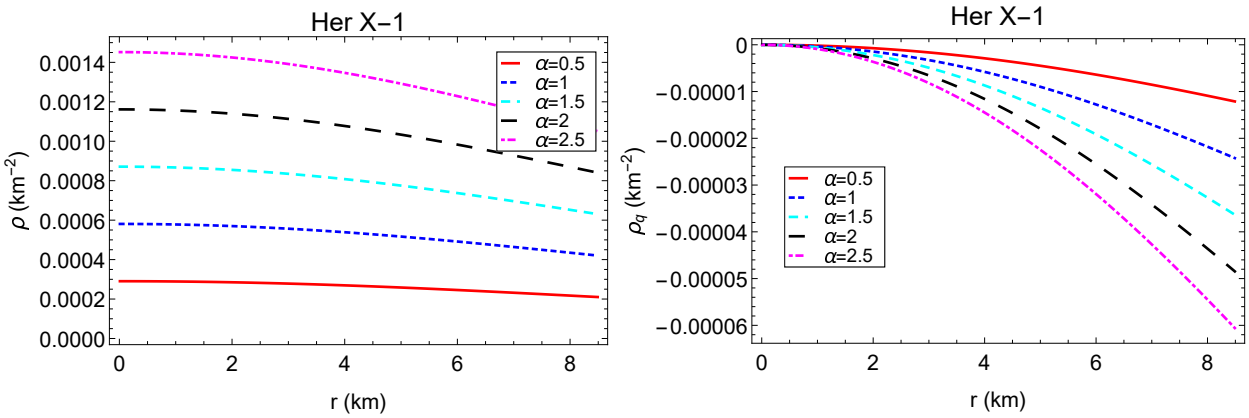

Fig. 3.2. The matter density and quintessence density are shown with respect to r for different values of α.

3.5.3 Pressure Profiles

Fig.3.3 shows variations of radial pressure and traverse pressure, respectively, for the α values ranging from 0.5 to 2.5. The plots depicted a monotonically decreasing nature from their maximum values at the center towards the boundary. In the case of radial pressure, it drops to zero, indicating the radius value of the star, while in the case of tangential pressure, it does not zero at the boundary. Also, it is inferred that for higher values of α, pressures pick up higher values.

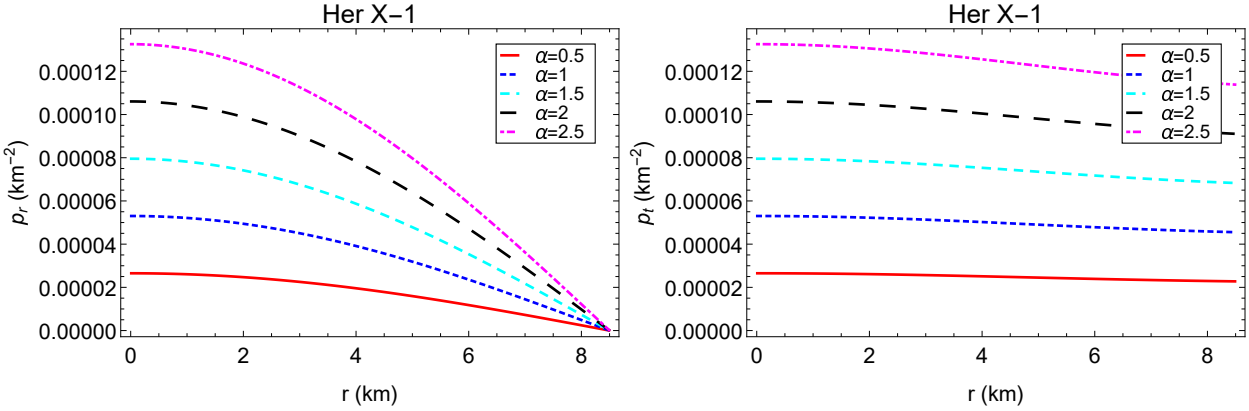

Fig. 3.3. Radial, transverse pressure and are shown with respect to r for different values of α.

3.5.4 Density and Pressure Gradients

For the current model, the pressure and density gradient are obtained as follows

$$\frac{\mathrm{d}\rho}{\mathrm{d}r} = \frac{-1}{2\pi(1+ar^2+br^4)^3(1+\gamma)}(r(a^2(2+Br^2)+a(B+6br^2+3bBr^4)+ 2b(-1+3br^4+B(r^2+br^6)))\alpha), \tag{3.5.1}$$

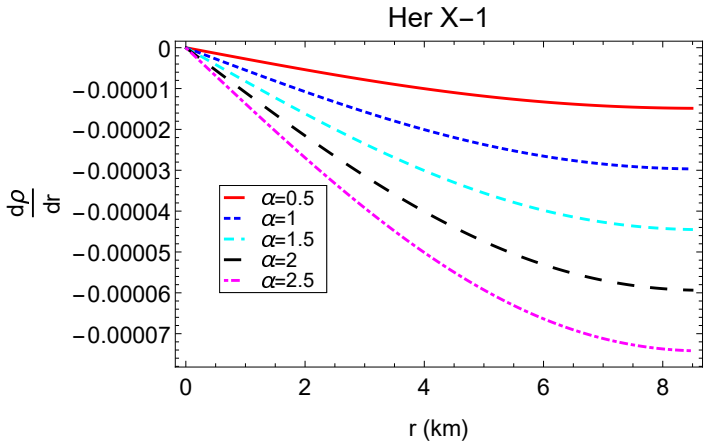

Fig. 3.4. The density is shown inside the stellar interior with respect to r for different values of α.

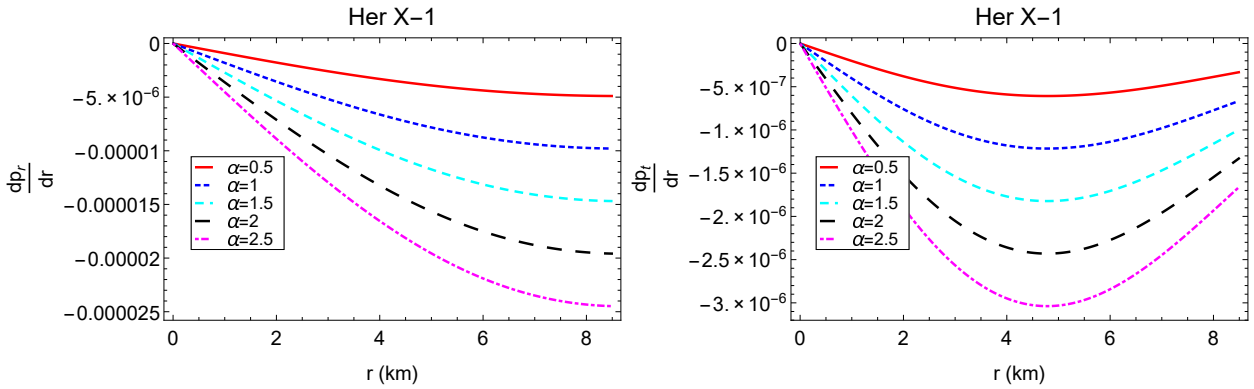

Fig. 3.5. The pressure gradient are shown inside the stellar interior with respect to r for different values of α.

$$\frac{\mathrm{d}p_r}{\mathrm{d}r} = \frac{-1}{2\pi(1+ar^2+br^4)^3(1+\gamma)}(r(a^2(2+Br^2)+a(B+6br^2+3bBr^4)+ 2b(-1+3br^4+B(r^2+br^6)))\alpha\gamma), \tag{3.5.2}$$

$$\begin{aligned}\frac{\mathrm{d}p_t}{\mathrm{d}r} &= \frac{1}{8\pi(1+ar^2+br^4)^3(1+\gamma)}r\alpha\Big[-5b-2B^2(-1+b^2r^8)(1+\gamma)+\\ &a^3r^2(1+\gamma)(1+3\omega)-4bBr^2\Big(5+4\gamma+3\omega+br^4(1+3\omega)\Big)\\ &+a^2\Big(5+9\gamma+3\omega+15\gamma\omega+3br^4(1+\gamma)(1+3\omega)-2Br^2(2+\gamma+3\omega)\Big)\\ &+a\Big\{-2B^2r^2(-1+br^4)(1+\gamma)\\ &+br^2\Big(13+25\gamma+3\omega+39\gamma\omega+3br^4(1+\gamma)(1+3\omega)\Big)-2B\Big(4+3\gamma+3\omega+\\ &3br^4(2+\gamma+3\omega)\Big)\Big\}+b\Big\{b^2r^8(1+\gamma)(1+3\omega)\\ &+12br^4\Big(1+\gamma(2+3\omega)\Big)-3\Big(\omega+\gamma(3+5\omega)\Big)\Big\}\Big]. \qquad (3.5.3)\end{aligned}$$

The gradients of density and radial and transverse pressures are shown in Fig.3.4, Fig.3.5, which are negative inside the stellar structure, which confirms the monotonically decreasing nature of physical parameters from the centre to the boundary.

3.5.5 Pressure Anisotropy

For the current model, the anisotropic factor Δ is calculated as follows

$$\begin{aligned}\Delta &= p_t-p_r\\ &= \frac{1}{32\pi(1+ar^2+br^4)^2(1+\gamma)}\big[48\pi\delta-\Big\{10br^2\alpha+2b^2r^6\alpha+3\beta+6br^4\beta+3b^2r^8\beta\\ &+34br^2\alpha\gamma+2b^2r^6\alpha\gamma+3\beta\gamma+6br^4\beta\gamma+3b^2r^8\beta\gamma-4B^2r^2(1+br^4)\alpha(1+\gamma)\Big\}\\ &+96\pi r^4\delta+48b^2\pi r^8\delta-3(\beta+\beta\gamma-16\pi\delta)-2br^2\Big\{\alpha+5\alpha\gamma+r^2(\beta+\beta\gamma-16\pi\delta)\Big\}\\ &-b^2r^6\Big\{2\alpha(1+\gamma)+r^2(\beta+\beta\gamma-16\pi\delta)\Big\}\omega-6ar^2(1+br^4)(\beta+\beta\gamma-16\pi\delta)(1+\omega)\\ &+2a\alpha(2B^2r^4(1+\gamma)-2Br^2\Big\{-2+\gamma-3\omega)-3(1+3\gamma)(1+\omega)-2br^4(1+\gamma)\\ &(1+3\omega)\Big\}-a^2r^2\Big\{3r^2(\beta+\beta\gamma-16\pi\delta)(1+\omega)+2\alpha(1+\gamma)(1+3\omega)\Big\}\\ &+4B\alpha\Big\{3(1+\omega)+br^4(1-2\gamma+3\omega)\Big\}\big]. \qquad (3.5.4)\end{aligned}$$

The variation of the anisotropy inside the star has been shown in Fig.3.6. The anisotropy is zero at the center since the radial and transverse components are equal as expected and reach their maximum at the surface. Also, it is clear that the anisotropy increases as the α increases.

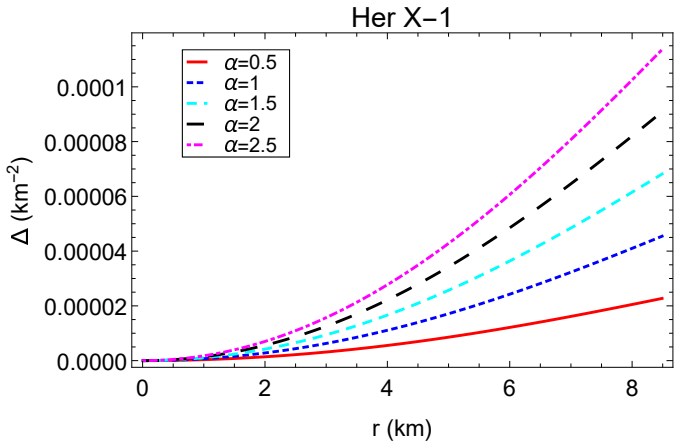

Fig. 3.6. The anisotropic factor is shown for different values of α.

3.5.6 Equation of State Parameters

The equation of state parameters, given by $\omega_r = p_r/\rho$ and $\omega_t = p_t/\rho$ lie within 0 and 1, as depicted in the plot of Fig.3.7. For the matter to be non-exotic in nature, it should satisfy the conditions $0 \leq \omega_r \leq 1$ and $0 \leq \omega_t \leq 1$, which are ensured by the plot. The expression of ω_r and ω_t for the present model is given as follows

$$\omega_r = \frac{p_r}{\rho} = \frac{(a+B+(2b+aB)r^2+bBr^4)\alpha\gamma - 4\pi(1+ar^2+br^4)^2\delta}{(a+B+(2b+aB)r^2+bBr^4)\alpha + 4\pi(1+ar^2+br^4)^2\delta} \tag{3.5.5}$$

$$\begin{aligned}
\omega_t &= \frac{p_t}{\rho} \\
&= \frac{(1+3\omega)}{128\pi^2(1+ar^2+br^4)^4\Big((a+B+(2b+aB)r^2+bBr^4)\alpha + 4\pi(1+ar^2+br^4)^2\delta\Big)} \\
&\quad \frac{1}{(1+\gamma)}\Big[-\beta(1+ar^2+br^4)^2 - 2\Big\{a^2r^2\alpha + 2abr^4\alpha - \frac{8\pi(1+ar^2+br^4)^2\delta}{1+\gamma} \\
&\quad + \frac{\alpha\Big\{-2B(1+br^4)+a(1-2Br^2+3\gamma)+br^2\Big(1+5\gamma+br^4(1+\gamma)\Big)\Big\}}{1+\gamma} + \\
&\quad \frac{-2\Big\{-a+2B+\Big(-2b+B(a+B)\Big)r^2+aB^2r^4+bB^2r^6\Big\}\alpha+(1+ar^2+br^4)^2\beta}{1+3\omega}\Big\}\Big]
\end{aligned} \tag{3.5.6}$$

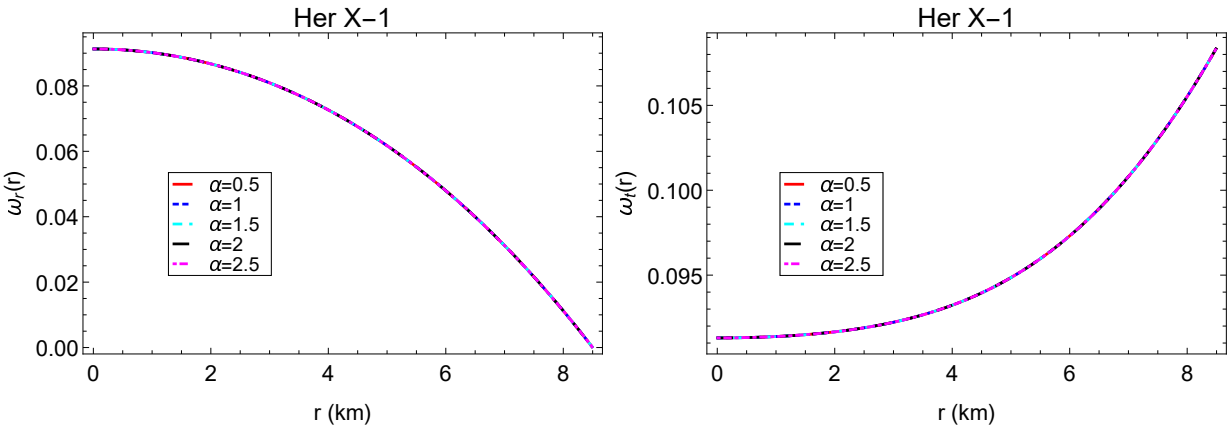

Fig. 3.7. ω_r and ω_t are shown inside the stellar interior for different values of α.

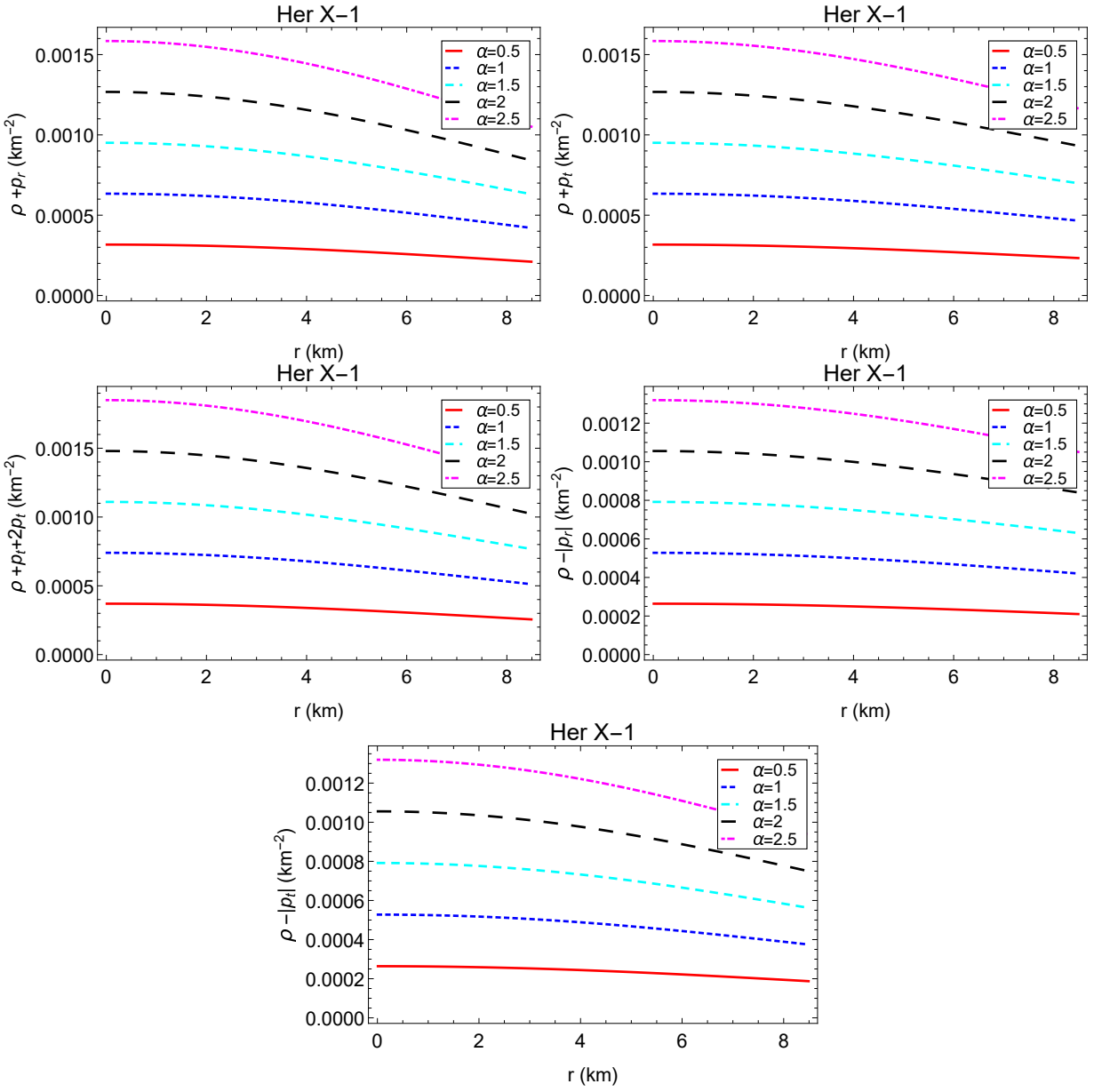

Fig. 3.8. The Energy conditions are shown against r for different values of α.

Table 3.2: Central density, surface density, central pressure, compactness factor and surface redshift have been presented for the compact star Her X-1 [Abubekerov et al. (2008)] for different values of α.

α	ρ_c	ρ_s	p_{rc}	$u(R)$	$z_s(R)$
0.5	3.9184×10^{14}	2.83428×10^{14}	3.21983×10^{34}	0.0115149	0.0117177
1.08	7.83679×10^{14}	5.66856×10^{14}	6.43966×10^{34}	0.0230299	0.0238572
1.5	1.17552×10^{15}	8.50283×10^{14}	9.65948×10^{34}	0.0345448	0.0364445
2.0	1.56736×10^{15}	1.13371×10^{15}	1.28793×10^{35}	0.0460597	0.0495077
2.5	1.9592×10^{15}	1.41714×10^{15}	1.60991×10^{35}	0.0575747	0.0630777

3.5.7 Energy Conditions

A model representing a physically realistic anisotropic fluid sphere demands satisfaction of the following energy conditions at all internal points, including the surface of the sphere [Brassel et al. (2021)]

- Null Energy Condition (NEC) : $\rho + p_r \geq 0; \;\; \rho + p_t \geq 0,$
- Weak Energy Condition (WEC) : $\rho + p_r \geq 0; \;\; \rho \geq 0, \rho + p_t \geq 0,$
- Strong Energy Condition (SEC) : $\rho + p_r \geq 0; \;\; \rho + p_r + 2p_t \geq 0,$
- Dominant Energy Condition (DEC) : $\rho \geq 0; \;\; \rho - p_r \geq 0; \;\; \rho - p_t \geq 0.$

In Fig.3.8, the different energy conditions have been plotted and in this model, the necessary energy conditions hold good.

3.5.8 Mass, Compactness and Surface Redshift

The mass function of the present model of a quintessence star can be obtained as follows,

$$
\begin{aligned}
m(r) \;\; = \;\; \int_0^r 4\pi\rho r^2 \, \mathrm{d}r \;\; = \frac{1}{1+\gamma}\Bigg[& -\frac{r\alpha}{2(1+ar^2+br^4)} + \frac{4}{3}\pi r^3\delta + \\
& \frac{\Big(b + (-a+\sqrt{a^2-4b})B\Big)\alpha \tan^{-1}\left[\frac{\sqrt{2b}r}{\sqrt{a-\sqrt{a^2-4b}}}\right]}{\sqrt{2b}\sqrt{a-\sqrt{a^2-4b}}\sqrt{a^2-4b}} \\
& + \frac{\Big(-b + (a+\sqrt{a^2-4b})B\Big)\alpha \tan^{-1}\left[\frac{\sqrt{2b}r}{\sqrt{a+\sqrt{a^2-4b}}}\right]}{\sqrt{2b}\sqrt{a+\sqrt{a^2-4b}}\sqrt{a^2-4b}}\Bigg]
\end{aligned}
\tag{3.5.7}
$$

Fig.3.9 shows the variation of mass, compactness and surface redshift with radial parameters. The mass function is a monotonically increasing function of r and $m(0) = 0$, i.e., the mass function is regular at the center. The compactness of a star, which is defined as $u(r) = m(r)/r$, should lie within a limit as suggested by Buchdahl (1959) and the limit for the ratio of mass to the radius is $2M/r < 8/9$. For different α plots, it shows that $m(r)/r < 4/9 = 0.44$, i.e., Buchdahl conditions are satisfied in this model. Surface redshift is defined as

$$z_s = (1 - \frac{2M}{R})^{-1/2} - 1. \tag{3.5.8}$$

Using Eqs.(3.3.10), (3.3.11) and (3.5.8) the values of central density, surface density, central pressure, compactness factor and surface redshift have been calculated for different values of α for the star Her X-1, shown in Table.3.2. The variation of z_s is shown as a radial function in the lower panel of the Fig.3.9. According to Boehmer and Harko (2006), the surface redshift should always be ≤ 5, which is satisfied in this model for all values of α.

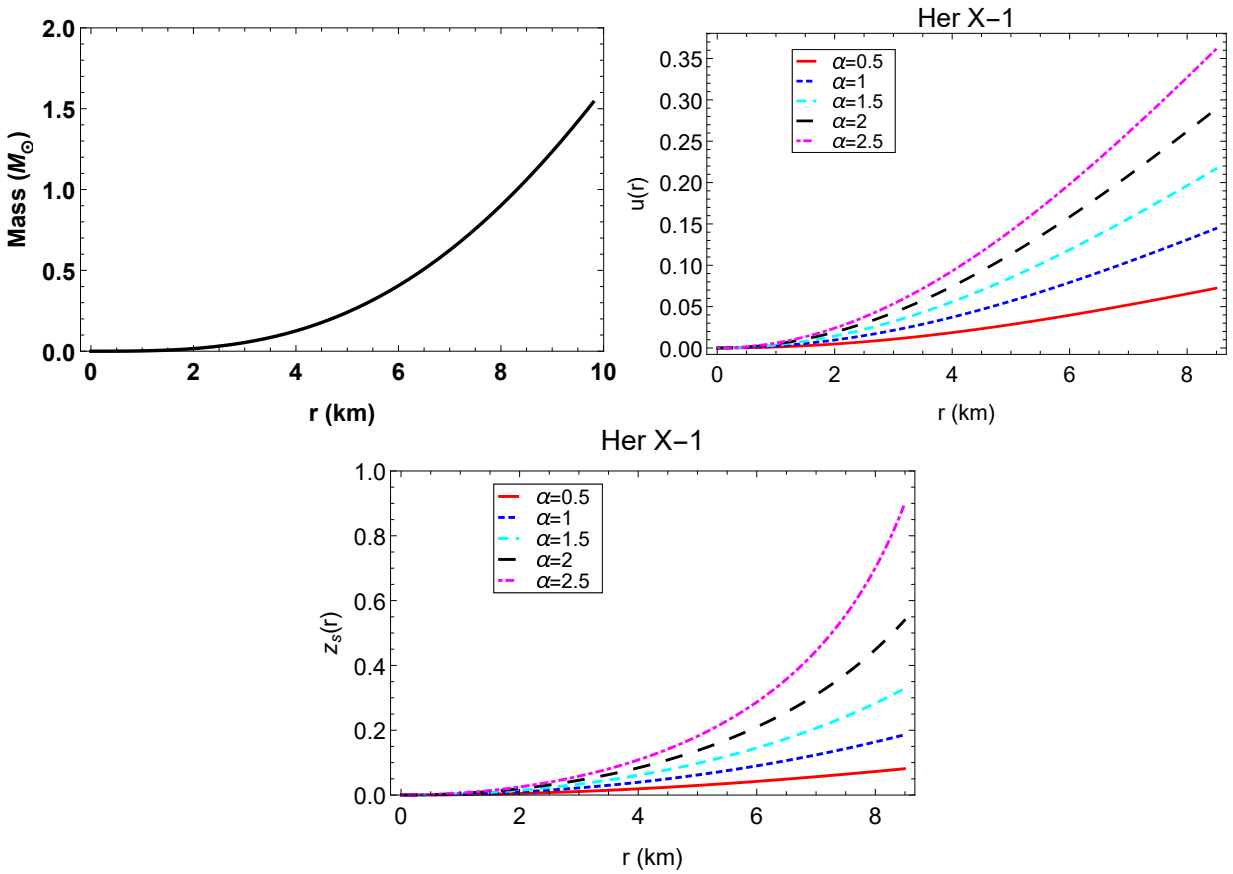

Fig. 3.9. Mass, compactness and surface redshift are shown inside the stellar interior for different values of α.

3.6 Stability and Equilibrium Conditions for the Present Model

The stability and equilibrium conditions are crucial for understanding their structure and behavior these ensure that the star remains in a steady state, neither collapsing nor exploding under normal circumstances. Now the stability and equilibrium conditions of the present model of this chapter is going to be discussed with the help of different criteria.

3.6.1 Causality Condition

The causality condition of a stellar model depends on the radial and transverse speeds of sound. The radial and transverse speeds of sound for the present model are obtained as follows,

$$V_r^2 = \frac{\mathrm{d}p_r}{\mathrm{d}\rho} = \gamma, \tag{3.6.1}$$

$$\begin{aligned} V_t^2 &= \frac{\mathrm{d}p_t}{\mathrm{d}\rho}, \\ &= \frac{1}{\Big[4\Big\{a^2(2+Br^2)+a(B+6br^2+3bBr^4)+2b\Big(-1+3br^4+B(r^2+br^6)\Big)\Big\}\Big]} \\ &\Big[5b+2B^2(-1+b^2r^8)(1+\gamma)-a^3r^2(1+\gamma)(1+3\omega)+4bBr^2 \\ &\Big(5+4\gamma+3\omega+br^4(1+3\omega)\Big)-a^2\Big(5+9\gamma+3\omega+15\gamma\omega+3br^4(1+\gamma) \\ &(1+3\omega)-2Br^2(2+\gamma+3\omega)\Big)-a\Big\{-2B^2r^2(-1+br^4)(1+\gamma) \\ &+br^2\Big(13+25\gamma+3\omega+39\gamma\omega+3br^4(1+\gamma)(1+3\omega)\Big) \\ &-2B\Big(4+3\gamma+3\omega+3br^4(2+\gamma+3\omega)\Big)\Big\}-b\Big(b^2r^8(1+\gamma)(1+3\omega) \\ &-12br^4(1+\gamma(2+3\omega)\Big)+3\Big(\omega+\gamma(3+5\omega)\Big)\Big\}\Big] \end{aligned} \tag{3.6.2}$$

For a physically acceptable stellar model, both the radial and transverse speeds of sound should remain within the limit $[0, 1]$, known as the 'causality condition'. In Fig.3.10, the variation of the radial and transverse sound speeds has been demonstrated with radial parameters. It is found that the sound speeds lie within the prescribed limit, which ensures the non-violation of the causality condition in the interior of the star. Based on Herrera's

cracking method [Herrera (1992)], Abreu et al. (2007) set a condition for a potentially stable compact stellar structure that reads $-1 \leq V_t^2 - V_r^2 \leq 0$. The plot confirms this feature of stability.

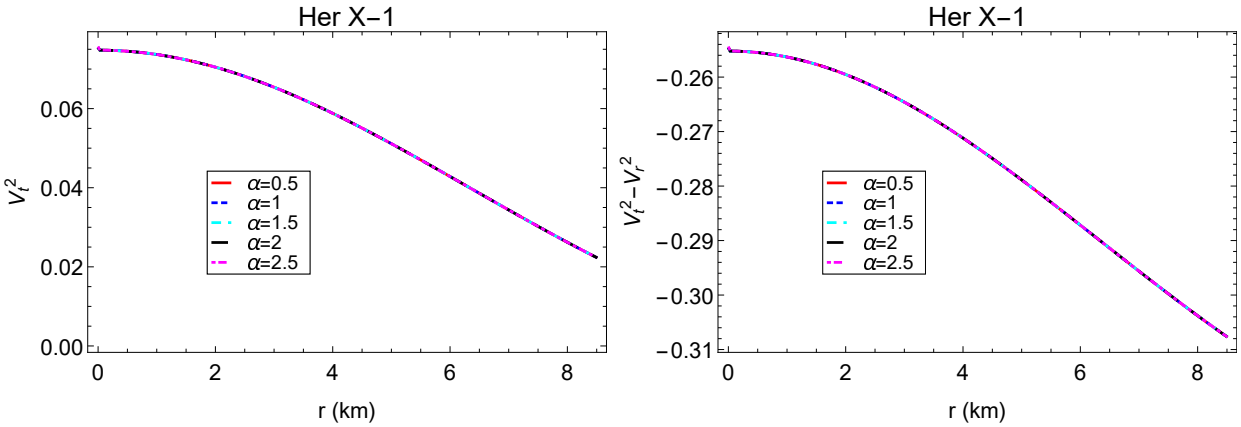

Fig. 3.10. The square of the sound velocity and stability factor $V_t^2 - V_r^2$ is shown against r for different values of α.

3.6.2 Adiabatic Index

The stability of a relativistic anisotropic stellar configuration is closely related to an important thermodynamical quantity known as the adiabatic index. The adiabatic index, mathematically defined as $\Gamma = \frac{\rho+p_r}{p_r}\frac{\mathrm{d}p_r}{\mathrm{d}\rho}$, depends on the EoS and interior fluid density. The stability of an anisotropic fluid sphere is preserved when the adiabatic index $> 4/3$. For the present model, the expression of the relativistic adiabatic index is calculated as follows

$$\Gamma = \frac{(a+B+(2b+aB)r^2+bBr^4)\alpha\gamma(1+\gamma)}{(a+B+(2b+aB)r^2+bBr^4)\alpha\gamma - 4\pi(1+ar^2+br^4)^2\delta}V_r^2, \tag{3.6.3}$$

Fig.3.11 clearly shows that Γ is greater than $4/3$ throughout the interior of the star and hence the stability condition is fulfilled in the model.

3.6.3 Equilibrium under Three Different Forces

The stability of an anisotropic star in static equilibrium depends on the different forces, namely, gravitational force (F_g), hydrostatic force (F_h) and anisotropic force (F_a). The anisotropic and hydrostatic forces are directed in a radially outward direction and strong gravitational forces point inwardly. The condition of balancing the different forces in stable

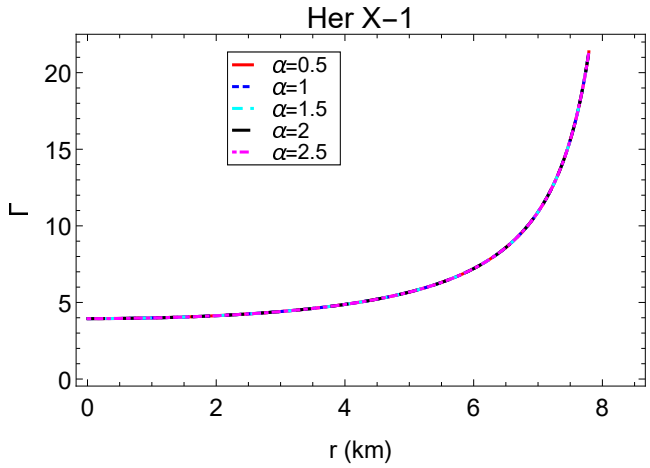

Fig. 3.11. Relativistic adiabatic index is shown inside the stellar interior, for different values of α.

equilibrium is mathematically formulated as a Tolman-Oppenheimer-Volkoff (TOV) equation

$$-\frac{\nu'}{2}(\rho + p_r) + \frac{2}{r}(p_t - p_r) - \frac{\mathrm{d}p_r}{\mathrm{d}r} = 0, \tag{3.6.4}$$

which may be rewritten in the form

$$F_g + F_h + F_a = 0, \tag{3.6.5}$$

where,

- $F_g = -\frac{\nu'}{2}(\rho + p_r)$
- $F_h = -\frac{\mathrm{d}p_r}{\mathrm{d}r}$
- $F_a = \frac{2}{r}(p_t - p_r)$.

The nature of these forces is described in Fig.3.12, which shows that all forces increase from the center to attain maximum value at some interior point and then decrease towards the surface. The fact that the sum of all forces vanishes at all interior points results in null, indicating a stable configuration under the combined action of all forces. It is to be noted that the system remains in a static equilibrium condition for different values of α.

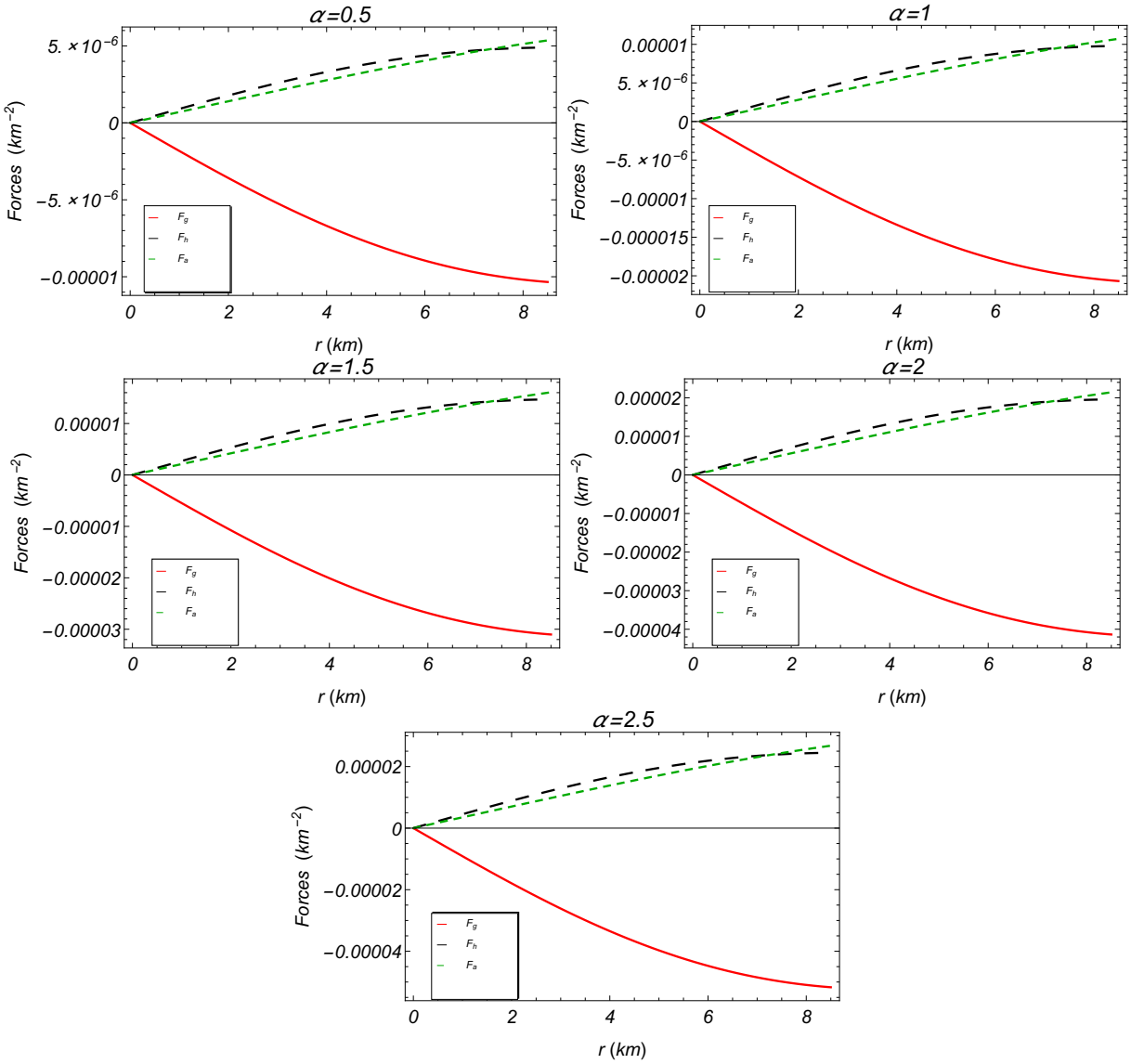

Fig. 3.12. Three different forces acting on the system are shown in the figure for different values of α.

3.7 Mass-Radius Relationship

One of the important features of compact stellar modeling is the ability to predict the mass and radius of stars that may exist in nature. One way is to do this by plotting the $M - R$ curve using the TOV equation. In this chapter, the mass-radius curve has been plotted with different surface densities for a particular value of $\alpha = 0.6$ in Fig.3.13. The different masses and radii of some observed pulsars have also been marked [Abbott et al. (2018), Abbott et al. (2020), Gonzalez-Caniulef et al. (2019), Ozel et al. (2016), Rybicki et al. (2006), and Webb and Barret (2007)]

- KS 1731-260 with $\mathrm{M} = 1.61^{+0.35}_{-0.37}\ M_{\odot}$ & $\mathrm{R} = 10.0^{+2.2}_{-2.2}\ km$;
- $4U1608-52$ with $\mathrm{M}= 1.57^{+0.30}_{-0.29}\ M_{\odot}$ & $\mathrm{R} = 9.8^{+1.8}_{-1.8}\ km$;
- $EXO1745-268$ with $\mathrm{M}= 1.65^{+0.21}_{-0.31}\ M_{\odot}$ & $\mathrm{R} = 10.5^{+1.6}_{-1.6}$ km;
- $SAXJ1748.9-2021$ with $\mathrm{M} = 1.81^{+0.25}_{-0.37}\ M_{\odot}$ & $\mathrm{R} = 11.7^{+1.7}_{-1.7}\ km$;
- $4U1820-30$ with $\mathrm{M} = 1.46^{+0.21}_{-0.21}\ M_{\odot}$ & $\mathrm{R} = 11.1^{+1.8}_{-1.8}\ km$;
- $4U1724-207$ with $\mathrm{M}= 1.81^{+0.25}_{-0.37}\ M_{\odot}$ & $\mathrm{R} = 12.2^{+1.4}_{-1.4}\ km$;
- $M13$ with $\mathrm{M} = 1.38^{+0.08}_{-0.23}\ M_{\odot}$ & $\mathrm{R} = 9.95^{+0.24}_{-0.27}\ km$;
- $J0030+0451$ with $\mathrm{M} = 1.34^{+0.15}_{-0.16}\ M_{\odot}$ & $\mathrm{R} = 12.71^{+1.14}_{-1.19}\ km$;
- $J0437-4715$ with $\mathrm{M} = 1.44^{+0.07}_{-0.07}\ M_{\odot}$ & $\mathrm{R} = 13.6^{+0.9}_{-0.8}\ km$;
- $GW170817-1$ with $\mathrm{M} = 1.45^{+0.09}_{-0.09}\ M_{\odot}$ & $\mathrm{R} = 11.9^{+1.4}_{-1.4}\ km$;
- $GW170817-2$ with $\mathrm{M} = 1.27^{+0.09}_{-0.09}\ M_{\odot}$ & $\mathrm{R} = 11.9^{+1.4}_{-1.4}\ km$.

with their recent data in the plot. The observed values corresponding to mass and radius are found to fit in the $M-R$ curve. The plot also predicts the possibility of the existence of higher mass for a certain range of boundary surface density.

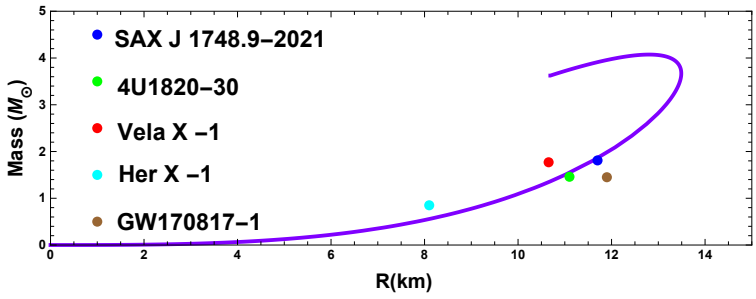

Fig. 3.13. The mass-radius curve for three different surface densities along with mass-radius points of some observed pulsars.

3.8 Discussion and Conclusion

Within the context of $f(T)$ gravity theory, an analytical relativistic anisotropic quintessence spherical model has been developed in the current chapter. Three ingredients, which serve

as the main pillars of the resulting paradigm, were imposed to achieve this. The first of them was to take into account a straightforward, noteworthy and realistic modified gravity model given by $f(T) = \alpha T + \beta$, where T is the torsion, α is a coupling constant and β is another constant. The second step is to choose the metric coefficients and for this task, the coefficients suggested by TK have been opted for. The matter density and radial pressure possess a linear equation of state imposed between them. Using these components, expressions for matter density, radial and transverse pressure, as well as the matter density associated with the quintessence field, have been effectively generated. Once that was done, the constant parameters of the solution have been obtained. A matching between the internal and external Schwarzschild solutions at the boundary of the compact structure has been developed for this purpose. In terms of the mass and radius of the compact star, various model parameters have been successfully acquired by using the matching conditions. The existence, stability and equilibrium of spherical stars in the $f(T)$ theory are the next topics of interest to us. The behavior of the key distinguishing characteristics has been investigated for this purpose, including the radial and tangential pressure, matter density and anisotropy factor. Both the parameter ω and the parameter α have an impact on the model parameters, which is summarized here. Throughout the analysis, a wide range of α has been taken i.e., for the plotting of the model parameters, $\alpha \in [0, 2.5]$ has been chosen.

Central density, surface density,central pressure, compactness factor and surface redshift have been presented for the compact star $Her\ X-1$ for different values of α in the Table.3.2,

According to the findings, all three thermodynamic observables ρ, p_r and p_t remain positive and reach their highest values at the core of the compact star. This indicates that they behave monotonically, decreasing from the center to the boundary. It is interesting to see that ρ, p_r and p_t have higher central values when $\alpha = 2.5$ is applied; however, these values are lower when $\alpha = 0.5$. For all chosen values of α, the anisotropic factor Δ is a positive and monotonic increasing function throughout the object. In order to prevent point singularities or the creation of a black hole, a positive anisotropy factor signifies that the system is subject to an external repulsive force that works to balance the gravitational attraction. For all values of α, in this investigation, the energy conditions are valid. Since the material inside the object cannot travel faster than light, the current model satisfies the constraints of causality. The profiles of V_t^2 coincide for all values of α, as seen in Fig.3.10. It

has been discovered that the range [0, 1] encompasses the difference between the squares of the subliminal sound speeds, i.e., $|V_t^2 - V_r^2| \in [0, 1]$. Fig.3.9 illustrates the maximum feasible value of the surface redshift, which cannot be arbitrarily large. The compactness factor for the current model is below the maximum value found in the literature, i.e., $u|_{max} < 4/9$. The TOV equation is used to study the analysis of the balance mechanism in the context of the $f(T)$ model. It is demonstrated that the system is subject to three forces for the specific choice of the $f(T)$ model, namely the hydrostatic force F_h, gravitational force F_g and anisotropic force F_a, achieving the equilibrium condition by maintaining the sum of all the forces to be zero. Additionally, the equation of the state parameters ω_r and ω_t for all values of α have been shown and for the current model, the profiles of ω_r and ω_t coincide for all values of α. It should be mentioned that ω_r and ω_t both fall within the range $[0, 1]$. For the current model, the maximum permissible mass and associated radius were determined using the $M - R$ curve and they are shown in Fig.3.13. A comprehensive graphical analysis is used to support each of the concepts shown in Figs.3.1 to 3.13. In conclusion, the models described here have been meet all the physical requirements, making them perfect choices to represent reliable models in the context of $f(T)$ gravity.

Chapter 4

Complexity Characterization in Modeling Anisotropic Compact Stellar Structures

4.1 Introduction

Compact stars serve as distinctive laboratories for the study of physics at ultra-high densities. At such extreme densities (exceeding nuclear saturation), it is expected that exotic forms of matter exist within the stellar cores of these objects. Such stellar states can take the form of quark or hyperonic matter in place of normal baryonic matter. In general, to model such extreme objects theoretically one needs to know the interior properties of compact objects such as neutron stars and pulsars which are described by an equation of state (EoS) which relates the pressure with density. Based on the EoS, the physical properties of a compact star can be analyzed by solving the general relativistic Tolman-Oppenheimer-Volkov (TOV) equation governing stellar structure. In the absence of the adequate knowledge of particle interactions at extreme densities, researchers employ alternative routes such as assuming specific geometric forms or the behavior of density, pressures, anisotropy in theoretical modeling of compact objects. The concept of isotropy as well as anisotropy in the context of general relativity have been discussed elaborately in Sec.3.1 of Chapter.3.

In the framework of classical General Theory of Relativity (GTR), the exploration of compact objects relies on finding exact solutions of the corresponding field equations. Since

then the area of modeling compact stellar objects in GTR has become an active research avenue. In the pursuit of solutions describing self-gravitating configurations, researchers have adopted various approaches many of them were discussed in the introduction section of previous chapters, aligning with this approach, the concept of complexity is incorporated to solve the set of field equations and to construct realistic models that characterize compact stellar objects. Complexity in astrophysics refers to how complicated or intricate the structure and behavior of an astrophysical object are. Lloyd and Pagels (1988) explored statistical complexity, which measures the amount of information stored in the causal states of a system. Later, Calbet and López-Ruiz (2001) studied the complexity in the context of a simplified isolated ideal gas model, known as the "tetrahedral gas." They examined the Lopez-Ruiz–Mancini–Calbet complexity, which considers the balance between entropy and disequilibrium. Panos et al. (2009) explored the concept of complexity in nuclear physics. They applied complexity measures to the analysis of nuclear systems. Initially, the idea of complexity in physics began with work on algorithmic complexity by Kolmogorov (1965), who proposed a measure based on the length of the shortest possible description of an object or system. This laid the groundwork for understanding complexity in a broad sense, influencing various fields including astrophysics. The concept of complexity developed and [Herrera (2018)] revolves around a quantifiable measure of the structural characteristics of self-gravitating systems, like stars or fluid spheres. This measure is designed to capture the degree of inhomogeneity in energy density and anisotropy in pressure within these systems. Complexity refers to the degree of intricate structure and behavior within astrophysical objects such as stars, black holes and galaxies. It encompasses both the physical structure and the dynamical processes within these objects. Understanding complexity is crucial for developing accurate models of stellar evolution, galaxy formation and the behavior of compact objects. It is defined in terms of the structure and properties of the fluid that makes up these objects. This includes considerations of anisotropy, energy density inhomogeneity and the behavior of the fluid's constituents. Herrera uses the equations of relativistic hydrodynamics to describe the behavior of the fluid in a self-gravitating system. These relations are derived from the Einstein field equations. He introduces structure scalars derived from the orthogonal splitting of the Riemann tensor. These scalars are used to describe the energy density, pressure and anisotropy of the fluid. He defines a complexity factor for the fluid.

This factor is a function of the structure scalars and provides a measure of the deviation from simplicity.

In the literature, researchers have developed models of compact objects constrained by the condition of vanishing complexity. Das et al. (2024) have modelled superdense stars using the vanishing complexity condition by solving Einstein equations for exact solutions by employing the Vaidya–Tikekar background geometry.The various factors contributing to the complexity of a stellar interior, such as inhomogeneity refers to the variation in density and composition within the star and anisotropy have been thoroughly analyzed. By examining these components in detail, researchers aim to understand their impact on the overall structure and stability of compact objects. In the context of Vaidya–Tikekar background geometry, Govender et al. (2022) have examined the impact of spheroidicity parameter K on complexity in static, self-gravitating systems. Using the anisotropic generalization of the Vaidya-Tikekar superdense stellar model, they relate the spheroidal parameter to pressure anisotropy and density inhomogeneity through the complexity factor. Their results showed that deviations from spherical symmetry increase the complexity within the stellar body.

The complexity factor vanishes for a homogeneous and isotropic fluid distribution, implying that such a system has zero complexity. The complexity in compact stars can be attributed to the resultant effects of density inhomogeneity and anisotropy within their interiors. If the impact of anisotropy counteracts the effects caused by density inhomogeneity, the system becomes free of complexity. However, it's important to note that not all static systems are required to have zero complexity. Particularly, it may be interesting to study static compact systems by prescribing complexity factor suitably. In this chapter, the novel approach is to specify a particular reasonable form of the complexity in addition of assuming a particular geometry corresponds to g_{tt} component to solve the system. This approach diverges by admitting that not all solutions to the Einstein field equations for stellar structures are complexity-free, thereby not utilizing the vanishing complexity condition.Various factors contributing to the complexity within the interior of the star are also analyzed.

This chapter has been organized as follows: In section 4.2, the fundamental Einstein field equations describing anisotropic compact objects are introduced. In section 4.3, a generalized metric potential for g_{tt} is adopted, along with a specific complexity factor for the matter distribution, to solve the associated field equations analytically. The physical conditions nec-

essary for modeling realistic compact stars are then outlined section 4.4. Subsequently in section 4.5, the interior solution is matched with the Schwarzschild exterior space-time at the star's boundary and the corresponding boundary conditions are formulated. Recent observational data from well-known pulsars are used to validate the proposed model in section 4.6. Following this, an in-depth analysis of the physical properties is presented in section 4.7 with some graphical representations. The stability of the model under different conditions is also explored in section 4.8. The importance of mass-radius relationship is depicted in section 4.9. Finally, the chapter concludes with a summary of key findings and insights, in section 4.10.

4.2 Einstein Field Equations

The interior space-time geometry of a static, spherically symmetric object is assumed to be described by the line element in standard coordinates $x^0 = t$, $x^1 = r$, $x^2 = \theta$, $x^3 = \phi$ as

$$ds^2 = -A_0^2(r)dt^2 + B_0^2(r)dr^2 + r^2(d\theta^2 + \sin^2\theta d\phi^2), \tag{4.2.1}$$

here,

- $A_0(r)$ and $B_0(r)$: the gravitational potentials, dimensionless.

This is assumed that the compact star is composed of matter which is anisotropic in nature with respect to pressure. Apart from the physical processes which give rise to anisotropy within the stellar fluid, one expects density inhomogeneity in the energy density profile. It is possible that these two factors, anisotropy and density inhomogeneity not to cancel out thus giving rise to the notion of complexity in stellar systems. To describe the anisotropic fluid system, an energy-momentum tensor is employed which is of the form

$$T_{\alpha\beta} = (\rho + p_t)u_\alpha u_\beta + p_t g_{\alpha\beta} + (p_r - p_t)\chi_\alpha\chi_\beta, \tag{4.2.2}$$

where ρ represents the energy-density, p_r and p_t denote fluid pressures along the radial and transverse directions respectively. The quantity u^α is the 4-velocity of the fluid and χ^α is a unit space-like 4-vector along the radial direction so that the following relations holds: $u^\alpha u_\alpha = -1$, $\chi_\alpha\chi_\beta = -1$ and $u^\alpha\chi_\beta = 0$.

The Einstein field equations of the system corresponding to the line element Eq.(4.2.1) is given by

$$8\pi\rho = \left[\frac{1}{r^2} - \frac{1}{r^2 B_0^2} + \frac{2B_0'}{rB_0^3}\right], \tag{4.2.3}$$

$$8\pi p_r = \left[-\frac{1}{r^2} + \frac{1}{B_0^2 r^2} + \frac{2A_0'}{rA_0B_0^2}\right], \tag{4.2.4}$$

$$8\pi p_t = \left[\frac{A_0''}{A_0B_0^2} + \frac{A_0'}{rA_0B_0^2} - \frac{B_0'}{rB_0^3} - \frac{A_0'B_0'}{A_0B_0^3}\right]. \tag{4.2.5}$$

Where, $(')$ denotes differentiation with respect to the radial coordinate r.

Utilizing the Eqs.(4.2.4) and (4.2.5), the pressure anisotropy of the stellar interior can be defined as

$$\begin{aligned}\Delta(r) &= 8\pi(p_t - p_r) \\ &= \left[\frac{A_0''}{A_0B_0^2} - \frac{A_0'}{rA_0B_0^2} - \frac{B_0'}{rB_0^3}\frac{A_0'B_0'}{A_0B_0^3} - \frac{1}{r^2B_0^2} + \frac{1}{r^2}\right].\end{aligned} \tag{4.2.6}$$

In principle, Δ may be positive as well as negative in nature depending upon whether $p_t > p_r$ or $p_t < p_r$. The model of this chapter has been considered to be $p_t > p_r$ for the matter distribution to obtain a stable structure of compact objects.

The complexity factor Y_{TF} is introduced [Herrera (2018)] to quantify the structural inhomogeneities and anisotropies within these systems. The complexity of the system is quantified using the orthogonal splitting of the Riemann tensor, which decomposes the gravitational field into its constituent parts. For the metric of a spherically symmetric, static fluid distribution, the structure scalars are defined by

$$Y_{TF} = 8\pi\Pi - \frac{4\pi}{r^3}\int_0^r \bar{r}^3\rho' dr, \tag{4.2.7}$$

where, $\Pi = p_r - p_t$. Now from Eqs.(4.2.3)-(4.2.6), the form of Complexity factor is obtained as

$$Y_{TF}(r) = \frac{1}{B_0(r)^2}\left[\frac{A_0{}''(r)}{A_0(r)} - \frac{A_0{}'(r)\left(\frac{2B_0{}'(r)}{B_0(r)} + \frac{1}{r}\right)}{A_0(r)}\right]. \tag{4.2.8}$$

The mass contained within a stellar radius r is defined as

$$m(r) = \frac{1}{2}\int_0^r r^2\rho(r)\ dr. \tag{4.2.9}$$

Thus basically a system of three independent equations are there Eqs.(4.2.3)- (4.2.5) in 5 independent variables, viz. A_0, B_0, ρ, p_r and p_t. The Eq.(4.2.6) representing Δ is basically a dependent equation in p_r and p_t.Two of them must be prescribed to solve the system. The most general metric for a spherically symmetric static body with anisotropic pressure within the context of GTR was obtained by Herrera and co-workers. They showed that in order to obtain the full gravitational behavior of a compact stellar object on needs to employ an ansatz for the one of the metric functions and a the anisotropy factor must be specified [Herrera et al. (2008)].

In this chapter, A novel approach is adopted which involves choosing a metric ansatz for one of the metric potentials and prescribing a physically viable form for the complexity factor. Under these assumptions, the governing equations is solved in the Sec.4.3.

4.3 A New Model with Complexity

To create a physically plausible model of a star's configuration and derive exact solutions, two physical parameters can be selected independently. For the model of this chapter, a particular metric potential and an appropriate form of the complexity are assumed. The metric potential for the g_{tt} metric [Das et al. (2019)] is given by

$$A_0(r) = \beta + \frac{\alpha}{1-\frac{r^2}{L^2}}, \tag{4.3.1}$$

where α, β are constants and will be determined from the matching conditions. Here L is the curvature parameter. It is interesting to note that the assumed form of the metric potential can be transformed to Tolmann-IV like metric potential. Under the restriction of $\frac{r^2}{L^2} << 1$, the metric potential $A_0(r)$ can reduces to

$$A_0(r) = \beta + \alpha\left(1-\frac{r^2}{L^2}\right)^{-1}, \tag{4.3.2}$$

$$A_0(r) = \beta + \alpha\left(1 + \frac{r^2}{L^2} + \frac{r^4}{L^4} + ...\right), \tag{4.3.3}$$

neglecting higher order terms of $\frac{r^2}{L^2}$, the metric potential becomes,

$$A_0(r) = \left(\beta + \alpha + \frac{\alpha r^2}{L^2} + \frac{\alpha r^4}{L^4}\right). \tag{4.3.4}$$

Now setting $\alpha + \beta = 1$, $\frac{\alpha}{L^2} = a$ and $\frac{\alpha}{L^4} = b$, the following form of the metric is obtained.

$$A_0(r) = (1 + ar^2 + br^4), \tag{4.3.5}$$

which is commonly associated with the Tolman IV metric family in the context of exact solutions to Einstein's field equations for a static, spherically symmetric perfect fluid distribution.

With this choice of $A_0(r)$, Eq.(4.2.7) then reduces to

$$Y_{TF}(r) = \frac{4\alpha r L^2\left(\left(L^2 - r^2\right)B_0{}'(r) - 2rB_0(r)\right)}{B_0(r)^3\left(r^2 - L^2\right)^2\left(\beta r^2 - L^2(\alpha + \beta)\right)}. \tag{4.3.6}$$

The equation for $B_0(r)$ will be solved by choosing a specific form of Y_{TF} as follows

$$Y_{TF}(r) = \frac{8\alpha r^2\left(r^2 - L^2\right)^2}{L^6\left(\beta r^2 - L^2(\alpha + \beta)\right)}. \tag{4.3.7}$$

The reasons for the choice

1. To simplify the equation.
2. To make the form dimensionally correct.

Now using Eq.(4.3.6) and Eq.(4.3.7) the following equation is obtained,

$$\frac{\alpha r\left(L^8\left(r^2 - L^2\right)B_0{}'(r) + 2rB_0(r)^3\left(r^2 - L^2\right)^4 + 2rL^8B_0(r)\right)}{L^6B_0(r)^3\left(L^2 - r^2\right)^2\left(\beta r^2 - L^2(\alpha + \beta)\right)} = 0. \tag{4.3.8}$$

which reduces to

$$L^8\left(r^2 - L^2\right)B_0{}'(r) + 2rB_0(r)^3\left(r^2 - L^2\right)^4 + 2rL^8B_0(r) = 0, \tag{4.3.9}$$

the solution of which is

$$B_0(r) = \frac{L^4}{(r^2 - L^2)^2}. \tag{4.3.10}$$

Now it's time to determine the physical quantities such as matter density, radial pressure, transverse pressure and pressure anisotropy which can be cast as

$$8\pi\rho = \frac{-9r^6 + 28r^4L^2 - 30r^2L^4 + 12L^6}{L^8}, \tag{4.3.11}$$

$$8\pi p_r = \frac{r^6 - 4r^4L^2 + 6r^2L^4 - 4L^6}{L^8} + \frac{4\alpha\left(L^2 - r^2\right)^3}{L^6[L^2(\alpha+\beta) - \beta r^2]}, \tag{4.3.12}$$

$$8\pi p_t = \frac{4r^6 - 12r^4L^2 + 12r^2L^4 - 4L^6}{L^8} + \frac{4\alpha\left(L^2 - r^2\right)^3}{L^6[L^2(\alpha+\beta) - \beta r^2]}, \tag{4.3.13}$$

$$8\pi\Delta = \frac{3r^6 - 8r^4L^2 + 6r^2L^4}{L^8}. \tag{4.3.14}$$

4.4 Constraints on Physical Parameters

The following conditions must be met for a stellar model to be physically viable,

(i) The gravitational potentials $A_0(r)$, $B_0(r)$ and the physical quantities ρ, p_r, p_t must be well-defined at the center of the star and remain regular and non-singular throughout its interior.

(ii) The energy density must remain positive throughout the star's interior and should monotonically decrease from its maximum value at the center towards the boundary. Mathematically i.e., $\rho \geq 0$, $\frac{d\rho}{dr} \leq 0$.

(iii) The radial and tangential pressures must remain positive throughout the entire interior of the star i.e., $p_r \geq 0$, $p_t \geq 0$. The pressures should decrease monotonically with respect to the radial coordinate r. This is ensured by the negative signature of the gradient of the pressures inside the stellar body, i.e., $\frac{dp_r}{dr} < 0$, $\frac{dp_t}{dr} < 0$. Additionally, at the boundary $r = R$ of the star the radial pressure must approach zero. The condition $p_r(R) = 0$ is defines the radius of the star. However, the tangential pressure on the surface may be nonzero. At the center of the star, both the radial and transverse pressures are equal, implying that the anisotropy vanishes at the center, $\Delta(r = 0) = 0$.

(iv) For a stable anisotropic compact star, certain energy conditions must be met at every interior point of the fluid sphere. In the framework of general relativity, the energy conditions are basically expressed through local inequality relations between the energy density and the pressures. The energy conditions are the Weak, Null, Strong and Dominant Energy Condition respectively, defined by the following inequalities.

- WEC : $\rho > 0,\ \ p_r + \rho \geq 0,\ p_t + \rho \geq 0.$
- NEC : $p_r + \rho \geq 0,\ \ \rho + p_t \geq 0.$
- SEC : $\rho + p_r + 2p_t \geq 0.$
- DEC: $\rho - |p_r| \geq 0$ and $\rho - |p_t| \geq 0.$

In this context it is interesting to check the trace energy condition (TEC) as suggested by the authors [Bondi (1999) and Tello-Ortiz et al. (2020)]. The trace of the energy tensor must remain positive throughout the interior of the star, represented mathematically as : $\rho - p_r - 2p_t \geq 0.$

(v) The causality condition states that the speed of sound, both radial and transverse, must be less than 1 (in natural units where the speed of light c=1) throughout the interior of the star. For a physically acceptable realistic model the causality condition, i.e., $0 \leq \frac{dp_r}{d\rho} \leq 1$, $0 \leq \frac{dp_t}{d\rho} \leq 1$ must be satisfied.

(vi) The interior geometry of the star, represented by the metric functions, must smoothly match the exterior Schwarzschild space-time metric at the stellar boundary.

(vii) Adiabatic index (Γ), the ratio of two specific heats is related to the stability of an anisotropic stellar configuration. For a stable model, the well known condition for the stability of a Newtonian isotropic sphere is: $\Gamma > 4/3$. For a relativistic anisotropic sphere this condition modified to some extent.

4.5 The Space-time at the Exterior and Junction Conditions

In general relativity theory, the Schwarzschild metric is defined uniquely as spherically symmetric solution to the vacuum Einstein field equations. The Schwarzschild metric, describes

the exterior vacuum spacetime of a non-radiating star can be cast as

$$ds^2 = -\left(1-\frac{2M}{r}\right)dt^2 + \left(1-\frac{2M}{r}\right)^{-1}dr^2 + r^2\left(d\theta^2+\sin^2\theta d\phi^2\right), \tag{4.5.1}$$

where M being the total mass of the stellar object.

The matching conditions determine the numerical values of the model parameters. The junction conditions require the continuity of both the first and second fundamental forms (representing intrinsic and extrinsic curvature, respectively) across the non-radiating boundary surface. Here, the condition of the continuity of the first fundamental form is applied in the development of compact stars, resulting in the creation of static solutions. The continuity of the second fundamental is not required. For a static scenario, the continuity of the first fundamental form at the boundary enables the matching of the interior spacetime metric Eq.(4.2.1) to the vacuum exterior Schwarzschild solution Eq.(4.5.1). This continuity of the metric functions at the boundary results in

Continuity of g_{tt} :

$$A_0^2(R) = \left(1-\frac{2M}{R}\right), \tag{4.5.2}$$

Continuity of g_{rr} :

$$B_0^2(R) = \left(1-\frac{2M}{R}\right)^{-1}. \tag{4.5.3}$$

Radial pressure disappears at a finite value of the radial parameter r which defines the star's radius. Therefore, the radius of the star can be determined by applying the condition $p_r(r=R)=0$.

The above boundary conditions determine the model parameters. 3 model parameters with three equations are obtained in total. By fixing mass and radius of stars, the model parameters can be determined in principle. These parameters are utilized to represent all the physically relevant quantities graphically.

4.6 Model with Observational Data

A specific pulsar $4U\ 1608-52$ has been chosen and the following criteria has been checked.

It's the right time to validate this theoretical model against experimentally observed data from various reliable sources on neutron star masses and radii. For this purpose the mass

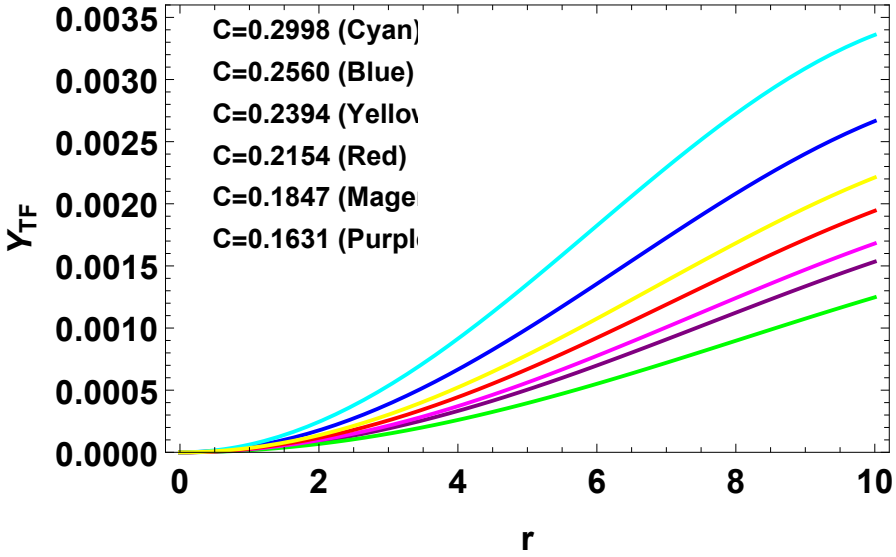

Fig. 4.1. Variation of Complexity function Y_{TF} with radial parameter 'r'

and radius of observed pulsars were used as input parameters and the physical consistency of the model was assessed. The pulsar $4U\ 1608-52$ km [Roupas and Nashed (2020)] with its recent estimated mass has been considered $= 1.57^{+0.30}_{-0.29}\ M_{\odot}$ and radius $= 9.8 \pm 1.8$. With these mass and radius constrains $\alpha = 0.80375$, $\beta = -0.20676$ and $L = 25.81$ are obtained, using the junction conditions. The values of these constants thus obtained various physical quantities have been plotted graphically.

The regular and well-behaved nature of all relevant physical quantities, along with the fulfillment of the necessary conditions, suggests that the model aligns with the experimental data, making it suitable for describing a physically realistic and plausible star.

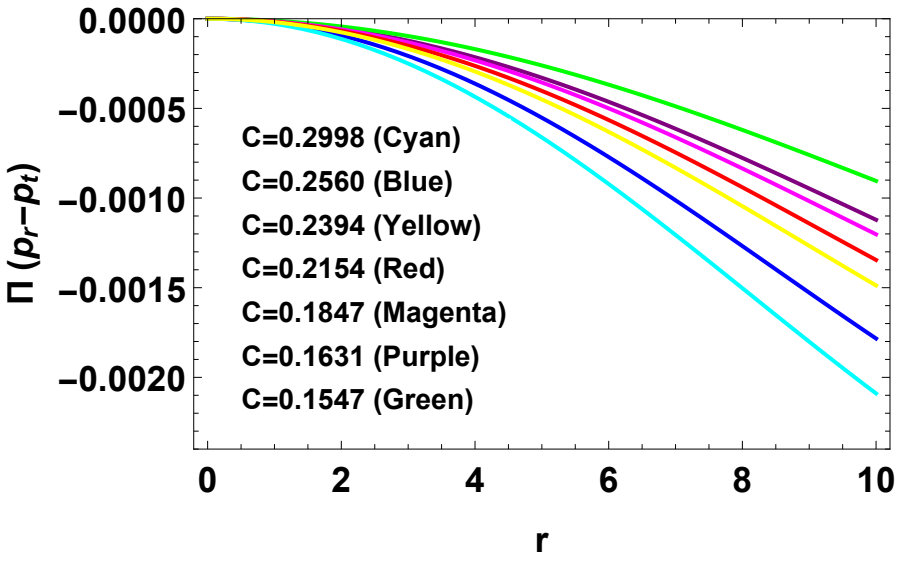

Fig. 4.2. Variation of $\Pi(p_r - p_t)$ with radial parameter 'r'

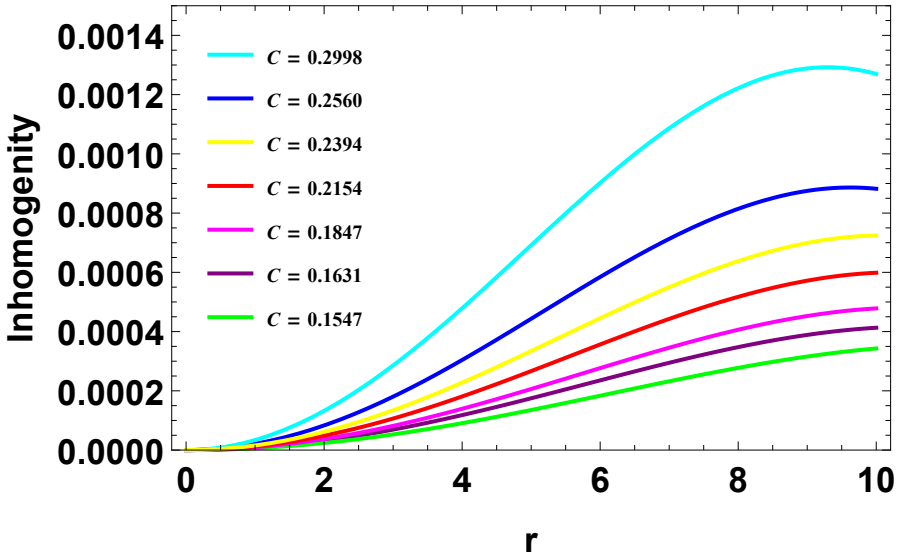

Fig. 4.3. Variation of density inhomogeneity with radial parameter 'r'

Measure of the deviation from uniformity in the physical characteristics of the system that is complexity is depicted in Fig.4.1. From this figure it can be shown that there is a definite variation of complexity factor Y_{TF} with compactness C, complexity is increasing when compactness is increasing. One can note the same pattern with the anisotropy and energy density inhomogeneity depending on compactness refers in Figs.4.2-4.3.

4.7 Validation of the Model: Physical Analysis

In this section, the goal is to demonstrate that all the physical requirements stated in the previous Sec.4.5 are satisfied for this model.

4.7.1 Metric Coefficients

The gravitational potentials at the origin of the star are finite at the center ($r = 0$) of the stellar configuration. $A_0^2(0) = (\alpha+\beta)^2 = \text{constant}$, $B_0^2(0) = 1$. Also this has been checked that $(A_0^2(r))'_{r=0} = (B_0^2(r))'_{r=0} = 0$. These imply that the metric is regular at the center and regular throughout the stellar interior.

In Fig.4.4, the metric potentials for the pulsar 4U $1608-52$ have been graphically depicted, highlighting their regularity and non-singular nature. This figure depicts the smooth matching of the interior space time with that of the exterior metric over the bounding surface.

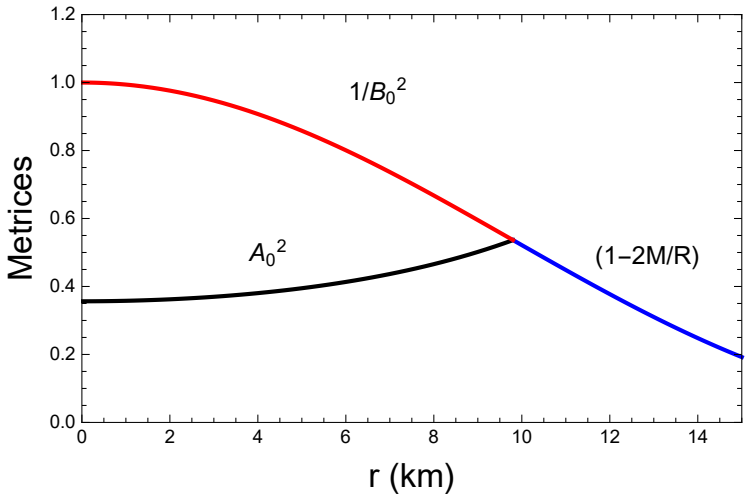

Fig. 4.4. Metric potential $A_0^2(r)$ and $B_0^2(r)$

4.7.2 Density Profile

The value of the density at the centre in this model is $\rho(0) = \frac{12}{L^2}$,

Note that the density is always positive as the curvature parameter L is positive.

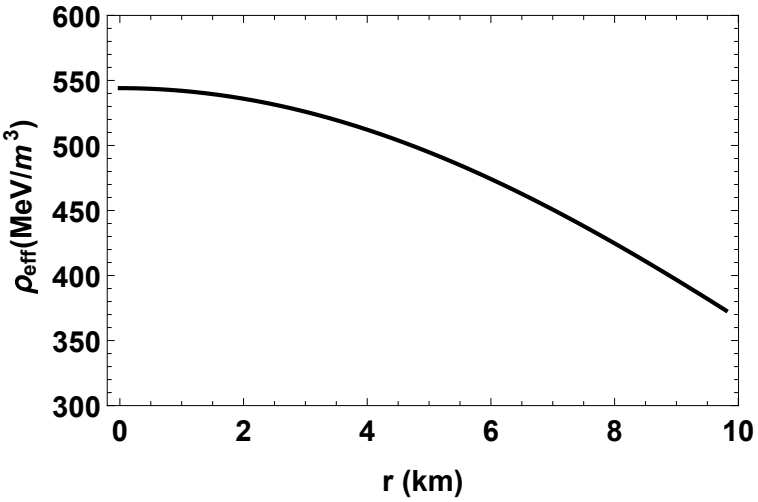

Fig. 4.5. Density Profile

Fig.4.5 demonstrates that the energy density monotonically decreases from its maximum value at the center to the surface, as expected.

4.7.3 Pressures Profile

For this model the values of the radial pressure and tangential pressure at the center are

$p_r(0) = -\frac{4\beta}{L^2(\alpha+\beta)}$,

$p_t(0) = -\frac{4\beta}{L^2(\alpha+\beta)}$.

That is at the center, the radial pressure and tangential pressure are equal, indicating that pressure anisotropy vanishes, as expected. According to Zeldovich's condition, p_r/ρ must be ≤ 1 at the centre. Therefore, $-\frac{\beta}{3(\alpha+\beta)} \leq 1$ i.e., $3\alpha + 4\beta \leq 0$.

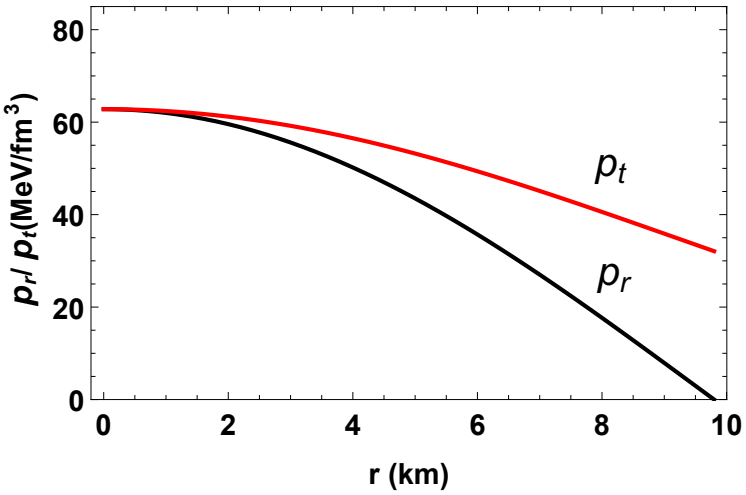

Fig. 4.6. Radial and transverse pressure profiles

The variations of radial and tangential pressures are plotted in Fig.4.6, showing that both decrease radially from their maximum value at the center towards the boundary. The plot confirms that while the radial pressure drops to zero at the boundary, the tangential pressure remains non-zero at the surface.

4.7.4 Anisotropy

Anisotropy mentioned in Eq.4.3.14 is depicted in the following figure.

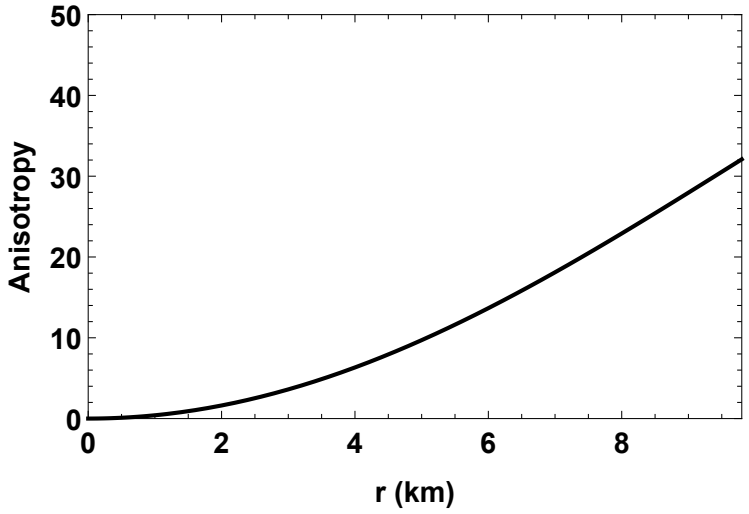

Fig. 4.7. Anisotropy profile

The radial variation of anisotropy, shown in Fig.4.7, is zero at the center and reaches its maximum value at the surface.

4.7.5 Causality Condition

The radial($\frac{dp_r}{d\rho}$) and transverse velocity ($\frac{dp_t}{d\rho}$) of sound ($c = 1$) are obtained from the expressions

$$\begin{aligned} v_{sr}^2 &= \frac{2}{\left(-60L^4+112L^2r^2-54r^4\right)\left(\beta r^2-L^2(\alpha+\beta)\right)^2} \\ &\times\Big[4\alpha\beta L^2\left(L^2-r^2\right)^3+\left(6L^4-8L^2r^2+3r^4\right)\left(\beta r^2-L^2(\alpha+\beta)\right)^2 \\ &+12\alpha\left(L^3-Lr^2\right)^2\left(\beta r^2-L^2(\alpha+\beta)\right)\Big], \qquad (4.7.1) \\ v_{st}^2 &= -\frac{4\beta\left(L^2-r^2\right)^3\left(L^2(4\alpha+3\beta)-3\beta r^2\right)}{\left(30L^4-56L^2r^2+27r^4\right)\left(\beta r^2-L^2(\alpha+\beta)\right)^2}. \qquad (4.7.2) \end{aligned}$$

In this model the speed of sound is smaller than 1 in the interior of the star, i.e., $0 \leq \frac{dp_r}{d\rho} \leq 1$, $0 \leq \frac{dp_t}{d\rho} \leq 1$ which has been shown graphically in Fig.4.8.

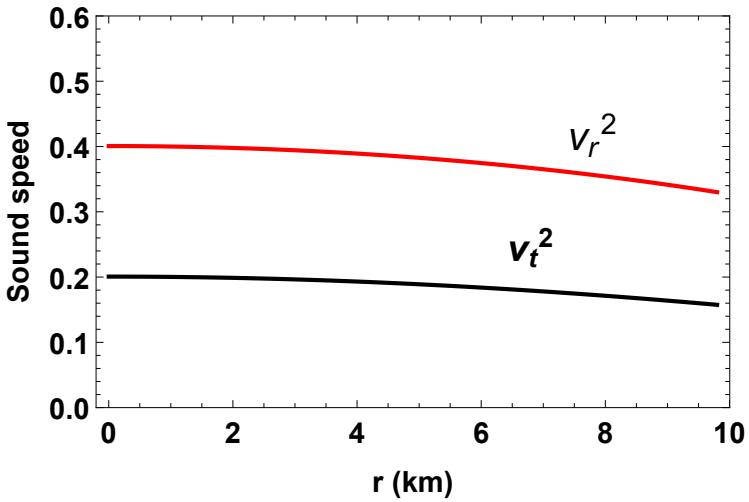

Fig. 4.8. Radial and transverse sound speed profile

In Fig.4.8, the sound speeds in the radial and transverse directions are plotted as a function of the radial coordinate. The speeds stay within the required range throughout the interior of the star ($c = 1$), ensuring that the causality condition is not violated.

4.7.6 Energy Conditions

The energy conditions for an anisotropic fluid sphere require that the following terms remain positive throughout the stellar interior:

$\rho + p_r \geq 0$, $\rho + p_t \geq 0$ and $\rho + p_r + 2p_t \geq 0$.

As evidenced by the graphical plot in Fig.4.9, these quantities are observed to remain positive throughout the compact sphere, as expected. Also, trace energy condition refers as $TEC = \rho - p_r - 2p_t \geq 0$.

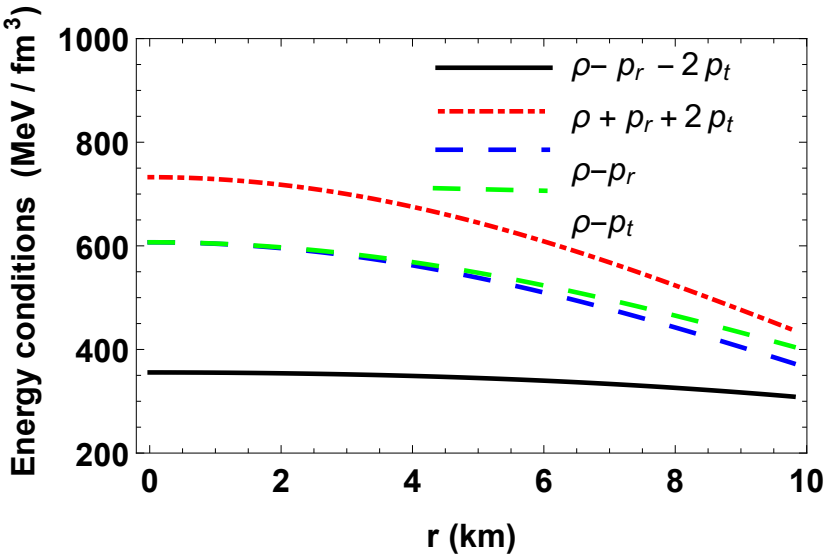

Fig. 4.9. Energy Conditions

The Trace Energy Condition (TEC) is a less commonly discussed, but still important, energy condition in general relativity. TEC can also be examined graphically ensuring the combination of energy density and radial pressure within a compact object remains non-negative, preserving the physical integrity of the object and preventing the occurrence of exotic matter or unstable configurations. In this model TEC it is found to be satisfied denoted by black curve in Fig.4.9.

4.7.7 Mass Function

The mass function of a compact object describes how the mass is distributed within the object as a function of its radial coordinate. In the context of general relativity, for a spherically symmetric compact object such as a star or a neutron star, the mass function is used to determine the total mass enclosed within a given radius.

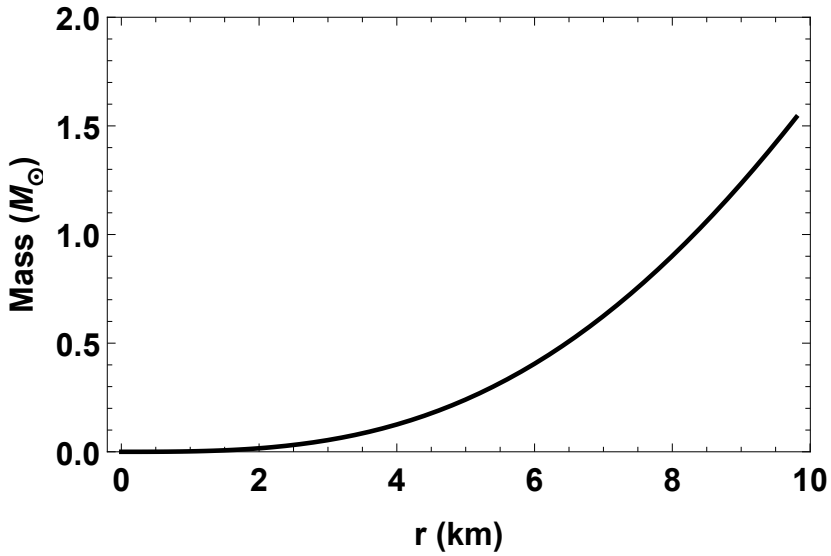

Fig. 4.10. Mass profile

The mass function is monotonically increasing the function of r. Also $m(0) = 0$ and $m(9.8) = 1.57M\odot$ corresponds to centre and surface as shown in Fig.4.10. It is also shown that mass function is regular at the centre.

4.7.8 EoS Parameter

EoS parameter is given by

$$\omega_r = \frac{p_r}{\rho}; \qquad \omega_t = \frac{p_t}{\rho}. \tag{4.7.3}$$

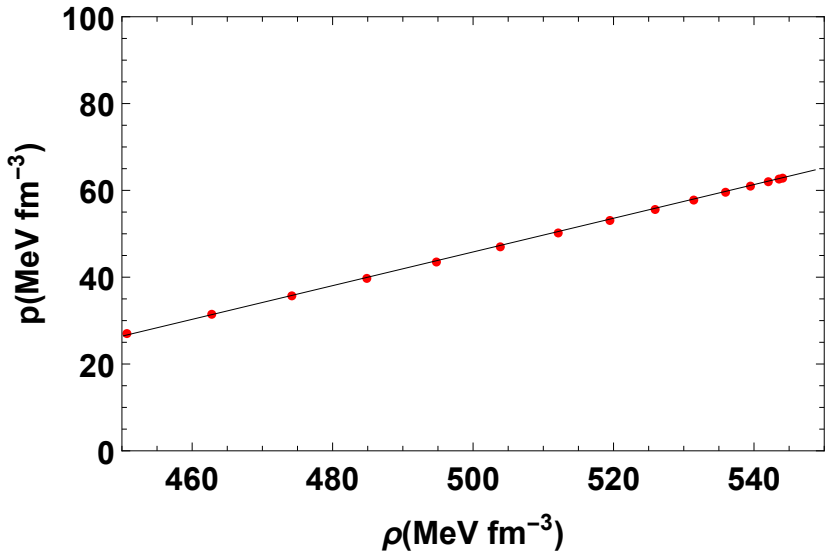

Fig. 4.11. Curve Fitting

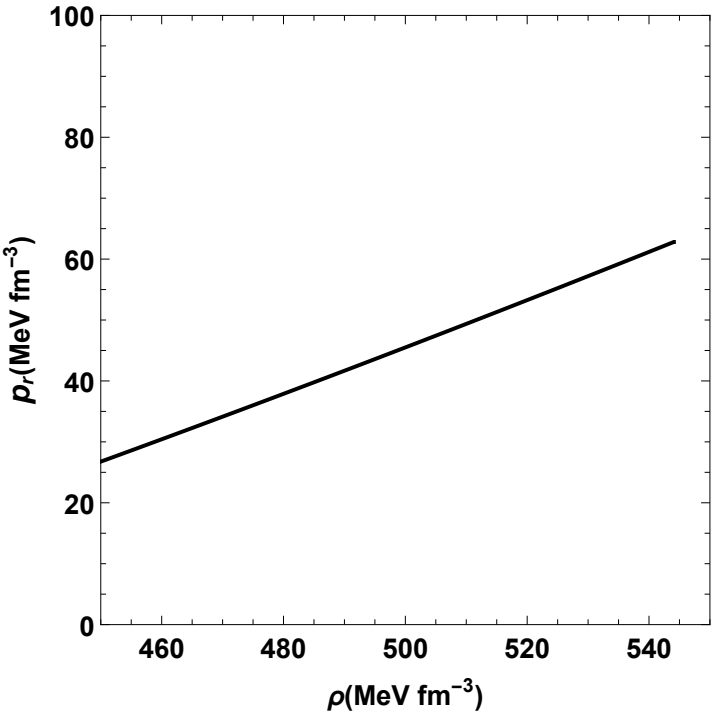

Fig. 4.12. EoS profile

To be non-exotic in nature the value of ω_r and ω_t should lie within 0 and 1. Our model is shown to satisfies the condition $0 \leq \omega_r \leq 1$, $0 \leq \omega_t \leq 1$.

It is to be noted that in developing this model any EoS has not been considered. The relationship between ρ and p_r is inferred almost linear according to the relation given as $p_r = -140.524 + 0.372848\rho$ in Fig.4.11. The relationship between the thermodynamic parameters, energy density and pressure, is presented graphically without prescribing any specific EoS. Thus, the nature of the EoS for the matter distribution is illustrated in Fig.4.12.

4.8 Analysis of the Model's Stability

The stability of a compact star is governed by a delicate balance of gravitational forces, internal pressure, thermodynamics and relativistic effects. Compact stars are stable as long as they maintain hydrostatic equilibrium, resist both radial and non-radial instabilities and stay within their mass limits.

4.8.1 Equilibrium Condition

The stability of a star can be characterized by the well-known TOV equilibrium conditions. A star maintains static equilibrium due to the combined effects of gravitational force, hydrostatic pressure and anisotropic pressure. This equilibrium is mathematically described by the TOV equation, which is given by

$$-\frac{M_G}{r}(\rho+p_r)\frac{A_0(r)}{B_0(r)}-\frac{dp_r}{dr}+\frac{2}{r}(p_t-p_r)=0, \tag{4.8.1}$$

Here, $M_G(r)$ represents the gravitational mass of the star at a radial distance r. The value of $M_G(r)$ can be derived using the Tolman-Whittaker formula in conjunction with Einstein's field equations and is expressed as

$$M_G(r)=\frac{rB_0(r)A_0'(r)}{A_0^2(r)}. \tag{4.8.2}$$

Using the expression of $M_G(r)$ in Eq.(4.8.1) this is obtained

$$-\frac{A_0'(r)}{A_0(r)}(\rho+p_r)-\frac{dp_r}{dr}+\frac{2}{r}(p_t-p_r)=0. \tag{4.8.3}$$

The above equation is equivalent to $F_g+F_h+F_a=0$, where,

$$F_g = -\frac{A_0'(r)}{A_0(r)}(\rho+p_r), \tag{4.8.4}$$

$$F_h = -\frac{dp_r}{dr}, \tag{4.8.5}$$

$$F_a = \frac{2}{r}(p_t-p_r), \tag{4.8.6}$$

represents the gravitational, hydrostatics and anisotropic forces respectively. The expressions for different forces F_g, F_h and F_a can be expressed as,

$$F_g = \frac{8\alpha r\left(L^2-r^2\right)^2\left(L^2(3\alpha+2\beta)-2\beta r^2\right)}{L^6\left(\beta r^2-L^2(\alpha+\beta)\right)^2}, \tag{4.8.7}$$

$$F_h = -\frac{2r}{L^8}\Big[4\alpha\beta L^2\left(L^2-r^2\right)^3+\left(6L^4-8L^2r^2+3r^4\right)\left(\beta r^2-L^2(\alpha+\beta)\right)^2 +12\alpha\left(L^3-Lr^2\right)^2\left(\beta r^2-L^2(\alpha+\beta)\right)\Big], \tag{4.8.8}$$

$$F_a = \frac{2\left(6L^4r-8L^2r^3+3r^5\right)}{L^8}. \tag{4.8.9}$$

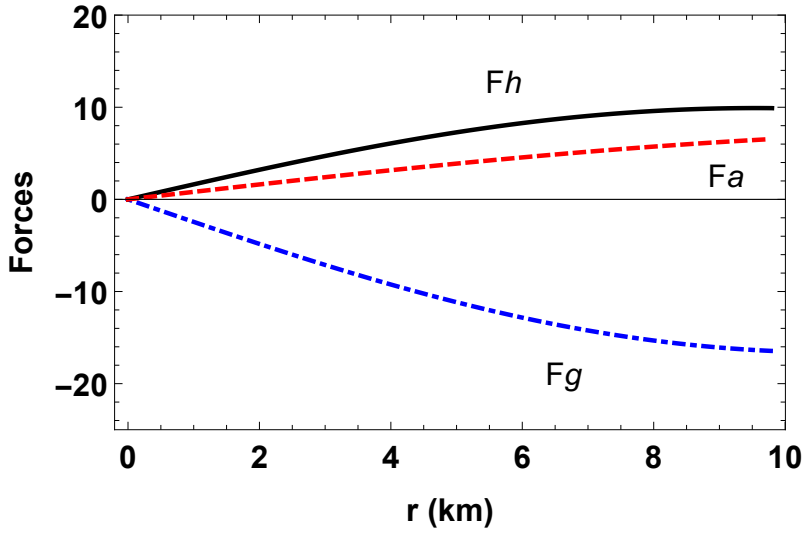

Fig. 4.13. Different forces

Fig.4.13 depicts the nature of all these forces thus satisfying the TOV equation.

4.8.2 Adiabatic Index

One important criterion for the stability of any stellar configuration is to examine the adiabatic index. The adiabatic index (denoted by Γ) is defined as the ratio of two specific heats [Chan et al. (1993)] is expressed as

$$\Gamma = \frac{\rho + p_r}{p} \frac{dp_r}{d\rho}. \tag{4.8.10}$$

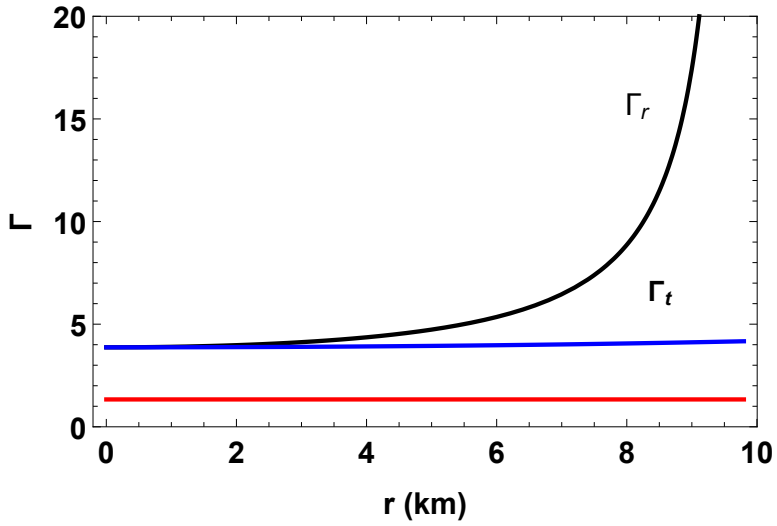

Fig. 4.14. Adiabatic index profile

The stability of a relativistic anisotropic compact star maintain as long as the value of the adiabatic index $\Gamma > 4/3$. This feature is shown to satisfy in Fig.4.14.

4.8.3 Herrera Cracking Condition

Another key method for analyzing the stability of anisotropic stars is the cracking condition, introduced by Herrera (1992). In the cracking method, a small perturbation is introduced at a specific point, causing a slight deviation or split from the equilibrium configuration, without leading to collapse or expansion. The cracking method investigates the behavior of the matter distribution after it deviates from equilibrium, allowing for the examination of potentially stable or unstable anisotropic configurations. Subsequently, Abreu et al. (2007) identified the stable region of an anisotropic fluid sphere by imposing a constraint on the sound speeds, expressed as $-1 \leq v_t^2 - v_r^2 \leq 0$. This condition is satisfied in the current model, as depicted graphically in Fig.4.15.

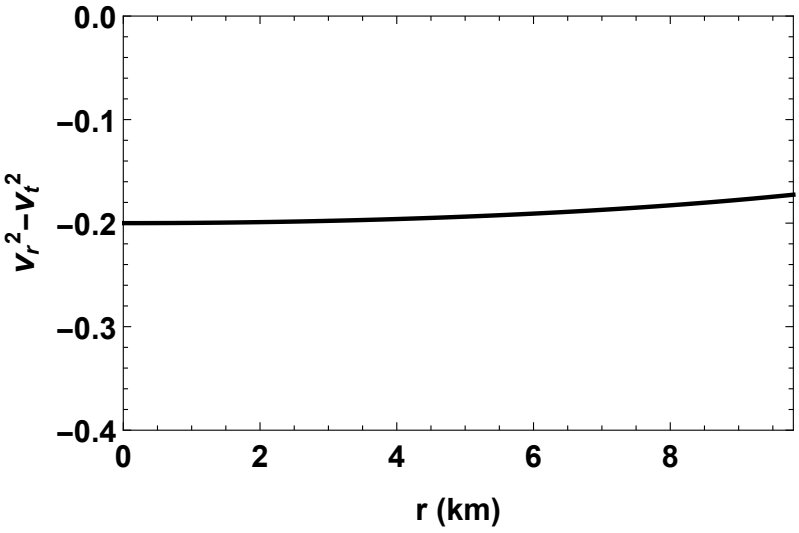

Fig. 4.15. Difference in sound speeds

4.9 Mass-Radius Relationship

The mass-radius relationship of compact stars is a critical aspect of their stability. This relationship describes how the mass of a star correlates with its radius and it provides important insights into the internal structure and physical limits of compact stars.

In Fig.4.16, the mass-radius ($M - R$) relationship is presented which is derived for a

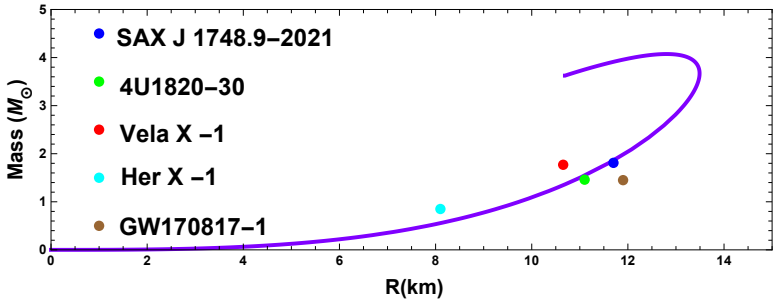

Fig. 4.16. Mass-Radius (M-R) profile

fixed surface density of $4.7 \times 10^{14}\,\mathrm{g/cm}^3$. Notably, several known pulsars namely SAX J1748.9 − 2021 (M = $1.81^{+0.25}_{-0.37} M_\odot$; R = 11.7 ± 1.7 km), 4U1820 − 30 (M = $1.46 \pm 0.21 M_\odot$; R = 11.1 ± 1.8 km), Vela X-1 (M = $1.77 \pm 0.08 M_\odot$; R = 10.654 km), Her X - 1 (M = $0.85 \pm 0.15 M_\odot$; R = 8.1 km), GW170817 − 1 (M = $1.45 M_\odot$; R = 11.9 km) and the secondary component of GW190814 ($2.59^{+0.08}_{-0.09} M_\odot$) align with this plot, indicating that this model accurately predicts the characteristics of these well-known stars.

4.10 Discussion

This study develops and validates an exact solution to the Einstein field equations for a static, spherically symmetric, anisotropic stellar fluid sphere with non-zero complexity, using pulsar data for validation and standard stability conditions. In this chapter, despite not prescribing a specific EOS, this was possible to identify the linkage between the density and pressure distributions which is almost linear.

It has been observed that the parameter Y_{TF} exhibits a definite pattern of variation with the compactness C of stars. Y_{TF} increases with compactness of stars. Also, the anisotropy parameter Π follows a consistent pattern with respect to C as Y_{TF} and density inhomogeneity. This suggests that as the compactness of the stars changes, both anisotropy and density inhomogeneity adjust in a manner that ensures a regular and predictable behavior in the Y_{TF} parameter. The combined influence of anisotropy and density inhomogeneity appears to be coordinated to maintain a specific trend in Y_{TF} as the compactness C varies.

One interesting outcome of the study is the generation of $M - R$ curves that predicts the mass-radii characteristics of some well-known pulsars. One can note that this model predicts the existence of compact objects with masses more than $2M_\odot$ in addition of low-mass stars.

The complexity factor can be utilized to explore variations in stellar complexity across different polytropic indices and anisotropic models, offering insights into how anisotropy affects overall complexity.

Chapter 5

A Reissner-Nordström+Λ Black Hole in the Friedman-Robertson-Walker Universe

5.1 Introduction

Ever since their advent black holes have been studied in a great detail. However, almost all previous studies have focused either on isolated or binary black holes. But in reality black holes are neither isolated nor only in binaries. They are actually embedded in the background of expanding universe. Therefore, one must study black holes in non-flat backgrounds in order to understand the black holes in real universe.

The main motivation to study $(2+1)$-dimensional spacetimes admitting black hole solutions is that the $d = 3$ cases have now attracted more attention and interest as compared to other $(d \geq 4)$ spacetimes with special mass and charge dependence. The solution of the Einstein field equations in $(2+1)$-d exhibit many characteristics of the $(3+1)$-d black hole. Moreover the structure of $(2+1)$-d black hole is simple enough to derive a number of exact computations, particularly in the quantum realm and string theory, which are not possible in $(3+1)$ dimensions. Such study may also give a way to unify gravity and quantum theory. It's known that the entropy of a black hole is proportional to its surface area, which is also consistent with a $(2+1)$-d black hole. Further exploration is focused on deriving the equation of motion for geodesics in vicinity of spacetime of a $(2+1)$-dimensional charged

black hole.

It is well known also that at the core or center of a black hole, according to general relativity, is a gravitational singularity, which is indeed a one-dimensional point. Its huge mass is located in an infinitesimal small space, where density as well as gravity is infinite and space-time curves infinitely. Hence, the notion of an actual physical singularity appears quite unlikely and possibly points to general relativity being rather incomplete.

The work on $(2+1)$-d gravity theories has seen a great increase after the discovery that $(2+1)$-d general relativity possesses a black hole solution [Banados et al. (1992)]. It is the first example in this regard. The authors have observed that the fascinating properties of classical and especially quantum black hole, have long made it desirable to work on a lower-dimensional analog which could exhibit the key features and avert the unnecessary complications. It has been observed that such analog does exist in standard $(2+1)$-d Einstein-Maxwell theory with a negative cosmological constant. This has further motivated us to work on $(2+1)$-d black hole including the cosmological constant inside it.

Later on, Einstein-Maxwell [Martinez et al. (2000)] and Einstein-Maxwell-dilaton [Chan and Mann (1994)] extensions were also found. The authors studied black hole solutions which include all special characteristics that are observed in $(3+1)$ or higher dimensional black holes like horizon(s), black hole thermodynamics as well as Hawking radiation.

The dimensional reduction of black hole solutions in 4D general relativity is done and new 3D black hole solutions with an isotropic event horizon are obtained by Zanchin et al. (2002). Such event horizon is a typical characteristic of black hole and is an important study in our research too. The authors considered a 4D spacetime with one spacelike Killing vector and observed that it is possible to split the Einstein-Hilbert-Maxwell action with a cosmological term in terms of 3D quantities. The authors Zanchin and Miranda (2004) have further formulated the three-dimensional Einstein-Maxwell-dilaton theory from the usual four-dimensional Einstein-Maxwell-Hilbert action for general relativity and observed that the 3D static spherically symmetric solution is analogous to the 4D Reissner-Nordström anti-de Sitter black hole. A particular case of the 3D action which presents Maxwell field, dilaton field and an extra scalar field, besides gravity field and a negative cosmological constant is chosen by them and new 3D static black hole solutions are obtained.

Gurtug et al. (2012) have constructed a large class of black hole solutions by the power

Maxwell field. Here the Maxwell scalar has the form $(F_{\mu\nu}F^{\mu\nu})^k$. The particular choice of $k = \frac{d}{4}$, yields in general a traceless Maxwell's energy-momentum tensor. They however observed that $k = \frac{3}{4}$ yields a general solution in $(2+1)$-dimensional Einstein-power-Maxwell spacetime which is devoid of the traceless condition.

The references are much more, but limited here, which have aroused the interest to study the Reissner-Nordström+Λ (RN+Λ) black hole in the Friedman-Robertson-Walker universe.

The study on black holes is not completely new. It started long back in 1933 when McVittie (1933) obtained his celebrated metric for a mass-particle in an expanding universe. This metric is nothing but the Schwarzschild black hole which is embedded in the Friedman-Robertson-Walker universe. In 1993, Kastor and Traschen found the multi-black holes solution in the background of de Sitter universe [Kastor and Traschen (1993a, 1993b)]. The Kastor-Traschen solution describes the dynamical system of arbitrary number of extreme Reissner-Nordström (RN) black holes in the background of de Sitter universe. In 1999, Shiromizu and Gen studied charged rotating black hole in de Sitter background[Shiromizu and Gen (2000)]. In 2000, Nayak et al. studied the solutions for the Schwarzschild and Kerr black holes in the background of the Einstein universe [Nayak et al. (2000) and Nayak and Vishveshvara (2000)]. In 2004 Gao et al. studied RN black hole in the expanding universe [Gao and Zhang (2004)].

In this chapter, the above studies are extended from charged black holes into charged black holes which have cosmological constant inside them. It has been found in the literature that there are three possible black hole solutions depending on the cosmological constant being (i) positive (ii) negative and (iii) zero [Bousso (2011)]. First a RN+Λ metric is deduced for a black hole in the expanding universe.It's shown that several special cases of our solution are exactly the same as some solutions discovered previously.Then the effects of the evolution of the universe on the size, mass and charge of the black hole are studied.

It's known that black holes exert a strong gravitational influence due to their mass, just like every other massive object in the Universe. This is how the mass of black holes is actually discovered and measured, by watching their effect through gravitational lensing, accretion, X-ray emissions etc. The next chapter explores the effects of strong gravitational lensing around a black hole and its shadow. For instance, the supermassive black hole at the center of the Milky Way galaxy is so strong gravitationally that the stars very near to

it, orbit at a very, very high rate. Using this and the equations that describe the orbits of these stars, the mass of the black hole can be actually estimated.

Kaloper et al. (2010) has analyzed the McVittie solutions of Einstein's field equations for describing the gravitational fields of spherically symmetric mass distributions in expanding FRW universes. They focused on spatially flat McVittie geometries and showed that the McVittie solutions which asymptote to FRW universes and dominated by a positive cosmological constant at late times are black holes with regular event horizons. Near the black hole the charge contributions correct the effective potential for the scalar and give it a large mass, as the supersymmetric attractor mechanism in asymptotically flat black holes.

Maki and Shiraishi (1993) have studied (N + 1)-dimensional cosmological solutions describing the multi-black hole configuration in the same system with a cosmological constant. They investigated that the cosmological evolution of the scale factor depends on the coupling of the dilaton to the cosmological constant. The outline of this chapter is envisaged as follows:

In section 5.2 the Einstein-Maxwell field equations have been solved for the static spherically symmetric line element for interior spacetime of a RN+Λ black hole. The event horizons have been studied. The pressure, matter density and proper charge density of the black hole has been expressed in terms of the mass, charge and the cosmological constant (Λ). The geodesics have been further verified. In section 5.3 the RN+Λ metric is transformed to the McVittie form [McVittie (1933)] under suitable transformation conditions for compatible study with respect to the FRW universe. The various subconditions are specified. In section 5.4 the boundary conditions are discussed and the negative value of cosmological constant inside the black hole is further confirmed. The value of the curvature parameter k in the FRW metric is discussed. That the transformed RN+Λ metric is an exact solution of the Einstein-Maxwell field equations and the metric is physically relevant has been studied in section 5.5 .The Darmois-Israel matching conditions are discussed in section 5.6. In section 5.7 the surface continuity is further studied.

5.2 Interior Reissner-Nordström with Λ Metric

It's known that if an electrically charged particle falls into the Schwarzschild black hole it becomes charged. To describe such a black hole one has to solve the Einstein-Maxwell

equations considering the stress-energy tensor of the electromagnetic field. RN+Λ metric is a static solution to the Einstein-Maxwell field equations, which corresponds to the electrovacuum gravitational field of a charged, non-rotating, spherically symmetric black hole of mass M. Hence, the analogue of the RN+Λ solution with exterior FRW metric for a space-time with a cosmological constant is followed. Under such conditions, the metric of the line element for the interior space-time of a static spherically symmetric charged distribution of matter in $(2+1)$ dimensions is of the form,

$$ds^2 = -\left(1 - \frac{2M}{r} + \frac{Q^2}{r^2} - \frac{\Lambda r^2}{3}\right) dt^2 + \left(1 - \frac{2M}{r} + \frac{Q^2}{r^2} - \frac{\Lambda r^2}{3}\right)^{-1} dr^2 + r^2 d\theta^2, \quad (5.2.1)$$

where,

- Q : the charge of the black hole,
- Λ : the cosmological constant.

The charge Q has been included inside the metric. Unlike our $2+1$-d metric, it is found that the $3+1$-d metric [DeWitt-Morette and DeWitt (1973), Lake (1979), and Weyl (1919)] is devoid of any charge. The coordinate speed of light signal (Null geodesic) is obtained with $ds^2 = 0$, hence it is obtained from Eq.(5.2.1),

$$0 = -\left(1 - \frac{2M}{r} + \frac{Q^2}{r^2} - \frac{\Lambda r^2}{3}\right) dt^2 + \left(1 - \frac{2M}{r} + \frac{Q^2}{r^2} - \frac{\Lambda r^2}{3}\right)^{-1} dr^2 + r^2 d\theta^2. \quad (5.2.2)$$

This implies,

$$\left(\frac{dr}{dt}^2\right) = \left(1 - \frac{2M}{r} + \frac{Q^2}{r^2} - \frac{\Lambda r^2}{3}\right) \times \left[\left(1 - \frac{2M}{r} + \frac{Q^2}{r^2} - \frac{\Lambda r^2}{3}\right) - r^2 \left(\frac{d\theta}{dt}\right)^2\right]. \quad (5.2.3)$$

At the surface $r = R$ on which $\frac{dr}{dt} = 0$ (i.e on the RN+Λ black hole surface), light cannot escape from this black hole surface thus,

$$1 - \frac{2M}{R} + \frac{Q^2}{R^2} - \frac{\Lambda R^2}{3} = 0, \quad (5.2.4)$$

Besides the cosmological constant the charged black hole is characterized by two parameters, the mass M and the electric charge Q.

5.2.1 Horizons in the RN+Λ Spacetime

On solving the above Eq.(5.2.4), four values of the radial parameter r are obtained and given by,

$$r_1 = \frac{1}{2}\left[\frac{2}{\Lambda} - \frac{a_1}{\Lambda b_1} - \frac{b_1}{c_1}\right]^{\frac{1}{2}} - \frac{1}{2}\left[\frac{4}{\Lambda} + \frac{a_1}{\Lambda b_1} + \frac{b_1}{c_1} - \frac{12M}{\Lambda(\frac{2}{\Lambda} - \frac{a_1}{\Lambda b_1} - \frac{b_1}{c_1})^{\frac{1}{2}}}\right]^{\frac{1}{2}}, \quad (5.2.5)$$

$$r_2 = \frac{1}{2}\left[\frac{2}{\Lambda} - \frac{a_1}{\Lambda b_1} - \frac{b_1}{c_1}\right]^{\frac{1}{2}} + \frac{1}{2}\left[\frac{4}{\Lambda} + \frac{a_1}{\Lambda b_1} + \frac{b_1}{c_1} - \frac{12M}{\Lambda(\frac{2}{\Lambda} - \frac{a_1}{\Lambda b_1} - \frac{b_1}{c_1})^{\frac{1}{2}}}\right]^{\frac{1}{2}}, \quad (5.2.6)$$

$$r_3 = -\frac{1}{2}\left[\frac{2}{\Lambda} - \frac{a_1}{\Lambda b_1} - \frac{b_1}{c_1}\right]^{\frac{1}{2}} - \frac{1}{2}\left[\frac{4}{\Lambda} + \frac{a_1}{\Lambda b_1} + \frac{b_1}{c_1} - \frac{12M}{\Lambda(\frac{2}{\Lambda} - \frac{a_1}{\Lambda b_1} - \frac{b_1}{c_1})^{\frac{1}{2}}}\right]^{\frac{1}{2}}, \quad (5.2.7)$$

$$r_4 = -\frac{1}{2}\left[\frac{2}{\Lambda} - \frac{a_1}{\Lambda b_1} - \frac{b_1}{c_1}\right]^{\frac{1}{2}} + \frac{1}{2}\left[\frac{4}{\Lambda} + \frac{a_1}{\Lambda b_1} + \frac{b_1}{c_1} - \frac{12M}{\Lambda(\frac{2}{\Lambda} - \frac{a_1}{\Lambda b_1} - \frac{b_1}{c_1})^{\frac{1}{2}}}\right]^{\frac{1}{2}}, \quad (5.2.8)$$

where

$$a_1 = 32^{\frac{1}{3}}(1 - 4Q^2\Lambda), \quad (5.2.9)$$

$$b_1 = \left[54 - 972M^2\Lambda + 648Q^2\Lambda + \left[(54 - 972M^2\Lambda + 648Q^2\Lambda)^2 - 4(9 - 36Q^2\Lambda)^3\right]^{\frac{1}{2}}\right]^{\frac{1}{3}} \quad (5.2.10)$$

$$c_1 = 3.2^{\frac{1}{3}}\Lambda, \quad (5.2.11)$$

From the above equations this can be observed that a_1 depends on the charge of the black hole and the cosmological constant, b_1 depends on the mass, the charge of the black hole and the cosmological constant whereas c_1 depends only on the cosmological constant.

This is found from Eq.(5.2.7) that r_3 is negative and hence unphysical, from Eqs.(5.2.5), (5.2.6) and (5.2.8) that r_1, r_2, r_4 are real and positive, depending upon suitable choice of M, Q, Λ. Hence there are three possible horizons, from the innermost (depending on the

values of r), they are Cauchy horizon, event horizon and the cosmological horizon.

The horizons for RN metric are obtained by setting $\Lambda = 0$ in Eq.(5.2.4). Hence the values of the radius of the horizon of the charged black hole in case of RN metric is,

$$r_{\pm} = M \pm \sqrt{M^2 - Q^2}, \tag{5.2.12}$$

The larger one r_+ is the event horizon, while the smaller one, r_- is the inner or Cauchy horizon located inside the black hole. The event horizon corresponds to,

$$r_{+} = M + \sqrt{M^2 - Q^2}, \tag{5.2.13}$$

This is analog of the Schwarzschild radius and for $Q = 0$, $r_+ = r_s = 2M$.

5.2.2 Solutions of Einstein-Maxwell Equations in RN+Λ Spacetime

The metric Eq.(5.2.1) (considering spherical and planar (2+1)-dimensional black holes as [Zanchin et al. (2002), Zanchin and Miranda (2004)]) can be written in the form,

$$ds^2 = -e^{\nu(r)}dt^2 + e^{\lambda(r)}dr^2 + r^2 d\theta^2, \tag{5.2.14}$$

where the following form is taken,

$$e^{\nu(r)} \;=\; e^{-\lambda(r)} \;=\; \left(1 - \frac{2M}{r} + \frac{Q^2}{r^2} - \frac{\Lambda r^2}{3}\right), \tag{5.2.15}$$

The Hilbert action coupled given by ,

$$I = \int \sqrt{-g}\left(\frac{R - 2\Lambda}{16\pi} - \frac{1}{4}F^c_a F_{bc} + \mathcal{L}_m\right) dx^3, \tag{5.2.16}$$

where, $\mathcal{L}_m$ is the Lagrangian for matter. The variation with respect to the metric gives the following self consistent Einstein-Maxwell equations with cosmological constant Λ for a charged (cosmological constant effective fluid) distribution,

$$G_{ab} \;=\; R_{ab} - \frac{1}{2}Rg_{ab} + \Lambda g_{ab} \;= -8\pi\left(T^{PF}_{ab} + T^{EM}_{ab}\right), \tag{5.2.17}$$

The explicit forms of the energy momentum tensor components for the matter source, this was assumed that the matter distribution at the interior of the black hole is (cosmological constant effective fluid) type and electromagnetic fields are given by,

$$T_{ab}^{PF} = (\rho + p)u_a u_b + p g_{ab}, \tag{5.2.18}$$

$$T_{ab}^{EM} = -\frac{1}{4\pi}\left(F_a^c F_{bc} - \frac{1}{4} g_{ab} F_{cd} F^{cd}\right), \tag{5.2.19}$$

where,

- ρ : matter density of a fluid element,
- p : fluid pressure of a fluid element,
- u_i : velocity three vector of a fluid element,
- F_{ab} : electromagnetic field tensor.

Here, the electromagnetic field is related to current three vector

$$J^c = \sigma(r) u^c, \tag{5.2.20}$$

as

$$F^{ab}_{;b} = -4\pi J^a, \tag{5.2.21}$$

where,

- $\sigma(r)$: the proper charge density of the distribution.

In this consideration, the three velocity is assumed as $u_a = \delta_a^t$ and consequently the electromagnetic field tensor can be given as,

$$F_{ab} = E(r)\left(\delta_a^t \delta_b^r - \delta_a^r \delta_b^t\right), \tag{5.2.22}$$

where,

- $E(r)$: the electric field.

The Einstein-Maxwell equations with the assumption, cosmological constant ($\Lambda < 0$), for the black hole metric in Eq.(5.2.14) together with the energy-momentum tensor given in Eqs.(5.2.18), (5.2.19) along with Eqs. (5.2.20), (5.2.21) and (5.2.22) yield (rendering $G = c = 1$)

$$\frac{\lambda' e^{-\lambda}}{2r} = 8\pi\rho(r) + E^2(r) + \Lambda \tag{5.2.23}$$

$$\frac{\nu' e^{-\lambda}}{2r} = 8\pi p(r) - E^2(r) - \Lambda \tag{5.2.24}$$

$$\frac{e^{-\lambda}}{2}\left(\frac{1}{2}\nu'^2 + \nu'' - \frac{1}{2}\nu'\lambda'\right) = 8\pi p(r) + E^2(r) - \Lambda \tag{5.2.25}$$

$$\sigma(r) = \frac{e^{-\frac{\lambda}{2}}}{4\pi r^2}\left(r^2 E(r)\right)' \tag{5.2.26}$$

where a ($'$) denotes differentiation with respect to the radial parameter r. When $E = 0$, the Einstein-Maxwell system given above reduces to the uncharged Einstein system.

Here the term $\sigma(r)e^{\frac{\lambda(r)}{2}}$ [Usmani et al. (2011)] is equivalent to the volume charge density in $(2+1)$-d. The proper charge density $\sigma(r)$ is considered as a polynomial function of r.

The Einstein-Maxwell equations in Eqs.(5.2.23), (5.2.24) and (5.2.25), using Eq.(5.2.15) reduce to,

$$8\pi\rho(r) + E^2(r) + \Lambda = -\frac{1}{r}\left(\frac{M}{r^2} - \frac{Q^2}{r^3} - \frac{\Lambda r}{3}\right) \tag{5.2.27}$$

$$8\pi p(r) - E^2(r) - \Lambda = \frac{1}{r}\left(\frac{M}{r^2} - \frac{Q^2}{r^3} - \frac{\Lambda r}{3}\right) \tag{5.2.28}$$

$$8\pi p(r) + E^2(r) - \Lambda = \frac{3Q^2}{r^4} - \frac{2M}{r^3} - \frac{\Lambda}{3} \tag{5.2.29}$$

On adding Eqs.(5.2.27) and (5.2.28) it is obtained,

$$16\pi p(r) = -16\pi\rho(r) = \frac{2Q^2}{r^4} - \frac{M}{r^3} + \frac{4\Lambda}{3} \tag{5.2.30}$$

The equations for pressure and matter density are evident from Eq.(5.2.30). Both should be dependent on the radial parameter r. It is observed from the above Eq.(5.2.30), that the

particular case of $(\Lambda = 0, r^2 < \frac{2Q^2}{M})$ is not valid, which makes the energy density negative. Hence the cosmological constant should be negative, which is further verified in the following sections. Now solving Eq.(5.2.27) and Eq.(5.2.30), the $E(r)$ can be obtained,

$$E(r) = \left(\frac{2Q^2}{r^4} - \frac{3M}{2r^3}\right)^{\frac{1}{2}} \tag{5.2.31}$$

It is observed that the electric field $E(r)$ which is dependent on r but is independent of the cosmological constant. It can also be observed that the electric field is non-vanishing and imaginary, if $Q = 0$ and hence the field is limited to our $RN + \Lambda$ black hole and cannot be reduced to the Schwarzschild form, as a particular case.

Now using Eq.(5.2.31) in Eq.(5.2.26) it is evaluated that,

$$\sigma(r) = \frac{\left(1 - \frac{2M}{r} + \frac{Q^2}{r^2} - \frac{\Lambda r^2}{3}\right)^{\frac{1}{2}} \left(\frac{3M}{2r^3} - \frac{3Q^2}{r^4}\right)}{2\pi r \left(\frac{2Q^2}{r^4} - \frac{3M}{2r^3}\right)^{\frac{1}{2}}}. \tag{5.2.32}$$

This shows the proper charge density is also dependent on r.

5.2.3 Physical Significance of Pressure and Matter Density

For interior solutions $p = -\rho$ is deduced. It is equivalent to $p = \omega\rho$, where it's taken $\omega = -1$. This type of equation of state is available in the literature and is known as a false vacuum, degenerate vacuum or ρ-vacuum and represents a repulsive pressure [Blome and Priester (1984)].

The following values of the parameters are chosen

$$\Lambda = -10^{-46}\text{km}^{-2}, \quad M = 3.8M_{\odot}, \quad Q = 0.00089\text{km},$$

The Fig.5.1 shows the variation of $p(r)$ and $\rho(r)$ against r.

Hence, this is observed from the Figs.5.1 and 5.2 that the black hole has a negative pressure positive matter density respectively, which is due to the presence of exotic matter. The pressure $p(r)$ increases with the increase in radius and the matter density $\rho(r)$ decreases with the increase in radius.

This has been assumed that the effective mass of the black hole is $M = 3.8M_{\odot}$. It can

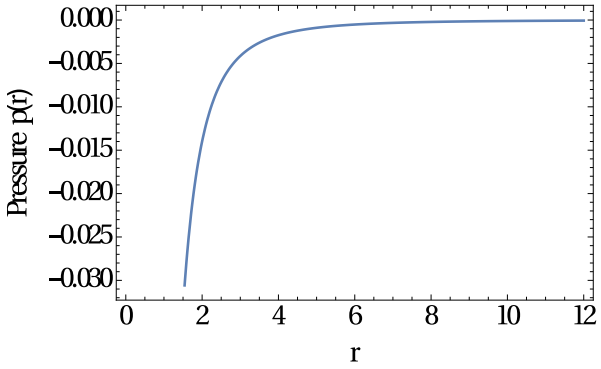

Fig. 5.1. Pressure $p(r)$ has been depicted against r. The geometric unit of pressure here is in km^{-2}.

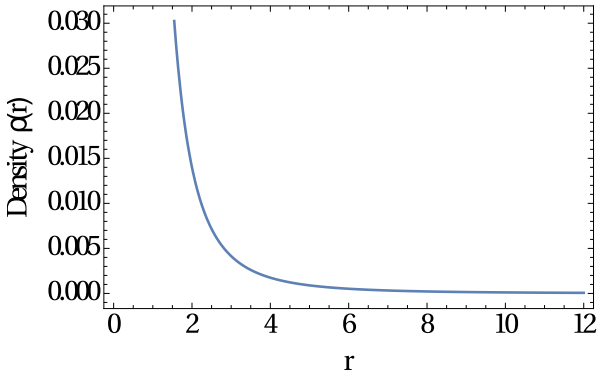

Fig. 5.2. Density $\rho(r)$ has been depicted against r. The geometric unit of density here is km^{-2}.

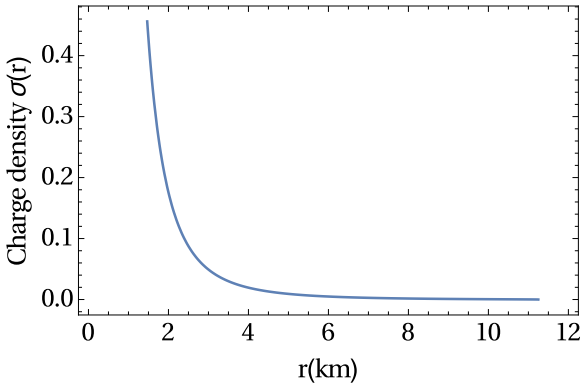

Fig. 5.3. Proper charge density $\sigma(r)$ has been depicted against r. The geometric unit of proper charge density here is km^{-2}.

also be observed via Eq.(5.2.30), that the physical parameters, viz. density and pressure are dependent on the charge. Also, if $\sigma(r) = 0$, then from Eq.(5.2.32), it's obtained that $M = \frac{2Q^2}{r}$ and both the parameters $p(r)$ and $\rho(r)$ in Eq.(5.2.30), become constant, being dependent only on Λ. Therefore, our solutions provide *electromagnetic mass* model, such that for vanishing charge density $\sigma(r)$, the physical parameters (pressure and density) becomes constant.

Fig.5.3 shows the variation of the proper charge density against r. This is observed that the proper charge density is maximum at the centre and decreases with the increase in radius.

5.2.4 Geodesic Equations in RN+Λ Spacetime

The geodesic equations is written as follows

$$\frac{d^2t}{ds^2} + \nu' \frac{dt}{ds}\frac{dr}{ds} = 0, \tag{5.2.33}$$

$$\frac{d^2r}{ds^2} + \frac{1}{2}\nu' e^{(\nu-\lambda)}\left(\frac{dt}{ds}\right)^2 + \frac{1}{2}\lambda'\left(\frac{dr}{ds}\right)^2 - re^{-\lambda}\left(\frac{d\theta}{ds}\right)^2 = 0, \tag{5.2.34}$$

$$\frac{d^2\theta}{ds^2} + \frac{2}{r}\frac{d\theta}{ds}\frac{dr}{ds} = 0, \tag{5.2.35}$$

Using Eq.(5.2.15), since $\nu = -\lambda$, $\nu' = -\lambda'$ and $\nu - \lambda = 2\nu$, it is found that

$$\nu' = \frac{2}{\left(1 - \frac{2M}{r} + \frac{Q^2}{r^2} - \frac{\Lambda r^2}{3}\right)}\left(\frac{M}{r^2} - \frac{Q^2}{r^3} - \frac{\Lambda r}{3}\right), \tag{5.2.36}$$

On integrating Eqs.(5.2.33) and (5.2.35), this is obtained

$$\frac{d\theta}{ds} = \frac{k_1^2}{r^2}, \tag{5.2.37}$$

$$\frac{dt}{ds} = \frac{k_2^2}{\left(1 - \frac{2M}{r} + \frac{Q^2}{r^2} - \frac{\Lambda r^2}{3}\right)}. \tag{5.2.38}$$

here, k_1, k_2 are integrating constant will be determine in next part.

Putting the above values of $\frac{d\theta}{ds}$ and $\frac{dt}{ds}$ in Eq.(5.2.34), this results in,

$$\begin{aligned} 0 &= \frac{d^2r}{ds^2} + \frac{k_2^2\left(\frac{M}{r^2} - \frac{Q^2}{r^3} - \frac{\Lambda r}{3}\right)}{\left(1 - \frac{2M}{r} + \frac{Q^2}{r^2} - \frac{\Lambda r^2}{3}\right)} - \frac{\left(\frac{M}{r^2} - \frac{Q^2}{r^3} - \frac{\Lambda r}{3}\right)}{\left(1 - \frac{2M}{r} + \frac{Q^2}{r^2} - \frac{\Lambda r^2}{3}\right)}\left(\frac{dr}{ds}\right)^2 \\ &\quad -\frac{k_1^2}{r^3}\left(1 - \frac{2M}{r} + \frac{Q^2}{r^2} - \frac{\Lambda r^2}{3}\right) \end{aligned} \tag{5.2.39}$$

Also from the metric Eq.(5.2.14), on dividing each side by ds^2, this is found that,

$$1 = -e^{\nu}\left(\frac{dt}{ds}\right)^2 + e^{\lambda}\left(\frac{dr}{ds}\right)^2 + r^2\left(\frac{d\theta}{ds}\right)^2, \tag{5.2.40}$$

Using Eqs.(5.2.37), (5.2.38) and (5.2.40) reduces to,

$$\left(\frac{dr}{ds}\right)^2 = k_2^2 + \left(1 - \frac{2M}{r} + \frac{Q^2}{r^2} - \frac{\Lambda r^2}{3}\right)\left(1 - \frac{k_1^2}{r^2}\right). \tag{5.2.41}$$

Using Eq.(5.2.41) in Eq. (5.2.39), it is obtained,

$$\frac{d^2r}{ds^2} = \left(\frac{M}{r^2} - \frac{Q^2}{r^3} - \frac{\Lambda r}{3}\right) + k_1^2\left(\frac{1}{r^3} - \frac{3M}{r^4} + \frac{2Q^2}{r^5}\right). \tag{5.2.42}$$

Multiplying the Eq.(5.2.42) by $2\frac{dr}{ds}$ and integrating both sides w.r.t ds it is obtained that

$$\left(\frac{dr}{ds}\right)^2 = 2\left[-\frac{M}{r} + \frac{Q^2}{2r^2} - \frac{\Lambda r^2}{6} + k_1^2\left(-\frac{1}{2r^2} + \frac{M}{r^3} - \frac{Q^2}{2r^4}\right)\right], \tag{5.2.43}$$

On equating Eqs.(5.2.41) and (5.2.43), it is observed that

$$k_2^2 = -\left(\frac{\Lambda k_1^2}{3} + 1\right). \tag{5.2.44}$$

Hence this can be observed that the cosmological constant can have a negative value as is confirmed from the above Eq.(5.2.44) [Maeda and Ohta (2014)]. Therefore, our assumption has been confirmed to be correct.

5.3 Metric for Interior RN+Λ and Exterior FRW Spacetimes

The metric for RN+Λ black hole in $(2+1)$ dimensions is given by Eq.(5.2.1). For the sake of convenience the metric is transformed under isotropic conditions with the following transformations, using $x^0 = v$ and $x^1 = x$, as

$$2t = v,\ 2s = l,\ 2r = x\left[\left(1+\frac{M}{x}\right)^2 - \frac{Q^2}{x^2} + \Lambda e^{-2x}\right]. \tag{5.3.1}$$

Hence Eq.(5.2.1) is transformed as,

$$dl^2 = -\frac{\left(1-\frac{M^2}{x^2}+\frac{Q^2}{x^2}-\Lambda e^{-2x}\right)^2}{\left[\left(1+\frac{M}{x}\right)^2-\frac{Q^2}{x^2}+\Lambda e^{-2x}\right]^2}dv^2 + \left[\left(1+\frac{M}{x}\right)^2 - \frac{Q^2}{x^2}+\Lambda e^{-2x}\right]^2(dx^2+x^2d\theta^2), \tag{5.3.2}$$

The line element for the exterior space-time in FRW metric is considered in the form,

$$dl^2 = -dv^2 + \frac{a^2(v)}{(1+\frac{kx^2}{4})^2}(dx^2+x^2d\theta^2). \tag{5.3.3}$$

Here $a(v)$ is the scale factor of the universe and k denotes the space-time curvature. The above RN+Λ metric embedded in FRW universe is represented as follows

$$dl^2 = -P^2(v,x)\,dv^2 + T^2(v,x)\left(dx^2+x^2d\theta^2\right). \tag{5.3.4}$$

where,

$$T(v,x) = \left[g(v,x)+\frac{z(v)}{x}\right]^2 - \frac{h(v)}{x^2} + \Lambda g^2 e^{-2bgx}, \tag{5.3.5}$$

$$\begin{aligned} P(v,x) &= f(v)\frac{\dot{T}}{2T} \\ &= \left[\frac{\dot{g}f}{g} + (g\dot{z}+\dot{g}z)\frac{f}{g^2x} + \frac{z\dot{z}f}{g^2x^2} - \frac{\dot{h}f}{2g^2x^2} - \Lambda e^{-2bgx}\right] \\ &\quad \times \left[\left(1+\frac{z}{gx}\right)^2 - \frac{h}{g^2x^2} + \Lambda e^{-2bgx}\right]^{-1}. \end{aligned} \tag{5.3.6}$$

where ($\dot{}$) denotes differentiation with respect to v and $b(v)$ is the scale factor under the transformed conditions.The limit is considered when $f\dot{g}\left(bx-\frac{1}{g}\right)\to 1$.

Asymptotic flat conditions is considered where $P(v=const.,x)$ is reduced to $\sqrt{g_{00}}$ term in Eq.(5.3.2). Hence on comparing the $\sqrt{g_{00}}$ term of Eq.(5.3.6) with that of Eq.(5.3.2), it is found that the following identities hold

(i) $\frac{\dot{g}f}{g}=1$,

(ii) $(g\dot{z}+\dot{g}z)\frac{f}{g^2x}=0$,

(iii) $\frac{z\dot{z}f}{g^2x^2}=-(\frac{z}{gx})^2$

(iv) $-\frac{\dot{h}f}{2g^2x^2}=\frac{h}{g^2x^2}$.

Now, (i)-(iv) reduce to (v)

(v) $\dot{g}f=g,\dot{z}f=-z,\dot{h}f=-2h$;

On suitable transformations assuming, $f=\frac{b}{\dot{b}}$ and $g=\frac{b(v)}{\sqrt{1+\frac{kx^2}{4}}}$, it is obtained,

(vi) $z=\frac{M}{b}$, $h=\frac{Q^2}{b^2}$.

Here the integration constants M and Q are related to the mass and charge of the black hole respectively.

On substituting the above Eqs.(5.3.4), (5.3.5) and (5.3.6) in Eq.(5.3.2) with the above transformations under suitable conditions, the final RN+Λ metric in $(2+1)$ dimensions in the FRW background is observed as follows

$$
\begin{aligned}
dl^2 &= -\frac{\left(1-\frac{M^2\left(1+\frac{kx^2}{4}\right)}{a^2x^2}+\frac{Q^2\left(1+\frac{kx^2}{4}\right)}{a^2x^2}-\Lambda e^{-\frac{2ax}{\sqrt{1+\frac{kx^2}{4}}}}\right)^2}{\left[\left(1+\frac{M\sqrt{1+\frac{kx^2}{4}}}{ax}\right)^2-\frac{Q^2\left(1+\frac{kx^2}{4}\right)}{a^2x^2}+\Lambda e^{-\frac{2ax}{\sqrt{1+\frac{kx^2}{4}}}}\right]^2}dv^2+\left(dx^2+x^2d\theta^2\right)\\
&\quad\times\frac{a^2}{\left(1+\frac{kx^2}{4}\right)^2}\left[\left(1+\frac{M\sqrt{1+\frac{kx^2}{4}}}{ax}\right)^2-\frac{Q^2\left(1+\frac{kx^2}{4}\right)}{a^2x^2}+\Lambda e^{-\frac{2ax}{\sqrt{1+\frac{kx^2}{4}}}}\right]^2,
\end{aligned}
\tag{5.3.7}
$$

here $a = a(v) \to b^2(v)$.

If $k = 0$, the above Eq.(5.3.7) reduces to,

$$dl^2 = -\frac{\left(1 - \frac{M^2}{a^2x^2} + \frac{Q^2}{a^2x^2} - \Lambda e^{-2ax}\right)^2}{\left[\left(1 + \frac{M}{ax}\right)^2 - \frac{Q^2}{a^2x^2} + \Lambda e^{-2ax}\right]^2} dv^2 + a^2 \left[\left(1 + \frac{M}{ax}\right)^2 - \frac{Q^2}{a^2x^2} + \Lambda e^{-2ax}\right]^2 \left(dx^2 + x^2 d\theta^2\right), \tag{5.3.8}$$

It's known that $a(v) = e^{Hv}$ where H is the Hubble constant. If further $H = 0$, then $a(v) = 1$ and the Eq.(5.3.2) is restored from Eq.(5.3.8). However $Q = 0$ reduces the above Eq.(5.3.7) to,

$$\begin{aligned} dl^2 &= -\frac{\left(1 - \frac{M^2\left(1+\frac{kx^2}{4}\right)}{a^2x^2} - \Lambda e^{-\frac{2ax}{\sqrt{1+\frac{kx^2}{4}}}}\right)^2}{\left[\left(1 + \frac{M\sqrt{1+\frac{kx^2}{4}}}{ax}\right)^2 + \Lambda e^{-\frac{2ax}{\sqrt{1+\frac{kx^2}{4}}}}\right]^2} dv^2 + \frac{a^2}{(1+\frac{kx^2}{4})^2} \\ &\times \left[\left(1 + \frac{M\sqrt{1+\frac{kx^2}{4}}}{ax}\right)^2 + \Lambda e^{-\frac{2ax}{\sqrt{1+\frac{kx^2}{4}}}}\right]^2 \left(dx^2 + x^2 d\theta^2\right), \end{aligned} \tag{5.3.9}$$

which is just the McVittie solution. For the extreme RN black hole case $M = Q$ and $k = 0$ in presence of cosmological constant, the Eq.(5.3.7) is reduced to

$$dl^2 = -\frac{\left(1 - \Lambda e^{-2ax}\right)^2}{\left(1 + \frac{2M}{ax} + \Lambda e^{-2ax}\right)^2} dv^2 + a^2 \left(1 + \frac{2M}{ax} + \Lambda e^{-2ax}\right)^2 \left(dx^2 + x^2 d\theta^2\right), \tag{5.3.10}$$

If $\Lambda = 0$ the above Eq.(5.3.10) further takes the form,

$$dl^2 = -\frac{1}{\left(1 + \frac{2M}{ax}\right)^2} dv^2 + a^2 \left(1 + \frac{2M}{ax}\right)^2 \left(dx^2 + x^2 d\theta^2\right), \tag{5.3.11}$$

If the scale factor $a(v) = 1$, when $H = 0$, the above Eq.(5.3.11) reduces to the Schwarzschild metric in an FRW present day accelerating universe.

5.4 Boundary and Matching Conditions with the Exterior FRW Universe

Matching conditions of g_{vv}, g_{xx} and $\frac{\partial g_{vv}}{\partial x}$ at $x = R$ are used. It's found from Eq.(5.3.3) and Eq.(5.3.7) three results which are enunciated below,

5.4.1 Continuity of g_{vv}

$$\frac{\left(1-\frac{M^2\left(1+\frac{kx^2}{4}\right)}{a^2x^2}+\frac{Q^2\left(1+\frac{kx^2}{4}\right)}{a^2x^2}-\Lambda e^{-\frac{2ax}{\sqrt{1+\frac{kx^2}{4}}}}\right)^2}{\left[\left(1+\frac{M\sqrt{1+\frac{kx^2}{4}}}{ax}\right)^2-\frac{Q^2\left(1+\frac{kx^2}{4}\right)}{a^2x^2}+\Lambda e^{-\frac{2ax}{\sqrt{1+\frac{kx^2}{4}}}}\right]^2}=1. \tag{5.4.1}$$

Thus the scale factor $a(v)$ is expressed by the following equation,

$$\frac{M^2\left(1+\frac{kx^2}{4}\right)}{a^2x^2}+\frac{M\sqrt{1+\frac{kx^2}{4}}}{ax}-\frac{Q^2\left(1+\frac{kx^2}{4}\right)}{a^2x^2}+\Lambda e^{-\frac{2ax}{\sqrt{1+\frac{kx^2}{4}}}}=0, \tag{5.4.2}$$

Hence Λ is negative for a positive mass. For the extreme RN case when $Q = M$,

$$\frac{M\sqrt{1+\frac{kx^2}{4}}}{ax}+\Lambda e^{-\frac{2ax}{\sqrt{1+\frac{kx^2}{4}}}}=\frac{Q\sqrt{1+\frac{kx^2}{4}}}{ax}+\Lambda e^{-\frac{2ax}{\sqrt{1+\frac{kx^2}{4}}}}=0. \tag{5.4.3}$$

As Λ is constant the above Eq.(5.4.3) indicates that, for an observer at infinity, the mass and charge of the black hole decreases with the expansion of the universe whereas both increases with the contraction of the universe.

If $Q = 0$ it is obtained,

$$\left[\frac{M\sqrt{1+\frac{kx^2}{4}}}{ax}\right]\left[1+\frac{M\sqrt{1+\frac{kx^2}{4}}}{ax}\right]+\Lambda e^{-\frac{2ax}{\sqrt{1+\frac{kx^2}{4}}}}=0, \tag{5.4.4}$$

5.4.2 Continuity of g_{xx}

$$\frac{a^2(v)}{\left(1+\frac{kx^2}{4}\right)^2}=\frac{a^2(v)}{\left(1+\frac{kx^2}{4}\right)^2}\left[\left(1+\frac{M\sqrt{1+\frac{kx^2}{4}}}{ax}\right)^2-\frac{Q^2\left(1+\frac{kx^2}{4}\right)}{a^2x^2}+\Lambda e^{-\frac{2ax}{\sqrt{1+\frac{kx^2}{4}}}}\right]^2 \quad (5.4.5)$$

The above Eq.(5.4.5) gives another expression for $a(v)$ as,

$$\frac{M^2\left(1+\frac{kx^2}{4}\right)}{a^2x^2}+\frac{2M\sqrt{1+\frac{kx^2}{4}}}{ax}-\frac{Q^2\left(1+\frac{kx^2}{4}\right)}{a^2x^2}+\Lambda e^{-\frac{2ax}{\sqrt{1+\frac{kx^2}{4}}}}=0, \quad (5.4.6)$$

It can be observed via Eq.(5.4.2) and Eq.(5.4.6) that as Λ has a negative value of the order 10^{-46}, the term containing Λ can be eliminated to obtain the value of the constant $k=-0.0278$ in both the equations, considering the scale factor, $a(v)=1$ for the present day accelerating universe.

5.4.3 Continuity of $\frac{\partial g_{vv}}{\partial x}$ at $x=R$

$$2\left(2-\frac{\sqrt{1+\frac{kx^2}{4}}}{ax}\right)\left[\frac{M^2}{\left(\frac{ax}{\sqrt{1+\frac{kx^2}{4}}}\right)^3}-\frac{Q^2}{\left(\frac{ax}{\sqrt{1+\frac{kx^2}{4}}}\right)^3}+\Lambda e^{-\frac{2ax}{\sqrt{1+\frac{kx^2}{4}}}}\right]+\frac{\sqrt{1+\frac{kx^2}{4}}}{ax}=0, \quad (5.4.7)$$

Hence at $x=R$ it is obtained,

$$2\left(2-\frac{\sqrt{1+\frac{kR^2}{4}}}{aR}\right)\left[\frac{M^2}{\left(\frac{aR}{\sqrt{1+\frac{kR^2}{4}}}\right)^3}-\frac{Q^2}{\left(\frac{aR}{\sqrt{1+\frac{kR^2}{4}}}\right)^3}+\Lambda e^{-\frac{2aR}{\sqrt{1+\frac{kR^2}{4}}}}\right]+\frac{\sqrt{1+\frac{kR^2}{4}}}{aR}=0 \quad (5.4.8)$$

In the extreme RN case when $Q=M$ it is found,

$$\Lambda = -\frac{e^{\frac{2aR}{\sqrt{1+\frac{kR^2}{4}}}}}{2\left(\frac{2aR}{\sqrt{1+\frac{kR^2}{4}}}-1\right)} \tag{5.4.9}$$

As Λ is negative, $\frac{2aR}{\sqrt{1+\frac{kR^2}{4}}}>1$. Hence $R>\frac{2}{\sqrt{16a^2-k}}$, where k is the curvature of space-time. The curvature parameter k may take values of 0, +1 or -1, depending on whether 3-D spacetime is assumed to be Euclidean, spherical, or hyperbolic, respectively. Here this can be observed that R is always positive for the accelerating universe, if it's taken $a(v) = 1$ and $k = 1$.

For $Q = 0$ in Eq.(5.4.7),

$$\Lambda = -e^{\frac{2aR}{\sqrt{1+\frac{kR^2}{4}}}}\left[\frac{M^2}{\left(\frac{aR}{\sqrt{1+\frac{kR^2}{4}}}\right)^3}+\frac{1}{2\left(\frac{2aR}{\sqrt{1+\frac{kR^2}{4}}}-1\right)}\right] \tag{5.4.10}$$

which represents the cosmological constant inside the Schwarzschild black hole and also has a negative value.

$Q = 0.00089\ km$ and c=1 are considered as geometric units. However when converted to SI units, it is obtained $Q = 1.03419 \times 10^{17}\ coulomb$.

5.5 Physical Relevance of RN+Λ Metric

It is found that the final RN+Λ metric in Eq.(5.3.7) satisfies the field equations Eqs.(5.2.23)-(5.2.26). The Einstein tensor $G_{\mu\nu}$ and the energy momentum tensor T^{PF}_{ab} and T^{EM}_{ab} for cosmological constant effective fluid and electromagnetic fields w.r.t the metric are easily obtained. Using Eqs.(5.2.18) - (5.2.22) the non-vanishing components of the electromagnetic tensor F_{ab} is deduced as,

$$F^{01} = E^1 = \Bigg[2(4+kx^2)\Bigg(e^{\frac{4ax}{\sqrt{4+kx^2}}}\Big(-4a^2x^2+M^2(4+kx^2)-Q^2\left(4+kx^2\right)\Big)+4a^2x^2\Lambda\Bigg)$$
$$\Bigg(e^{\frac{4ax}{\sqrt{4+kx^2}}}\Big(4a^2x^2+4aMx\sqrt{4+kx^2}+M^2(4+kx^2)-Q^2(4+kx^2)\Big)$$
$$+4a^2x^2\Lambda\Bigg)^4\Bigg]^{-\frac{1}{2}}\Bigg[32a^3e^{\frac{12ax}{\sqrt{4+kx^2}}}x^3\Bigg((4+kx^2)\Big(e^{\frac{8ax}{\sqrt{4+kx^2}}}M(M^2-Q^2)^2$$
$$(-2+kx^2)(4+kx^2)^{\frac{5}{2}}+4ae^{\frac{8ax}{\sqrt{4+kx^2}}}\times(M^2-Q^2)x(4+kx^2)^2$$
$$\Big(2kM^2x^2+Q^2(4-kx^2)\Big)+8a^2e^{\frac{4ax}{\sqrt{4+kx^2}}}M(M^2-Q^2)x^2(4+kx^2)^{\frac{3}{2}}$$
$$\Big(3e^{\frac{4ax}{\sqrt{4+kx^2}}}(2+kx^2)+8\Lambda\Big)+16a^3e^{\frac{4ax}{\sqrt{4+kx^2}}}x^3(4+kx^2)\Bigg(e^{\frac{4ax}{\sqrt{4+kx^2}}}\Big(2M^2$$
$$(4+kx^2)-Q^2(8+kx^2)\Big)+\Big(8M^2-Q^2(8+kx^2)\Big)\Lambda\Bigg)+16a^4Mx^4$$
$$\sqrt{4+kx^2}(6+kx^2)\Big(e^{\frac{8ax}{\sqrt{4+kx^2}}}-\Lambda^2\Big)\Bigg)+16a^3x^3\Lambda\Bigg(e^{\frac{4ax}{\sqrt{4+kx^2}}}\Big(M^3$$
$$(-16+kx^2)(4+kx^2)^2+6aM^2x\sqrt{4+kx^2}(-40-6kx^2+k^2x^4)$$
$$+2ax\sqrt{4+kx^2}\Big(4a^2x^2(2+kx^2)+Q^2(88+18kx^2-k^2x^4)\Big)-M(4$$
$$+kx^2)\Big(-12a^2x^2(-4+kx^2)+Q^2(-64-12kx^2+k^2x^4)\Big)\Bigg)$$
$$+4a^2x^2\Big(2ax(2+kx^2)\sqrt{4+kx^2}+M(32+12kx^2+k^2x^4)\Big)\Lambda\Bigg)$$
$$+128a^4x^4\Bigg(2ae^{\frac{4ax}{\sqrt{4+kx^2}}}(3M^2-Q^2)x(4+kx^2)+e^{\frac{4ax}{\sqrt{4+kx^2}}}M$$
$$(M^2-Q^2)(4+kx^2)^{\frac{3}{2}}+8a^3x^3\Big(e^{\frac{4ax}{\sqrt{4+kx^2}}}-2\Lambda\Big)$$
$$+4a^2Mx^2\sqrt{4+kx^2}\Big(3e^{\frac{4ax}{\sqrt{4+kx^2}}}-2\Lambda\Big)\Bigg)\Lambda\Bigg]^{\frac{1}{2}} \tag{5.5.1}$$

which reduces significantly as follows when $Q = M$,

$$F^{01} = E^1 = \Bigg[2(4+kx^2)\Big(e^{\frac{4ax}{\sqrt{4+kx^2}}}(-4a^2x^2)+4a^2x^2\Lambda\Big)\Big(e^{\frac{4ax}{\sqrt{4+kx^2}}}(4a^2x^2+4aMx\sqrt{4+kx^2}) +4a^2x^2\Lambda\Big)^4\Bigg]^{-\frac{1}{2}}\Bigg[32a^3e^{\frac{12ax}{\sqrt{4+kx^2}}}x^3((4+kx^2)(16a^3e^{\frac{4ax}{\sqrt{4+kx^2}}}x^3(4+kx^2)\Big(e^{\frac{4ax}{\sqrt{4+kx^2}}}(kM^2x^2) -kM^2x^2\Lambda\Big)+16a^4Mx^4\sqrt{4+kx^2}(6+kx^2)\Big(e^{\frac{8ax}{\sqrt{4+kx^2}}}-\Lambda^2\Big)+16a^3x^3\Lambda\Big(e^{\frac{4ax}{\sqrt{4+kx^2}}} (M^3(-16+kx^2)(4+kx^2)^2+6aM^2x\sqrt{4+kx^2}(-40-6kx^2+k^2x^4) +2ax\sqrt{4+kx^2}(4a^2x^2(2+kx^2)+M^2(88+18kx^2-k^2x^4))-M(4+kx^2) (-12a^2x^2(-4+kx^2)+M^2(-64-12kx^2+k^2x^4)))+4a^2x^2(2ax(2+kx^2)\sqrt{4+kx^2} +M(32+12kx^2+k^2x^4))\Lambda\Big)+128a^4x^4\Big(4aM^2e^{\frac{4ax}{\sqrt{4+kx^2}}}x(4+kx^2)+8a^3x^3 Big(e^{\frac{4ax}{\sqrt{4+kx^2}}}-2\Lambda\Big)+4a^2Mx^2\sqrt{4+kx^2}\Big(3e^{\frac{4ax}{\sqrt{4+kx^2}}}-2\Lambda\Big)\Big)\Lambda\Bigg]^{\frac{1}{2}} \tag{5.5.2}$$

Also since $F_{ab} = A_{a;b} - A_{b;a}$, using Eq.(5.5.1), the non-vanishing components of the potential A_a is obtained as,

$$A_0 = \int F^{01} g_{00} g_{11} dx \tag{5.5.3}$$

Furthermore the Eq.(5.5.1) satisfies $F^{ab}_{;b} = 0$. From Eq.(5.2.17) $G^{ab}_{;b} = 0$ always holds, hence this can be obtained, $T^{PF}_{ab;b} + T^{EM}_{ab;b} = 0$. This can be also found that the above relation is satisfied using equations Eqs.(5.2.18) and (5.2.19) as,

$$u_a T^{PF}_{ab;b} = T^{PF}_{0b;b} = p_{,b} g_{0b} + p g_{0b;b} + (\rho + p)_{,b} u_b u_0 + (\rho + p)[u_{b;b} u_0 + u_{0;b} u_b] = 0$$

and

$$4\pi T^{ab(EM)}_{;b} = F^{a\alpha}_{;b} F^b_\alpha + F^{a\alpha} F^b_{\alpha;b} - \tfrac{1}{2} g^{ab} F_{\alpha\beta} F^{\alpha\beta} = F^{a\alpha} F^b_{\alpha;b} + \tfrac{1}{2} g^{a\zeta} F^{b\kappa}(F_{\zeta\kappa;b} - F_{\zeta b;\kappa} - F_{\kappa b;\zeta}) = -F^{a\alpha} J_\alpha = 0.$$

So both T^{PF}_{ab} and T^{EM}_{ab} satisfy Bianchi identity. The proof is indicative of the fact that Eq.(5.3.7) is an exact solution of the EM field equations and the metric is physically relevant.

5.6 Darmois-Israel Matching Conditions

The Darmois-Israel matching conditions have been studied [Darmois (1927), Lanczos (1924), Perry and Mann (1992), and Sen (1924),Papapetrou and Hamoui (1968)]. The junction conditions to match the inner and exterior metrics across the boundary surface $x = x_0$, are the continuity of first and second fundamental forms across that surface.A surface $\sum$ is defined by the metric (where $x = x_0$, the junction surface being an one dimensional ring of matter) [Lemos and Zanchin (2011)],

$$dl^2_{\sum} = -d\tau^2 + x_0^2 d\theta^2, \tag{5.6.1}$$

with the intrinsic coordinates of $\sum$ being $\xi^m = (\tau, \theta)$. The inner and outer metrics from Eqs.(5.3.7) and (5.3.3) are given as,

$$\begin{aligned} dl^2_- &= -\frac{\left(1 - \frac{M^2\left(1+\frac{kx^2}{4}\right)}{a^2x^2} + \frac{Q^2\left(1+\frac{kx^2}{4}\right)}{a^2x^2} - \Lambda e^{-\frac{2ax}{\sqrt{1+\frac{kx^2}{4}}}}\right)^2}{\left[\left(1 + \frac{M\sqrt{1+\frac{kx^2}{4}}}{ax}\right)^2 - \frac{Q^2\left(1+\frac{kx^2}{4}\right)}{a^2x^2} + \Lambda e^{-\frac{2ax}{\sqrt{1+\frac{kx^2}{4}}}}\right]^2} \\ &\quad dv^2 + \frac{a^2}{\left(1+\frac{kx^2}{4}\right)^2}\left[\left(1 + \frac{M\sqrt{1+\frac{kx^2}{4}}}{ax}\right)^2\right. \\ &\quad \left. - \frac{Q^2\left(1+\frac{kx^2}{4}\right)}{a^2x^2} + \Lambda e^{-\frac{2ax}{\sqrt{1+\frac{kx^2}{4}}}}\right]^2 \times (dx^2 + x^2 d\theta^2), \end{aligned} \tag{5.6.2}$$

$$dl^2_+ = -dv^2 + \frac{a^2(v)}{\left(1+\frac{kx^2}{4}\right)^2}(dx^2 + x^2 d\theta^2), \tag{5.6.3}$$

Here the coordinates (v, x, θ) are recognised in both the regions of the spacetime.

Now the boundary surface $\sum$ is considered which would imply as timelike

$$\frac{\left(1 - \frac{M^2\left(1+\frac{kx^2}{4}\right)}{a^2x^2} + \frac{Q^2\left(1+\frac{kx^2}{4}\right)}{a^2x^2} - \Lambda e^{-\frac{2ax}{\sqrt{1+\frac{kx^2}{4}}}}\right)^2}{\left[\left(1 + \frac{M\sqrt{1+\frac{kx^2}{4}}}{ax}\right)^2 - \frac{Q^2\left(1+\frac{kx^2}{4}\right)}{a^2x^2} + \Lambda e^{-\frac{2ax}{\sqrt{1+\frac{kx^2}{4}}}}\right]^2} > 0 \tag{5.6.4}$$

The radial coordinate x is used as the matching parameter along the generators on $\sum$, the normal η_m to the surface has only the radial component $\eta_x = \sqrt{g_{xx}}$. The extrinsic curvature is obtained in the form (where,$x^0 = v, x^1 = x, x^2 = \theta$),

$$K^{\pm}_{mn} = -\eta^{\pm}_{x}\Gamma^{x(\pm)}_{ab}\frac{\partial x^a}{\partial \xi^m}\frac{\partial x^b}{\partial \xi^n}. \tag{5.6.5}$$

Now, the line elements in Eqs.(5.6.2) and (5.6.3) are continuous at $x = x_0$. The continuity of the first fundamental form at the boundary indicates that $g^{+}_{vv} = g^{-}_{vv}$ and $g^{+}_{xx} = g^{-}_{xx}$, i.e,

$$\frac{\left(1 - \frac{M^2\left(1+\frac{kx_0^2}{4}\right)}{a^2x_0^2} + \frac{Q^2\left(1+\frac{kx_0^2}{4}\right)}{a^2x_0^2} - \Lambda e^{-\frac{2ax_0}{\sqrt{1+\frac{kx_0^2}{4}}}}\right)^2}{\left[\left(1 + \frac{M\sqrt{1+\frac{kx_0^2}{4}}}{ax_0}\right)^2 - \frac{Q^2\left(1+\frac{kx_0^2}{4}\right)}{a^2x_0^2} + \Lambda e^{-\frac{2ax_0}{\sqrt{1+\frac{kx_0^2}{4}}}}\right]^2} = 1, \tag{5.6.6}$$

and

$$\begin{aligned}\frac{a^2(v)}{\left(1+\frac{kx_0^2}{4}\right)^2} &= \frac{a^2(v)}{\left(1+\frac{kx_0^2}{4}\right)^2}\left[\left(1 + \frac{M\sqrt{1+\frac{kx_0^2}{4}}}{ax_0}\right)^2\right. \\ &\quad \left. - \frac{Q^2\left(1+\frac{kx_0^2}{4}\right)}{a^2x_0^2} + \Lambda e^{-\frac{2ax_0}{\sqrt{1+\frac{kx_0^2}{4}}}}\right]^2.\end{aligned} \tag{5.6.7}$$

Hence Eqs.(5.4.1) and (5.4.5) are retrieved on replacing x_0 by x in the above Eqs.(5.6.6) and (5.6.7) respectively. It is also evident that,

$$K^{-}_{\tau\tau} = -\eta^{-}_{x}\Gamma^{(-)x}_{vv}\frac{dv}{d\tau}\frac{dv}{d\tau}, \tag{5.6.8}$$

But $g^{\pm}_{vv}\frac{dv^2}{d\tau^2} = -1$ (by construction) and

$$\eta^{-}_{x} = \frac{a}{\left(1+\frac{kx_0^2}{4}\right)}\left[\left(1 + \frac{M\sqrt{1+\frac{kx_0^2}{4}}}{ax_0}\right)^2 - \frac{Q^2\left(1+\frac{kx_0^2}{4}\right)}{a^2x_0^2} + \Lambda e^{-\frac{2ax_0}{\sqrt{1+\frac{kx_0^2}{4}}}}\right]. \tag{5.6.9}$$

Now,

$$\frac{\partial g^{-}_{vv}}{\partial x} = \Bigg[(4+kx_0^2)^{-3/2}\Big(e^{\frac{4ax_0}{\sqrt{4+kx_0^2}}}(4a^2x_0^2+4aMx_0\sqrt{4+kx_0^2}+M^2(4+kx_0^2)-Q^2 (4+kx_0^2))+4a^2x_0^2\Lambda\Big)^{-3}\Bigg]\Bigg[32ae^{\frac{4ax_0}{\sqrt{4+kx_0^2}}}\Bigg(e^{\frac{4ax_0}{\sqrt{4+kx_0^2}}}\Big(4ax_0^2-M^2(4+kx_0^2)+Q^2(4+kx_0^2)\Big) -4a^2x_0^2\Lambda\Bigg)\Bigg((4+kx_0^2)\Big(e^{\frac{4ax_0}{\sqrt{4+kx_0^2}}}\Bigg(4aM^2x_0\sqrt{4+kx_0^2}-4aQ^2x_0\sqrt{4+kx_0^2}+M^3(4+kx_0^2) -M\Big(-4a^2x_0^2+Q^2(4+kx_0^2)\Big)\Bigg)-4a^2Mx_0^2\Lambda\Big)+16a^3x_0^3\Big(2ax_0+M\sqrt{4+kx_0^2}\Big)\Lambda\Bigg)\Bigg]. \tag{5.6.10}$$

It is found that

$$\Gamma^{x(-)}_{vv} = \Bigg[e^{\frac{4ax_0}{\sqrt{4+kx_0^2}}}\Big(4a^2x_0^2+4aMx_0\sqrt{4+kx_0^2}+M^2(4+kx_0^2)-Q^2(4+kx_0^2)\Big)+4a^2x_0^2\Lambda\Bigg]^{-5} \times\Bigg[16a^3e^{\frac{12ax_0}{\sqrt{4+kx_0^2}}}x_0^4\sqrt{4+kx_0^2}\Big(e^{\frac{4ax_0}{\sqrt{4+kx_0^2}}}(-4a^2x_0^2+M^2(4+kx_0^2)-Q^2(4+kx_0^2))+4a^2x_0^2\Lambda\Big) ((4+kx_0^2)(e^{\frac{4ax_0}{\sqrt{4+kx_0^2}}}\Bigg(4aM^2x_0\sqrt{4+kx_0^2}-4aQ^2x_0\sqrt{4+kx_0^2}+M^3(4+kx_0^2) -M\Big(-4a^2x_0^2+Q^2(4+kx_0^2)\Big)\Bigg)-4a^2Mx_0^2\Lambda)+16a^3x_0^3(2ax_0+M\sqrt{4+kx_0^2})\Lambda)\Bigg]. \tag{5.6.11}$$

Thus,

$$K^{-}_{\tau\tau} = -\Bigg[16a^2e^{\frac{8ax_0}{\sqrt{4+kx_0^2}}}x_0^2\Bigg((4+kx_0^2)\Bigg(e^{\frac{4ax_0}{\sqrt{4+kx_0^2}}}\Bigg(4aM^2x_0\sqrt{4+kx_0^2}-4aQ^2x_0\sqrt{4+kx_0^2}+M^3 (4+kx_0^2)-M\Big(-4a^2x_0^2+Q^2(4+kx_0^2)\Big)\Bigg)-4a^2Mx_0^2\Lambda\Bigg)+16a^3x_0^3\Big(2ax_0+M\sqrt{4+kx_0^2}\Big) \Lambda\Bigg)\Bigg]\times\Bigg[\sqrt{4+kx_0^2}\Big(e^{\frac{4ax_0}{\sqrt{4+kx_0^2}}}(-4a^2x_0^2+M^2(4+kx_0^2)-Q^2(4+kx_0^2))+4a^2x_0^2\Lambda\Big) \Bigg(e^{\frac{4ax_0}{\sqrt{4+kx_0^2}}}\Big(4a^2x_0^2+4aMx_0\sqrt{4+kx_0^2}+M^2(4+kx_0^2)-Q^2(4+kx_0^2)\Big)+4a^2x_0^2\Lambda\Bigg)^2\Bigg]^{-1}. \tag{5.6.12}$$

Similarly, the extrinsic curvature arising from the exterior FRW region is calculated and this can be found,

$$K^{+}_{\tau\tau} = 0. \tag{5.6.13}$$

In order to match $K^{-}_{\tau\tau}$ and $K^{+}_{\tau\tau}$, this would simply imply,

$$\Big(4+kx_0^2\Big)\Bigg(e^{\frac{4ax_0}{\sqrt{4+kx_0^2}}}\Bigg(4aM^2x_0\sqrt{4+kx_0^2}-4aQ^2x_0\sqrt{4+kx_0^2}+M^3(4+kx_0^2)-M\Big(-4a^2x_0^2 +Q^2(4+kx_0^2)\Big)\Bigg)-4a^2Mx_0^2\Lambda\Bigg)+16a^3x_0^3\Bigg(2ax_0+M\sqrt{4+kx_0^2}\Bigg)\Lambda=0. \tag{5.6.14}$$

Hence the metric as well as the extrinsic curvature are continuous at the boundary surface.

5.7 Further Discussion on Surface Continuity

The surface continuity is now going to be proved alternatively. Let the surface be discontinuous. Then on the contrary, the discontinuity in the extrinsic curvature determine the surface stress energy and surface tension of the junction surface at $x = x_0$ where the surface stress-energy tensor components are determined [Rahaman et al. (2012),Banerjee (2013),Övgün and Sakalli (2017),Habib Mazharimousavi et al. (2017)].

Let,

$$f(x)=\frac{(1-\frac{M^2(1+\frac{kx^2}{4})}{a^2x^2}+\frac{Q^2(1+\frac{kx^2}{4})}{a^2x^2}-\Lambda e^{-\frac{2ax}{\sqrt{1+\frac{kx^2}{4}}}})^2}{[(1+\frac{M\sqrt{1+\frac{kx^2}{4}}}{ax})^2-\frac{Q^2(1+\frac{kx^2}{4})}{a^2x^2}+\Lambda e^{-\frac{2ax}{\sqrt{1+\frac{kx^2}{4}}}}]^2}, \tag{5.7.1}$$

$$g(x)=\frac{a^2}{(1+\frac{kx^2}{4})^2}[(1+\frac{M\sqrt{1+\frac{kx^2}{4}}}{ax})^2-\frac{Q^2(1+\frac{kx^2}{4})}{a^2x^2}+\Lambda e^{-\frac{2ax}{\sqrt{1+\frac{kx^2}{4}}}}]^2, \tag{5.7.2}$$

$$h(x)=\frac{a^2x^2}{(1+\frac{kx^2}{4})^2}[(1+\frac{M\sqrt{1+\frac{kx^2}{4}}}{ax})^2-\frac{Q^2(1+\frac{kx^2}{4})}{a^2x^2}+\Lambda e^{-\frac{2ax}{\sqrt{1+\frac{kx^2}{4}}}}]^2, \tag{5.7.3}$$

Hence,

$$\begin{aligned}f'(x)=[(4+kx^2)^{-3/2}(e^{\frac{4ax}{\sqrt{4+kx^2}}}(4a^2x^2+4aMx\sqrt{4+kx^2}+M^2(4+kx^2)-Q^2\\(4+kx^2))+4a^2x^2\Lambda)^{-3}][32ae^{\frac{4ax}{\sqrt{4+kx^2}}}(e^{\frac{4ax}{\sqrt{4+kx^2}}}(4ax^2-M^2(4+kx^2)+Q^2(4+kx^2))\\-4a^2x^2\Lambda)((4+kx^2)(e^{\frac{4ax}{\sqrt{4+kx^2}}}(4aM^2x\sqrt{4+kx^2}-4aQ^2x\sqrt{4+kx^2}+M^3(4+kx^2)\\-M(-4a^2x^2+Q^2(4+kx^2)))-4a^2Mx^2\Lambda)+16a^3x^3(2ax+M\sqrt{4+kx^2})\Lambda)],\end{aligned} \tag{5.7.4}$$

The jump of the extrinsic curvature components at the surface $x=x_0$, is associated with the surface energy density [Bejarano et al. (2014)] as,

$$\lambda(x_0)=-\frac{1}{8\pi}\frac{h'(x_0)}{h(x_0)}\sqrt{\frac{1+\dot{x_0}^2g(x_0)}{g(x_0)}}, \tag{5.7.5}$$

and the surface pressure as,

$$P(x_0)=\frac{1}{8\pi}\sqrt{\frac{1+\dot{x_0}^2g(x_0)}{g(x_0)}}[2\ddot{x_0}+\dot{x_0}^2(\frac{f'(x_0)}{f(x_0)}+\frac{g'(x_0)}{g(x_0)})+\frac{f'(x_0)}{f(x_0)g(x_0)}]. \tag{5.7.6}$$

For a static configuration of radius x_0, this is obtained (assuming $\dot{x}_0=0$ and $\ddot{x}_0=0$)

$$\begin{aligned}\lambda(x_0)=-\frac{1}{8\pi}\frac{h'(x_0)}{h(x_0)}\sqrt{\frac{1}{g(x_0)}}=[4\pi x_0(4+kx_0^2)^{\frac{3}{2}}(e^{\frac{4ax_0}{\sqrt{4+kx_0^2}}}(4a^2x_0^2+4aMx_0\\\sqrt{4+kx_0^2}+M^2(4+kx_0^2)-Q^2(4+kx_0^2))+4a^2x_0^2\Lambda)]^{-1}[4ae^{\frac{4ax_0}{\sqrt{4+kx_0^2}}}kMx_0^3(4+kx_0^2)\\+e^{\frac{4ax_0}{\sqrt{4+kx_0^2}}}(M^2-Q^2)(4+kx_0^2)^{\frac{5}{2}}+4a^2x_0^2(-4+kx_0^2)\sqrt{4+kx_0^2}(e^{\frac{4ax_0}{\sqrt{4+kx_0^2}}}+\Lambda)+64a^3x_0^3\Lambda]\\\times[\frac{(4+kx_0^2)}{4a(1+\frac{M\sqrt{4+kx_0^2}}{ax_0}+\frac{(M^2-Q^2)(4+kx_0^2)}{4a^2x_0^2}+\Lambda e^{-\frac{4ax_0}{\sqrt{4+kx_0^2}}})}],\end{aligned} \tag{5.7.7}$$

and

$$P(x_0) = \frac{1}{8\pi}\sqrt{\frac{1}{g(x_0)}}[\frac{f'(x_0)}{f(x_0)g(x_0)}] = -[\pi(e^{\frac{4ax_0}{\sqrt{4+kx_0^2}}}(-4a^2x_0^2 + M^2(4+kx_0^2) - Q^2(4+kx_0^2))$$
$$+4a^2x_0^2\Lambda)(e^{\frac{4ax_0}{\sqrt{4+kx_0^2}}}(4a^2x_0^2 + 4aMx_0\sqrt{4+kx_0^2} + M^2(4+kx_0^2) - Q^2(4+kx_0^2)) + 4a^2x_0^2\Lambda)^3]^{-1}$$
$$\times[a^2e^{\frac{12ax_0}{\sqrt{4+kx_0^2}}}x_0^4(4+kx_0^2)^{\frac{3}{2}}(1 + \frac{M\sqrt{4+kx_0^2}}{ax_0} + \frac{(M^2-Q^2)(4+kx_0^2)}{4a^2x_0^2} + \Lambda e^{-\frac{4ax_0}{\sqrt{4+kx_0^2}}})^{-1}((4+kx_0^2)$$
$$(e^{\frac{4ax_0}{\sqrt{4+kx_0^2}}}(4aM^2x_0\sqrt{4+kx_0^2} - 4aQ^2x_0\sqrt{4+kx_0^2} + M^3(4+kx_0^2) - M(-4a^2x_0^2 + Q^2(4+kx_0^2)))$$
$$-4a^2Mx_0^2\Lambda) + 16a^3x_0^3(2ax_0 + M\sqrt{4+kx_0^2})\Lambda)], \tag{5.7.8}$$

which significantly reduces to $P(x_0) = 0$ using Eq.(5.6.14). The vanishing surface pressure thus proves the metric continuity at the boundary surface, i.e on the horizon $x = x_0$, as envisaged.

5.8 Discussion and Conclusions

Thus a charged, non-rotating, spherically symmetric black hole which has cosmological constant Λ (RN+Λ), active gravitational mass M and electric charge Q in exterior Friedman-Robertson-Walker (FRW) universe is studied. The Einstein-Maxwell equations of the RN+Λ black hole embedded in the FRW background are solved. As a procedure, starting with a (2+1)-d RN+Λ black hole and then performed a simple transformation only under suitable conditions to obtain a metric which matches with the exterior Friedman-Robertson-Walker universe and also derived a negative cosmological constant inside the black hole. New classes of exact solutions of the charged black hole are found. Literature reveals that there are three possible black hole solutions where the cosmological constant is (1) positive (2) negative and (3) zero. The cosmological constant found negative inside the black hole is also confirmed by the geodesic equations. Here, the cosmological constant is dependent on R, Q and $a(v)$ which correspond to the areal radius, charge, of the black hole and the scale factor of the universe respectively.

The century-old problem of describing a gravitationally bound system in an expanding universe in the frame-set of general relativity has seen many attempts to find a solution.

Assuming that scale factor does not alter with the metric transformation, a maximum limit of the universal expansion is found. Despite its apparent simplicity, a full understanding of the mechanisms involved when general and realistic systems are considered has yet to be found. It is observed that the size, mass and charge of the black hole are affected by the expansion of the universe. An important observation is that, for an observer at infinity, both the mass and charge of black hole increase with the contraction of the universe and decrease with the expansion of the universe. The cosmological constant has been found to be negative in a previous work too [Landry et al. (2012)]. The anti-de Sitter space or conformal field theories correspondence tells us that the case $\Lambda < 0$ is still worthy of consideration.

The use of two different methods for matching spacetimes is justified. Boundary and matching conditions with the exterior FRW universe are studied in Sec.5.4, to arrive at a conclusion that the cosmological constant can have a negative value inside the black hole. However, the Darmois-Israel matching conditions have been studied in Sec.5.6, to deduce that the metric as well as the extrinsic curvature are continuous at the boundary surface. Alternatively the vanishing surface pressure also proves the metric continuity at the boundary surface, i.e on the horizon ($x = x_0$).

The shadow of $M87^*$'s supermassive Black Hole, captured by the Event Horizon Telescope in 2019 [Akiyama et al. (2019)], serves as a profound source of inspiration, showcasing the remarkable power of modern science to reveal the unseen. This iconic image pushes us to explore even deeper mysteries of the universe, such as shadows of compact objects as well as the hypothetical shadows of wormholes. The shadow itself is the observable outcome of gravitational lensing process. So, in the following chapter the effect of gravitational lensing on a black hole is studied.

Chapter 6

Shadows and Strong Gravitational Lensing around Black Hole Like Solution in Quadratic Gravity

6.1 Introduction

The study of black holes offers a unique opportunity to test the predictions of general relativity under extreme conditions. In the high-curvature regions surrounding black holes [Kerr (1963) and Schwarzschild (1916)], general relativity predicts phenomena such as time dilation, gravitational redshift and the warping of space, which have been observed and confirmed through astrophysical measurements. The Schwarzschild and Kerr solutions to Einstein's field equations describe the spacetime around non-rotating and rotating black holes respectively and provide the framework to understand black hole properties. Observing black holes is pivotal in gravitational and cosmological physics. Recent developments in observational astrophysics such as gravitational wave detection [Abbott et al. (2016)] from black hole mergers and direct imaging of black hole shadows [Akiyama et al. (2019, 2022c)], have provided empirical support for general relativity in strong gravitational fields. These observations not only affirm the theoretical predictions of general relativity but also open new avenues for exploring potential extensions to general relativity. Thus, black holes serve as natural laboratories allowing scientists to probe the limits of general relativity and explore the fundamental nature of gravity. General relativity is not renormalizable when

treated perturbatively, except in the case of pure gravity without interactions involving scalar fields at the one-loop level [Aharony and Banks (1999) and Birrell and Davies (1982)]. Nevertheless, gravity can be accurately described within a specific range of energy and length scales by imposing a suitable cutoff at high energy scales. However, beyond these limits, particularly near black hole singularities, the classical formulation of general relativity becomes inadequate, necessitating the development of a new physical theory.

A deeper investigation into the complex features of black holes, particularly the formation of relativistic images, is required. Key phenomena including gravitational lensing [Kumar et al. (2023)], black hole shadows [Anjum et al. (2023)] and quasinormal modes [Cao et al. (2023)] play a crucial role in enhancing our understanding of general relativity, modified gravity theories. Increasing attention has been directed towards understanding the impact of quadratic gravity effects near singularities. Quadratic gravity is an extension of general relativity that includes terms quadratic in the curvature tensors in the gravitational action. It arises as a natural framework to explore higher-order corrections to general relativity. A comprehensive formulation of quadratic gravity is presented in [Held and Zhang (2023)]. Recent studies in the field of quadratic gravity have been conducted [Lin et al. (2017), Podolský et al. (2020), and Pravda et al. (2017)].

The study of black hole shadows and gravitational lensing further enhances our understanding of general relativity and its predictions around these extreme objects. The images of the supermassive black holes $M87^*$ [Akiyama et al. (2019) and Collaboration et al. (2019)] and $Sgr\ A^*$ [Akiyama et al. (2022a, 2022b)] offer critical insights for testing gravitational effects in the strong field regime. A key characteristic of a black hole's image is its shadow, formed by light rays captured by the outer event horizon. The shape and size of the shadow depend on several factors including the parameters of the black hole, the paths followed by the light rays and the observer's location. When light rays approach a black hole, these trap photons with low orbital angular momentum, while those with higher angular momentum escape their gravitational pull. As a result, a distant observer perceives a dark region in the sky, referred to as the black hole's shadow. This shadow, a silhouette of the event horizon outlined against the bright background of accreting material is a direct observational indicator of the black hole's presence and characteristics. The shadow's shape and size depend on the mass of the black hole, spin and curvature of the surrounding spacetime offering a

valuable opportunity to test the predictions of general relativity in the strong-field regime. For a detailed discussion of black hole shadows and their potential for testing general relativity, see [Afrin et al. (2021), Al-Badawi et al. (2024), Bambi et al. (2019), Bronzwaer and Falcke (2021), Hamil and Lütfüoğlu (2023), Kumar and Ghosh (2020), Li et al. (2020), Mirzaev et al. (2023), Molla and Debnath (2023b), Narzilloev et al. (2021a), Perlick and Tsupko (2022), Ror et al. (2024), Singh (2022), and Vagnozzi and Visinelli (2019)].

Gravitational lensing has become an invaluable tool for probing fundamental properties of gravitational fields. It plays a crucial role in the study of the large-scale structure of the Universe, the behavior of massive stellar objects and the search for dark matter candidates. In this work, we suggest that gravitational lensing can also be employed to distinguish between different gravitational theories, particularly between quadratic gravity and general relativity. The deflection of light by black holes and galaxies and the phenomenon of strong gravitational lensing form a significant area of research. It can potentially reveal novel astrophysical effects providing unique signatures for testing modified theories of gravity. Observables obtained from relativistic images in strong lensing scenarios can help distinguish between different black hole metrics through high-precision observations. Gravitational lensing, a phenomenon predicted by Einstein (1936), though initially doubted by him if would ever be observed. There are three primary types of gravitational lensing based on the alignment of the source, lens and observer. The resulting effects on the observed light offer unique insights into the nature of these extreme objects. On the other hand, weak gravitational lensing involves minor distortions in the shape of background objects when light passes through a less intense gravitational field near a black hole. Microlensing occurs when a black hole or another compact object momentarily magnifies the light of a background star, creating multiple images but the images are so close together that they cannot be distinguished from one another. Strong gravitational lensing is particularly significant in the study of black holes because it produces highly visible and distinct effects such as multiple images, arcs, Einstein rings, which can be directly observed and analyzed. The clarity and magnitude of the distortions caused by strong lensing make it an exceptionally powerful tool for probing the fundamental nature of black holes and the behavior of light and matter in their extreme gravitational fields. The study of strong gravitational lensing around black holes has made substantial progress since Darwin's initial work on photon

orbits [Darwin (1959)], in the Schwarzschild black hole spacetime. Building on this foundation, Virbhadra and Ellis formalized the concept of relativistic images [Virbhadra and Ellis (2000)], focusing on the strong-field regime where light passing near a black hole's photon sphere can generate multiple, highly curved images. A significant breakthrough came with Bozza's development of the strong deflection limit (SDL) [Bozza (2002)], which provided an accurate framework for calculating light deflection in the proximity of black holes. Further advancements were made by Frittelli, Killing and Newman, who enhanced analytical methods for solving the lens equation [Frittelli et al. (2000)], while Bozza extended the SDL approach. This approach has been utilized across various spacetimes including rotating and charged black holes such as Reissner-Nordström and Kerr black holes [Bozza (2003) and Eiroa et al. (2002)]. The SDL has proven to be a versatile tool, applied to classical black hole spacetimes and to modified scenarios like braneworld black holes and those arising in modified gravity theories [Bhadra (2003), Eiroa and Sendra (2012), Eiroa and Torres (2004), Islam and Ghosh (2021), Kumar et al. (2022a, 2022b), and Whisker (2005)]. Ongoing research continues to investigate gravitational lensing in diverse black hole spacetimes including those described by higher-curvature gravity theories [Islam et al. (2024, 2020), Kumar et al. (2020b), and Narzilloev et al. (2021b)], as well as modifications of the traditional Schwarzschild geometry [Bronnikov and Baleevskikh (2019), Eiroa and Sendra (2011), Molla et al. (2024), Övgün (2019), and Panpanich et al. (2019)]. Several researchers have extensively explored the physical observables associated with strong lensing effects across a variety of gravitational models and black hole solutions. These studies have analyzed various astrophysical implications by examining parameters such as the angular positions of images, separations between them, magnifications, Einstein ring characteristics and time delays in the formation of relativistic images [Islam et al. (2024, 2021), Kumar et al. (2022a), Kumar et al. (2020a), Molla and Debnath (2022, 2023a), and Narzilloev et al. (2021b)].

The present study investigates the shadow and strong gravitational lensing characteristics of black holes in quadratic gravity emphasizing unique geometric properties absent in other well-known black hole like solutions. This chapter aims to extend the analysis of black hole shadows and strong gravitational lensing by incorporating the spacetime geometry of black holes in quadratic gravity. In particular, we focus on key lensing observables such as the

black hole shadow, deflection angle, image magnifications and time delays and compare them with predictions from the classical lensing scenario around a black hole in a vacuum. These results carry significant implications for understanding the environment surrounding black holes, testing general relativity and alternative gravity theories and probing the fundamental properties of quadratic gravity through astrophysical observations.

The present chapter is organized as follows: section 6.2 provides a brief overview of the black hole like solutions in quadratic gravity with a focus on the non-rotating case. In section 6.3, we derive the expression for the black hole shadow in quadratic gravity and present the first set of constraints on the solution parameters based on comparisons with observational data from $M87^*$ and $Sgr\ A^*$. Section 6.4 explores the strong gravitational lensing properties of the quadratic gravity black hole with a detailed investigation of the associated lensing observables. Specific predictions for these observables are made using realistic astrophysical data. Finally, the conclusions and implications of our findings are discussed in section 6.5.

In what follows, we use natural units with $G = c = 1$ and adopt a signature convention of {- + + +}.

6.2 Black Hole like Solutions in Quadratic Gravity

Black holes like solutions are derived from the quadratic action. These solutions are formulated within the quadratic gravity framework and have been recently explored numerically by Pawlowski and Tränkle (2024). The effective action is given by

$$\Gamma[g_{\mu\nu}] = \frac{1}{16\pi}\int_x d^4x\,\sqrt{g}\Big[R(\Delta,R) + R\,f_{R^2}(\Delta)\,R + R_{\mu\nu}\,f_{R^2_{\mu\nu}}(\Delta)\,R^{\mu\nu}\Big]. \tag{6.2.1}$$

Here, the functions $f_{R^2}(\Delta)$ and $f_{R^2_{\mu\nu}}(\Delta)$ correspond to two-point correlation functions of the curvature scalar and Ricci tensor, respectively. These functions, often referred to as form factors, capture generalized dispersion effects. Studies of such form factors have been presented in works such as Denz et al. (2018). To derive black hole solutions within the framework of quadratic gravity one must solve the field equations obtained from the effective action.

The static, spherically symmetric metric in quadratic gravity can be expressed as [Pawlowski

and Tränkle (2024)]

$$ds^2 = -f(r)dt^2 + g(r)^{-1}dr^2 + r^2(d\theta^2 + \sin^2\theta d\phi^2), \tag{6.2.2}$$

where the metric function can be expressed as

$$f(r) = 1 - \frac{2M}{r} + S_0\frac{e^{-m_0 r}}{r} + S_2\frac{e^{-m_2 r}}{r}, \tag{6.2.3}$$

$$g(r) = 1 - \frac{2M}{r} - S_0\frac{e^{-m_0 r}}{r}(1 + m_0 r) + \frac{1}{2}S_2\frac{e^{-m_2 r}}{r}(1 + m_2 r). \tag{6.2.4}$$

The two free parameters, S_0 and S_2, govern the strength of the exponentially decaying Yukawa corrections. The masses m_0 and m_2 correspond to the spin-0 and spin-2 modes, respectively, linked to the couplings of various curvature terms. For the initial conditions $(S_0, S_2) = (0, 0)$, the quadratic gravity black hole metric Eq.(6.2.2) reduces to the classical Schwarzschild metric. The event horizon, located at r_h, is determined by the solution to the equation $g(r_h) = 0$.

6.3 Shadow in Quadratic Gravity

In this section, we initiate our investigation of the black hole shadow within the quadratic gravity framework, focusing on the motion of photons and the resulting shadow. Our analysis begins by examining the trajectories of light in the spacetime of an quadratic gravity black hole. Furthermore, we aim to constrain the black hole parameters associated with this quadratic gravity model. Now using Eq.(6.2.3) we can introduce the function $\gamma(r)$ (it was recently introduced in Refs. [‘Ghorani et al. (2023), Perlick and Tsupko (2022), and Vagnozzi et al. (2023)])

$$\gamma^2(r) = \frac{r^2}{f(r)}. \tag{6.3.1}$$

The radius of a circular light orbit, particularly the one defining the photon sphere with

radius r_{ph} is found by solving the following condition [Perlick and Tsupko (2022)]

$$\left.\frac{d(\gamma^2(r))}{dr}\right|_{r=r_{ph}} = 0. \tag{6.3.2}$$

The photon orbit radii r_{ph} in quadratic gravity can be determined numerically using this equation.

When the parameters $S_0 = S_2 = 0$, the solution yields $r_{ph} = 3M$ [Perlick and Tsupko (2022) and Vagnozzi et al. (2023)], corresponding to the photon orbit radius in the Schwarzschild spacetime. We now analyze the shadow of the black hole within the quadratic gravity framework.

The angular radius of the black hole shadow is given by the following relation [Perlick and Tsupko (2022)],

$$\sin^2 \alpha_{sh} = \frac{\gamma^2(r_{ph})}{\gamma^2(r_{obs})}, \tag{6.3.3}$$

where, α_{sh} denotes the angular radius of the black hole shadow and r_{obs} is the observer's distance, assumed to be very large but finite. For instance, the observer distance for $Sgr\ A^*$ is $r_{obs} = D \simeq 8.3\,\text{kpc}$ [Akiyama et al. (2022a)], while for $M87^*$, it is $r_{obs} = D \simeq 16.8\,\text{Mpc}$ [Akiyama et al. (2019)].

By combining Eqs.(6.3.1) and (6.3.2), it follows that for a distant observer, Eq.(6.3.3) can be rewritten as [Atamurotov et al. (2023) and Perlick and Tsupko (2022)]

$$\sin^2 \alpha_{sh} = \frac{r_{ph}^2}{f(r_{ph})} \frac{f(r_{obs})}{r_{obs}^2}. \tag{6.3.4}$$

The radius of the black hole shadow for an observer at large distances can be determined using Eq.(6.3.4), yielding the following expression [Atamurotov et al. (2023) and Perlick and Tsupko (2022)]

$$R_{sh} \simeq r_{obs} \sin \alpha_{sh} \simeq \frac{r_{ph}}{\sqrt{f(r_{ph})}}. \tag{6.3.5}$$

This equation allows us to examine how the shadow radius of the black hole depends on the parameters of quadratic gravity.

The dependence of the black hole shadow on the parameters S_0, S_2, m_0 and m_2 is

illustrated in Fig.6.1. It is observed from Fig.6.1(a) that as the numerical values of the parameter $S_0 > 0$ increase while keeping the other parameters fixed, the size of the black hole shadow decreases and similar result holds for the parameter S_2 shown in Fig.6.1(b). Conversely, an increase in the values of the parameters $m_0 > 0$ with the other parameters held constant, increases the size of the black hole shadow, shown in Fig.6.1(c) and similar result holds for the parameter m_2 shown in Fig.6.1(d).

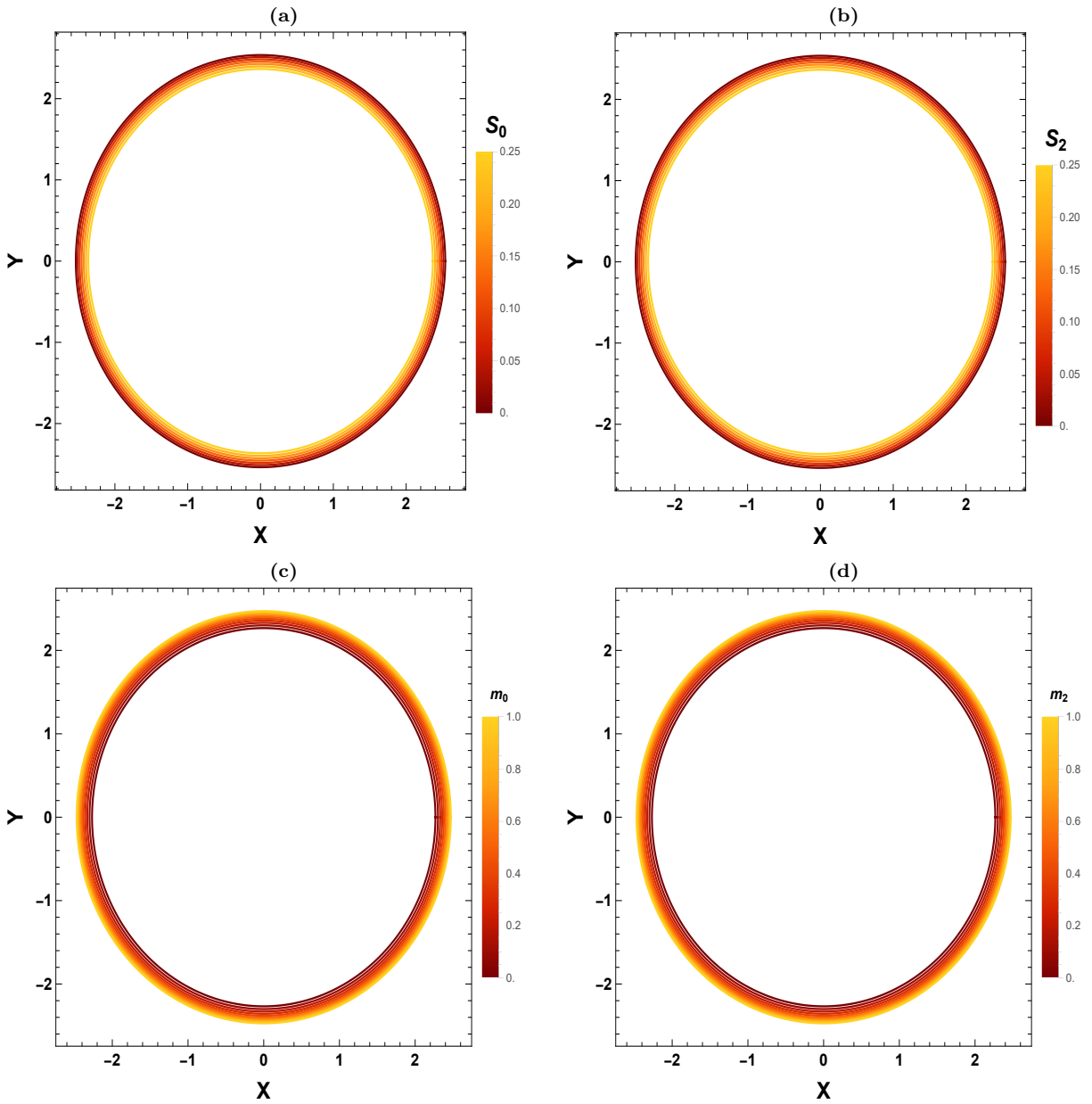

Fig. 6.1. The shadow silhouette of the black hole in quadratic gravity is presented in the X-Y plane ($R_{sh} = \sqrt{X^2 + Y^2}$), with black hole parameters (a) S_0, (b) S_2, (c) m_0 and (d) m_2 varied independently (while other parameters are kept fixed with respect to one).

6.3.1 Constraints the Black Hole Parameters with the Observational Data from $M87^*$ and $Sgr\ A^*$

Now, we aim to determine the possible ranges of the free parameters of the black hole in quadratic gravity by utilizing observational data from $M87^*$ and $Sgr\ A^*$. Specifically, we will explore the theoretical constraints on the black hole parameters S_0, S_2, m_0 and m_2 pairwise while keeping the remaining two parameters fixed.

To achieve this, we use the shadow data provided by the EHT project. The objective is to constrain the parameter pairs (S_0, S_2) and (m_0, m_2) by fitting them against the observed shadow sizes of $M87^*$ and $Sgr\ A^*$ within the framework of quadratic gravity. This approach will allow us to impose meaningful constraints on these parameters using real observational data.

The angular diameter of the shadow, the distance from the Sun to the black hole and the mass of the black hole at the center of the galaxy $M87$ are given as $\Omega_{M87^*} = 42 \pm 3\,\mu as$, $D = 16.8 \pm 0.8\,\text{Mpc}$ and $M_{M87^*} = (6.5 \pm 0.7) \times 10^9\, M_\odot$, respectively [Akiyama et al. (2019)].

For $Sgr\ A^*$, the most recent data obtained by the EHT project are $\Omega_{Sgr\ A^*} = 51.8 \pm 2.3 \mu as$, $D = 8277 \pm 9 \pm 33\,\text{pc}$ and $M_{Sgr\ A^*} = 4.297 \pm 0.013 \times 10^6\, M_\odot$ (from VLTI observations) [Akiyama et al. (2022a)].

Using these observational data, we can estimate the diameter of the shadow cast by the black hole per unit mass, using the following expression [Arora et al. (2023), Atamurotov et al. (2023), and Bambi et al. (2019)]

$$d_{\text{sh}} = \frac{D\,\Omega}{M}\,. \tag{6.3.6}$$

Now we can obtain the diameter of the shadow from the expression $d_{\text{sh}}^{\text{theo}} = 2R_{\text{sh}}$. Thus, the diameter of the black hole shadow image is $d_{\text{sh}}^{M87^*} = (11 \pm 1.5)M$ for $M87^*$ and $d_{\text{sh}}^{Sgr\ A^*} = (9.5 \pm 1.4)M$ for $Sgr\ A^*$. The angular diameters of the shadows of the black hole in quadratic gravity, obtained using the $M87^*$ and $Sgr\ A^*$ data, are depicted in Fig.6.2, respectively.

Constraints from $M87^*$: The shadow's angular diameter (Ω) for the $M87^*$ black hole, averaged within the range of $32\,\mu as$ to $45\,\mu as$ with a 1σ region from EHT observations, imposes constraints on the parameter pairs (S_0, S_2) and (m_0, m_2) of the black hole in quadratic gravity as shown in Figs.6.2(a) and 6.2(c).

Table 6.1: Estimated ranges of the quadratic gravity black hole parameters S_0, S_2 and m_0, m_2 from the known shadow observables $\Omega(\mu as)$ for $M87^*$ and $Sgr\ A^*$.

Supermassive black hole	$\Omega(\mu as)$	$S_0/2M$	$S_2/2M$	$2Mm_0$	$2Mm_2$
$M87^*$	39.1	$0 < S_0/2M \leq 0.09$	$0 < S_2/2M \leq 0.09$	1	1
	39.5	$0 < S_0/2M \leq 0.047$	$0 < S_2/2M \leq 0.047$	1	1
	39.3	0.01	0.01	$0 < 2Mm_0 \leq 0.39$	$0 < 2Mm_2 \leq 0.39$
	39.4	0.01	0.01	$0 < 2Mm_0 \leq 0.78$	$0 < 2Mm_2 \leq 0.78$
$Sgr\ A^*$	51.4	$0 < S_0/2M \leq 0.11$	$0 < S_2/2M \leq 0.11$	1	1
	51.8	$0 < S_0/2M \leq 0.079$	$0 < S_2/2M \leq 0.079$	1	1
	52.2	0.01	0.01	$0 < 2Mm_0 \leq 1.8$	$0 < 2Mm_2 \leq 1.8$
	52	0.01	0.01	$0 < 2Mm_0 \leq 0.55$	$0 < 2Mm_2 \leq 0.55$

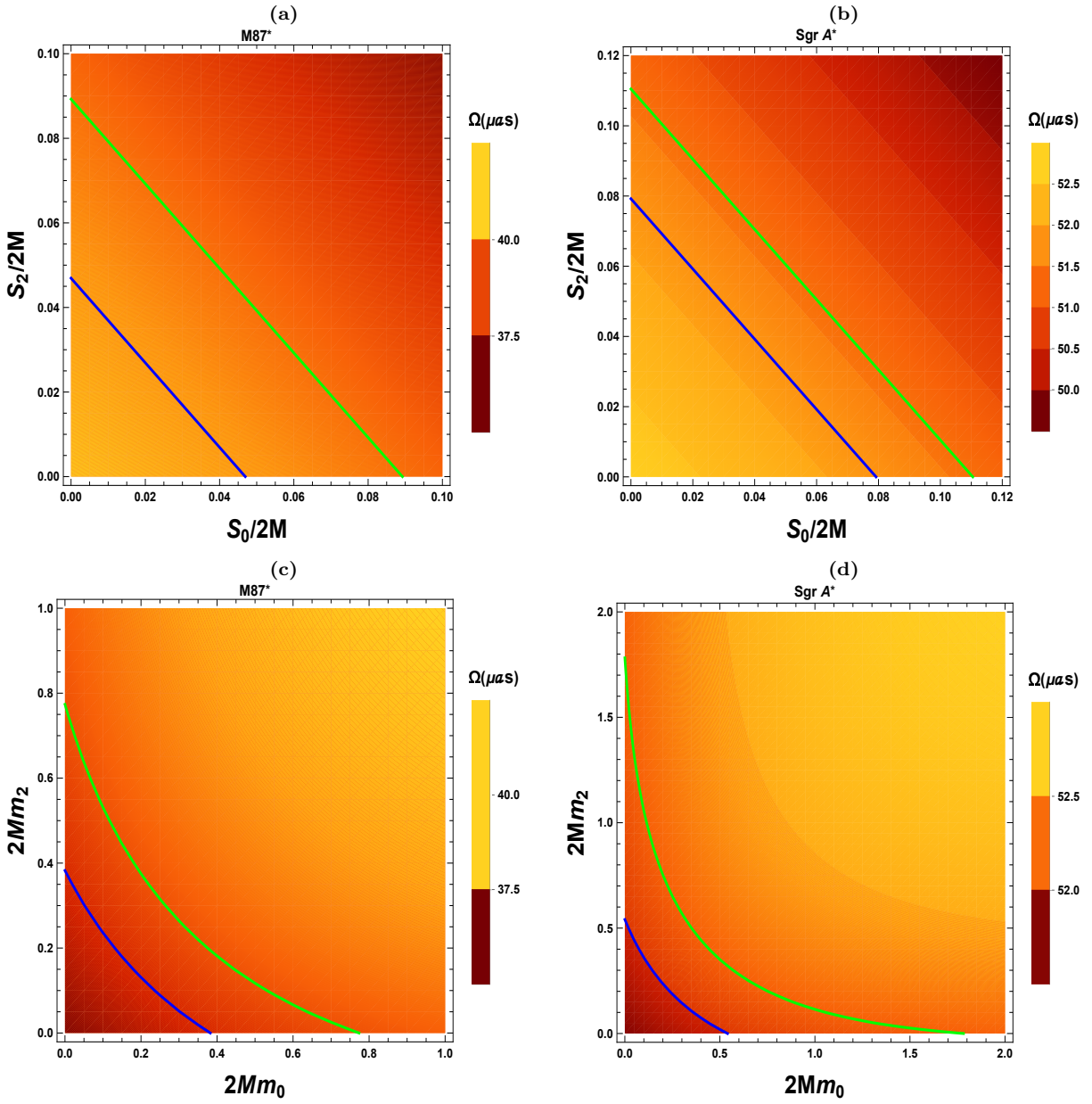

Fig. 6.2. The angular diameter $\Omega(\mu as)$ of the black hole shadow is presented as a function of the parameters S_0, S_2 and m_0, m_2 for the $M87^*$ (panels (a) and (c)) and $Sgr\ A^*$ (panels (b) and (d)) supermassive black holes. The enclosed regions satisfy the 1-σ shadow bounds for $M87^*$ and $Sgr\ A^*$, respectively. In panel (a) the green and blue lines correspond to $\Omega = 39.1\,\mu as$ and $\Omega = 39.5\,\mu as$, respectively; in panel, (b) they correspond to $\Omega = 51.4\,\mu as$ and $\Omega = 51.8\,\mu as$, respectively; in panel, (c) to $\Omega = 39.4\,\mu as$ and $\Omega = 39.3\,\mu as$, respectively; and in panel and (d) to $\Omega = 52.2\,\mu as$ and $\Omega = 52\,\mu as$, respectively.

Here, the shadow's angular diameter (Ω) is expressed as a function of the parameter pairs (S_0, S_2) and (m_0, m_2). In Fig.6.2(a), the green and blue lines correspond to $\Omega = 39.1\,\mu as$ and $\Omega = 39.5\,\mu as$, respectively. Similarly, in Fig.6.2(c), the green and blue lines correspond to $\Omega = 39.4\,\mu as$ and $\Omega = 39.3\,\mu as$, respectively. The blue and green curves in Figs.6.2(a) and 6.2(c) align with the shadow size of $M87^*$ observed by the EHT.

The constraints on the parameter pair (S_0, S_2) are given by (see Table.6.1) $0 \leq S_2/2M \leq 0.09$ and $0 \leq S_2/2M \leq 0.09$, corresponding to $\Omega = 39.1\,\mu as$. Similarly, the constraints on the parameter pair (m_0, m_2) are: $0 \leq 2Mm_0 \leq 0.78$ and $0 \leq 2Mm_0 \leq 0.78$, corresponding to $\Omega = 39.4\,\mu as$.

Thus, $M87^*$ can be modeled within this constrained parameter space as a black hole in quadratic gravity. The numerous possible parameter points within the parameter spaces (S_0, S_2) and (m_0, m_2) indicate that the compatibility of the black hole model in quadratic gravity with $M87^*$ observations makes it a strong candidate for describing astrophysical black holes.

Constraints from Sgr A* : The shadow's angular diameter (Ω) for the $Sgr\ A^*$ black hole, averaged within the range of $49.5\,\mu as$ to $54.1\,\mu as$ with a 1σ region from EHT observations, imposes constraints on the parameter pairs (S_0, S_2) and (m_0, m_2) of the black hole in quadratic gravity as shown in Figs.6.2(b) and 6.2(d).

Here, the shadow's angular diameter (Ω) is expressed as a function of the parameter pairs (S_0, S_2) and (m_0, m_2) (see in Fig.6.2). In Fig.6.2(b), the green and blue lines correspond to $\Omega = 51.4\,\mu as$ and $\Omega = 51.8\,\mu as$, respectively. Similarly, in Fig.6.2(d), the green and blue lines correspond to $\Omega = 52.2\,\mu as$ and $\Omega = 52\,\mu as$, respectively. The blue and green curves in Figs.6.2(b) and 6.2(d) align with the shadow size of $Sgr\ A^*$ observed by the EHT.

The constraints on the parameter pair (S_0, S_2) are given by (See Table.6.1) $0 \leq S_0/2M \leq 0.11$, and $0 \leq S_2/2M \leq 0.11$, corresponding to $\Omega = 51.4\,\mu as$. Similarly, the constraints on the parameter pair (m_0, m_2) are: $0 \leq 2Mm_0 \leq 0.78$ and $0 \leq 2Mm_2 \leq 0.78$, corresponding to $\Omega = 52.2\,\mu as$.

Thus, $Sgr\ A^*$ can be modeled as a black hole in quadratic gravity within this constrained parameter space. The numerous possible parameter points within the parameter spaces (S_0, S_2) and (m_0, m_2) indicate that the compatibility of the black hole model in quadratic gravity with $Sgr\ A^*$ observations makes it a strong candidate for describing astrophysical

black holes.

6.4 Observational Features of Strong Gravitational Lensing

In this section, the phenomenon of strong gravitational lensing is examined in the vicinity of a black hole in quadratic gravity. The goal is to understand how the black hole parameters S_0, S_2, m_0 and m_2 influence the observable outcomes of strong lensing and to compare the lensing behavior of the quadratic gravity black hole with that of the Schwarzschild black hole ($S_0 = 0 = S_2$).

We begin our analysis by considering the strong deflection angle of a light ray within the equatorial plane ($\theta = \frac{\pi}{2}$) of the black hole.

6.4.1 The strong Lensing Angle

At first, we rewrite the metric Eq.(6.2.2) to obtain the strong deflection angle of a light ray in the black hole's equatorial plane ($\theta = \frac{\pi}{2}$) by redefining the quantities r, t, S_0, S_2, m_0 and m_2 to $t \to t/2M$, $r \to r/2M$, $S_0 \to S_0/2M$, $S_2 \to S_2/2M$, $m_0 \to 2Mm_0$ and $m_2 \to 2Mm_2$, respectively to get in units of the radius $2M$. Hence, the quadratic geometric metric Eq.(6.2.2) takes in the equatorial approximation form

$$d\bar{s}^2 = -A(r)dt^2 + B(r)dr^2 + C(r)d\phi^2, \tag{6.4.1}$$

where the metric function can be expressed as

$$A(r) = 1 - \frac{1}{r} + S_0\frac{e^{-m_0 r}}{r} + S_2\frac{e^{-m_2 r}}{r}, \tag{6.4.2}$$

$$B(r) = \frac{1}{1 - \frac{1}{r} - S_0\frac{e^{-m_0 r}}{r}(1 + m_0 r) + \frac{1}{2}S_2\frac{e^{-m_2 r}}{r}(1 + m_2 r)}. \tag{6.4.3}$$

and

$$C(r) = r^2, \tag{6.4.4}$$

respectively. In the strong-field regime gravitational lensing is governed by the interplay between the lens equation and the deflection angle. The geodesic (null) equation is given by

$$\dot{r} = \frac{dr}{d\tau} = \pm\sqrt{\frac{1}{B(r)}\left(\frac{E^2}{A(r)} - \frac{L^2}{r^2}\right)}, \tag{6.4.5}$$

where,

- E = Energy of the particle (constant),
- L = Angular momentum of the particle (constant),
- τ = Affine parameter along the geodesic.

The conditions for unstable circular photon orbit, with radius r_{ph} are $\frac{dV_{eff}}{dr}\Big|_{r_{ph}} = 0$ and $\frac{d^2V_{eff}}{dr^2}\Big|_{r_{ph}} < 0$. Thus, [Adler and Virbhadra (2022), Claudel et al. (2001), and Virbhadra and Ellis (2002)] the radius of the photon sphere, r_{ph} is obtained as the largest real root of the equation below

$$2A(r_{ph}) - r_{ph}A'(r_{ph}) = 0. \tag{6.4.6}$$

When a particle approaches the black hole at the closest possible distance $r = r_0$, where $\frac{dr}{d\tau} = 0$, the minimum impact parameter u_0 can be defined in terms of the closest distance r_0 [Bozza (2002)] as

$$u_0 = \frac{r_0}{\sqrt{A(r_0)}}. \tag{6.4.7}$$

Thus we get the critical impact parameter as

$$u_{ph} = \frac{r_{ph}}{\sqrt{A(r_{ph})}}, \tag{6.4.8}$$

The behavior of the photon sphere radius, r_{ph} and the critical impact parameter, u_{ph}, are expressed as functions of the parameter pairs (S_0, S_2) and (m_0, m_2) (see Figs.6.3 and 6.4). It is observed from Fig.6.3(a) that as the numerical values of the parameters $S_0 > 0$ or $S_2 > 0$ increase while keeping the other parameters fixed, the photon sphere radius r_{ph} decreases. Conversely from Fig.6.3(b), an increase in the values of the parameters $m_0 > 0$ or $m_2 > 0$, with the other parameters held constant, increases the photon sphere radius, r_{ph}. Furthermore, the photon sphere radius r_{ph} reaches its maximum ($r_{ph} = 1.5$) when both $S_0 \to 0$ and $S_2 \to 0$, corresponding to Schwarzschild black hole.

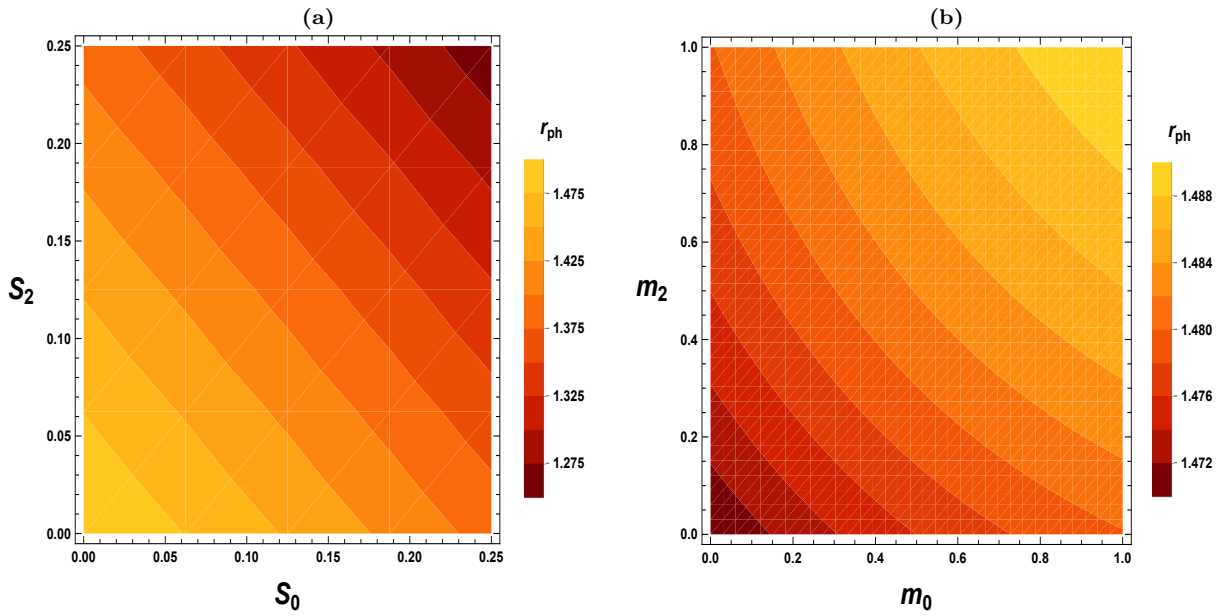

Fig. 6.3. The minimal impact parameter r_{ph} is depicted in terms of the parameters (a) S_0 and S_2, (b) m_0 and m_2.

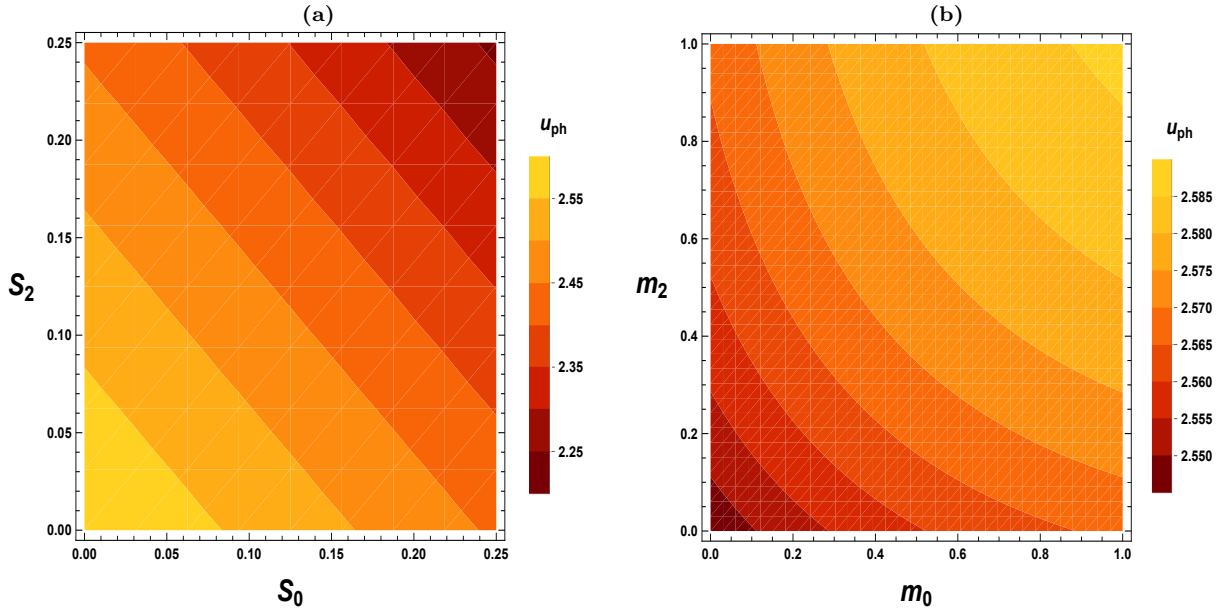

Fig. 6.4. The critical impact parameter u_{ph} is depicted in terms of the parameters (a) S_0 and S_2, (b) m_0 and m_2.

It is also observed from Fig.6.4(a) that as the numerical values of the parameters $S_0 > 0$ or $S_2 > 0$ increase while keeping the other parameters fixed, u_{ph} decreases. Conversely from Fig.6.4(b), an increase in the values of the parameters $m_0 > 0$ or $m_2 > 0$, with the other parameters held constant, results in an increase in u_{ph} (see Table.6.2). Furthermore, u_{ph} reaches its maximum ($u_{ph} = 2.59808$) when both $S_0 \to 0$ and $S_2 \to 0$, corresponding to

Schwarzschild black hole.

The strong deflection angle in the quadratic gravity black hole spacetime can be obtained as a function of the closest possible distance r_0 as [Virbhadra et al. (1998)]

$$\alpha_D(r_0) = I(r_0) - \pi = 2\int_{r_0}^{\infty} \frac{\sqrt{B(r)}dr}{\sqrt{C(r)}\sqrt{\frac{A(r_0)C(r)}{A(r)C(r_0)} - 1}} - \pi. \tag{6.4.9}$$

$\alpha_D(r_0)$, the strong deflection angle is dependent on the relationship between r_0 and r_{ph} and it increases when these two values are approximately equal (i.e., $r_0 \approx r_{ph}$). Hence, we introduce a new variable z defined as [Tsukamoto (2016, 2017)]

$$z = 1 - \frac{r_0}{r}. \tag{6.4.10}$$

When $r_0 \approx r_{ph}$, the deflection angle takes on the following form [Bozza (2002)]

$$\alpha_D(u) = -\bar{a}\ log\left(\frac{u}{u_{ph}} - 1\right) + \bar{b} + \mathcal{O}((u - u_{ph})log(u - u_{ph})), \tag{6.4.11}$$

where,

$$\begin{aligned}\bar{a} \quad = \quad & \left[4e^{(m_0+m_2)r_{ph}}\left((r_{ph}-1)e^{(m_0+m_2)r_{ph}} + S_2e^{m_0r_{ph}} + S_0e^{m_2r_{ph}}\right)\right]^{\frac{1}{2}}\left[\left(-2S_0\left(m_0r_{ph}+1\right)\right.\right. \\ & e^{m_2r_{ph}} + S_2e^{m_0r_{ph}}\left(m_2r_{ph}+1\right) + 2\left(r_{ph}-1\right)e^{(m_0+m_2)r_{ph}}\Big) \\ & \left.\left(m_0S_0\left(m_0r_{ph}+2\right)\left(-e^{m_2r_{ph}}\right) - m_2S_2e^{m_0r_{ph}}\left(m_2r_{ph}+2\right) + 2e^{(m_0+m_2)r_{ph}}\right)\right]^{-\frac{1}{2}}\end{aligned} \tag{6.4.12}$$

and

$$\bar{b} \quad = \quad b + I_R(r_{ph}), \tag{6.4.13}$$

where,

$$b = \bar{a} \times \log\left(-\frac{r_{ph}\left(m_0S_0\left(m_0r_{ph}+2\right)e^{m_2r_{ph}} + m_2S_2e^{m_0r_{ph}}\left(m_2r_{ph}+2\right) - 2e^{(m_0+m_2)r_{ph}}\right)}{\left(r_{ph}-1\right)e^{(m_0+m_2)r_{ph}} + S_2e^{m_0r_{ph}} + S_0e^{m_2r_{ph}}}\right), \tag{6.4.14}$$

$$I_R(r_{ph}) = 2\int_0^1 r_{ph}\left(\left[\sqrt{\frac{B(z)}{C(z)}}\left(\frac{A(r_{ph})}{C(r_{ph})}\frac{C(z)}{A(z)}-1\right)^{-\frac{1}{2}}\frac{1}{(1-z)^2}\right]-\frac{\bar{a}}{z\ r_{ph}}\right)dz, \qquad (6.4.15)$$

where the integral must be evaluated numerically. We numerically calculate the values of u_{ph} and of the strong lensing coefficients $\bar{a}$ and $\bar{b}$ at $r = r_{ph}$ for the quadratic gravity black hole parameters $S_0 = 0, 0.5$, $S_2 = 0, 0.1, 0.2, 0.3$, $m_0 = 0.5, 1$ and $m_2 = 0.3, 0.6, 0.9, 1.1$, respectively. The results are presented in Table.6.2.

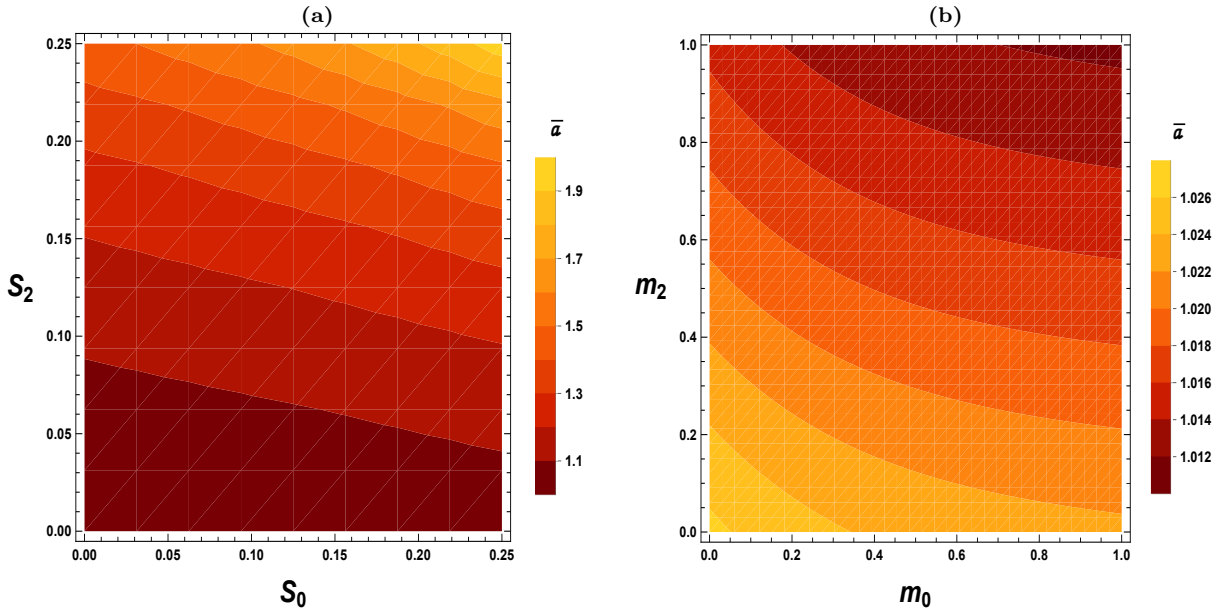

Fig. 6.5. The deflection angle coefficient $\bar{a}$ is depicted in terms of the parameters (a) S_0 and S_2, (b) m_0 and m_2.

The dependency of the lensing coefficients $\bar{a}$ and $\bar{b}$ on the parameter pairs (S_0, S_2) and (m_0, m_2) are depicted in Figs.6.5 and 6.6. Among them, Fig.6.5(a) depicts that as the numerical values of the parameters $S_0 > 0$ or $S_2 > 0$ increase (other parameters kept fixed) the lensing coefficient $\bar{a}$ increases whereas $\bar{a}$ decreases if the numerical values of the parameters $m_0 > 0$ or $m_2 > 0$ increase (other parameters kept fixed) shown in Fig.6.5(b). All the numerical values are exhibited in tabular format (see Table.6.2). The lensing coefficient $\bar{a}$ reaches the minimum value $\bar{a} = 1$ [Bozza (2002)] when both $S_0 \to 0$ and $S_2 \to 0$, corresponding to Schwarzschild black hole. Meanwhile, Fig.6.6(a) depicts that as the numerical values of the parameters $S_0 > 0$ or $S_2 > 0$ increase (other parameters kept fixed) the lensing coefficient $\bar{b}$ initially decreases and attains a minimum value then increases whereas $\bar{b}$ increases if the

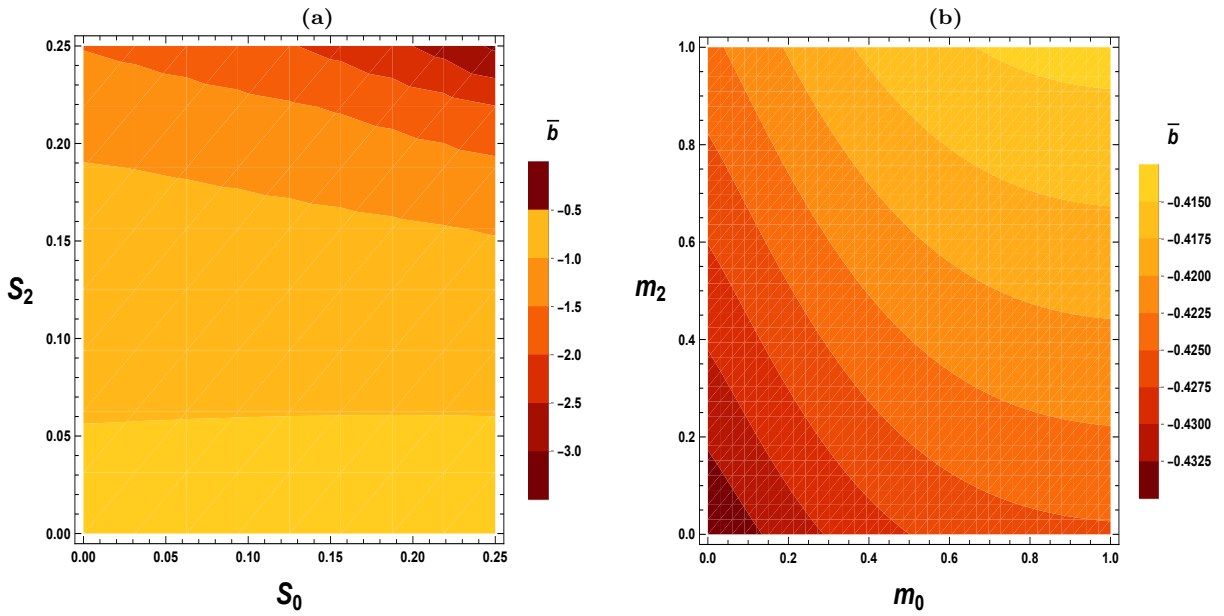

Fig. 6.6. The deflection angle coefficient $\bar{b}$ is presented as a function of the parameters $S_0,\ S_2$ and $m_0,\ m_2$.

numerical values of the parameters $m_0 > 0$ or $m_2 > 0$ increase (other parameters kept fixed) shown in Fig.6.6(b) (see Table.6.2). The lensing coefficient $\bar{b}$ reaches the value $\bar{b} = -0.40023$ [Bozza (2002)] when both $S_0 \to 0$ and $S_2 \to 0$, corresponding to Schwarzschild black hole.

The behavior of α_D, the strong deflection angle, is expressed as a function of the parameter pairs (S_0, S_2) and (m_0, m_2) (see Fig.6.7). It is observed from Fig.6.7(a) depicts that as the numerical values of the parameters $S_0 > 0$ or $S_2 > 0$ increase (other parameters kept fixed) the strong deflection angle α_D increases whereas α_D decreases if the numerical values of the parameters $m_0 > 0$ or $m_2 > 0$ increase (other parameters kept fixed) shown in Fig.6.7(b).

Next it is shown that $\alpha_D \to \infty$ as $u \to u_{ph}$, i.e. α_D gets undoubtedly large when $u \to u_{ph}$. The relationship between α_D and the impact parameter u with respect to the parameter S_0 and S_2 are shown in the Figs.6.7(c) and 6.7(d) respectively, similar impact happens with respect to the parameters m_0 and m_2. These will produce images similar to Figs.6.7(c) and 6.7(d), which is why those figures are not included here.

Furthermore, the strong deflection angle, α_D, in the context of an quadratic gravity black hole is more significant than that of a Schwarzschild black hole. The quadratic gravity black hole, with the presence of parameters S_0, S_2, m_0 and m_2, can significantly intensify the gravitational lensing effect compared to other black holes. From this it can be understood that

the gravitational lensing effect produced by an quadratic gravity black hole is significantly amplified with respect to ordinary astrophysical black holes such as the Schwarzschild black hole ($S_0 = S_2 = 0$). Consequently, we may detect moving fluids and sound waves more quickly near the quadratic gravity black hole aids in differentiating astrophysical ordinary black holes such as the Schwarzschild black hole.

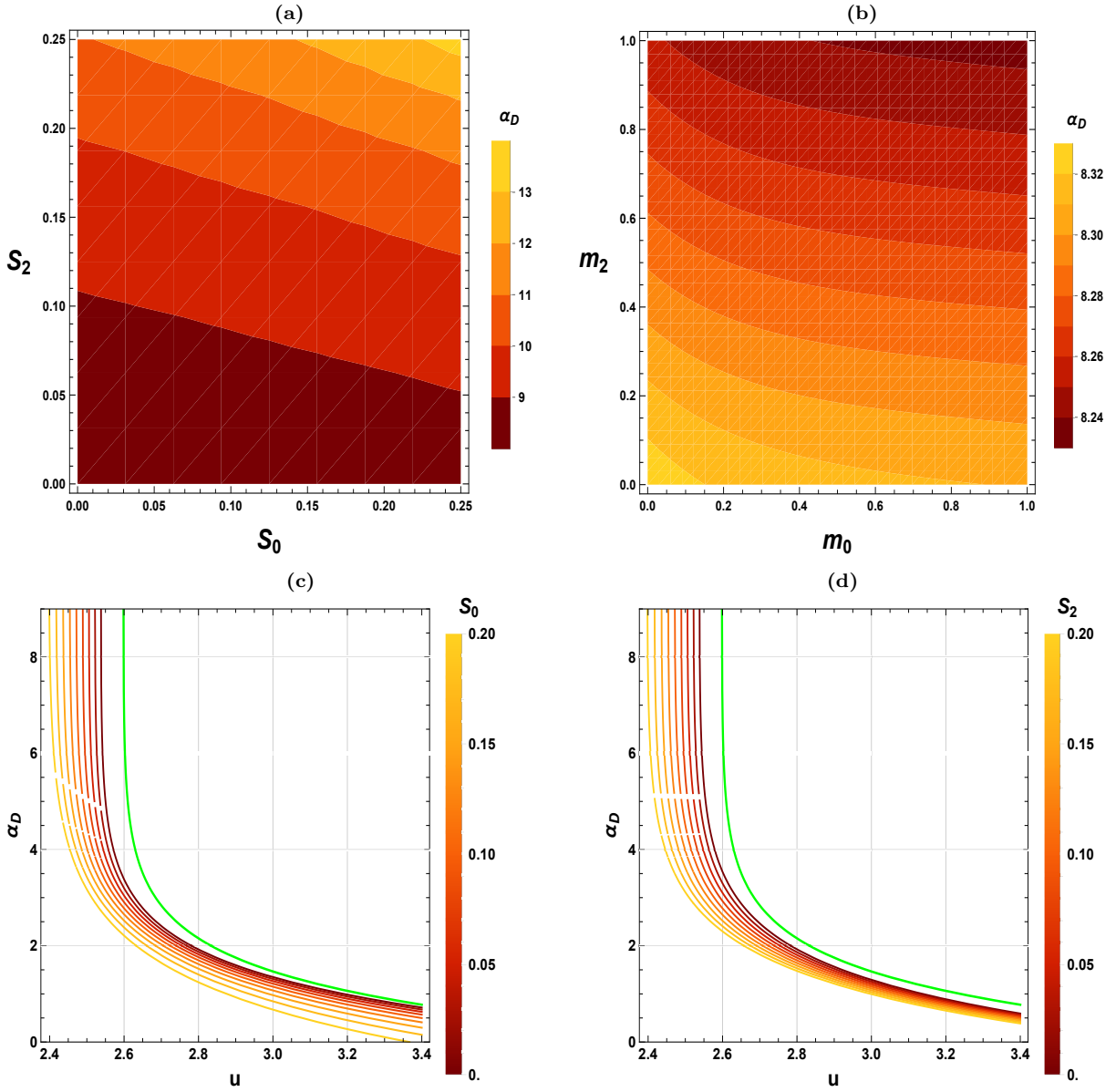

Fig. 6.7. The strong deflection angle α_D is depicted in terms of the parameters (a) S_0 and S_2, (b) m_0 and m_2. Then the relationship between α_D and the impact parameter u is depicted with respect to the parameter (c) S_0 and (d) S_2. In (c), (d) α_D diverges as $u \to r_{ph}$. The green curve corresponds to Schwarzschild black hole ($S_0 = S_2 = 0$).

Table 6.2: Estimation of the strong lensing coefficients for different values of the quadratic gravity black hole parameters $S_0 = 0, 0.1$, $S_2 = 0, 0.1, 0.2, 0.3$, $m_0 = 0.5, 1$ and $m_2 = 0.3, 0.6, 0.9, 1.1$ respectively.

Strong Lensing Coefficients						
S_0	m_0	S_2	m_2	$\bar{a}$	$\bar{b}$	u_{ph}
0		0		1	-0.40023	2.59808
0.1	0.5	0.1	0.3	1.319	-1.00257	2.28715
			0.6	1.27941	-0.882235	2.34857
			0.9	1.25713	-0.821543	2.39032
			1.1	1.24752	-0.800193	2.41006
		0.2	0.3	1.52133	-1.5402	2.09035
			0.6	1.3881	-1.0993	2.21375
			0.9	1.32338	-0.910493	2.30134
			1.1	1.29772	-0.849069	2.34341
		0.3	0.3	2.03915	-3.44553	1.87746
			0.6	1.58237	-1.60264	2.06229
			0.9	1.42174	-1.08157	2.20068
			1.1	1.36647	-0.936446	2.26848
	1.0	0.1	0.3	1.20153	-0.753994	2.35682
			0.6	1.17352	-0.675696	2.41898
			0.9	1.15807	-0.638187	2.46065
			1.1	1.15139	-0.626371	2.48013
		0.2	0.3	1.33508	-1.04248	2.16208
			0.6	1.24902	-0.78693	2.28751
			0.9	1.20606	-0.676661	2.37513
			1.1	1.18869	-0.643378	2.41666
		0.3	0.3	1.61347	-1.84353	1.95072
			0.6	1.37237	-1.02851	2.13973
			0.9	1.27383	-0.753786	2.27858
			1.1	1.23801	-0.678277	2.34553

6.4.2 Lensing Observables

Let's explore the observable features of strong gravitational lensing here. In this analysis, we assume that both the source and the observer are located far from the black hole (acting as the lens) with near-perfect coordination. Furthermore, the source is assumed to lie directly behind the black hole. Under these conditions, the lens equation is expressed as [Bozza et al. (2001)]

$$\beta = \theta - \frac{D_{ls}}{D_{os}}\Delta\alpha_n. \tag{6.4.16}$$

where, the offset deflection angle is denoted by $\Delta\alpha_n = \alpha_D(\theta) - 2n\pi$ with the primary deflection angle represented by $\alpha_D(\theta)$ and the number of orbits or complete revolutions a photon makes around the black hole is denoted by n. Where, the angular separations between the lens (black hole) and the source and between the image and the source are denoted by the angles β and θ, respectively and the distances between the source-observer, observer-lens and lens-source are denoted by D_{os}, D_{ol} and D_{ls} respectively resulting the relation $D_{os} = D_{ol} + D_{ls}$.

From Eqs.(6.4.11) and (6.4.16), the angular separation between the black hole (lens) and the n^{th} relativistic image is given by

$$\theta_n = \theta_n^0 - \frac{u_{ph}e_n(\theta_n^0 - \beta)D_{os}}{\bar{a}D_{ol}D_{ls}}. \tag{6.4.17}$$

Here, $\theta_n^0 = \frac{u_{ph}(1+e_n)}{D_{ol}}$, the angular position of the image corresponding to a photon completing $2n\pi$ rotational movements around the black hole (lens) and $e_n = e^{\frac{\bar{b}-2n\pi}{\bar{a}}}$. In the framework of strong gravitational lensing, where the brightness of the surface remains preserved, magnification of the relativistic effect is specified as the ratio of the solid angle subtended by the n^{th} image to that [Virbhadra and Ellis (2000)].

The magnification for the n^{th} relativistic image is given by [Bozza (2002)]

$$\mu_n = \left(\frac{\beta}{\theta}\frac{d\beta}{d\theta}\right)^{-1}\Bigg|_{\theta_n^0} = \frac{u_{ph}^2(1+e_n)e_nD_{os}}{\beta\ \bar{a}D_{ls}D_{ol}^2}. \tag{6.4.18}$$

This indicates that the first relativistic image exhibits the highest brightness, with the magnification exponentially decreasing as n increases. This implies the brightness of the first image is stronger comparing to the other subsequent relativistic images. Moreover,

Eq.(6.4.18) becomes unbounded as $\beta \to 0$, implying the enhancement of the chances of detecting relativistic images due to perfect alignment.

We focus on the scenario where the brightest image means the outermost image at θ_1, is resolved as a distinct image, while the remaining inner images cluster near θ_∞, defined as $\theta_n | n \to \infty := \theta\infty$. Using the deflection angle from Eq.(6.4.11), one can derive key strong lensing observables, including the angular position of the image cluster at θ_∞, the angular separation S between the outermost and innermost images and the relative magnification r_{mag} between the inner and outermost relativistic images. These quantities are given as [Bozza (2002) and Kumar et al. (2022b)]

$$\theta_\infty = \frac{u_{ph}}{D_{ol}}, \tag{6.4.19}$$

$$X = \theta_1 - \theta_\infty \approx \theta_\infty e^{\frac{(\bar{b}-2\pi)}{\bar{a}}}, \tag{6.4.20}$$

$$r_{mag} = \frac{\mu_1}{\Sigma_{n=2}^{\infty}\mu_n} \approx \frac{5\pi}{\bar{a}\ log(10)}. \tag{6.4.21}$$

If the strong lensing observables θ_∞, X and r_{mag} are determined from observations, the lensing coefficients $\bar{a}$, $\bar{b}$ and u_{ph} can be computed by inverting Eqs.(6.4.19), (6.4.20) and (6.4.21), respectively. Additionally, the observed data can be compared with the corresponding theoretical predictions. These results enable the identification and distinction of the quadratic gravity black hole from a Schwarzschild black hole.

Lensing Observables and the Quadratic Gravity Black Hole Parameters : Considering the supermassive black holes $M87^*$ and $Sgr\ A^*$ in the center of the nearby galaxies, we numerically obtain the observable quantities θ_∞, X and r_{mag} for the quadratic gravity black hole (see Table.6.3). The mass and distance from the earth for $M87^*$ [Akiyama et al. (2019)] are $M \approx 6.5 \times 10^9 M_\odot$, $D_{ol} \approx 16.8 Mpc$, for $Sgr\ A^*$ are $M \approx 4.28 \times 10^6 M_\odot$,$D_{ol} \approx 8.32 kpc$ [Gillessen et al. (2017)]. The behavior of the observable quantities θ_∞, X and r_{mag} for $M87^*$ and $Sgr\ A^*$ are expressed as functions of the parameter pairs (S_0, S_2) and (m_0, m_2) (see Figs.6.8, 6.9 and 6.10). It is observed from Fig.6.8 that as the numerical values of the parameters $S_0 > 0$ or $S_2 > 0$ increase while keeping the other parameters fixed, the observable quantity θ_∞ decreases.

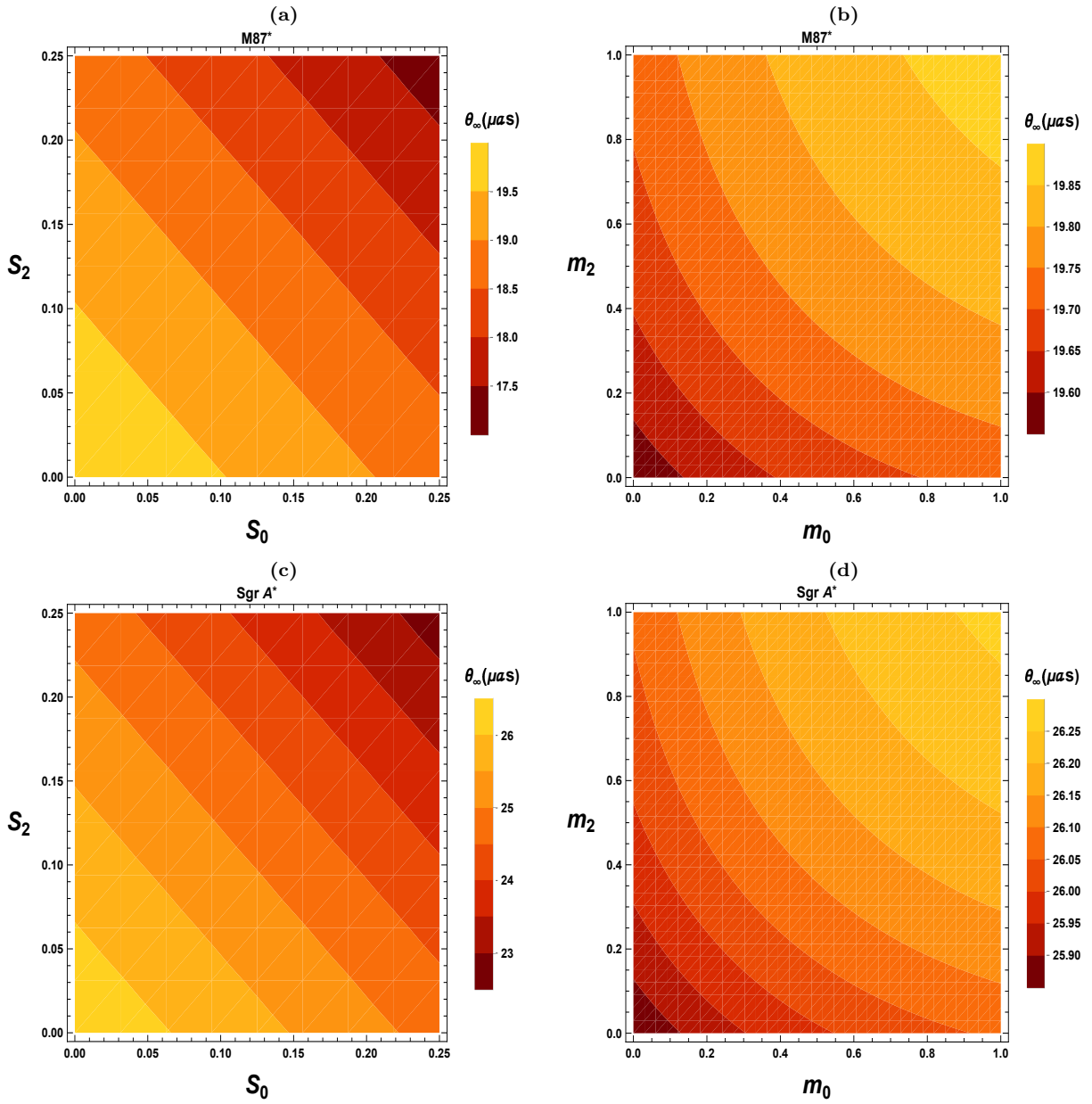

Fig. 6.8. The angular position of the images θ_∞ is depicted in terms of the parameters (a) S_0 and S_2, (b) m_0 and m_2 for $M87^*$ and similarly θ_∞ is depicted in terms of the parameters (c) S_0 and S_2, (d) m_0 and m_2 for $Sgr\ A^*$.

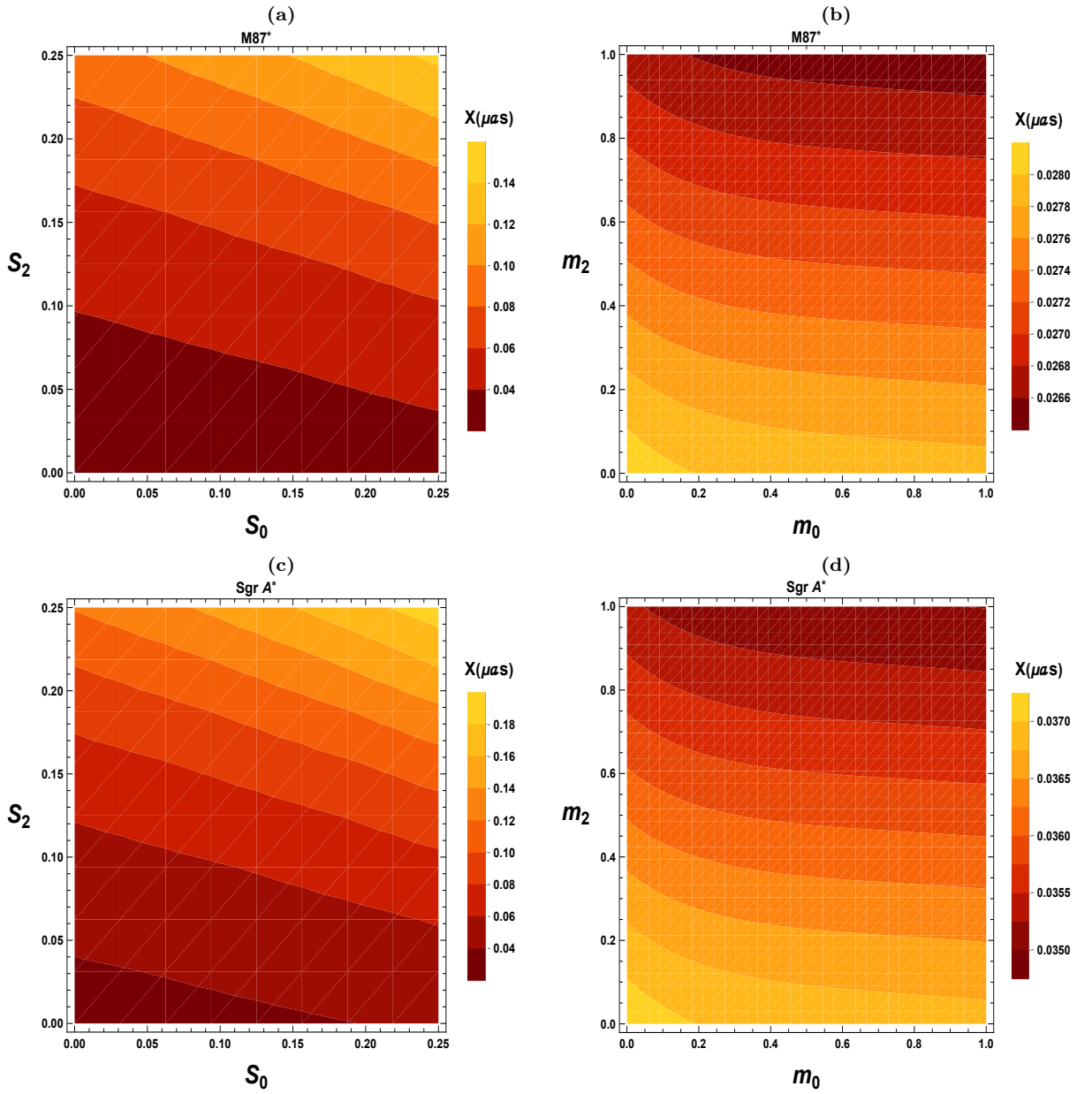

Fig. 6.9. The angular separation of the images $X(\mu as)$ is depicted in terms of the parameters (a) S_0 and S_2, (b) m_0 and m_2 for $M87^*$ and similarly $X(\mu as)$ is depicted in terms of the parameters (c) S_0 and S_2, (d) m_0 and m_2 for $Sgr\ A^*$.

Table 6.3: Estimation of the strong lensing observables for $M87^*$, $Sgr\ A^*$ for different values parameters $S_0 = 0.1$, $m_0 = 0.5, 1$, $m_2 = 0.3, 0.6, 0.9, 1.1$ and $S_2 = 0.1, 0.2, 0.3$ respectively. The observable quantity r_{mag} does not depend on the mass or the distance of the black hole from the observer.

Parameters				$M87^*$		$Sgr\ A^*$		$M87^*$,$Sgr\ A^*$
S_0	m_0	S_2	m_2	$\theta_\infty(\mu as)$	$X(\mu as)$	$\theta_\infty(\mu as)$	$X(\mu as)$	r_{mag}
0		0		19.9632	0.0249839	26.3826	0.0330177	6.82188
0.1	0.5	0.1	0.3	17.5741	0.0702727	23.2252	0.0928695	5.17023
			0.6	18.0461	0.0666955	23.849	0.0881421	5.33203
			0.9	18.3668	0.0645049	24.2729	0.085247	5.42657
			1.1	18.5185	0.0633437	24.4733	0.0837124	5.46834
		0.2	0.3	16.0619	0.0938527	21.2268	0.124032	4.48417
			0.6	17.0101	0.0833594	22.4799	0.110164	4.91454
			0.9	17.6831	0.0770561	23.3693	0.101834	5.15489
			1.1	18.0064	0.0738842	23.7965	0.0976423	5.25682
		0.3	0.3	14.4262	0.12222	19.065	0.161522	3.34546
			0.6	15.8463	0.108542	20.9418	0.143445	4.31118
			0.9	16.9097	0.0951575	22.3472	0.125756	4.79827
			1.1	17.4306	0.0884627	23.0356	0.116909	4.99233
	1.0	0.1	0.3	18.1094	0.0517972	23.9327	0.068453	5.67767
			0.6	18.5871	0.0494169	24.5639	0.0653073	5.81319
			0.9	18.9073	0.0479746	24.987	0.0634013	5.89072
			1.1	19.0569	0.0471875	25.1849	0.0623611	5.92491
		0.2	0.3	16.6131	0.068777	21.9552	0.0908929	5.10973
			0.6	17.5769	0.0611796	23.2289	0.0808525	5.46178
			0.9	18.2502	0.0568936	24.1187	0.0751882	5.65635
			1.1	18.5693	0.0547179	24.5404	0.072313	5.73901
		0.3	0.3	14.9891	0.0973464	19.8089	0.128649	4.22809
			0.6	16.4413	0.079819	21.7282	0.105486	4.97088
			0.9	17.5083	0.0698379	23.1383	0.0922948	5.3554
			1.1	18.0227	0.065123	23.8181	0.0860639	5.51037

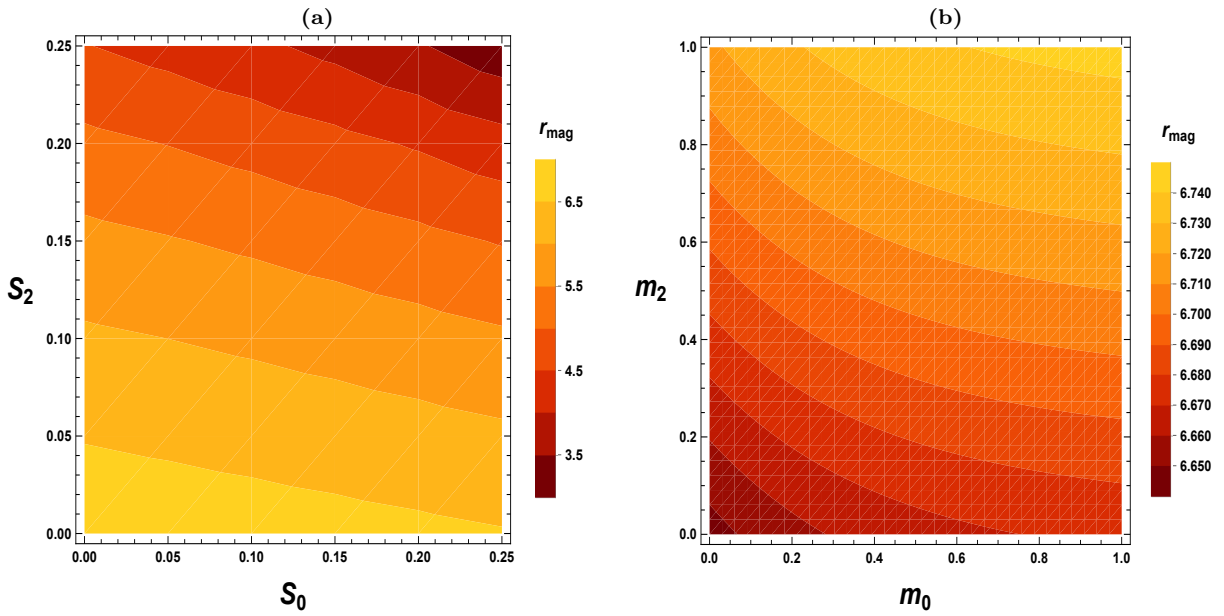

Fig. 6.10. The relative magnification of the images r_{mag} is depicted in terms of the parameters (a) S_0 and S_2, (b) m_0 and m_2.

Similarly, an increase in the values of the parameters $m_0 > 0$ or $m_2 > 0$, with the other parameters held constant, also increases the value of the observable quantity θ_∞ (see Table.6.3). The observable quantity θ_∞ reaches the maximum value when both $S_0 \to 0$ and $S_2 \to 0$, corresponding to Schwarzschild black hole.

Furthermore, Fig.6.9 shows that as the numerical values of the parameters $S_0 > 0$ or $S_2 > 0$ increase, while keeping the other parameters fixed, X increases. Conversely, an increase in the values of the parameters $m_0 > 0$ or $m_2 > 0$, with the other parameters held constant, results in a decrease in the value of the observable quantity X (see Table.6.3). The observable quantity X reaches the minimum value when both $S_0 \to 0$ and $S_2 \to 0$, corresponding to Schwarzschild black hole.

It is also observed from Fig.6.10 that as the numerical values of the parameters $S_0 > 0$ or $S_2 > 0$ increase while keeping the other parameters fixed, the observable quantity r_{mag} decreases. Similarly, an increase in the values of the parameters $m_0 > 0$ or $m_2 > 0$, with the other parameters held constant, also increases the value of the observable quantity r_{mag} (see Table.6.3). The observable quantity r_{mag} reaches the maximum value when $S_0 \to 0$ and $S_2 \to 0$ correspond to Schwarzschild's black hole.

It is also observed that the relative magnification r_{mag} of the relativistic images remains independent of the black hole's mass and distance.

6.4.3 Einstein Rings

When the source, the black hole (lens) and the observer are perfectly aligned, corresponding to $\beta = 0$, the black hole deflects light rays in all directions, producing a ring-shaped image.

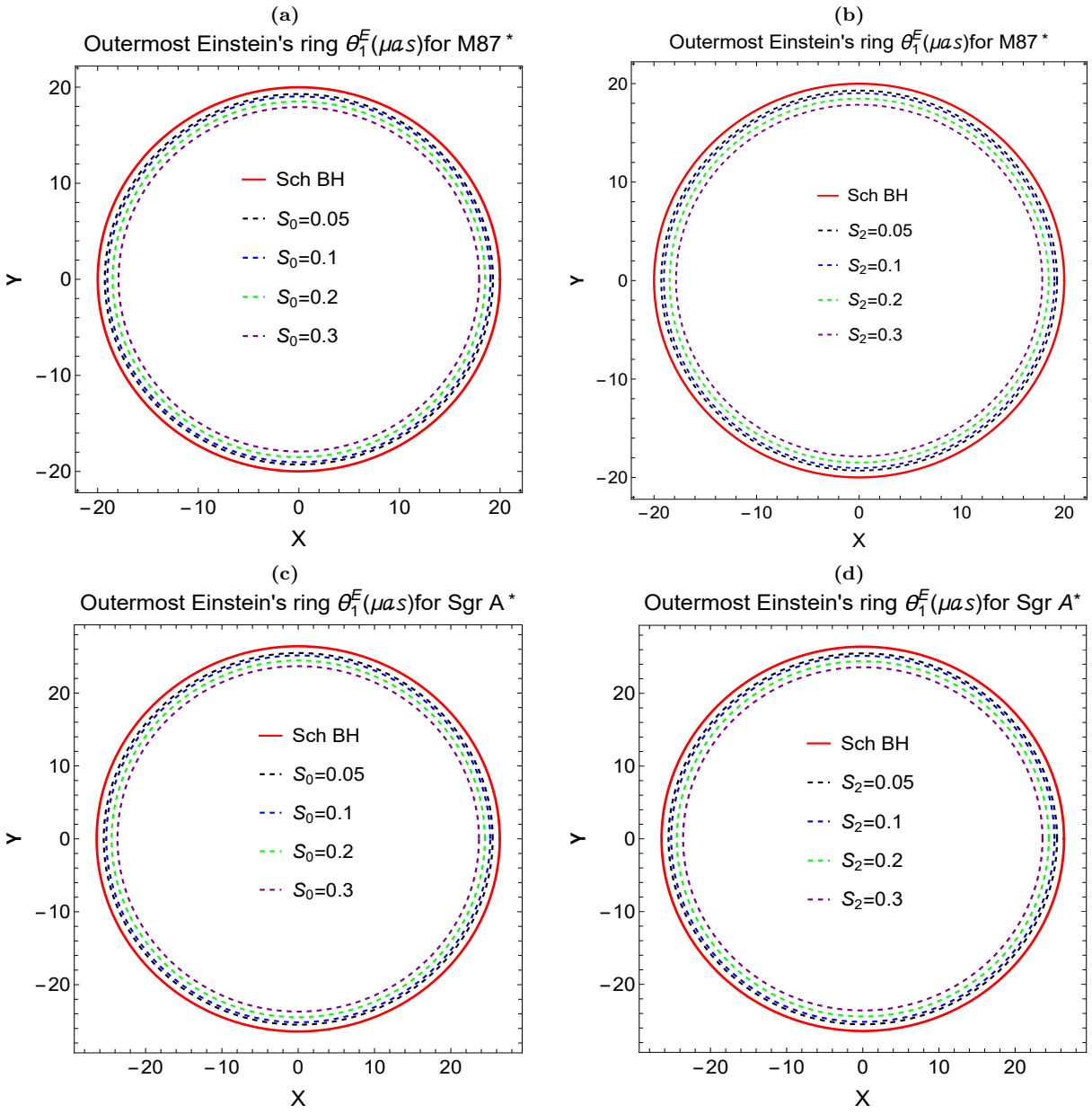

Fig. 6.11. The outermost Einstein ring θ_1^E (μas) is depicted in the X-Y plane in terms of the parameters (a) S_0, (b) S_2 for $M87^*$ and similarly θ_1^E (μas) is depicted in terms of the parameters (c) S_0, (d) S_2 for $Sgr\ A^*$.

This phenomenon, known as the Einstein ring, has been extensively studied in [Bartelmann and Schneider (2001), Einstein (1936), Guzik et al. (2010), Liebes (1964), Mellier (1999), and Schmidt (2008)]. By simplifying Eq.(6.4.17) for $\beta = 0$, the angular radius of

the n^{th} relativistic image can be expressed as

$$\theta_n = \theta_n^0\left(1 - \frac{u_{ph}e_n D_{os}}{\bar{a}D_{ls}D_{ol}}\right). \tag{6.4.22}$$

In the scenario where the black hole (lens) is positioned at a distance halfway between the source and the observer, denoted as $D_{os} = 2D_{ol}$ and assuming that $D_{ol} \gg u_{ph}$, the angular radius of the n^{th} relativistic Einstein ring within the spacetime of an quadratic gravity black hole can be expressed as follows

$$\theta_n^E = \frac{u_{ph}(1+e_n)}{D_{ol}}. \tag{6.4.23}$$

The angular radius θ_1^E represents the outermost Einstein ring, as displayed in Fig.6.11 for $M87^*$ and $Sgr\ A^*$. From Fig.6.11, it is observed that the angular radius θ_1^E of the outermost Einstein ring decreases with the increasing value of the parameter S_0 or parameter S_2. From Fig.6.11, it is also evident that the angular radius θ_1^E of the outermost Einstein ring for the quadratic gravity black hole is smaller than the corresponding angular radius of the Schwarzschild black hole.

6.4.4 Time Delay in the Strong Field Limit

Time delay is one of the most significant observables in the strong gravitational lensing effect. It arises from the time difference between the formation of two relativistic images. This time difference occurs because the photon traverses different paths around the black hole. Since the travel time for photon paths associated with distinct relativistic images is different, a time difference exists between these images. If the time signals from two relativistic images are obtained through observations, one can calculate the time delay between the two signals [Bozza and Mancini (2004)]. The time taken by a photon to orbit the black hole is given by [Bozza and Mancini (2004)]

$$\tilde{T} = \tilde{a}\log\left(\frac{u}{u_{ph}} - 1\right) + \tilde{b} + \mathcal{O}(u - u_{ph}). \tag{6.4.24}$$

Using the above Eq.(6.4.24), one can calculate the time difference between two relativistic images. In the context of a spherically symmetric static black hole spacetime, the time delay

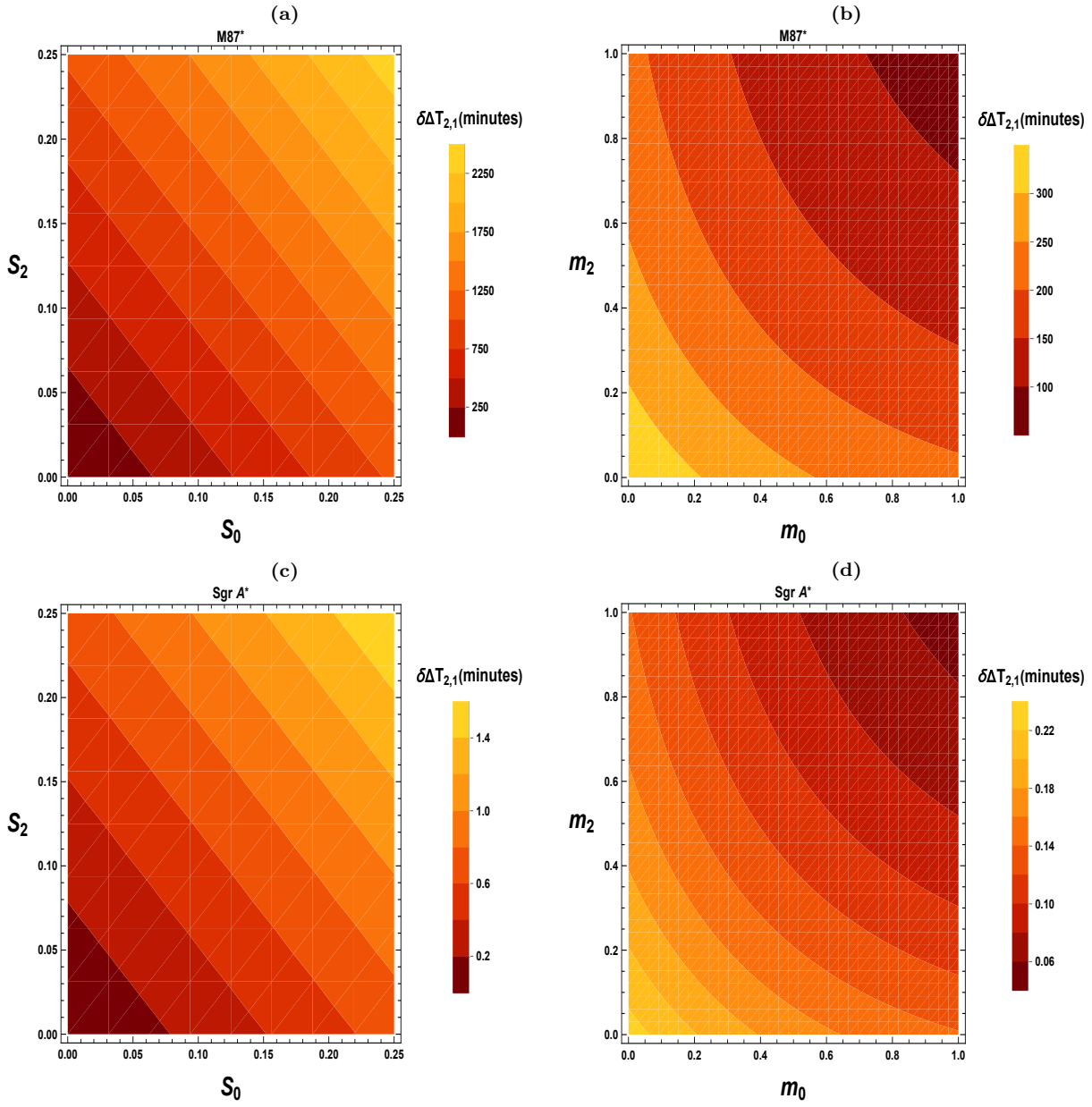

Fig. 6.12. The deviation of the time delays between the first and second relativistic images, for the quadratic gravity black hole from Schwarzschild black hole $\delta\Delta T_{2,1} = \Delta T_{2,1}^{Sch} - \Delta T_{2,1}^{ASGQ}$minutes is presented as a function of the parameters $S_0,\ S_2$ and $m_0,\ m_2$.

Table 6.4: Estimation of the time delay for various supermassive black holes for the Schwarzschild metric and for the quadratic gravity black holes, respectively. The masses are expressed in Solar Masses and the distances are expressed in Mpc units [Kormendy and Ho (2013)]. The time delays $\Delta T_{2,1}$ are estimated in minutes.

Galaxy	$M(M_\odot)$	$D_{ol}(Mpc)$	$\Delta T_{2,1}$ Schwarzschild black hole ($S_0 = S_2 = 0$)	$\Delta T_{2,1}$ ASQG Black Hole ($S_0 = S_2 = 0.1$, $m_0 = m_2 = 1$)
NGC 4395	3.6×10^5	4.3	0.962522	0.915472
Milky Way	4.3×10^6	0.0083	11.4968	10.9348
NGC 7457	8.95×10^6	12.53	23.9294	22.7596
NGC 4486A	1.44×10^7	18.36	38.5009	36.6189
NGC 2778	1.45×10^7	23.44	38.7682	36.8732
NGC 3607	1.37×10^8	22.65	366.293	348.388
NGC 4026	1.80×10^8	13.35	481.261	457.736
NGC 5576	2.73×10^8	25.68	729.912	694.233
NGC 7052	3.96×10^8	70.4	1058.77	1007.02
NGC 3379	4.16×10^8	10.70	1112.25	1057.88
NGC 4261	5.29×10^8	32.36	1414.37	1345.23
NGC 6251	6.14×10^8	108.4	1641.63	1561.39
NGC 5077	8.55×10^8	38.7	2285.99	2174.25
NGC 7768	1.34×10^9	116.0	3582.72	3407.59
NGC 6861	2.10×10^9	28.71	5614.71	5340.25
NGC 4751	2.44×10^9	32.81	6523.76	6204.86
Cygnus A	2.66×10^9	242.7	7111.95	6764.32
NGC 5516	3.69×10^9	55.3	9865.85	9383.59
NGC 4649	4.72×10^9	16.46	12619.7	12002.9
M87	6.5×10^9	16.68	17378.9	16529.4
NGC 3842	9.09×10^9	92.2	24303.7	23115.7

between two relativistic images, when both images are on the same side of the black hole, is expressed as follows

$$\Delta T_{2,1} = 2\pi u_{ph} = 2\pi D_{ol}\theta_{\infty}. \tag{6.4.25}$$

Using the above Eq.(6.4.25), the time delays for a Schwarzschild black hole ($S_0 = S_2 = 0$) and the quadratic gravity black hole, with $S_0 = S_2 = 0.1$ and $m_0 = m_2 = 1$ have been estimated in Table.6.4 for several supermassive black holes located in the centers of nearby galaxies. The deviation of the time delays between the first and second relativistic images, for the quadratic gravity black hole from Schwarzschild black hole $\delta\Delta T_{2,1} = \Delta T_{2,1}^{Sch} - \Delta T_{2,1}^{ASQG}$minutes with $S_0 = S_2 = 0.1$ and $m_0 = m_2 = 1$ has been displayed for the cases of $M87^*$ and $Sgr\ A^*$ in Fig.6.12. This figure shows that as the numerical values of the parameters $S_0 > 0$ or $S_2 > 0$ increase while keeping the other parameters fixed, $\delta\Delta T_{2,1}$ increases. Conversely, an increase in the values of the parameters $m_0 > 0$ or $m_2 > 0$, with the other parameters held constant, decreases the value of the observable quantity $\delta\Delta T_{2,1}$.

6.4.5 Results and Discussions

Using observations of strong gravitational fields, we have applied the methodology introduced by Bozza (2002) to distinguish between various types of spherically symmetric black holes and investigate their astrophysical implications, particularly for supermassive black holes located at the centers of nearby galaxies. This methodology has been extensively employed to test the key properties of quadratic gravity black holes and compare them with the standard Schwarzschild general relativity solution. In our analysis, we investigated several key aspects of astrophysical relevance. First, we computed the strong lensing coefficients $\bar{a}$, $\bar{b}$ and u_{ph} (see Table.6.2). Utilizing these coefficients, we derived the strong deflection angle along with several observable quantities such as the angular position of the innermost image θ_{∞}, the image separation X and the magnification ratio r_{mag}, specifically for $M87^*$ and $Sgr\ A^*$ (see Table.6.3). Furthermore, we examined the time delay between relativistic images (see Table.6.4) for multiple supermassive black holes located at the centers of nearby galaxies.

Angular position θ_∞ for the set of images: We have numerically determined the angular positions of the relativistic images for various supermassive black holes within the quadratic gravity framework. The results for $M87^*$ and $Sgr\ A^*$ are summarized in Table.6.5.

Table 6.5: Admissible range for the angular position of the innermost relativistic images θ_∞, is analyzed for $M87^*$ and $Sgr\ A^*$. This range is determined for varying values of the quadratic gravity black hole parameters S_2, m_0 and m_2 while keeping the parameter S_0 constant.

SMBH	S_0	m_0	S_2	m_2	$\theta_\infty\ (\mu as)$
$M87^*$	0.1	0.5	0.1	$0.3 \leq m_2 \leq 1.1$	$\theta_\infty \in (17.57, 18.52)$
$Sgr\ A^*$	0.1	0.5	0.1	$0.3 \leq m_2 \leq 1.1$	$\theta_\infty \in (23.22, 24.48)$
$M87^*$	0.1	0.5	0.2	$0.3 \leq m_2 \leq 1.1$	$\theta_\infty \in (16.06, 18.01)$
$Sgr\ A^*$	0.1	0.5	0.2	$0.3 \leq m_2 \leq 1.1$	$\theta_\infty \in (21.22, 23.80)$
$M87^*$	0.1	0.5	0.3	$0.3 \leq m_2 \leq 1.1$	$\theta_\infty \in (14.42, 17.44)$
$Sgr\ A^*$	0.1	0.5	0.3	$0.3 \leq m_2 \leq 1.1$	$\theta_\infty \in (19.06, 23.04)$
$M87^*$	0.1	1	0.1	$0.3 \leq m_2 \leq 1.1$	$\theta_\infty \in (18.10, 19.06)$
$Sgr\ A^*$	0.1	1	0.1	$0.3 \leq m_2 \leq 1.1$	$\theta_\infty \in (23.93, 25.19)$
$M87^*$	0.1	1	0.2	$0.3 \leq m_2 \leq 1.1$	$\theta_\infty \in (16.61, 18.57)$
$Sgr\ A^*$	0.1	1	0.2	$0.3 \leq m_2 \leq 1.1$	$\theta_\infty \in (21.95, 24.55)$
$M87^*$	0.1	1	0.3	$0.3 \leq m_2 \leq 1.1$	$\theta_\infty \in (14.98, 18.03)$
$Sgr\ A^*$	0.1	1	0.3	$0.3 \leq m_2 \leq 1.1$	$\theta_\infty \in (19.80, 23.82)$

As one can see from Tables.6.2 and 6.5, the angular position of the innermost relativistic images θ_∞ depends on the values of the quadratic gravity black hole parameters S_2, m_0 and m_2. An increase in the value of m_2 from 0.3 to 1.1 will lead, for the black holes $M87^*$ and $Sgr\ A^*$, to an increase in θ_∞ for fixed values of the remaining parameters, while θ_∞ decreases with an increase in the parameter S_2 from 0.1 to 0.3, assuming the other parameters are fixed. Furthermore, considering the same mass and distance of the black hole, it is observed that the angular position of the innermost relativistic images θ_∞ for the quadratic gravity black hole is smaller than that in the case of a Schwarzschild black hole. Consequently, the fundamental quadratic gravity has a significant effect on the potentially observable angular positions of the images θ_∞, enabling a distinction between these images and those associated with other classical black holes.

The Angular Separation: We have numerically obtained the angular separation between the outermost and innermost relativistic images X for $M87^*$ and $Sgr\ A^*$ within the framework of quadratic gravity, as summarized in Table.6.6.

Table 6.6: Admissible range for the angular separation between outermost and innermost relativistic images X, is analyzed for $M87^*$ and $Sgr\ A^*$. This range is determined for varying values of the quadratic gravity parameters S_2, m_0 and m_2 while keeping the parameter S_0 constant.

SMBH	S_0	m_0	S_2	m_2	$X\ (\mu as)$
$M87^*$	0.1	0.5	0.1	$0.3 \leq m_2 \leq 1.1$	$X \in (0.06, 0.08)$
$Sgr\ A^*$	0.1	0.5	0.1	$0.3 \leq m_2 \leq 1.1$	$X \in (0.08, 0.10)$
$M87^*$	0.1	0.5	0.2	$0.3 \leq m_2 \leq 1.1$	$X \in (0.07, 0.10)$
$Sgr\ A^*$	0.1	0.5	0.2	$0.3 \leq m_2 \leq 1.1$	$X \in (0.09, 0.13)$
$M87^*$	0.1	0.5	0.3	$0.3 \leq m_2 \leq 1.1$	$X \in (0.08, 0.13)$
$Sgr\ A^*$	0.1	0.5	0.3	$0.3 \leq m_2 \leq 1.1$	$X \in (0.11, 0.17)$
$M87^*$	0.1	1	0.1	$0.3 \leq m_2 \leq 1.1$	$X \in (0.04, 0.06)$
$Sgr\ A^*$	0.1	1	0.1	$0.3 \leq m_2 \leq 1.1$	$X \in (0.06, 0.07)$
$M87^*$	0.1	1	0.2	$0.3 \leq m_2 \leq 1.1$	$X \in (0.05, 0.07)$
$Sgr\ A^*$	0.1	1	0.2	$0.3 \leq m_2 \leq 1.1$	$X \in (0.07, 0.10)$
$M87^*$	0.1	1	0.3	$0.3 \leq m_2 \leq 1.1$	$X \in (0.06, 0.10)$
$Sgr\ A^*$	0.1	1	0.3	$0.3 \leq m_2 \leq 1.1$	$X \in (0.08, 0.13)$

As one can see from Tables.6.2 and 6.6, the angular separation between outermost and innermost relativistic images X depends on the values of the quadratic gravity black hole parameters S_2, m_0 and m_2. An increase in the value of m_2 from 0.3 to 1.1 will lead, for the black holes $M87^*$ and $Sgr\ A^*$, to a decrease in X for fixed values of the remaining parameters, while X increases with an increase in the parameter S_2 from 0.1 to 0.3, assuming the other parameters are fixed. Furthermore, considering the same mass and distance of the black hole, it is observed that the angular separation between outermost and innermost relativistic images X for the quadratic gravity black hole is larger than that in the case of a Schwarzschild black hole. Consequently, the fundamental quadratic gravity has a significant effect on the potentially observable angular separation between the outermost and innermost relativistic images X, enabling a distinction between these images and those associated with other classical black holes.

Relative Magnification: We have numerically obtained the relative magnification of the relativistic images r_{mag} for $M87^*$ and $Sgr\ A^*$ within the framework of quadratic gravity, as summarized in Table.6.7.

Table 6.7: Admissible range for r_{mag}, is analyzed for $M87^*$ and $Sgr\ A^*$. This range is determined for varying values of the quadratic gravity parameters S_2, m_0 and m_2 while keeping the parameter S_0 constant.

SMBH	S_0	m_0	S_2	m_2	r_{mag} magnitude
$M87^*$,$Sgr\ A^*$	0.1	0.5	0.1	$0.3 \leq m_2 \leq 1.1$	$r_{mag} \in (5.17, 5.47)$
$M87^*$,$Sgr\ A^*$	0.1	0.5	0.2	$0.3 \leq m_2 \leq 1.1$	$r_{mag} \in (4.48, 5.26)$
$M87^*$,$Sgr\ A^*$	0.1	0.5	0.3	$0.3 \leq m_2 \leq 1.1$	$r_{mag} \in (3.34, 5.00)$
$M87^*$,$Sgr\ A^*$	0.1	1	0.1	$0.3 \leq m_2 \leq 1.1$	$r_{mag} \in (5.67, 5.93)$
$M87^*$,$Sgr\ A^*$	0.1	1	0.2	$0.3 \leq m_2 \leq 1.1$	$r_{mag} \in (5.10, 5.74)$
$M87^*$,$Sgr\ A^*$	0.1	1	0.3	$0.3 \leq m_2 \leq 1.1$	$r_{mag} \in (4.22, 5.52)$

As illustrated in Tables.6.2 and 6.7, the relative magnification of the relativistic images, denoted as r_{mag}, is influenced by the parameters of the quadratic gravity black hole, specifically S_2, m_0 and m_2. Increasing the value of m_2 from 0.3 to 1.1 results in a corresponding rise in r_{mag} for $M87^*$ and $Sgr\ A^*$, assuming the other parameters remain constant. Conversely, r_{mag} decreases as the parameter S_2 increases from 0.1 to 0.3, again with other parameters held fixed.

Moreover, when comparing black holes of the same mass and distance, it is found that the relative magnification r_{mag} for the quadratic gravity black hole is less than that for a Schwarzschild black hole. This indicates that the fundamental aspects of quadratic gravity significantly affect the observable relative magnification of the relativistic images, allowing for differentiation between these images and those linked to other classical black holes. It is also important to note that the relative magnification of the relativistic images is independent of the black hole's mass or distance.

The Einstein Rings: For $M87^*$ and $Sgr\ A^*$, the outermost Einstein rings θ_1^E are presented in Figs.6.11(a) and 6.11(c) for the parameter values $m_0 = m_2 = 1$, $S_2 = 0.1$ and $S_0 = 0, 0.05, 0.1, 0.2,\ \&\ 0.3$. Additionally, the cases with $m_0 = m_2 = 1$, $S_0 = 0.1$ and $S_2 = 0, 0.05, 0.1, 0.2,\ \&\ 0.3$ are shown in Figs.6.11(b) and 6.11(d). Our findings indicate that the radius of the outermost Einstein ring, θ_1^E, decreases as the values of the quadratic gravity black hole parameters S_0 or S_2 increase while keeping the remaining parameters

fixed. Notably, the Einstein ring θ_1^E for an quadratic gravity black hole is significantly smaller than that of the standard classical Schwarzschild black hole ($S_0 = S_2 = 0$).

Relativistic Time Delay: We have also evaluated the time delays $\Delta T_{2,1}$ between the first and second-order relativistic images for various supermassive black holes within the framework of the quadratic gravity black hole, using the parameter values ($S_0 = S_2 = 0.1$, $m_0 = m_2 = 1$), as well as for the Schwarzschild black hole ($S_0 = S_2 = 0$). The time delay $\Delta T_{2,1}$ for the quadratic gravity black hole (e.g., ~ 23115.7 minutes for NGC 3842) is significantly smaller compared to the Schwarzschild black hole (e.g., ~ 24303.7 minutes for NGC 3842). Thus, the deviation in the time delays for the quadratic gravity black hole with ($S_0 = S_2 = 0.1$, $m_0 = m_2 = 1$) from the standard Schwarzschild black hole ($S_0 = S_2 = 0$) is $\delta\Delta T_{2,1} = \Delta T_{2,1}^{Sch} - \Delta T_{2,1}^{ASQG} = 1188$ minutes. This suggests that if the first and second relativistic images are distinguishable, the time delay between them could serve as a valuable indicator to differentiate the quadratic gravity black hole from the classical Schwarzschild black hole.

6.5 Conclusions and Final Remarks

In the present chapter, we have discussed the shadow and strong gravitational lensing phenomena by the quadratic gravity black holes, described by a solution obtained by the quadratic gravity action. A black hole in quadratic gravity is described by five parameters, with M representing the mass of the black hole. The two free parameters S_0 and S_2 characterize the strength of the exponentially decaying Yukawa corrections. Additionally, the masses m_0 and m_2 of the spin-0 and spin-2 modes are associated with various curvature terms' couplings. This has been discussed in detail in [Pawlowski and Tränkle (2024)]. The classical Schwarzschild black hole is obtained when $S_0 = S_2 = 0$. The present study highlights that traditional black hole solutions derived from classical general relativity may not fully capture the complexities of black holes in the context of quadratic gravity. This black hole like solutions exhibit significant deviations from classical predictions, particularly outside the event horizon. These deviations could manifest in gravitational lensing phenomena, where the curvature of spacetime influences the paths of light rays passing near massive objects. In this study, we primarily restrict our analysis to positive values of the black hole

parameters S_0,S_2,m_0 and m_2. The study of light deflection (gravitational lensing) in the strong field limit, particularly in regions dominated by the gravitational effects of quadratic gravity black holes, offers powerful theoretical and observational tools for distinguishing between standard general relativistic models and modified gravity models. Although the radial coordinate dependence of the quadratic gravity metric takes a fixed form, when interpreted as a galactic metric, the bending angle of light and other optical effects are significantly influenced by the metric parameters, as well as by the baryonic mass and radius of the supermassive black hole. The quadratic gravity metric dictates the specific values of the bending angles and other lensing effects and these values differ substantially from those predicted by the classical Schwarzschild metric. For example, when $S_0 = 0.1$,$S_2 = 0.1$,$m_0 = 1$ and $m_2 = 1$, the time delay of the photons is much smaller in the quadratic gravity than in standard general relativity. This may be related to the gravitational light deflection angle being larger than the value predicted by the standard general relativistic approach. We observe significant differences in the lensing effects when comparing our results for the quadratic gravity black holes with those of standard Schwarzschild black holes. As a result, the quadratic gravity black hole, influenced by moving fluids and sound waves, can be detected more easily and distinguished from ordinary astrophysical black holes such as the Schwarzschild black hole. Consequently, the study of gravitational lensing may provide evidence for the existence of quadratic gravity effects in the Universe. Our findings represent a promising and significant step towards connecting the fundamental theory of quadratic gravity to potentially feasible black hole spacetimes.

Motivated by this shadow of back hole, the shadow of a wormhole is sought to be understood in terms of its potential appearance, investigating how light interacts with these exotic objects and whether such signatures could one day be observed, potentially offering insights into new physics and the nature of spacetime. So, in the following chapter the physical characteristics of non rotating wormholes are analyzed as well as shadow of them and in Chapter.8, the shadow of rotating wormholes are explored.

Chapter 7

Impact of Yukwa Potential on Wormhole Shadow

7.1 Introduction

In the early days of general relativity, wormholes were nothing more than a mathematical quirk, buried within the solutions to Einstein's equations. But in 1916, physicist Ludwig Flamm stumbled upon a second, hidden solution to the Schwarzschild metric [Flamm (1916)], sparking the earliest inkling of what would later be called a "wormhole". Fast-forward to 1935, when Einstein and his colleague Nathan Rosen explored these connections more deeply, crafting the idea of a bridge between two parts of spacetime, a so-called "Einstein-Rosen bridge". Although fascinating [Einstein and Rosen (1935)], it was sadly non-traversable, meaning one could never truly pass through it. But then came a breakthrough in 1988, physicists Kip Thorne and Michael Morris imagined a traversable wormhole, one that could connect distant points in the universe [Morris and Thorne (1988)]. Their work brought wormholes from the realm of theoretical curiosity into practical fascination, bridging not just space but also the curious minds of scientists in quantum mechanics, black hole physics and even science fiction writers. Today, wormholes stand at the forefront of cutting-edge theories, with physicists asking, "Could these gateways to distant galaxies really exist?"

Wormholes, theoretical constructs that bridge two separate regions of spacetime, have been a cornerstone in the study of general relativity and its extensions. However, the

Einstein-Rosen bridge model failed to serve its purpose in particle physics and it was later realized that these bridges were not traversable. A non-traversable wormhole is a structure that also connects two points in spacetime but cannot be used as a passage by any form of matter or radiation. These wormholes typically collapse or form singularities before anything can pass through, rendering them impassable, while a traversable wormhole is a hypothetical structure that connects two distinct points in spacetime, allowing matter (and potentially information) to pass through it without encountering singularities or extreme tidal forces that would destroy it. To be traversable, a wormhole must have certain conditions in its geometry, such as the presence of exotic matter [Visser (1995)] with negative energy density at the throat to keep it stable and prevent it from collapsing under gravitational forces. These would require exotic matter that violates standard energy conditions [Galloway et al. (2001, 1999)], such as the NEC. Although this concept seems counterintuitive in classical general relativity, it becomes more plausible in the context of quantum mechanics. Since then, researchers have explored alternatives to minimize or bypass the need for exotic matter. One approach is modified gravity, which alters general relativity's equations, adding extra degrees of freedom that might support traversable wormholes without violating energy conditions. For example, theories like $f(R), f(T), f(Q)$ and other modified gravity theories [Harko et al. (2013), Hochberg, D (1990), Kanti et al. (2012), and Mazharimousavi and Halilsoy (2016)], suggest that wormholes might be possible with ordinary matter.

In theoretical physics, macroscopic traversable wormholes, while still speculative, are a captivating concept. These hypothetical structures, large enough to allow human travel, require specific conditions to exist. To address this, researchers have explored the possibility of introducing a "dark sector" with properties conducive to constructing such wormholes. One promising approach involves the Randall-Sundrum model [Randall and Sundrum (1999)], which is a framework in physics that incorporates extra dimensions beyond the familiar three spatial and one temporal dimension. Among these, the Yukawa-modified gravitational potential has garnered attention due to its ability to modify the gravitational potential at both short and long distances, offering a more flexible framework for dark matter interactions. The Yukawa potential was first proposed by Japanese physicist Hideki Yukawa in 1935 [Yukawa (1935)] to describe the force between nucleons (protons and neutrons) in an atomic nucleus. Yukawa introduced this potential as a way to explain the strong nuclear

force, which binds nucleons together, in a manner similar to how the Coulomb potential describes electromagnetic interactions. The Yukawa potential is characterized by an exponentially decaying term, which introduces a finite range to the force, unlike the long-range Coulomb or gravitational potentials. Yukawa's theory predicted the existence of a particle, now known as the pion, as the mediator of the nuclear force. His work earned him the Nobel Prize in Physics in 1949, as it laid the foundation for our understanding of nuclear forces in the context of quantum field theory. The Yukawa potential is modified to include terms that decay over larger distances. It alters Newton's potential with an exponential decay term [Jusufi et al. (2023a)], providing a nuanced approach to gravity that aligns with observations of galactic dynamics and could offer insights into dark matter and dark energy. This potential, which depends on a parameter linked to the wavelength of a hypothetical massive graviton, has been used to explore modified Friedmann equations, which are central to cosmological models. The necessity of modifying the Yukawa potential in gravity stems from the desire to address phenomena where traditional gravity or dark matter hypotheses are insufficient. For example, the Yukawa potential has been proposed as an alternative to Modified Newtonian dynamics in explaining flat galaxy rotation curves, gravitational lensing anomalies and other astrophysical phenomena that challenge conventional gravitational theory. The potential's versatility allows it to account for both short-range and long-range modifications, bridging gaps in our understanding of gravity on different scales.

In the present chapter, a cosmologically motivated approach is explored that leverages the Yukawa potential [Sekhmani et al. (2024)] to study dark matter and its implications for gravity. This framework builds on Verlinde's concept of gravity as an emergent entropic force, which views gravitational effects as resulting from changes in a system's information content. Verlinde also proposed that what we interpret as dark matter may not be due to actual, unseen particles but rather an emergent effect resulting from ordinary baryonic matter, fundamentally altering our perspective on dark matter. By incorporating the Yukawa potential into this approach [Gonzalez et al. (2023)], we consider a modified gravitational interaction characterized by parameters such as the coupling strength β the wavelength λ and the Planck-scale length l. This coupling framework is particularly useful in deriving modified Friedmann equations, which relate dark matter, dark energy and baryonic matter densities under an entropic force interpretation. This model treats dark energy as a

manifestation of graviton self-interaction, with implications for the cosmological constant. Observationally, this framework aligns with recent studies suggesting that dark matter may be effectively described by long-range interactions between baryonic matter, mediated by a Yukawa-type gravitational potential.

In our wormhole study, the modified Yukawa potential was chosen because it offers a promising framework to explore non-standard gravitational structures like wormholes, especially in regions of high gravitational influence, such as galactic cores. We examined how the Yukawa modification affects the stability, traversability and shadow properties of wormholes, offering insights into their possible observational signatures within galactic environments. Recent studies [Arvanitaki et al. (2017), Berezhiani et al. (2009), Borka et al. (2013), Garny et al. (2016), Jusufi and Sheykhi (2023), Jusufi et al. (2023b), and Millano et al. (2023)] have suggested that incorporating the Yukawa potential into gravitational theories may lead to observable effects, particularly in the context of gravitational lensing and the behavior of cosmic structures. The advancement of modern physics and applied mathematics continues to push the boundaries of knowledge in fields as varied as signal processing and astrophysical theory. While adaptive algorithms optimize computational efficiency and resource management, corrections to gravitational metrics provide new perspectives on foundational cosmic structures.

Many studies in the literature have extensively examined various aspects of traversable wormhole geometries, as demonstrated in literature [Almheiri et al. (2020), Bronnikov and Kim (2003), Garcia and Lobo (2010), Garcia and Lobo (2011), Hawking (1988), Konoplya and Zhidenko (2022), Kuhfittig (2019), Kuhfittig (2021), Lemos et al. (2003), Penington et al. (2022), Sarkar et al. (2024), Sushkov (2005), and Visser (1989)]. Researchers have explored wormholes in the context of various modified gravity theories, taking into account a range of realistic scenarios [Botta Cantcheff et al. (2010), Garattini and Lobo (2007), Lobo and Oliveira (2009), Moraes and Sahoo (2017), and Richarte and Simeone (2007)]. Among the intriguing aspects of wormholes, the study of their shadows offers a unique avenue for exploring their properties and implications. In astrophysics, a shadow represents the apparent outline of an object as seen from a distant observer's perspective. This effect is closely related to gravitational lensing, caused by the bending of light around massive bodies. A wormhole's gravitational field can bend light in such a way that it creates multiple images

or a bright ring around its shadow. Unlike black holes, which have a distinct photon sphere shaping their shadow, wormholes can produce a more intricate shadow pattern due to light that traverses or loops around the wormhole's throat. In astrophysics, wormhole shadows have become a subject of significant interest, as observing one could indirectly support the existence of wormholes. However, no observational evidence has been obtained yet, making the study largely theoretical at this stage. Shadows have been widely investigated for black holes [Afrin and Ghosh (2023), Arora et al. (2023), and Molla and Debnath (2023b)] and the study of shadows in wormholes [Alloqulov et al. (2024), Shaikh (2022), and Zhu and Wang (2021)] is an emerging field with its own unique challenges and opportunities. Wormhole shadows provide valuable insights into their size, structure and the distribution of exotic matter within them. This line of research may shed light on the feasibility of traversable wormholes and their potential observable signatures.

The chapter is organized as follows: section 7.2 presents the interior spacetime with the Einstein Field Equations equations. In section 7.3, various physically viable models of wormholes have been explored. The density and stability conditions of wormholes have been discussed in section 7.4. section 7.5 delves into discussions related to three different models for distinct redshift functions. In section 7.6, the wormhole shadow cast by the throat is discussed for the three new wormhole models: Model-I, Model-II and Model-III. Finally, in section 7.7, a few concluding remarks are provided.

7.2 Interior Spacetime with the Einstein Field Equations

We examine the Morris–Thorne traversable wormhole spacetime [Morris and Thorne (1988)], which is described by a static, spherically symmetric metric in the Schwarzschild coordinate system (t, r, θ, ϕ),

$$ds^2 = -e^{2\Phi(r)}dt^2 + \left(1 - \frac{b}{r}\right)^{-1} dr^2 + r^2 d\Omega^2, \tag{7.2.1}$$

where,

$$d\Omega^2 = \left(d\theta^2 + \sin^2\theta d\phi^2\right).$$

Here, coordinates t, r, θ and ϕ are defined by $-\infty < t < \infty$, $r_0 \leq r < \infty$, $0 \leq \theta \leq \pi$ and $0 \leq \phi \leq 2\pi$ and in general, the metric functions Φ, b depend only on r and θ. $b(r)$ and $\Phi(r)$ are known as shape function and redshift function.

The stress-energy tensor for dark matter, assumed to have an anisotropic matter distribution, is given by

$$T^{\mu\nu} = \Big[\rho(r) + p_t(r)\Big]U^\mu U^\nu - p_t(r)g^{\mu\nu} + \Big[p_r(r) - p_t(r)\Big]\chi^\mu\chi^\nu, \tag{7.2.2}$$

where, $U^\mu U_\mu = -\chi^\mu\chi_\mu = 1$ and $U^\mu\chi_\mu = 0$. Here, $\rho(r)$, $p_r(r)$ and $p_t(r)$ denote the energy density, radial pressure and transverse pressure, respectively, of the dark matter distribution.

Thus, the energy-momentum tensor of the wormhole spacetime Eq.(7.2.1) is given by

$$T^\mu_\nu = diag[-\rho, p_r, p_t, p_t], \tag{7.2.3}$$

where, ρ is the wormhole matter density, p_t is tangential pressure and p_r is radial pressure.

The Einstein field equations for the line element Eq.(7.2.1) along with energy-momentum tensor Eq.(7.2.3) are obtained as (in the geometrized system of units having $G = 1$)

$$\kappa\rho(r) = \frac{b'(r)}{r^2}, \tag{7.2.4}$$

$$\kappa p_r(r) = \frac{2}{r}\Big(1 - \frac{b(r)}{r}\Big)\Phi'(r) - \frac{b(r)}{r^3}, \tag{7.2.5}$$

$$\kappa p_t(r) = \Big(1 - \frac{b(r)}{r}\Big)\left[\Phi''(r) + \Phi'(r)\Big(\Phi'(r) + \frac{1}{r}\Big)\right] - \frac{b'(r)r - b(r)}{2r^2}\Big(\Phi'(r) + \frac{1}{r}\Big). \tag{7.2.6}$$

where, the symbol ($'$) represents differentiation with respect to the radial coordinate r.

7.3 Generating a Physically Viable Model of Wormhole with Yukawa Potential

To develop a physically reasonable model of the stellar configuration, the regular non-singular Yukawa-type gravitational potential is assumed [Sekhmani et al. (2024)],

$$\Psi(r) = \frac{-GMm}{\sqrt{r^{D-2} + l^{D-2}}}(1 + \beta e^{-\frac{r}{\lambda}}), \tag{7.3.1}$$

here, the wavelength of massive graviton is

$$\lambda = \frac{h}{m_g c}. \tag{7.3.2}$$

Here, l is a Planck-scale parameter and β is a parameter. The Yukawa term decays exponentially over the Planck scale, which is associated with the mass m_g of the hypothetical graviton.

It is recognized that the energy density of modified matter can be explicitly determined by considering [Sekhmani et al. (2024)]

$$\rho(r) = \frac{1}{4\pi}\Delta\Psi(r). \tag{7.3.3}$$

Simplifying Eq.(7.3.3), one can obtain the following energy density [Sekhmani et al. (2024)]

$$\rho(r) = \frac{e^{-\frac{r}{\lambda}}\beta M}{4\pi r\lambda^2(r^2 + l^2)^{\frac{5}{2}}}A + \frac{3Ml^2}{4\pi(r^2 + l^2)^{\frac{5}{2}}}, \tag{7.3.4}$$

where,

$$A = 2\lambda l^4 + (3\lambda^2 l^2 - l^4)r + 2\lambda l^2 r^2 - 2l^2 r^3 - r^5. \tag{7.3.5}$$

Where the first term of the energy density expression is linearly proportional to β, dominates at large distances, while the second is proportional to l governs short-distance behavior. Specifically, when long-range modifications are ignored.

Now, substituting Eqs.(7.3.4) and (7.3.5) in Eq.(7.2.4) the shape function is calculated. All the wormhole's models of this chapter are analyzed by focusing on four distinct cases

based on different values of the parameter β. To simplify the calculation of the shape function $b(r)$, we initially chose $\lambda = 10^{11}$. To obtain the shape function, it is considered $l = 1$, $M = 10$, $m = 0.2$ and $\kappa = 0.001$.

For $\lambda = 10^{11}$ and using the above values, the equation of shape function can be obtained as

$$b(\mathrm{r},\beta) = \frac{1}{(r^2+1)^{3/2}}\Big((0.00795775\beta + 0.00795775)r^3 - 0.000711763(\beta - 701.481)\sqrt{r^2+1}r^2 - 0.000711763(\beta - 701.481)\sqrt{r^2+1} + 2.528688524056043 \times 10^{-18}\beta r\Big). \tag{7.3.6}$$

Now, the shape function of wormhole, along with the embedding and proper length related to this shape function, will be discussed. These quantities are interconnected, with the shape function governing the structure of the wormhole, the embedding providing a visual representation of that structure and the proper length describing the actual distances along the throat.

7.3.1 Shape Function

The shape function $b(r)$ is a crucial aspect of traversable wormhole models in general relativity. It defines the geometry of the wormhole and governs the structure of the throat, the narrowest part of the wormhole connecting two distinct regions of spacetime. The shape function must satisfy certain conditions [Morris and Thorne (1988)] to ensure that the wormhole is traversable and free from singularities. With all the mentioned necessary wormhole properties, it is very important to mention that the choice of Yukwa gravitational potential on wormhole geometry in the framework of general relativity is physically viable and compatible.

- **Positive**: From the minimum throat radius, shape function should be positive with the increased behavior. From Fig.7.1, it can be observed that the numerically calculated shape function is continuously going up with a positive behavior throughout the described range of the radial coordinate.

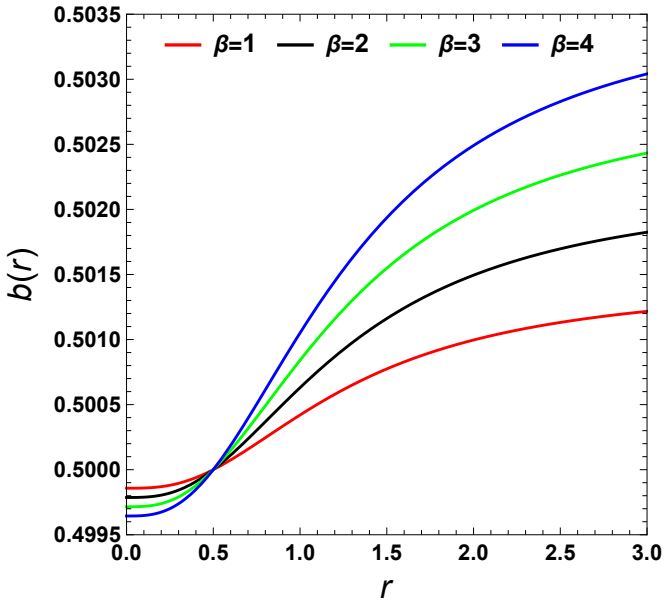

Fig. 7.1. The shape function $b(r)$ across the radial coordinate r is drawn varying β for fixed $\lambda = 10^{11}$. The positive values of $b(r)$ ensure that the wormhole's geometry conforms to the required structure for traversability, with $b(r)$ determining the spatial geometry and influencing the throat's characteristics.

- **Flaring out condition**: This condition ensures that the wormhole "flairs out" at the throat, preventing it from being pinched off. Mathematically, this condition is expressed as follows

$$\frac{b(r) - rb'(r)}{b^2(r)} > 0 \quad for \quad r = r_0. \tag{7.3.7}$$

  This ensures that the effective area of the throat is non-decreasing, which is necessary for a traversable wormhole. This condition $b^{'}(r_0) < 1$ is also satisfied for the numerically calculated shape function, which can be confirmed from the Fig.7.2.

- **Throat of Wormhole**: The throat acts as a bridge connecting two asymptotically flat regions of spacetime, allowing for shortcuts through spacetime. Its geometric properties impact the overall topology and curvature of the wormhole. A well-defined throat with positive curvature ensures that particles can travel through without being trapped or destabilized. Mathematically, the throat is defined as the minimum radius of the wormhole, which corresponds to the location where the shape function $b(r)$ equals zero

$$b(r_0) = r_0, \tag{7.3.8}$$

  where r_0 is the radius of the wormhole throat. Interestingly, the numerically calcu-

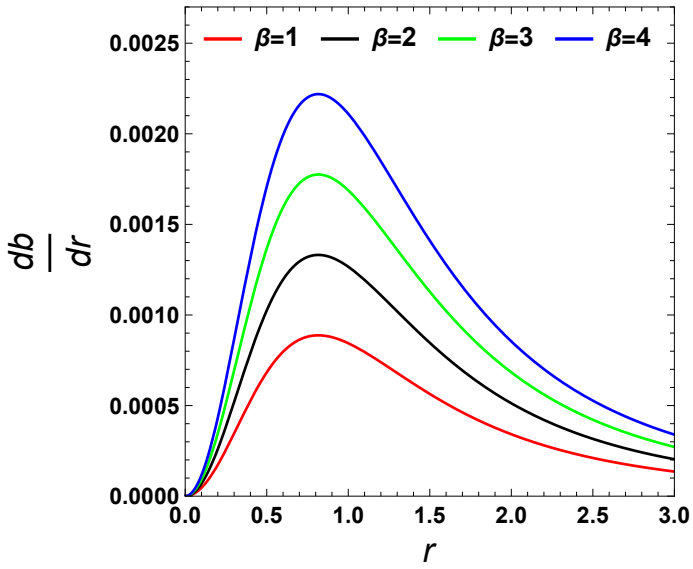

Fig. 7.2. $b'(r)$ the derivative of the shape function is plotted across the radial coordinate r, varying β for fixed $\lambda = 10^{11}$, which indicates the flare-out condition.

lated shape function is also providing the wormhole throat location which is measured around $r_0 = 0.5$. The measured value of wormhole throat can be confirmed from Fig.7.3.

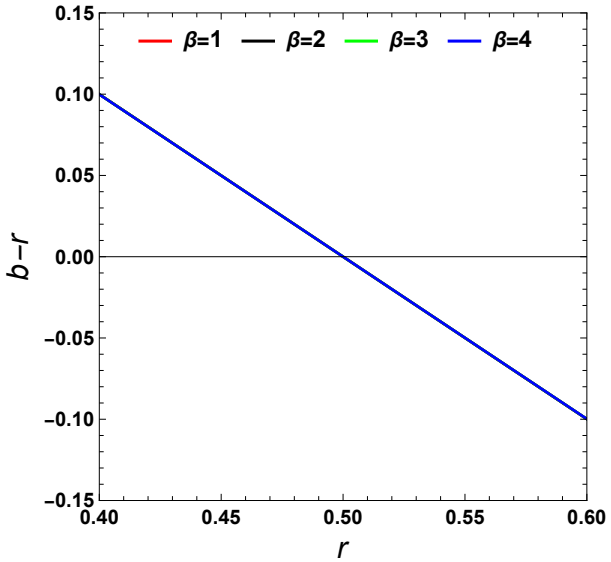

Fig. 7.3. $b(r) - r$ is plotted across the radial coordinate r, varying β for fixed $\lambda = 10^{11}$, indicating the wormhole throat locations.

- **Asymptotically Flat Condition**: For a traversable wormhole to be physically meaningful, it should asymptotically approach flat spacetime as one moves away from the

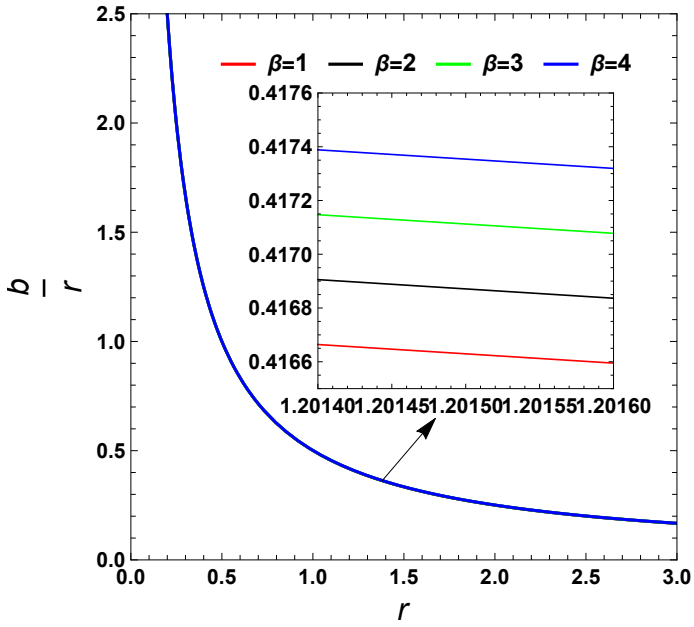

Fig. 7.4. $\frac{b(r)}{r}$ is plotted across the radial coordinate r, varying β for fixed $\lambda = 10^{11}$, as $r \to \infty$ this ratio should approach zero, satisfying the asymptotic flatness condition.

wormhole. This condition can be mathematically expressed as

$$lim_{r\to\infty}\frac{b(r)}{r} = 0. \tag{7.3.9}$$

The flatness condition is also satisfied for the numerically calculated shape function, which can be confirmed from the Fig.7.4.

It can be seen from the Figs.7.1, 7.2, 7.3 and 7.4 that all the values of all the different graphs of shape function slightly increase with the increasing value of β.

7.3.2 Proper Radial Length

In traversable wormhole models, the proper radial length, $l(r)$ is a crucial metric that quantifies the physical distance along the wormhole's radial coordinate from a reference point to the throat. For a given wormhole geometry, this radial length is determined by integrating the spatial component of the wormhole metric. The proper distance is influenced by the shape and size of the wormhole as well as the gravitational effects surrounding it. This can often be expressed in terms of an integral over the radial coordinate as

$$l(r) = \pm\int_{r_0}^{r}\sqrt{g_{rr}}dr. \tag{7.3.10}$$

Using the Eq.(7.2.1), the proper radial distance can be expressed as

$$l(r) = \pm \int_{r_0}^{r} \frac{dr}{\sqrt{\left(1 - \frac{b(r)}{r}\right)}}. \tag{7.3.11}$$

For any traversable wormhole, $l(r)$ must increase monotonically with respect to the increasing values of r. It can be seen in Fig.7.5 that the graph of $l(r)$ is strictly increasing and for different values of β. To get this graphical representation, Fig.7.5 of the proper radial distance, numerical integral is used.

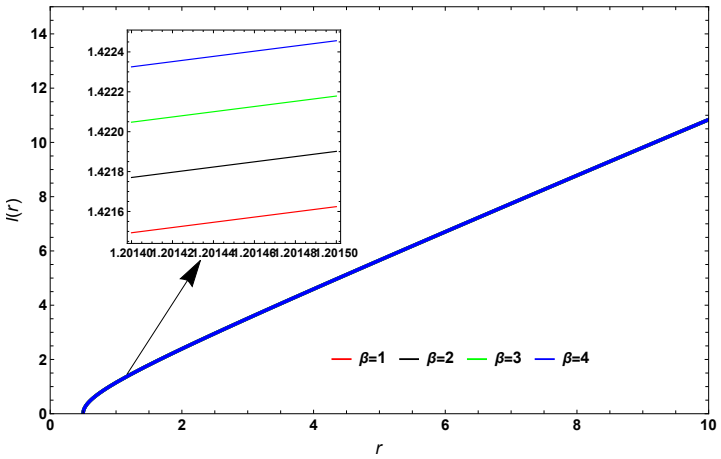

Fig. 7.5. The figure shows the variations of proper radial length $l(r)$ of wormhole for different values of β.

7.3.3 Embedding

The concept of embedding in wormhole physics provides a valuable way to visualize and understand the geometry of a wormhole spacetime. In particular, embedding diagrams allow us to represent a two-dimensional slice of the three-dimensional spatial geometry, illustrating the curvature and overall shape of the wormhole. The process involves embedding a surface defined by the wormhole's metric into a higher-dimensional space.

To construct an embedding diagram, we start by considering the wormhole's line element in spherical coordinates. For simplicity, we analyze a two-dimensional equatorial slice $\Big($with constant time and azimuthal angle $(\theta = \frac{\pi}{2})$ $\Big)$. Given the metric in the form

$$ds^2 = \frac{dr^2}{1 - \frac{b(r)}{r}} + r^2 d\phi^2. \tag{7.3.12}$$

We examine the embedded surface $z(r)$, which embeds into three-dimensional Euclidean space of cylindrical form as

$$ds^2 = d\xi^2 + dz^2 + \xi^2 d\eta^2, \tag{7.3.13}$$

where, $\xi = \xi(r, \phi)$, $z = z(r, \phi)$ and $\eta = \phi$. As we are working on symmetric metric so for axi-symmetry we can write $\xi = \xi(r)$, $z = z(r)$.

Now comparing Eq.(7.3.12) and Eq.(7.3.13), we get

$$\left(\frac{d\xi}{dr}\right)^2 + \left(\frac{dz}{dr}\right)^2 = \left(1 - \frac{b(r)}{r}\right)^{-1} \quad \text{and} \quad \xi^2 = r^2. \tag{7.3.14}$$

From Eq.(7.3.14), we get,

$$1 + \left(\frac{dz}{dr}\right)^2 = \frac{1}{1 - \frac{b(r)}{r}} \qquad \text{or} \qquad \frac{dz}{dr} = \pm\sqrt{\frac{r}{b(r)} - 1}. \tag{7.3.15}$$

Now, from Eq.(7.3.15), the embedding surface can now be expressed as a function

$$z(r) = \pm \int_{r_0}^{r} \frac{dr}{\sqrt{r/b(r) - 1}}. \tag{7.3.16}$$

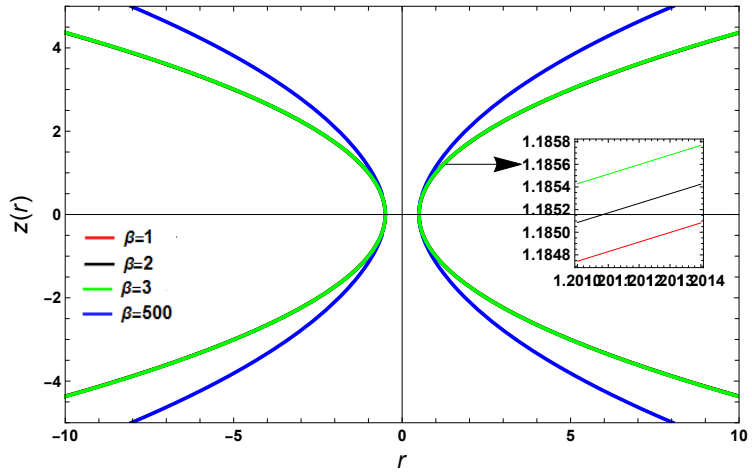

Fig. 7.6. Depicted for variations of embedding surface $z(r)$ of wormhole for different values of β.

Here, we employ the methodology originally introduced by Marolf [Marolf (1999)], along with the approach developed by Peter and David in a separate investigation [Collas and Klein (2012)], to construct the embedded diagram for the wormhole.

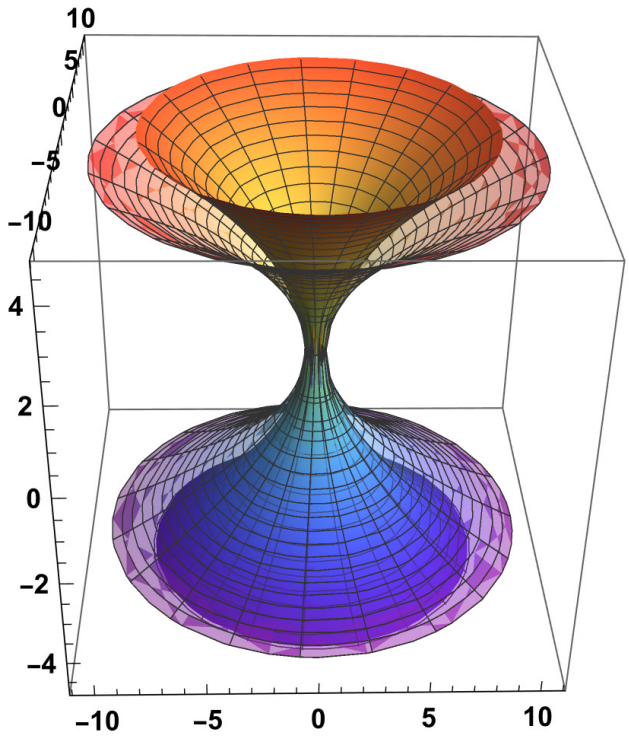

Fig. 7.7. Depicted for variations of 3D surface of wormholes for different values of β.

Using the numerical method, we solve the Eq.(7.3.16). The embedding surfaces are shown in Fig.7.6 and their revolutions are presented in Fig.7.7. These embedding diagrams help clarify how the involved parameters affect the wormhole's geometry. The 3D plot of a wormhole typically involves revolving the embedding surface around an axis to form a solid shape that represents the wormhole in a 3-dimensional view. Here the 3D plots of wormholes for different values of β are presented in single frame, demonstrating how the geometry of the wormhole varies with changing parameter settings. In Fig.7.7 the throat of the wormholes are shown narrow as the throat radius for all the models of this chapter is 0.5. This plot helps in visualizing how the wormholes bend and connect different regions of spacetime, making it easier to understand its geometrical properties.

7.4 Wormhole Physical Property and Stability

We are going to discuss some physical properties and will check stability condition for wormholes. For this discussion, we'll cover two main aspects. Density with energy conditions

and for stability analysis, we'll use the Tolman-Oppenheimer-Volkoff (TOV) equation, which applies to spherical objects in equilibrium.

7.4.1 Energy Conditions and Matter Distribution

In the context of general relativity, the fulfillment of energy conditions for matter plays a pivotal role, as they are crucial for the validity of the singularity theorems [Hawking and Ellis (1973)]. These energy conditions not only support the interpretation of spacetime singularities but also assist in exploring the broader structure of spacetime, even when exact solutions to Einstein's equations are unavailable. They are particularly important for analyzing wormhole solutions within the framework of modified gravity theories. The fundamental energy conditions—namely, the null, weak, dominant and strong energy conditions originate from the Raychaudhuri equation [Raychaudhuri (1955)], which is instrumental in describing the gravitational attraction and the positive energy density of matter. The evolution of radial and tangential pressures, along with energy density, plays a crucial role in forming wormhole structures. This study primarily aims to explore how energy conditions behave in the presence of an anisotropic matter source.

$$NEC \quad : \quad \rho + p_r \geq 0, \rho + p_t \geq 0, \tag{7.4.1}$$

$$WEC \quad : \quad \rho \geq 0, \rho + p_r \geq 0, \rho + p_t \geq 0, \tag{7.4.2}$$

$$DEC \quad : \quad \rho \geq 0, \rho - |p_r| \geq 0, \rho - |p_t| \geq 0, \tag{7.4.3}$$

$$SEC \quad : \quad \rho + p_r \geq 0, \rho + p_t \geq 0, \rho + p_r + 2p_t \geq 0. \tag{7.4.4}$$

The NEC states that for any null vector κ^μ the energy-momentum tensor $T_{\mu\nu}$, derived from

$$T_{\mu\nu}\kappa^\mu\kappa^\nu \geq 0. \tag{7.4.5}$$

For a traversable wormhole, the NEC is violated in most models. This is because wormholes typically require exotic matter that can produce negative energy densities, thus allowing the wormhole throat to remain open. From our models, it is clear that violations of the NEC are tied directly to the nature of the shape function. It has been presented in this chapter.

The regional behavior of the NEC and SEC expressions for both the chosen and derived

shape functions has been illustrated. Violations of these energy conditions, especially NEC and SEC, are necessary to maintain an open wormhole throat and indicate the presence of exotic matter, an unusual form of matter essential for wormhole formation. Exotic matter, which remains unobserved and theoretically challenging to verify physically, may emerge if these energy conditions are not met. These energy conditions provide valuable insights into the properties of wormhole geometry within general relativity. In general relativity, negative energy conditions are fundamental to create and sustain the exotic matter associated with wormholes, characterized by properties such as negative mass and energy that are not observed in ordinary matter. The behavior of the energy density $\rho(r)$ for different values of β is depicted in Fig.7.8 suggesting a validation of the wormhole models.

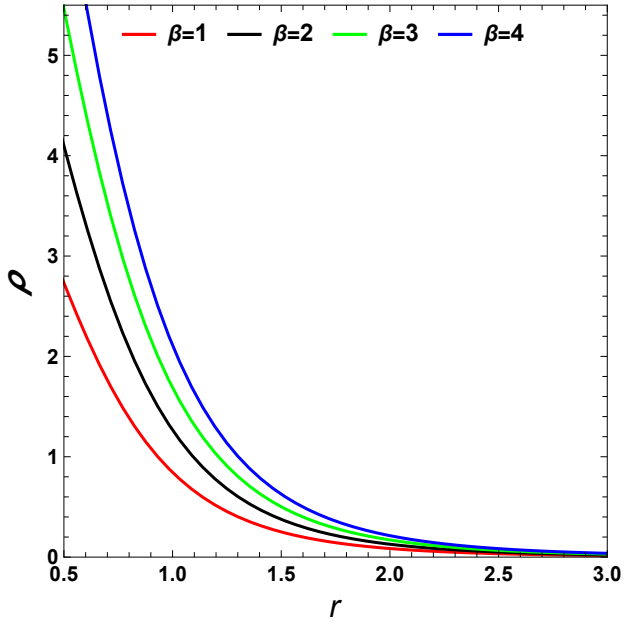

Fig. 7.8. The figure shows the variations of energy density ρ for different values of β.

7.4.2 Equilibrium Condition

In the context of wormhole stability analysis, the Tolman-Oppenheimer-Volkoff (TOV) equation [Oppenheimer and Volkoff (1939)] is adapted to examine the forces acting within a spherically symmetric, static spacetime. This equation is fundamental in assessing the equilibrium and stability of compact objects and can be generalized to incorporate the effects of anisotropic matter distributions. In a wormhole model, the TOV equation essentially

balances distinct forces. The generalized TOV equation is provided as

$$p_r^{'}(r)+\frac{2}{r}[p_r(r)-p_t(r)]+[\rho(r)+p_r(r)]\frac{\Phi^{'}(r)}{2}=0. \tag{7.4.6}$$

For a static equilibrium the generalized TOV equation for anisotropic matter distributions is structured as follows

$$F_h+F_a+F_g=0, \tag{7.4.7}$$

$$F_a=\frac{2}{r}[p_t(r)-p_r(r)], \qquad F_g=-\frac{\Phi^{'}(r)}{2}[\rho(r)+p_r(r)], \qquad F_h=-p_r^{'}(r). \tag{7.4.8}$$

The forces are hydrostatic force (F_h), anisotropic force (F_a) and the gravitational force (F_g). Here, each force contributes uniquely to the overall stability.

For a wormhole to remain in stable equilibrium, the sum of the forces in the modified TOV equation must indeed equal zero. This balance is necessary to counteract the gravitational collapse of the wormhole throat. The graphical behavior of the equilibrium condition, using the TOV equation, is presented separately for each of the three models: Model-I, Model-II and Model-III.

7.5 Different Models Corresponding to the Three Different Redshift Functions

Now, we will discuss three different models of wormholes. In the first two cases, we assume specific forms of the redshift function. In the last case, we use an EoS to determine the redshift function for new wormhole solutions.

7.5.1 Model:I

To analyze the complete wormhole configuration, we first use a specific redshift function given by

$$\Phi=\frac{a}{r}, \tag{7.5.1}$$

where a is the arbitrary constant.

Using this Eq.(7.5.1) we get from Eq.(7.2.5) and Eq.(7.2.6), the expression of radial pressure and transverse pressure respectively, as

$$p_r = \frac{(2a-r)b(r)-2ar}{\kappa r^4}, \tag{7.5.2}$$

$$\begin{aligned} p_t \;=\; & \frac{1}{8\kappa r^5\pi\lambda^2\left(l^2+r^2\right)^{\frac{5}{2}}}\Bigg[r(r-a)e^{-\frac{r}{\lambda}}\Bigg\{4\pi\lambda^2\left(l^2+r^2\right)^{5/2}e^{r/\lambda}b(r) \\ & +\kappa M r^2\Bigg(\beta l^4(r-2\lambda)+l^2 r\Big\{2\beta r^2-3\lambda^2\left(\beta+e^{r/\lambda}\right)-2\beta\lambda r\Big\}\Bigg)+\beta r^5\Bigg\}\Bigg] \\ & +\frac{8a(a+r)(r-b(r))}{8\kappa r^5}. \end{aligned} \tag{7.5.3}$$

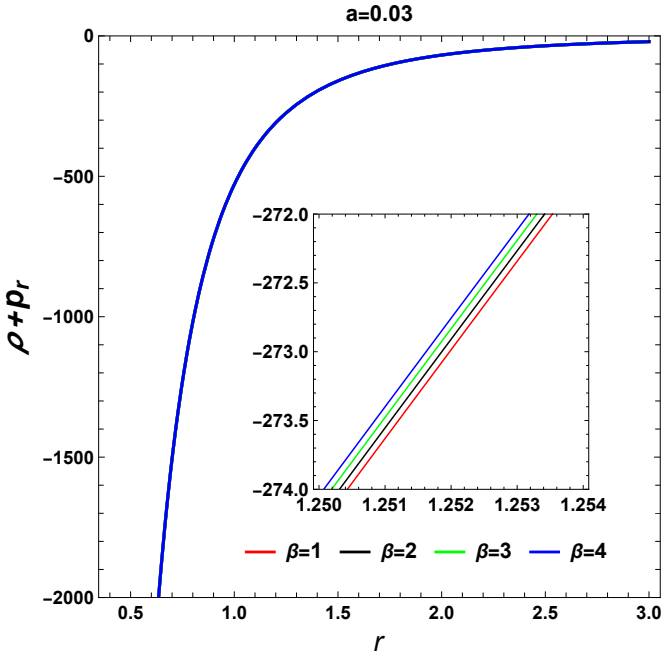

Fig. 7.9. Model:I, NEC: Illustrates the variation of $\rho + p_r$ for different values of the parameter β (1, 2, 3, 4) with $a = 0.03$ in the Model-I for $r_0 = 0.5$.

By examining the behavior of a with respect to different values of the parameter β in our Model-I, we gain insights into how the matter content, radial pressure (p_r) and transverse pressure (p_t) varies and whether these violations differ and also calculated the expressions for various combinations of the energy density (ρ) and pressures.

Using the redshift function in Eq.(7.5.1) and the NEC in Eq.(7.4.1) of energy conditions for Model-I are shown in Fig.7.9. The validity regions where these energy conditions fulfill

the necessary requirements are also provided in Fig.7.10 for Model-I. We get that NEC is violated in most regions for various ranges of the involved parameters in the context of Model-I.

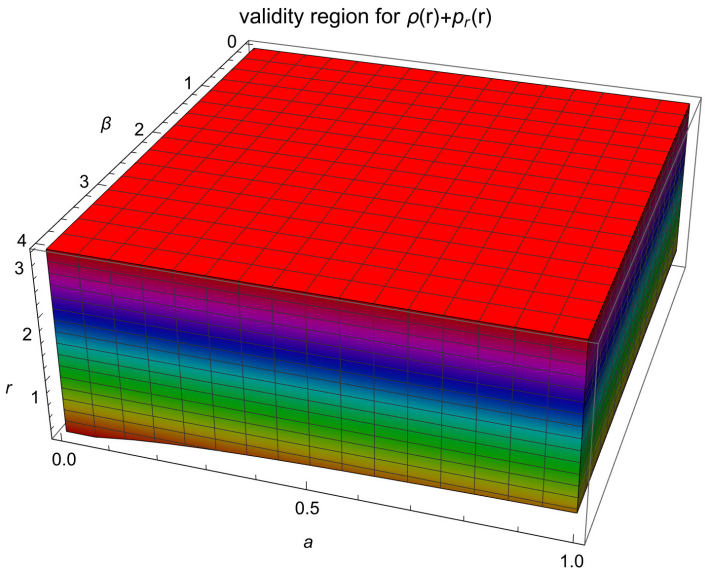

Fig. 7.10. Model:I, NEC(Region): Shows the valid region of $\rho + p_r$ with respect to the parameters β and a for the Model-I with $r_0 = 0.5$.

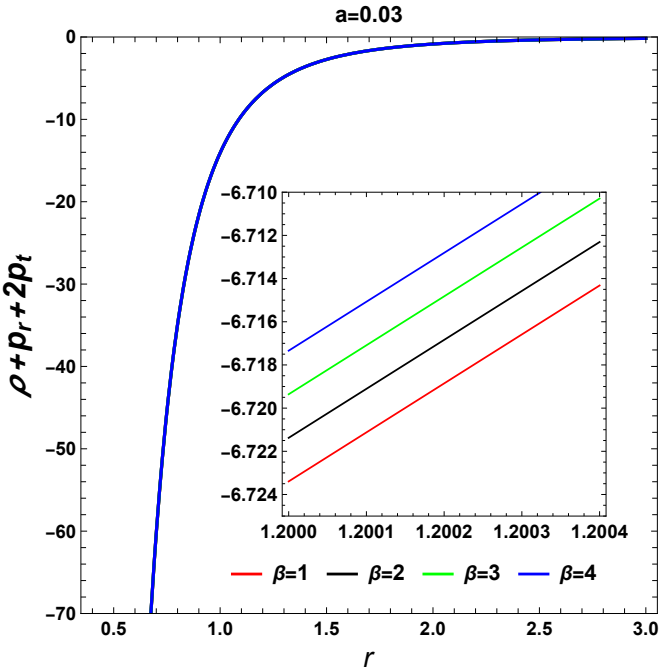

Fig. 7.11. Model:I, SEC: Illustrates the variation of $\rho + p_r + 2p_t$ for different values of the parameter β (1, 2, 3, 4) with $a = 0.03$ in the Model-I for $r_0 = 0.5$.

Using the redshift function in Eq.(7.5.1) and the SEC in Eq.(7.4.2) of energy conditions for Model-I are shown in Fig.7.11. The validity regions where these energy conditions fulfill

the necessary requirements are also provided in Fig.7.12 for Model-I. We get that SEC is violated in most regions for various ranges of the involved parameters in the context of Model-I. The violated region is shown in Fig.7.12.

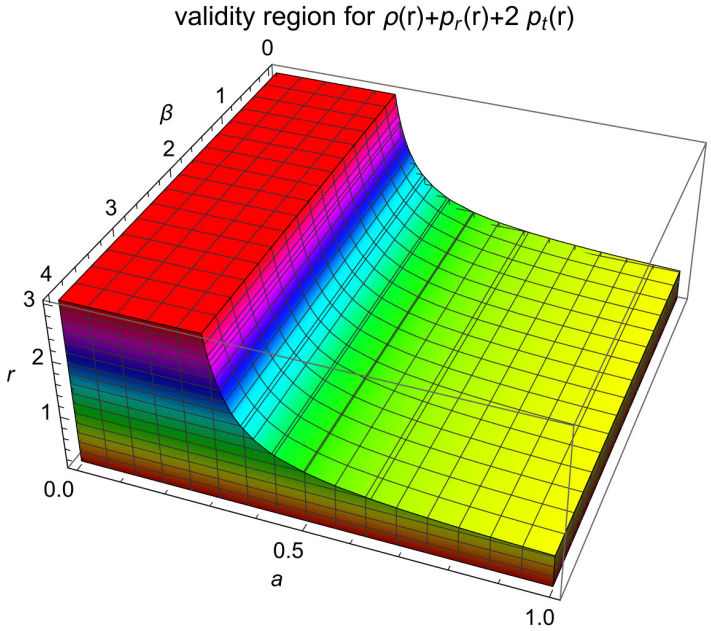

Fig. 7.12. Model:I, SEC(Region): Shows the valid region of $\rho + p_r + 2p_t$ with respect to the parameters β and a for the Model-I with $r_0 = 0.5$.

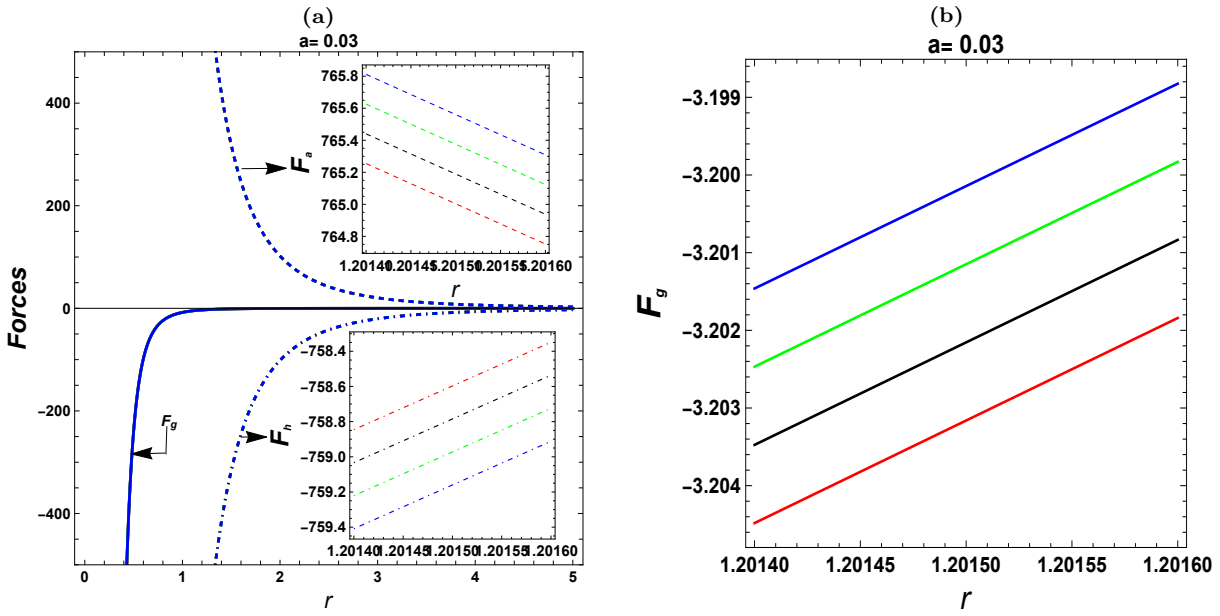

Fig. 7.13. Model:I, TOV: (a) The figure shows the variations of TOV analysis under the effect of three different forces for different values of β, for the Model-I with $r_0 = 0.5$. (b) The graph of magnification of gravitational force F_g is shown.

From Fig.7.13, it is evident that the stability of the wormhole in Model-I is achieved

through the interplay of forces. For the redshift function in Eq.(7.5.1), Model-I is shown to be stable, as illustrated in Fig.7.13(a), which displays the hydrostatic and anisotropic forces. Additionally, Fig.7.13(b) shows the gravitational force for further illustration.

7.5.2 Model: II

In this section, we use another specific redshift function is given by

$$\Phi = 1 + \frac{\gamma}{r^2}, \tag{7.5.4}$$

here γ is the arbitrary constant.

Now, using this Eq.(7.5.4) we get from Eq.(7.2.5) and Eq.(7.2.6), the expression of radial pressure and transverse pressure as

$$p_r = -\frac{\left(r^2 - 4\gamma\right) b(r) + 4\gamma r}{\kappa r^5}, \tag{7.5.5}$$

$$p_t = \frac{8\gamma\left(\gamma + r^2\right)\left(r - b(r)\right)}{2\kappa r^7} - \frac{\left(r^2 - 2\gamma\right)\left(\kappa M r^2\left(A\beta e^{-\frac{r}{\lambda}} + 3\lambda^2 l^2 r\right) - 4\pi\lambda^2\left(l^2 + r^2\right)^{5/2} b(r)\right)}{8\kappa\pi\lambda^2 r^5\left(l^2 + r^2\right)^{5/2}}. \tag{7.5.6}$$

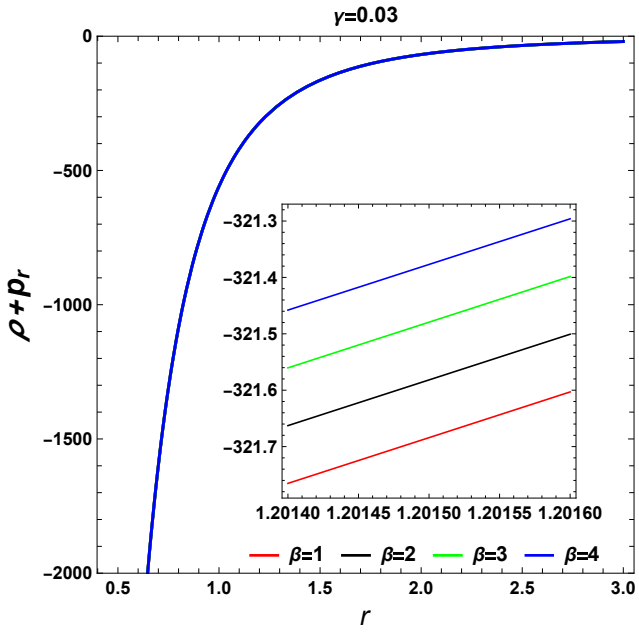

Fig. 7.14. Model:II, NEC: Illustrates the variation of $\rho + p_r$ for different values of the parameter β (1, 2, 3, 4) with $a = 0.03$ in the Model-I for $r_0 = 0.5$.

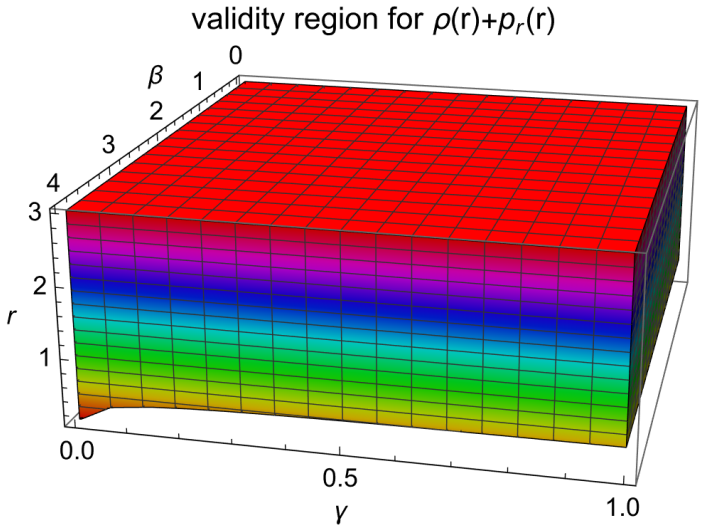

Fig. 7.15. Model:II, NEC(Region): Shows the valid region of $\rho + p_r$ with respect to the parameters β and a for the Model-I with $r_0 = 0.5$.

Using the redshift function in Eq.(7.5.4) and the NEC in Eq.(7.4.1) of energy conditions for Model-II are shown in Fig.7.14. The validity regions where these energy conditions fulfill the necessary requirements are also provided in Fig.7.15 for Model-II. We get that NEC is violated in most regions for various ranges of the involved parameters in the context of Model-II.

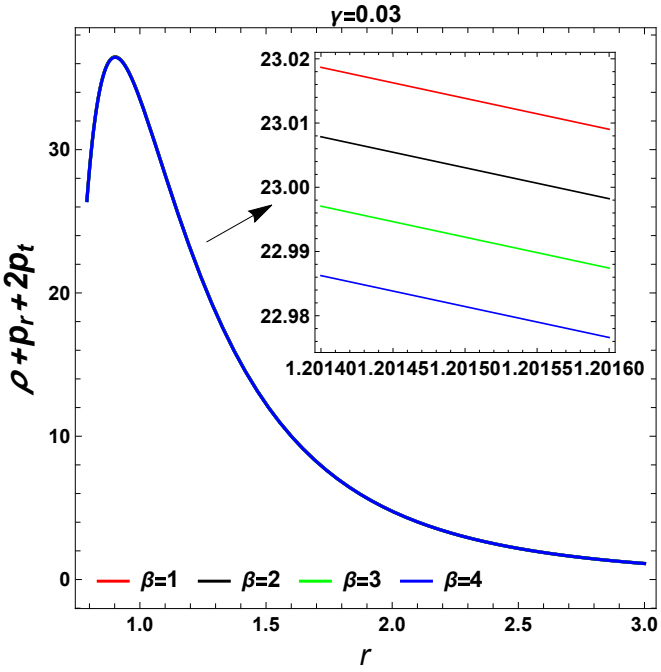

Fig. 7.16. Model:II, SEC: Illustrates the variation of $\rho + p_r + 2p_t$ for different values of the parameter β (1, 2, 3, 4) with $a = 0.03$ in the Model-I for $r_0 = 0.5$.

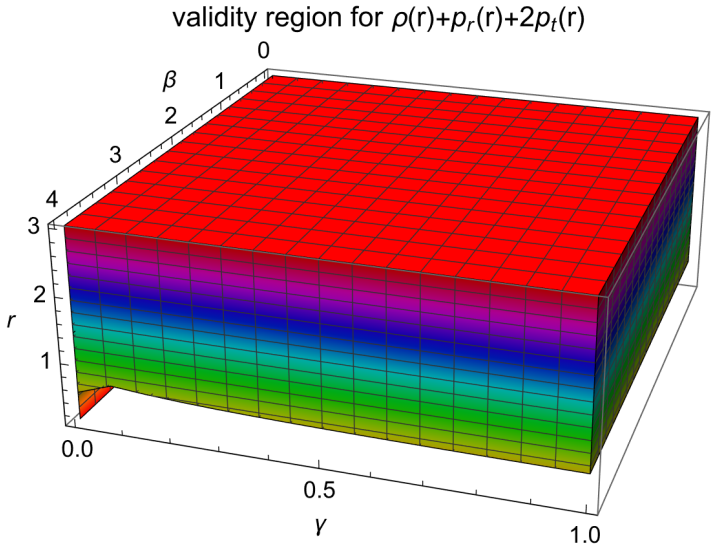

Fig. 7.17. Model:II, SEC(Region): Shows the valid region of $\rho + p_r + 2p_t$ with respect to the parameters β and a for the Model-I with $r_0 = 0.5$.

Using the redshift function in Eq.(7.5.4) and the SEC in Eq.(7.4.2) of energy conditions for Model-II are shown in Fig.7.16. The validity regions where these energy conditions fulfill the necessary requirements are also provided in Fig.7.17 for Model-II. We get that SEC is violated in most regions for various ranges of the involved parameters in the context of Model-II.

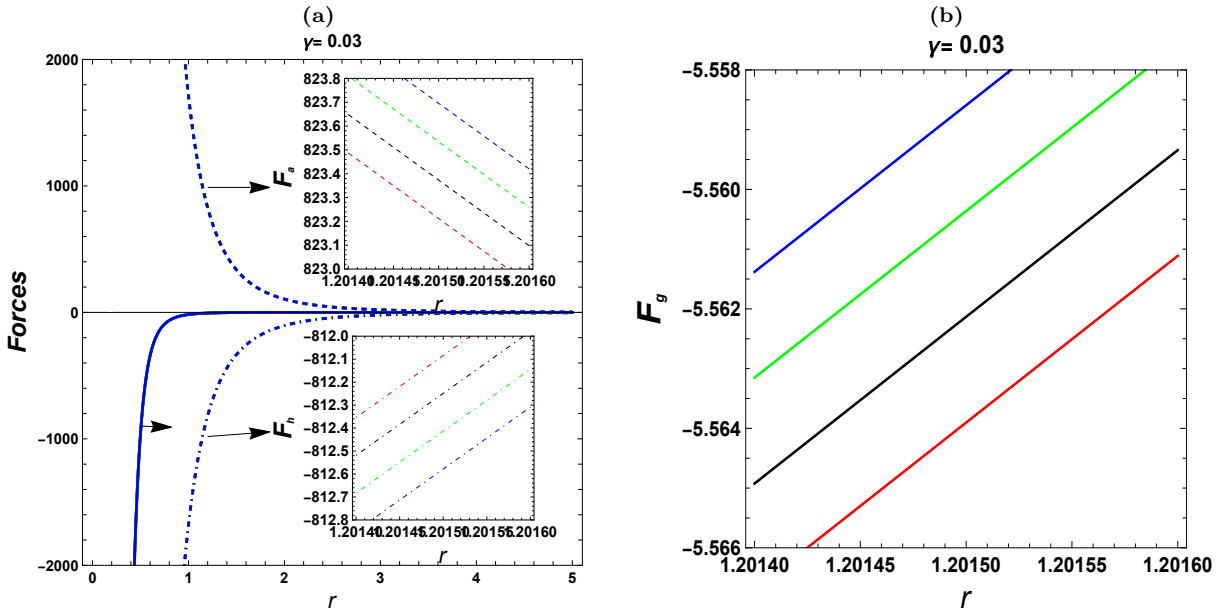

Fig. 7.18. Model:II, TOV:(a) The figure shows the variations of TOV analysis under the effect of three different forces for different values of β, for the Model-I with $r_0 = 0.5$. (b) The graph of magnification of gravitational force F_g is shown.

From Fig.7.18, it is evident that the stability of the wormhole in Model-II is achieved through the interplay of forces. For the redshift function in Eq.(7.5.4), Model-II is shown to be stable, as illustrated in Fig.7.18(a), which displays the hydrostatic and anisotropic forces. Additionally, Fig.7.18(b) shows the gravitational force for further illustration.

7.5.3 Model:III

In this section, we aim to analyze the wormhole configuration by calculating a new redshift function of the wormhole spacetime given in Eq.(7.2.1) using an EoS. To examine the matter content within our wormhole model, we introduce a straightforward EoS. The EoS provides a useful framework for relating the pressure and energy density within the wormhole model, which is crucial for assessing the types of matter needed to maintain the wormhole. The EoS is defined as $\omega = \frac{p_r}{\rho}$ and is classified as dark energy under the following conditions

- $-\frac{1}{3} < \omega < 0$: represents quintessence matter.
- $\omega < -\frac{1}{3}$: necessary for cosmic acceleration.
- $\omega < -1$: leads to the concept of phantom energy.

Using Eq.(7.2.5), we obtain the differential of the redshift function, which is given by

$$\Phi'(r,\beta,\omega) = \frac{r}{2\left(1-\frac{b(r,\beta)}{r}\right)} \times \left(\rho\,\omega + \frac{b(r,\beta)}{r^3}\right). \tag{7.5.7}$$

Integrating Eq.(7.5.7) w.r.t r, one can express the redshift function as

$$\Phi(r,\beta,\omega) = \int \left[\frac{r}{2\left(1-\frac{b(r,\beta)}{r}\right)} \times \left(\rho\,\omega + \frac{b(r,\beta)}{r^3}\right)\right] + C_1, \tag{7.5.8}$$

where C_1 is the integrating constant. For the complicated integrand in Eq.(7.5.8), the equation can be numerically integrated. Using the numerical value of the redshift function $\Phi(r)$, one can express the radial pressure p_r and the tangential pressure p_t as

$$p_r = \frac{2r^2\Phi'(r,\beta,\omega) - (2r\Phi'(r,\beta,\omega)+1)b(r)}{\kappa r^3}, \tag{7.5.9}$$

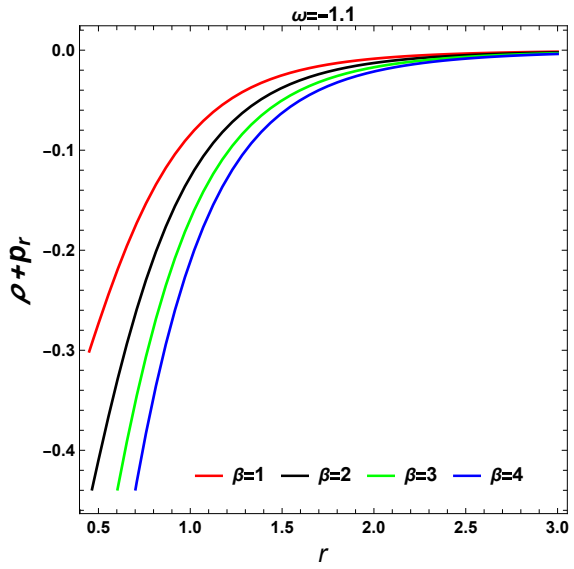

Fig. 7.19. Model:III, NEC: Illustrates the variation of $\rho + p_r$ for different values of the parameter β (1, 2, 3, 4) with $\omega = -1.1$ in the Model-III for $r_0 = 0.5$.

$$p_t = \frac{1}{2\kappa r^2}\Bigg[2(r-b(r))\left(\Phi^{'}(r,\beta,\omega)+r\Phi^{'}(r,\beta,\omega)^2+r\Phi^{''}(r,\beta,\omega)\right) - \left(\Phi^{'}(r,\beta,\omega)+\frac{1}{r}\right)\left(\frac{\kappa M r^2 e^{-\frac{r}{\lambda}}\left(A\beta+3\lambda^2 l^2 r e^{r/\lambda}\right)}{4\pi\lambda^2\left(l^2+r^2\right)^{5/2}}-b(r)\right)\Bigg]. \quad (7.5.10)$$

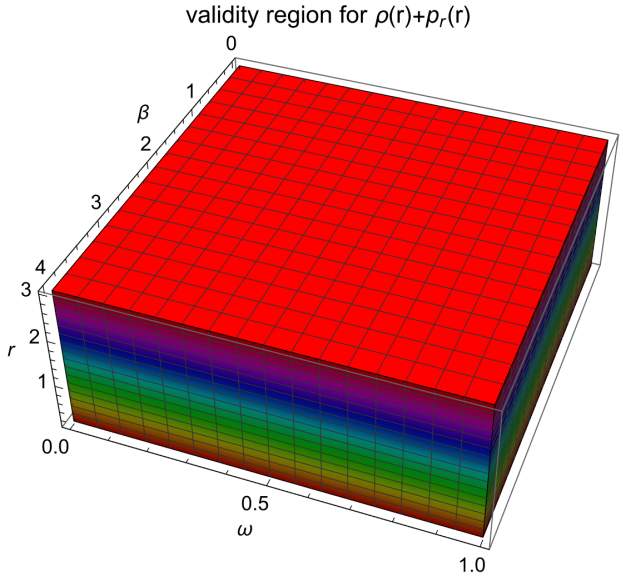

Fig. 7.20. Model:III, NEC(Region): Shows the valid region of $\rho + p_r$ with respect to the parameters β and ω for the Model-III with $r_0 = 0.5$.

The NEC for Model-III is satisfied for a physically viable wormhole if and only if $\omega < -1$, indicating support by phantom energy.

Using the redshift function in Eq.(7.5.8) and the NEC in Eq.(7.4.1) of energy conditions for Model-III are shown in Fig.7.19 . The validity regions where these energy conditions fulfill the necessary requirements are also provided in Fig.7.20 for Model-III. The energy condition NEC is violated in most regions for various ranges of the involved parameters in the context of Model-III.

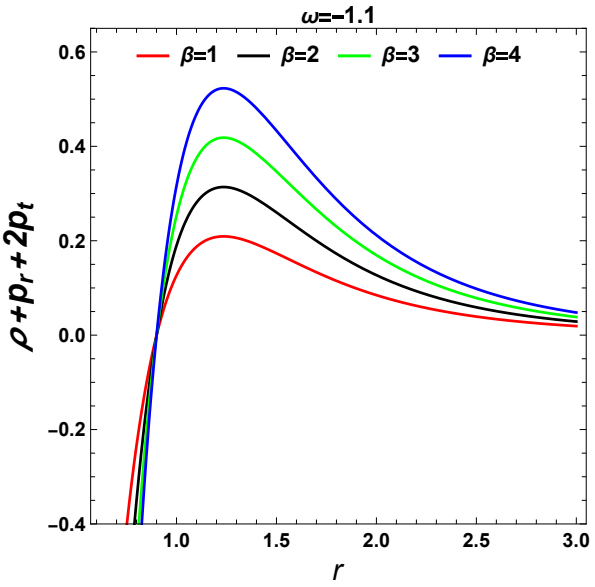

Fig. 7.21. Model:III, SEC: Illustrates the variation of $\rho + p_r + 2p_t$ for different values of the parameter β (1, 2, 3, 4) with $\omega = -1.1$ in the Model-III for $r_0 = 0.5$.

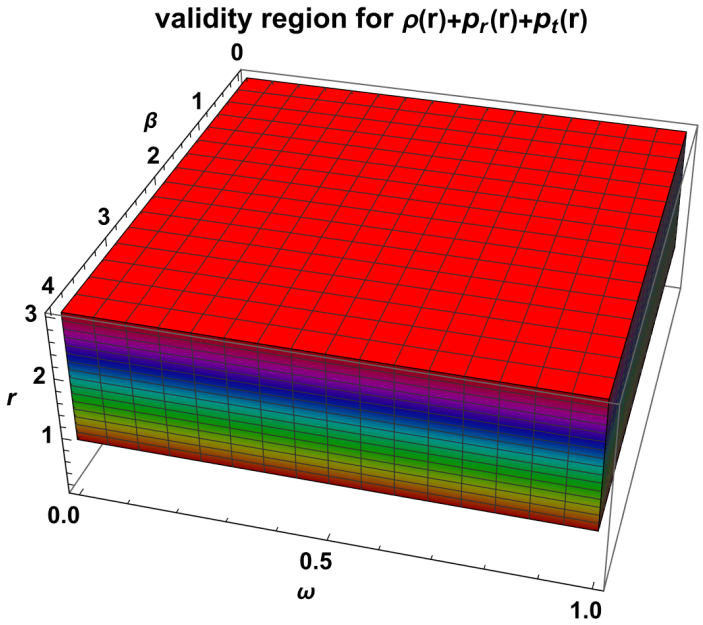

Fig. 7.22. Model:III, SEC(Region): Shows the valid region of $\rho + p_r + 2p_t$ with respect to the parameters β and ω for the Model-III with $r_0 = 0.5$.

Using the redshift function in Eq.(7.5.8) and the SEC in Eq.(7.4.2) of energy conditions for Model-III are shown in Fig.7.21. The validity regions where these energy conditions fulfill the necessary requirements are also provided in Fig.7.22 for Model-III. It is observed that the SEC is violated across a significant portion of the parameter space, with fulfillment limited to specific regions. For various ranges of the parameters involved, the SEC is not upheld in nearly half of the analyzed regions, shedding light on the intricate interplay between the redshift function and energy conditions in the framework of Model-III.

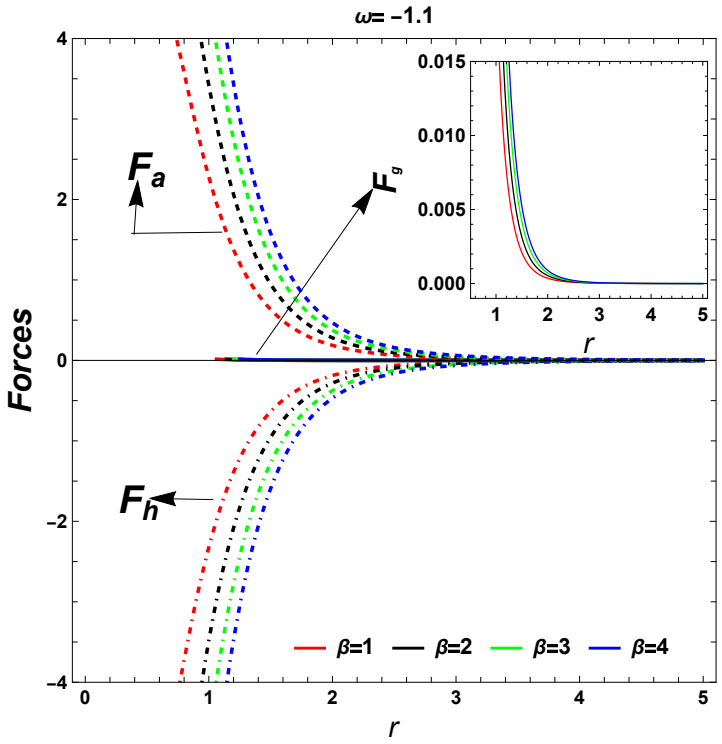

Fig. 7.23. Model:III, TOV: The figure shows the variations of TOV analysis under the effect of three different forces for different values of β, with $r_0 = 0.5$ and $\omega = -1.1$.

From Fig.7.23, it is evident that the stability of the wormhole in Model-III is achieved through the interplay of forces. For the redshift function in Eq.(7.5.7), Model-III is shown to be stable, as illustrated in Fig.7.23, which displays the hydrostatic and anisotropic forces.

7.6 Shadow of Wormhole

In this section, we analyze the shadow cast by a wormhole in the context of the Yukwa gravitational potential applied to wormhole geometry within a galactic region. The shadow forms near the wormhole throat and we aim to quantify how light rays behave in this

spacetime. By examining the trajectory of a light ray following the null geodesic equation, we can predict its path.

Since the wormhole spacetime Eq.(7.2.1) is both static and spherically symmetric, the projection of the photon's four-momentum along the Killing vectors associated with the spacetime's symmetries yields conserved quantities. Specifically, these are the energy,

$$E = -p_\mu \xi^\mu_{(t)},$$

and the angular momentum,

$$L = -p_\mu \xi^\mu_{(\phi)},$$

which remain constant along the geodesics. Here, $\xi^\mu_{(t)}$ and $\xi^\mu_{(\phi)}$ represent the Killing vectors corresponding to time translation and rotational invariance, respectively.

This leads to the following expressions on the equatorial plane $\frac{\pi}{2}$

$$\dot{t} = \frac{dt}{d\tau} = \frac{E}{e^{2\Phi(r)}}, \tag{7.6.1}$$

$$\dot{\phi} = \frac{d\phi}{d\tau} = \frac{L}{r^2}, \tag{7.6.2}$$

where τ is the affine parameter.

Using the Eqs.(7.6.1) and (7.6.2), one can obtain the orbit equation as

$$K_E + V_{eff} = \frac{1}{\tilde{b}^2}, \tag{7.6.3}$$

where, $\tilde{b} = \frac{L}{E}$ the kinetic energy function K_E and potential function V_{eff} is described by

$$K_E = \frac{e^{2\Phi(r)}}{1 - \frac{b(r)}{r}} \dot{r}^2, \tag{7.6.4}$$

$$V_{eff} = \frac{e^{2\Phi(r)}}{r^2}. \tag{7.6.5}$$

To describe the wormhole shadow boundary, one can introduce the celestial coordinates

(X, Y) defined as

$$X = \lim_{\tilde{r}_0 \to \infty} (-\tilde{r}_0^2 \sin(\theta_0)) \frac{d\phi}{dr}, \quad Y = \lim_{\tilde{r}_0 \to \infty} (\tilde{r}_0^2 \frac{d\theta}{dr}), \tag{7.6.6}$$

where $\tilde{r}_0$ is the radial distance of the wormhole with respect to the observer and θ_0 is the inclination angle between the wormhole and the observer. Assuming the static observer is located at infinity, the radius of the wormhole shadow r_s as seen from the equatorial plane, i.e. $\theta_0 = \pi/2$ can be expressed as

$$r_s = \sqrt{X^2 + Y^2} = \frac{r_0}{e^{\Phi(r_0)}}, \tag{7.6.7}$$

where the function $\Phi(r_0)$ is provided by Eq.(7.5.1) for Model-I, Eq.(7.5.4) for Model-II and Eq.(7.5.8) for Model-III.

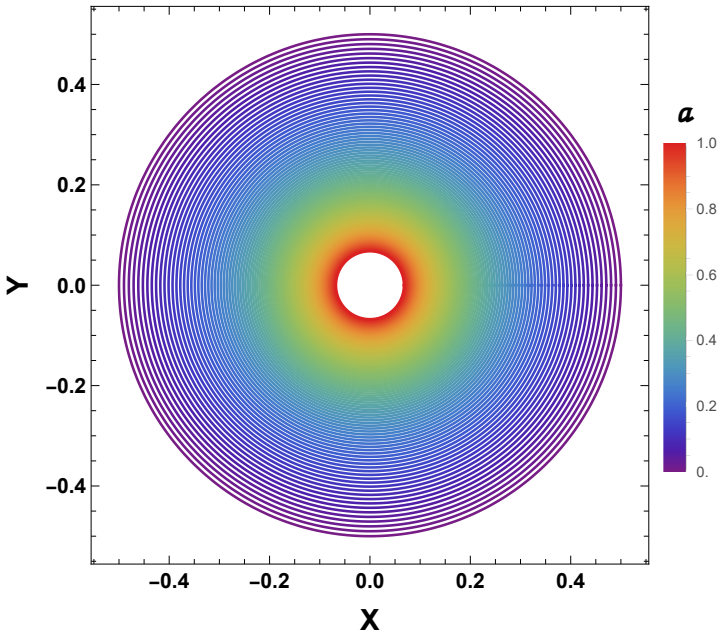

Fig. 7.24. The shadow silhouette of the wormhole is shown in the X-Y plane for varying values of the parameter a, considering the parameter values for Model-I.

The parametric plot of Eq.(7.6.7) in the $X-Y$ plane reveals a range of possible wormhole shadow silhouettes. The shadow profiles for the wormhole under the influence of the Yukawa gravitational potential are illustrated in Fig.7.24 for Model-I, Fig.7.25 for Model-II and Fig.7.26 for Model-III. From Figs.7.24 and 7.25, it can be observed that the radius of the wormhole shadow decreases as the parameters a and γ increase.

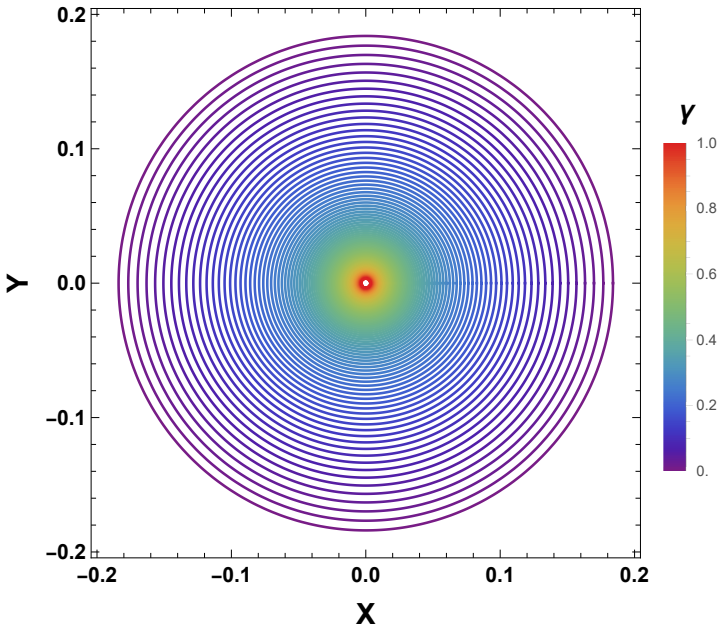

Fig. 7.25. The shadow silhouette is shown for varying values of the parameter γ, considering the parameter values for Model-II. Both are observed from the equatorial plane ($\theta_0 = \pi/2$) in the wormhole spacetime described by the Yukawa gravitational potential.

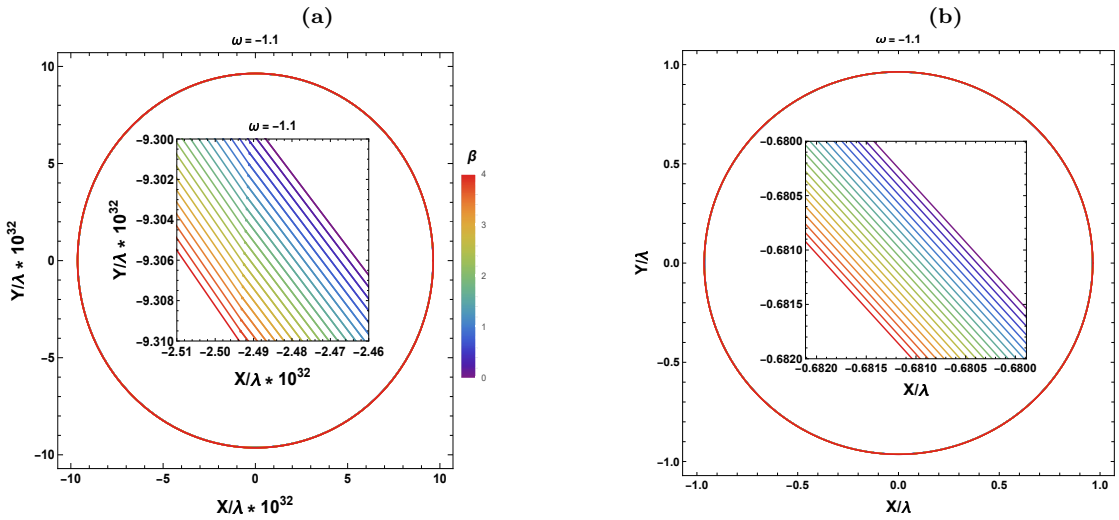

Fig. 7.26. The shadow silhouette of the wormhole Model-III is shown in X/λ-Y/λ plane with varying values of β by the considering the parameter value (a) $\lambda = 10^{11}$ and (b) $\lambda = 10^{44}$ as observed from the equatorial plane ($\theta_0 = \pi/2$) in the wormhole spacetime described by the Yukawa gravitational potential for $\omega = -1.1$.

To achieve a consistent shadow radius for Model-III, we express the celestial coordinates X and Y in dimensionless form, scaled by the wavelength λ as X/λ and Y/λ, respectively.

From Fig.7.26 for Model-III, it can be observed that the radius of the wormhole shadow increases as the parameter β increases, while the value of the graviton wavelength parameter

λ and ω(=-1.1) are held constant. This suggests that the Yukawa gravitational potential has a significant effect on the wormhole shadow.

7.7 Concluding Remarks

This chapter explores the impact of the Yukawa gravitational potential on the geometry of a wormhole in a galactic context, with a focus on traversable wormholes. These intriguing astrophysical objects, predicted by general relativity, theoretically link distant regions of spacetime. Although their existence has yet to be confirmed, traversable wormholes continue to be a subject of significant scientific inquiry. Theoretical models suggest that their existence requires an unusual type of energy, known as exotic matter, concentrated at the throat of the wormhole.

The current analysis presents three new wormhole solutions derived by considering two distinct redshift functions and one newly obtained redshift function based on the Yukawa gravitational potential. Notably, both newly calculated shape functions satisfy the necessary conditions for the existence of wormholes. All essential properties, including the flaring-out and flatness conditions, are met for various choices of parameters across Model-I, Model-II and Model-III. Embedded surface diagrams for the newly calculated wormhole solutions are provided. To examine the nature of matter, we analyzed the regional behavior of all energy conditions over different parameter ranges for the newly calculated wormhole solutions. It was observed that, in the majority of the parameter space, the energy conditions exhibit invalid or supportive regions, favoring the existence of the wormhole. The widespread violation of energy conditions in these regions confirms the presence of exotic matter, a crucial component for the existence of these new wormhole solutions. The stability analysis through the TOV equation has also been discussed in the current analysis for the Model-I, Model-II and Model-III.

Furthermore, we investigate the shadow cast due to the wormhole throat for the three new wormhole models. In this context, we assume the wormhole's throat acts as a photon sphere. It is concluded that, with all other parameters fixed, the parameters a for Model-I, γ for Model-II and β and $\omega = -1.1$ (phantom energy) for Model-III, under the Yukawa potential significantly affect the wormhole shadow.

Incorporating the Yukawa gravitational potential into wormhole models could further

expand our understanding by examining the impact of modified gravity on exotic spacetime structures, potentially offering observable signatures in the form of deviations in gravitational wave patterns. Through these models, researchers hope to bridge the gap between theoretical predictions and observational data, contributing to a deeper understanding of the universe's dark sector.

The shadow of a non-rotating wormhole was analyzed in detail in the this chapter, with its geometric and observational features thoroughly explored. In the subsequent chapter, attention is directed toward the shadow of a rotating wormhole, where the influence of spin on its shape and dynamics is examined.

Chapter 8

Shadows of Lorentzian Traversable Wormholes

8.1 Introduction

Apart from gravitational lensing effects [Cramer et al. (1995)], another possible method for probing wormholes is the usage of shadows (a dark region over a luminous contextual). One can recognize the shadow of a wormhole as the result of strong gravitational lensing generating a dark spot in the sky of a remote viewer. It is actually an optical look exhibited by the wormhole when there is a source of light from stars, accretion flows etc. around it. This manifestation has been investigated theoretically as well as observationally, by the application of very large baseline interferometry (VLBI) [Doeleman et al. (2008)] techniques at sub-mm wavelengths, for studying the shadow cast by supermassive objects, including the ongoing ambitious project involving Sagittarius A* in our galaxy center [Broderick et al. (2014)]. Being at sub mm wavelength this technique significantly reduces the interstellar scattering and may allow us to see beyond the compact synchrotron emitting region around $Sgr\ A^*$, since this region is expected to become optically thin at sub-mm wavelengths. Also, VLBI experiments can reach a resolution of the order of the angular size of the gravitational radius of $Sgr\ A^*$. Thus the spacetime geometry could be determined through the analysis of shadow in the vicinity of photon sphere. Similar ambitious projects include the Japanese VLBI Network (JVN), the Chinese VLBI Network (CVN), the Korean VLBI Network (KVN), the Chinese Space VLBI project [Li et al. (2007)].

Compact Objects can cause extreme local deflections of light and can bend light by an arbitrary large angle, causing the formation of light rings which are circular photon spheres, possessing distinct phenomenological signatures in terms of both electromagnetic and gravitational waves. And since this shadow outline depends on the gravitational lensing of nearby radiation, its proper surveillance can provide evidence about the parameters as well as spacetime geometry around the wormhole. Light propagation i.e. null geodesics in compact object (wormhole) spacetime can be perceived in two ways: trajectories which escape to distant observer and such that are apprehended by the compact object. Therefore, a black region appears in the viewer's sky, creating the shadow. The boundary of the shadow can be resolved by the wormhole spacetime metric itself, as it relates to the appearing shape of the photon detained orbits as observed by a remote viewer. Theoretically, although researchers seek to find an analytical closed form of the shadow edge, it is rarely possible to integrate the geodesic motion. In such cases the null geodesic equations have to be solved numerically. An efficient procedure involves a method called backwards ray-tracing, which requires the propagation of light rays from the observer backward in time and identifying their origin [Riazuelo (2019)], instead of evolving the light rays directly from a light source and detect the ones that reach the observer.

Ever since the remarkable image of the shadow of black holes, M87* at the center of the Virgo A galaxy was taken by Event Horizon Telescope in April 2019 [Akiyama et al. (2019) and Psaltis et al. (2020)], a new era of research on shadows of dark compact objects like black holes and wormholes have emerged. Following this, in 2020, [Kruglov (2020)] considered rational nonlinear electrodynamics and interpreted the super-massive $M87^*$ black hole as a regular (without singularities) magnetized black hole. The shadow observed from the center of $M87^*$ was consistent with the shadow generated through numerical simulation of a Kerr black hole of mass $(6.5 \pm 0.7)^9 M_\odot$ [Akiyama et al. (2019)]. This shadow can provide us with the properties of the black hole such as mass, spin, accretion disk and to verify the constraints on fundamental physics. The EHT data strongly suggest that the dimensionless spin parameter $a*$ is $\gtrsim 0.5$. This results in the non-existence of ultra-light boson of mass $\mu_b \sim 10^{-21}$eV, which was considered as a dark matter candidate in the distribution scales of $\sim$ kpc [Davoudiasl and Denton (2019)]. Vagnozzi and Visinelli (2019) used the $M87^*$ data to constraint the AdS_5 curvature radius in Randall-Sundrum AdS_5 brane-world.

Since in classical theory these black holes are not a source of radiation, the shadow actually targets exactly this feature, for lack of radiation. The shadow is an important observational evidence of the most standard problem in general relativity, the motion of light around compact objects. Earliest works on static Schwarzschild black hole shadows were done [Synge (1966)] and [Luminet (1979)]. The influence of charge on the measurements of shadow in case of Riessner-Nordström black hole were investigated [Zakharov (2014) and Zakharov et al. (2005b)]. Detailed study on rotating Kerr black hole were also conducted [Broderick and Loeb (2005), Falcke et al. (1999), Hioki and Maeda (2009), Takahashi (2004), and Zakharov et al. (2005a)]. Other pioneering works on black hole shadows include [Abdujabbarov et al. (2016a, 2017), Amarilla and Eiroa (2012, 2013), Amir and Ghosh (2016), Atamurotov et al. (2013a, 2013b, 2015), Cunha et al. (2015, 2018), Cunha et al. (2017), Dastan et al. (2016), de Vries (2000), Grenzebach et al. (2014), Hioki and Miyamoto (2008), Li and Bambi (2014), Papnoi et al. (2014), Saha et al. (2018), Shaikh (2019), Sharif and Iftikhar (2016), Shipley and Dolan (2016), Tsukamoto and Gong (2018), Wang et al. (2017), Wei and Liu (2013), Young (1976), Younsi et al. (2016), and Yumoto et al. (2012)]. The challenge of investigating the spacetime in the vicinity of the event horizon of a black hole, with angular resolution comparable to the event horizon, is almost a thing of the past. In fact direct detection of dynamics of matter at light speed and at strong gravity near a compact object is now almost possible. Very recently in 2020, shadow, quasinormal modes and quasiperiodic oscillations of rotating Kaluza-Klein black holes were investigated by [Ghasemi-Nodehi et al. (2020)], while Kala et al. (2020) studied the deflection of light and shadow cast by a dual-charged stringy black hole. Long et al. (2020) shown that the shadow size of disformal Kerr black hole in non-stealth rotating solutions in quadratic degenerate higher-order-scalar-tensor (DHOST) increases with a deformation parameter and the shape on both deformation and spin parameter. Quasi-normal modes and shadows of Schwarzschild and high-dimensional Einstein-Yang-Mills spacetimes were also discussed in [Guo and Miao (2020),Guo et al. (2020)].

While black holes continues to attract much attention, horizonless compact objects are fast gaining popularity recently in the literature for a number of reasons (for a review of the topic, see the recent work of [Cardoso and Pani (2019)]). One important class of horizonless objects are wormholes. Imaging the shadow of a wormhole may help to progress

observational investigation of differentiating the wormhole amongst other compact objects e.g. black holes, neutron stars etc. In an interesting paper in 2013, [Bambi (2013)] pointed out that there is insufficient evidence to confirm that the supermassive objects at the center of many galaxies, including our own, are in fact Kerr black holes. Instead exotic compact objects like wormholes might have been formed in the early universe. Though an exhaustive list of papers on wormhole shadows is not possible, yet [Abdujabbarov et al. (2016b), Azreg-Aïnou (2015), Lamy et al. (2018), Nedkova et al. (2013), Ohgami and Sakai (2015, 2016), Sarbach and Zannias (2012), and Vincent et al. (2021)] are many notable works. More recently, [Amir et al. (2019)] worked on the shadows of Kerr like wormholes and charged wormholes [Amir et al. (2019)] in Einstein-Maxwell-dilaton theory. Shadows of rotating wormholes were also investigated by [Gyulchev et al. (2018), Shaikh (2018) and Abdujabbarov et al. (2016b)]. Wielgus et al. (2020) constructed Reissner-Nordström (RN) wormhole by joining two different RN spacetime i.e. two different mass and charge. This kind of wormholes are not mirror-symmetric which affects the photon sphere and may have two photon rings to a distant observer. This doubling of photon ring was explained by doubling of effective potential maximum. However, mirror-symmetric wormholes can also have multiple photon rings and can exhibit interesting strong lensing effect [Shaikh et al. (2019a, 2019b) and Tsukamoto (2021)]. These recent ventures [Wang et al. (2020)] on the shadow of compact objects have inspired us to construct the shadow of wormholes, as well as, analyse the shape of the shadows.

8.2 The General Rotating Wormhole Spacetime

Let us consider a general stationary, axisymmetric spacetime metric, describing a Teo class rotating traversable wormhole [Teo (1998)] in Boyer-Linquist coordinates (t, r, θ, ϕ) as

$$ds^2 = -N^2 dt^2 + \left(1 - \frac{b}{r}\right)^{-1} dr^2 + r^2 K^2 \left[d\theta^2 + \sin^2\theta (d\phi - \omega\, dt)^2\right], \tag{8.2.1}$$

where,

- t, r, θ and ϕ : the spherical polar coordinates are defined by $-\infty < t < \infty$ and $r_0 \leq r < \infty$, $0 \leq \theta \leq \pi$ and $0 \leq \phi \leq 2\pi$ and in general,

- N, b, K and ω : the metric functions depend only on r and θ.

The orbits of the timelike and the spacelike Killing fields ($t^\mu\partial_\mu = \partial_t$ and $\phi^\mu\partial_\mu = \partial_\phi$ respectively) represent in terms of the parameters t and ϕ. This metric is actually a generalized rotating form of the static Morris-Thorne wormhole metric [Morris and Thorne (1988)]. Therefore, the metric functions must have some restrictions, which lead to the specific geometry and significant properties of the wormhole.

- N : The function which regulates the gravitational redshift is often called a redshift function. In order for the wormhole to be traversable, one has to ensure that there are no curvature singularities or event horizons. Therefore, the redshift function N should be nonzero and finite all over the region, i.e. from the throat to the spatial infinity.

- b : The function is known as the shape function which regulates the shape of the wormhole. It is always non-negative and possesses an apparent singularity at $r = r_0 = b \geq 0$, which is associated with the throat of the wormhole. The function b should be independent of θ to avoid any curvature singularity at the throat i.e. it obeys the restriction $\frac{\partial b(r,\theta)}{\partial\theta} = 0$. An important constraint is the flare-out condition at the throat: $\partial_r b|_{r=r_0} < 1$, while $b(r) < r$ near the throat.

- $K(r,\theta)$: Function is a regular, positive and non-decreasing function, defining the proper radial distance $R = rK$, measured at (r,θ) from the origin. Actually it regulates the area radius given by R.

- ω : The function is associated with the angular velocity of the wormhole.

Also to confirm that metric Eq.(8.2.1) is regular on the rotation axis $\theta = 0,\ \pi$, the derivatives of N and K with respect to θ should vanish on it, i.e. $\frac{\partial N(r,\theta)}{\partial\theta} = 0$, $\frac{\partial K(r,\theta)}{\partial\theta} = 0$. Although, a wide variety of choices for the metric functions N, K, b and ω can be freely adopted, we emphasize that all the solutions do not correspond to wormhole physics. One must choose such metric functions which satisfy the above-mentioned regularity conditions. That class of solutions are the certain cases of the rotating Teo wormhole. In this study the specific type of solutions will be considered, where entire metric coefficients are functions of radial coordinate r only. These solutions reduce to the static wormhole for zero rotation, i.e. when $\omega = 0$.

Recently, [Konoplya and Zhidenko (2016)] studied quasinormal rings of a wormhole, which rings like the Schwarzschild or the Kerr black holes and its metric is similar to Eq.(8.2.1). The specific form of g_{tt} and the shape function $b(r)$ are given by

$$N = \sqrt{1-\frac{2M}{r}}, \quad b(r) = \frac{r_0^2 + 2M(r-r_0)}{r}, \quad \omega = \frac{2J}{r^3} = \frac{2aM^2}{r^3}, \quad K = 1. \tag{8.2.2}$$

Here

- a : The spin parameter, $a = J/M^2$.
- M : Mass of the wormhole.
- r_0 : The throat of the wormhole, $r_0 \geq 2M \geq 0$.

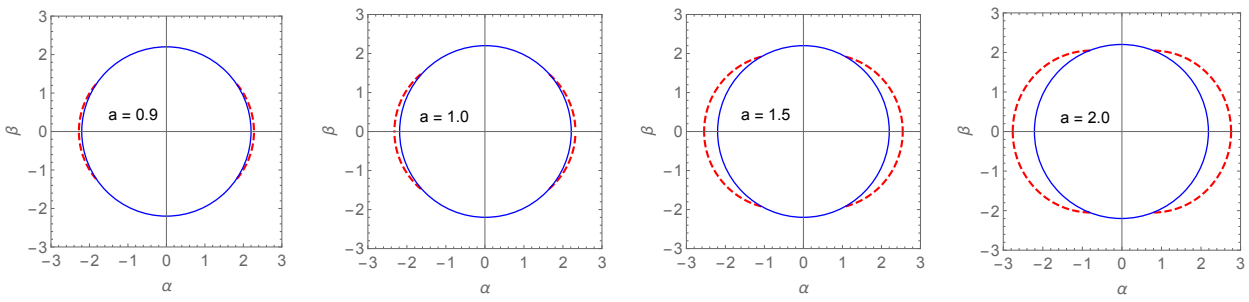

Fig. 8.1. Schematic diagram of ergosphere. The region between the ergosurface (red-dashed curve) and the wormhole throat (blue circle) is the ergoregion.

8.2.1 Ergoregion of Wormhole

The ergosphere is the outer region of a rotating black hole where spacetime is dragged around by the black hole's rotation. This dynamic boundary encloses the ergoregion, the space within which the dragging effect is so profound that all objects are compelled to move in the direction of the black hole's spin, regardless of whether they are falling into it. An ergoregion may be present around the throat of a rotating wormhole. This region can be determine when $g_{tt} = -(N^2 - \omega^2 r^2 \sin^2\theta) \geq 0$ and the ergosurface by $g_{tt} = 0$. The ergosurface for the metric Eq.(8.2.1) is given by

$$N^2 - \omega^2 r^2 K^2 \sin^2\theta = 0. \tag{8.2.3}$$

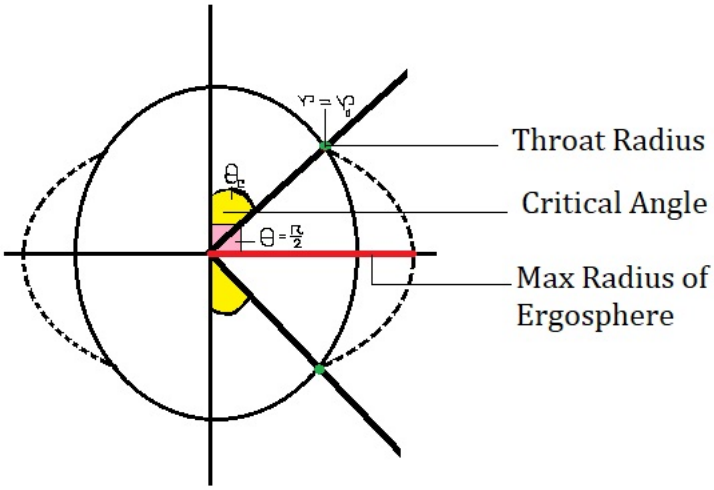

Fig. 8.2. Schematic diagram of ergosphere of the wormhole.

Since the ergoregion doesn't extent up to the poles $\theta = 0$ and $\theta = \pi$, there exist a critical angle θ_c, where the ergosphere exists in between θ_c and $\pi - \theta_c$, for all $0 < \theta_c \leq \pi/2$. This critical angle can determined at the throat of the wormhole using Eq.(8.2.3) as

$$\sin\theta_c = \left|\frac{N_0}{\omega_0 r_0 K_0}\right| \tag{8.2.4}$$

Further, the ergosphere will only exist when the spin parameter a crosses a critical limit a_c, corresponding to $\sin\theta_c = 1$ or $\omega_c = N_0/r_0K_0$. For the wormhole metric Eq.(8.2.2) with $M = 1$ and $r_0 = 2.2$, the critical value is $a_c = 0.729657$. The ergosphere for these values can be seen in Fig.8.1. A schematic diagram of ergosphere of the wormhole is given in Fig.8.2 depicting the critical angle(θ_c) and maximum radius of ergosphere with respect to the throat radius.

8.3 Propagation of light in a Rotating Wormhole Spacetime

When a wormhole is between a star (bright source of light) and a viewer, the light comes to the viewer after being deviated by the gravitational field of wormhole. However, certain portion of the photons (with small impact parameters) emanated by the star end up falling

into the wormhole, i.e. not able to reach the observer, giving as a result, a dark sector in the sky dubbed as shadow. The boundary of the shadow apparently is determined by unstable circular photon orbits. In order to find the unstable orbit, one is required to study the geodesic configuration.

The motion of a photon in the rotating wormhole spacetime Eq.(8.2.1) can be described by the Lagrangian, ($\mathbf{Ł} = \frac{1}{2} g_{\mu\nu}\dot{x}^{\mu}\dot{x}^{\nu}$) as

$$\mathbf{2Ł} = -N^2\dot{t}^2 + \frac{\dot{r}^2}{1-b/r} + r^2K^2[\ \dot{\theta}^2 + \sin^2\theta(\dot{\phi}-\omega\dot{t})^2\ ]. \tag{8.3.1}$$

Here an overdot denotes the derivative with respect to the affine parameter λ. Here the Lagrangian does not depend on t and ϕ, as a result, there are only two constants of motion, which are the energy E and the angular momentum L in the direction of the axis of symmetry of the photon.

$$\begin{aligned} p_t &= \frac{\partial \mathbf{Ł}}{\partial \dot{t}} = -N^2\dot{t} - \omega r^2K^2\sin^2\theta(\dot{\phi}-\omega\dot{t}) = -E, \\ p_\phi &= \frac{\partial \mathbf{Ł}}{\partial \dot{\phi}} = r^2K^2\sin^2\theta(\dot{\phi}-\omega\dot{t}) = L. \end{aligned}$$

These two equations yield

$$\dot{t} = \frac{E-\omega L}{N^2}, \quad \dot{\phi} = \frac{L}{r^2K^2\sin^2\theta} + \frac{\omega(E-\omega L)}{N^2}. \tag{8.3.2}$$

Now, the r and θ-component of the momentum are calculated as,

$$p_r = \frac{\partial \mathbf{Ł}}{\partial \dot{r}} = \frac{\dot{r}}{1-\frac{b}{r}}, \quad p_\theta = \frac{\partial \mathbf{Ł}}{\partial \dot{\theta}} = r^2K^2\dot{\theta}. \tag{8.3.3}$$

To achieve a general formula for finding the contour of a shadow Hamilton-Jacobi method is used for the null geodesic equations in the general rotating spacetime Eq.(8.2.1). The Hamilton-Jacobi method determines the geodesics via the equation

$$\frac{\partial S}{\partial \lambda} = -\frac{1}{2} g^{\mu\nu}\frac{\partial S}{\partial x^{\mu}}\frac{\partial S}{\partial x^{\nu}}, \tag{8.3.4}$$

where, λ is the affine parameter along the geodesics, $g_{\mu\nu}$ are the components of the metric

tensor and S is the Jacobi action with the following separable ansatz,

$$S = \frac{1}{2}\mu^2\lambda - Et + L\phi + S_r(r) + S_\theta(\theta), \tag{8.3.5}$$

where, S_r and S_θ are the functions of r and θ, respectively and μ is the mass of the test particle. For photons, $\mu = 0$. Here the rotating wormhole metric functions N, b, K and ω, depend only on the radial coordinate, therefore, following [Nedkova et al. (2013)], the Hamilton-Jacobi equation will be separable. Inserting Eq.(8.3.5) into Eq.(8.3.4) one can obtain the following equations for the functions $S_r(r)$ and $S_\theta(\theta)$ [Nedkova et al. (2013)]

$$\left(\frac{dS_\theta}{d\theta}\right)^2 = Q - \frac{L^2}{\sin^2\theta}, \tag{8.3.6}$$

$$\left(1 - \frac{b}{r}\right) N^2 \left(\frac{dS_r}{dr}\right)^2 = (E - \omega L)^2 - \left(\mu^2 N^2 + Q\frac{N^2}{r^2K^2}\right), \tag{8.3.7}$$

where, Q is the Carter constant.

It's known $p_r = \frac{\partial S}{\partial r} = \frac{dS_r}{dr}$ and $p_\theta = \frac{\partial S}{\partial \theta} = \frac{dS_\theta}{d\theta}$, therefore, Eqs.(8.3.3), (8.3.6) and (8.3.7) yield [Nedkova et al. (2013)],

$$\frac{N}{\sqrt{1 - b/r}}\frac{dr}{d\lambda} = \pm\sqrt{R(r)}, \quad r^2K^2\frac{d\theta}{d\lambda} = \pm\sqrt{T(\theta)}, \tag{8.3.8}$$

where,

$$T(\theta) = Q - \frac{L^2}{\sin^2\theta}, \tag{8.3.9}$$

$$R(r) = (E - \omega L)^2 - \left(\mu^2 N^2 + Q\frac{N^2}{r^2K^2}\right). \tag{8.3.10}$$

Hence, the Jacobi action assumes the following form,

$$S = \frac{1}{2}\mu^2\lambda - Et + L\phi + \int \sqrt{\frac{R(r)}{N^2(1 - b/r)}}\, dr + \int \sqrt{T(\theta)}\, d\theta. \tag{8.3.11}$$

The geodesic equations in stationary and axisymmetric spacetimes are parameterized by the constants of motions E, L and Q. However, the geodesic motion of a photon is described

by two independent parameters defined by

$$\xi = \frac{L}{E}, \quad \eta = \frac{Q}{E^2}.$$

Here, ξ and η are known as impact parameters and a new affine parameter $\widetilde{\lambda} = \lambda E$. After eliminating the energy from the geodesic equations, the path of the photon is parameterized only by ξ and η. One can write the functions $R(r)$ and $T(\theta)$ in terms of the impact parameters as,

$$R(r) = (1 - \omega\xi)^2 - \eta\frac{N^2}{r^2K^2}, \tag{8.3.12}$$

$$T(\theta) = \eta - \frac{\xi^2}{\sin^2\theta}. \tag{8.3.13}$$

For a photon $\mu = 0$.

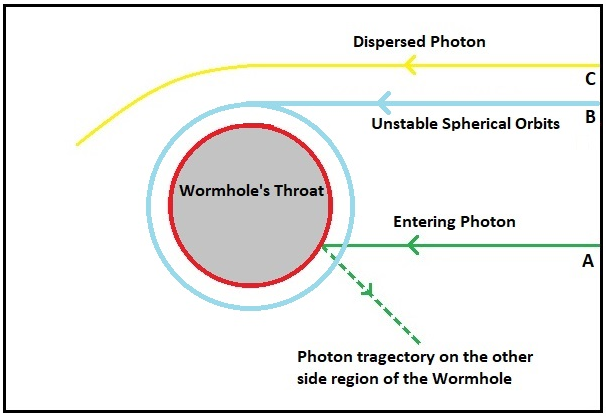

Fig. 8.3. Schematic diagram of the photon orbits around the wormholes.

8.4 Wormhole Shadow

Two regions of spacetime are joined through wormhole (a tunnel-like structure, without any horizon or singularity within it). Let us assume that the photons are coming from a star towards the wormhole, (placed between the observer and the star) and illuminate one region and no light sources are remaining in the neighborhood of the throat in the other region. In the first region, the possible orbit of the photons around the wormhole

are as follows: (i) orbits entering into the wormhole and passing through its throat (ii) dispersed from the wormhole to infinity. A remote viewer will be capable of observing only dispersed photons from the wormhole (see Fig.8.3). However the photon apprehended by the wormhole will form a dark patch. This dark region detected on the bright background is known as shadow of the wormhole. To find the wormhole shadow, i.e. dark region in the viewer's atmosphere in the presence of a shiny background, one would have to start finding out the critical orbits that separate the evading and falling photons. Actually the prime motive is to estimate these critical geodesics or unstable circular orbits. In order to acquire the boundary of the wormhole shadow, one needs to study the radial motion of photons around the wormholes. The critical orbits (described by certain critical values of the impact parameters ξ and η) distinguish the dispersed and apprehended photons. A slight disturbance in these critical values can change it either to a seepage or to a apprehend orbit. As a result, the critical impact parameters describe the boundary of a shadow. Thus the boundary of the shadow is determined by the unstable circular photon orbits. By studying the radial geodesic equation, one can calculate the critical orbit, which can be expressed in the form of an energy conservation equation,

$$\left(\frac{dr}{d\bar{\lambda}}\right)^2 + V_{eff} = 1, \quad V_{eff} = 1 - \frac{1}{N^2}\left(1 - \frac{b}{r}\right) R(r), \tag{8.4.1}$$

where, V_{eff} is the effective potential that describes the geodesic motion of a photon around the wormhole. The null geodesics are divided into two classes depending on their impact parameters: (i) trajectories of photon passing through the wormhole (ii) orbits of the photon dispersing to infinity. The boundary among the two classes is destined through a family of unstable spherical orbits fulfilling the following conditions,

$$V_{eff} = 1, \quad \frac{V_{eff}}{dr} = 0, \quad \frac{d^2 V_{eff}}{dr^2} \leq 0. \tag{8.4.2}$$

The first condition comes from the fact that the radial motion has a turning point $dr/d\bar{\lambda} = 0$, when the photon will scatter from the wormhole. The last conditions are due to the maximum of the effective potential for the critical orbit between seepage and plunge motion.

While writing down the above conditions in terms of $R(r)$, one could assume that the

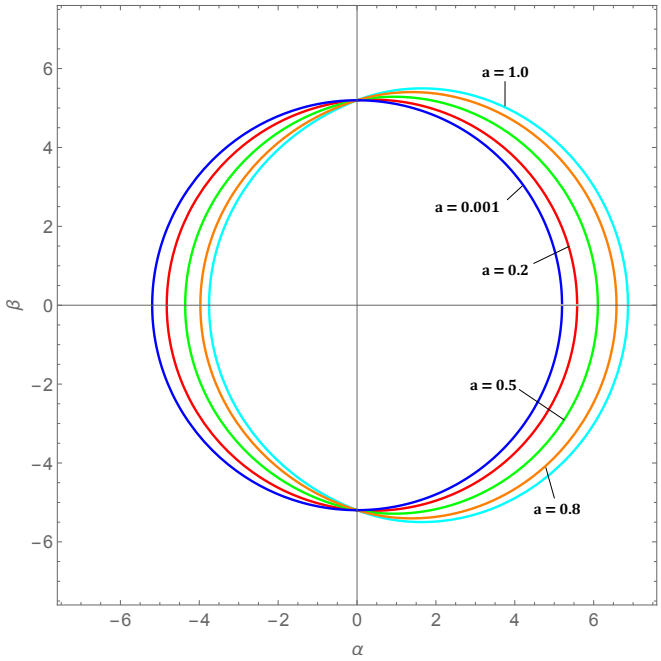

Fig. 8.4. Shadow of a wormhole for different a and $r_0 = 2.5$. The axes are in units of M.

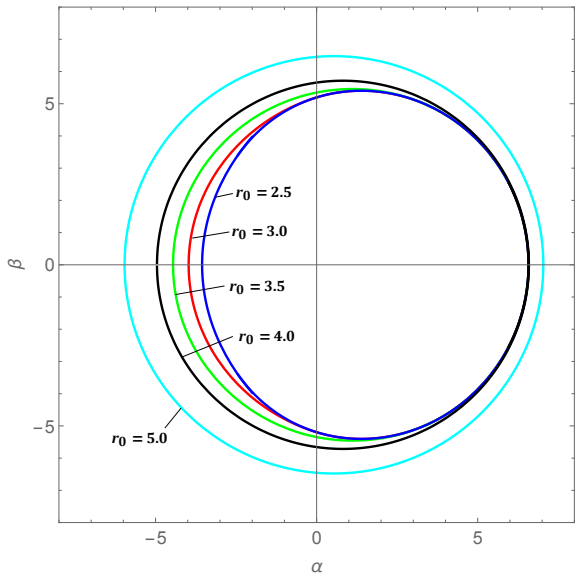

Fig. 8.5. Shadow of a wormhole for different r_0 and $a = 0.8$. The axes are in units of M.

functions N and $(1-\frac{b}{r})$ are finite and non-zero outside the throat of the wormhole. Therefore, for the unstable circular orbits lying outside the throat, i.e., having radii greater than r_0, the above set of conditions can be written in terms of $R(r)$ as,

$$R(r) = 0, \quad \frac{dR}{dr} = 0, \quad \frac{d^2R}{dr^2} \geq 0. \tag{8.4.3}$$

Using the equations $R(r) = 0, \quad dR/dr = 0$, one can easily find two expressions for the impact parameters ξ and η in terms of the radial coordinate of the unstable circular orbit as,

$$\eta = \frac{r^2K^2}{N^2}(1-\omega\xi)^2, \tag{8.4.4}$$

$$\xi = \frac{\Sigma}{\Sigma\omega - \omega'}, \quad \Sigma = \frac{1}{2}\frac{d}{dr}\ln\left(\frac{N^2}{r^2K^2}\right). \tag{8.4.5}$$

Here, prime denotes the differentiation with respect to radial coordinate r. This process of finding the location of the unstable spherical orbits in the impact parameter space as given in Eqs.(8.4.4) and (8.4.5) was originally derived in [Nedkova et al. (2013)]. However, it has been shown that a wormhole throat can act as a natural location of unstable circular orbits [Shaikh et al. (2019a)]. For such unstable orbits, $(1 - b/r)$ vanishes and hence, $V_{eff} = 1$ is automatically satisfied. Therefore, for unstable circular orbits located at the throat, the second conditions in Eq.(8.4.2) can be reduced to [Shaikh (2018)],

$$(1-\omega_0\xi)^2 - \eta\frac{N_0^2}{r_0^2K_0^2} = 0, \tag{8.4.6}$$

where, the subscript '0' implies that the functions are evaluated at the throat.

For the set of unstable photon orbits, Eqs.(8.4.4), (8.4.5) and (8.4.6) express the critical locus of the impact parameters. In other words, these equations express the boundary of the shadow in the impact parameter space. However, for true observation, the remote viewer will see the apparent shape of a shadow in his sky (a plane passing through the center of the wormhole and normal to the line linking it with the viewer). The celestial coordinates connected to the actual astronomical measurements that span a two-dimensional plane are

defined as [Vazquez and Esteban (2004)],

$$\alpha = \lim_{r_o\to\infty}\left(-r_o^2\sin\theta_o\left[\frac{d\phi}{dr}\right]_{(r_o,\theta_o)}\right), \tag{8.4.7}$$

$$\beta = \lim_{r_o\to\infty}\left(r_o^2\left[\frac{d\theta}{dr}\right]_{(r_o,\theta_o)}\right), \tag{8.4.8}$$

where,

- r_o : The position coordinate of the remote viewer taken very large (far away from the wormhole).
- θ_o : The angular coordinate. It is actually the angle of inclination between the axis of symmetry of the wormhole and the direction to the viewer.

The celestial coordinates α and β are the discernible perpendicular distances of the shadow image, as observed from the rotation axis and from its projection on the equatorial plane respectively. Using the geodesic equations and values of the four-velocity components and after some simple algebraic manipulation, the celestial coordinates assume the following forms

$$\alpha = -\frac{\xi}{\sin\theta_0}, \tag{8.4.9}$$

$$\beta = \left(\eta - \frac{\xi^2}{\sin^2\theta_0}\right)^{1/2}. \tag{8.4.10}$$

After knowing the expressions of celestial coordinates and impact parameters, one can construct the shadow of wormholes. In the (α,β)-plane, Eqs.(8.4.4), (8.4.5), (8.4.9) and (8.4.10) define the part of the shadow boundary formed by the unstable circular orbits which lie outside the throat. However, the part of the shadow boundary formed due to the unstable circular orbits which are located at the throats are obtained from Eqs.(8.4.6), (8.4.9) and (8.4.10),

$$(N_0^2 - \omega_0^2 r_0^2 K_0^2\sin^2\theta_{obs})\alpha^2 - 2\omega_0 r_0^2 K_0^2\sin\theta_{obs}\,\alpha - r_0^2K_0^2 + N_0^2\beta^2 = 0. \tag{8.4.11}$$

Therefore, the complete contour of the shadow is given by the combination of Eqs.(8.4.9)-

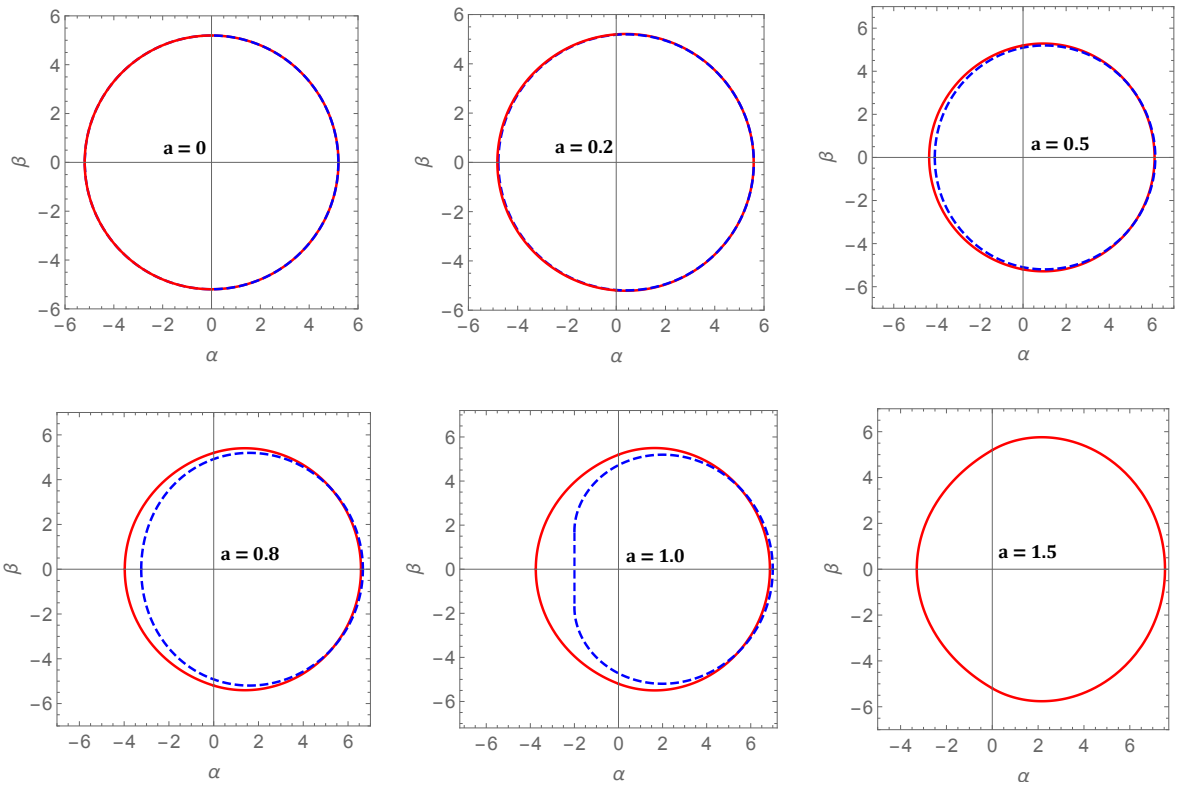

Fig. 8.6. Shadow of a wormhole (red solid curve) and a Kerr black hole (blue dashed curve) for different a. Here $r_0 = 3.0$. The axes are in units of M.

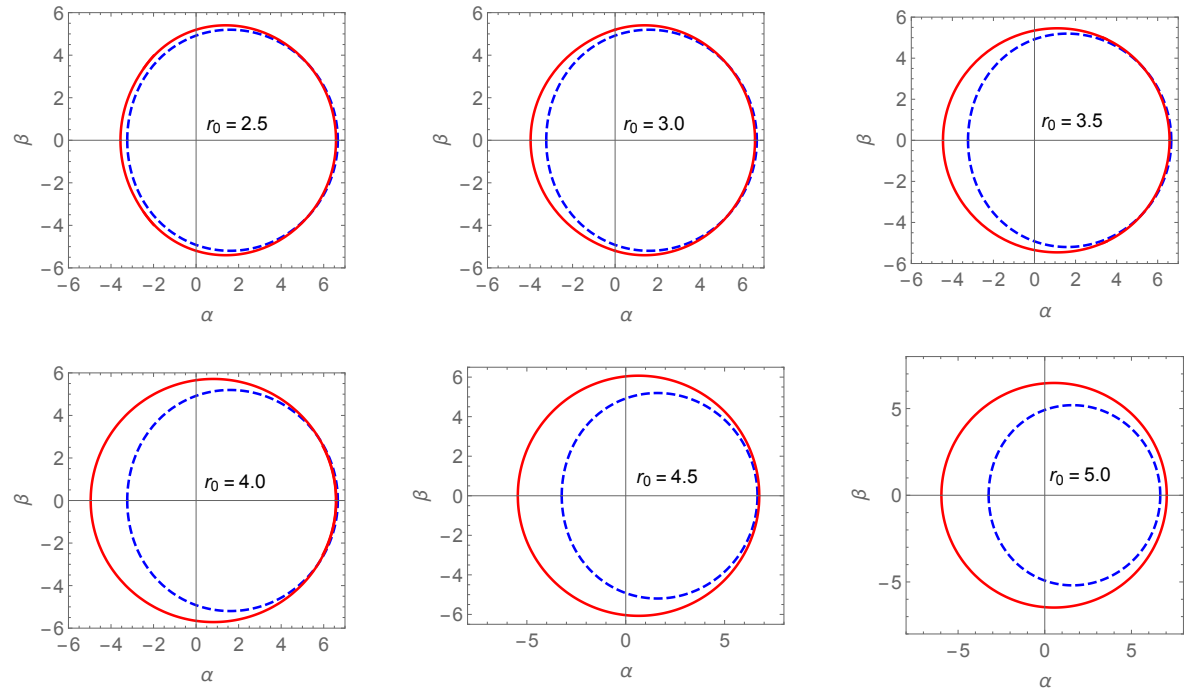

Fig. 8.7. Shadow of a wormhole (red solid curve) and a Kerr black hole (blue dashed curve) for different r_0. Here $a = 0.8$. The axes are in units of M.

(8.4.10) $\Big($with ξ and η given by Eqs.(8.4.4) and (8.4.5)$\Big)$ and Eq.(8.4.11) [Shaikh (2018)].

Figs.8.4 and 8.5 show the shadow the wormhole given above for different values of the spin and throat size. Note that, for a given wormhole size r_0, the shadow shape deviates from circularity as the spin a increases (see Fig.8.4). On the other hand, for a given spin a, the shadow becomes more and more circular as the wormhole size r_0 increases (see Fig.8.5). The results have been compared with those of a Kerr black hole in Figs.8.6 and 8.7. Note that, for small spin and smaller wormhole size, its shadow mimics those of the black hole. However, with increasing either the spin or the throat size, the shadow of a wormhole start deviating from that of a Kerr black hole. Detection of such deviation may possibly indicate the presence of a wormhole.

8.5 Constraining the Wormhole Parameters Using the M87* Results

The size and the spin of the wormhole are now constrained using the results from $M87^*$ observation [Akiyama et al. (2019)]. For this purpose, the average angular size of the shadow and its deformation from circularity are used. Since the shadow has reflection symmetry with respect to the α-axis, its geometric center (α_c, β_c) is given by $\alpha_c = 1/A \int \alpha \; dA$ and $\beta_c = 0$, dA being an area element. At first, an angle ϕ is defined between the α-axis and the vector connecting the geometric centre (α_c, β_c) with a point (α, β) on the boundary of a shadow. Therefore, the average radius R_{av} of the shadow is given by [Bambi et al. (2019)]

$$R_{av}^2 = \frac{1}{2\pi} \int_0^{2\pi} l^2(\phi) \; d\phi, \tag{8.5.1}$$

where, $l(\phi) = \sqrt{[\alpha(\phi) - \alpha_c]^2 + \beta(\phi)^2}$ and $\phi = \tan^{-1}[\beta(\phi)/(\alpha(\phi) - \alpha_c)]$. Following [Akiyama et al. (2019)], the deviation ΔC from circularity is defined as,

$$\Delta C = \frac{1}{R_{av}} \sqrt{\frac{1}{2\pi} \int_0^{2\pi} (l(\phi) - R_{av})^2 \; d\phi}. \tag{8.5.2}$$

Note that ΔC is the fractional root mean square (RMS) distance from the average radius of the shadow.

According to EHT collaboration [Akiyama et al. (2019)], the angular size of the observed

shadow is $\Delta\theta_{sh} = 42 \pm 3\ \mu$ as and the deviation ΔC is less than 10%. Also, following [Akiyama et al. (2019)], it's taken, the distance to $M87^*$ to be $D = (16.8 \pm 0.8)$ Mpc and the mass of the object to be $M = (6.5 \pm 0.7) \times 10^9 M_\odot$. These numbers imply that the average diameter of the shadow should be,

$$\frac{d_{sh}}{M} = \frac{D\Delta\theta_{sh}}{GM} = 11.0 \pm 1.5, \tag{8.5.3}$$

where the errors have been added in quadrature. The above quantity must be equal to $\frac{2R_{av}}{M}$. In Fig.8.8, the average diameter and the deviation from circularity of the shadow for different values of the spin and the wormhole throat size are shown. Here, the inclination angle is taken to be $\theta_o = 17°$, which the jet axis makes to the line of sight [Akiyama et al. (2019)]. Also, according to EHT collaboration, the spin lies within the range $0.5 \leq a_* \leq 0.94$, where $a_* = a/M$. Note that, for this spin range, the diameter of the shadow is always greater than the minimum allowed value of 9.5. However, the diameter will be within the maximum allowed value 12.5 if the wormhole throat size is restricted below some critical value $r_0 \leq r_{0c} = 4.76M$. Note that the deviation from circularity is always less than 2.75%, i.e., $\Delta C \leq 0.0275$ for the allowed throat size $r_0 < r_{0c} = 4.76M$ and spin range $0.5 \leq a_* \leq 0.94$.

Here it should be noted that, using integrable geodesic equations, shadows of rotating traversable wormhole geometries which belong to the class same as this chapter but with different forms of the metric functions were successfully studied in many prior works like references [Nedkova et al. (2013), Gyulchev et al. (2018), Shaikh (2018)] and similar conclusions about the dependency of the shadow boundary on the wormhole spin were obtained. However, these works did not considered constraining the wormhole parameters using observational data. In this work here, along with studying the dependence of the shadow on the wormhole spin as well as on the wormhole throat size, the parameters have been constrained using the $M87^*$ results.

8.6 Concluding Remarks

In this chapter, the shadow of a rotating traversable wormhole has been investigated and the results are compared with those of Kerr black hole of same mass and spin. The results

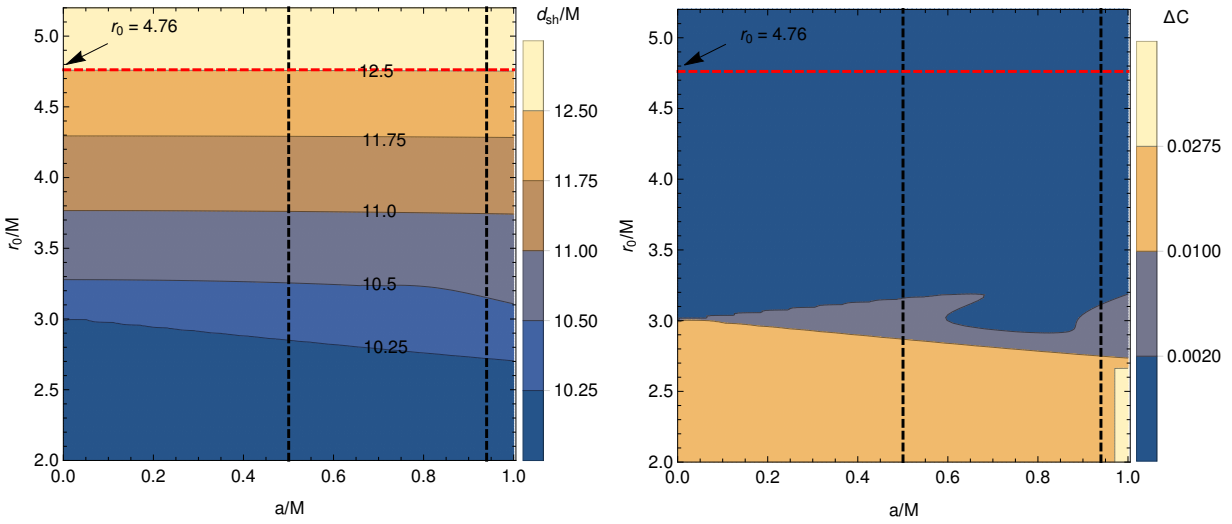

Fig. 8.8. Dependence of the angular size and the deviation of the shadow on r_0 and spin. The region between the two black dashed vertical lines indicate the spin range $0.5 \leq a_* \leq 0.94$. The horizontal red dashed line indicates the critical throat size $r_{0c} = 4.76M$, below which both the size and deviation from circularity of the shadow is consistent with the $M87^*$ results.

obtained here will have several implications in the study of shadow. The throat of a wormhole plays very crucial role in shadow formation. It's found that, for small spin and smaller wormhole throat size, the shadow of a wormhole mimics those of the black hole. However, with increasing either the spin or the throat size, the shadow of a wormhole start deviating from that of a black hole. Detection of such deviation may possibly indicate the presence of a wormhole. In Sec.8.5, the size and the spin of the wormhole has been constrained, using the results from $M87^*$ observation [Akiyama et al. (2019)]. In Fig.8.8, the average diameter and the deviation from circularity of the shadow for different values of the spin and the wormhole throat size are shown, taking inclination angle to be $\theta_o = 17°$, which the jet axis makes with the line of sight. Note that, the spin lies within the range $0.5 \leq a_* \leq 0.94$, where $a_* = a/M$ and the diameter of the shadow is always greater than the minimum allowed value of 9.5. However, the diameter will be within the maximum allowed value 12.5, if the wormhole throat size is restricted below some critical value $r_0 \leq r_{0c} = 4.76M$. Also, the deviation from circularity is always less than 2.75%, i.e., $\Delta C \leq 0.0275$ for the allowed throat size $r_0 < r_{0c} = 4.76M$ and spin range $0.5 \leq a_* \leq 0.94$. In other words, the results obtained here indicate that a wormhole having reasonable spin or throat size, can be distinguished from a black hole through observations of their shadow. Also worth noting a recent paper by [Gralla et al. (2019)] in which the emission profile originating near a black hole has been

discussed and the "photon rings" surrounding the dark black hole shadow has been studied, including the implications of the recent $M87^*$ Event Horizon Telescope observations and mass measurement on it. Previous studies claimed that the observed emission will peak near the photon ring, but this suggested otherwise. Distinguishing between a "photon ring" (light rays that complete at least $n = 5/4$ orbits) and a "lensing ring" (light rays that complete between 3/4 and 5/4 orbits); it showed that, for optically thin emission, "photon ring" produced a sharp feature near the critical impact parameter but the peak is so narrow and the brightness being logarithmic, it never makes a significant contribution to the observed flux.

Chapter 9

Summary of This Research Work and Future Directions

Researching compact stars, black holes and wormholes is essential for understanding the universe's most extreme environments, pushing the boundaries of physics. These objects allow us to test fundamental theories like general relativity and quantum mechanics such as black holes challenge our understanding of gravity and neutron stars offer insights into matter at extreme densities. They are also key to study astrophysical phenomena like gravitational waves. Wormholes, though hypothetical, open possibilities for exploring the nature of spacetime. This research not only addresses profound scientific questions but also drives technological innovation and inspires broader curiosity about the cosmos.

9.1 Summary

Chapter.2: In this chapter, a compact star model composed of Bose-Einstein Condensate (BEC) matter is modeled, satisfying a polytropic equation of state (EoS) with $\gamma = 2$ and a specific density profile. The model is tested through various physical criteria like non-singular pressure and density, energy conditions, causality condition etc. Additionally, stability is examined using the Bondi criterion, hydrostatic equilibrium and static stability criterion. The stiffness of the EoS, stability, adiabatic index and maximum mass M_{max} are found to depend on a single parameter k. As k increases, the central adiabatic index

Γ decreases near 4/3 and the compactness approaches 4/9 while the mass sustained with increasing central density due to radial perturbation decreases. This indicates that the system undergoes gravitational collapse sooner as k increases. Furthermore, it is demonstrated that this new category of compact star also follows that constraints provided by GW 170817 event. The possibility of a distinct category of compact stars composed of BEC matter, capable of mimicking neutron stars, is proposed.

Chapter.3: The primary objective of this chapter is to obtain analytically relativistic quintessence anisotropic spherical solutions within the $f(T)$ paradigm. To achieve this, the pressure anisotropy condition is imposed and a metric potential of the Tolman-Kuchowicz (TK) type is employed. Additionally, it is assumed that the current model incorporates a quintessence field characterized by a parameter ω_q, along with the anisotropic matter distribution. In the presence of the parameter α, the field equations are modified by the choice of the $f(T)$ function. The $f(T)$ gravity parameter α introduces new components to the basic physical characteristics, such as density, pressure, subliminal sound velocity and surface redshift of the present model. By selecting the compact star $HerX-1$ and varying α from 0.5 to 2.5, all the physical characteristics of the model parameter of the configuration are examined. It is demonstrated through the graphical process that a more compact object is produced with greater values of α. The hydrostatic equilibrium condition of the model is discussed and the mass-radius relationship for the current model is obtained.

Chapter.4: An exact solution to the Einstein field equations is presented, featuring a static, spherically symmetric, anisotropic compact stellar fluid sphere with non-zero complexity. The model is constructed using a specific metric potential for the g_{tt} component, along with a defined complexity profile. The model parameters are fixed by ensuring the continuity of the interior and exterior metrics across the surface of the star and by setting the radial pressure to zero across the boundary. The stability of the model has been analyzed by verification of different standard conditions. Validation of our model is supported by recent observational data from well-known pulsars.

Chapter.5: A charged, non-rotating, spherically symmetric black hole with cosmologi-

cal constant Λ (Reissner-Nordström+Λ or RN+Λ), active gravitational mass M and electric charge Q is studied in an exterior Friedmann-Robertson-Walker (FRW) universe in (2+1) dimensional spacetime. New classes of exact solutions for the charged black hole are found. It is discovered that the cosmological constant is negative inside the black hole, which is confirmed through the geodesic equations as well. The cosmological constant is found to depend on R, Q and $a(v)$, which correspond to the areal radius, charge of the black hole and the scale factor of the universe, respectively. It is noted that the expansion of the universe affects the size and mass of the black hole. An important observation is that, for an observer at infinity, both the mass and charge of the black hole increase with the contraction of the universe and decrease with the expansion of the universe.

Chapter.6: The astrophysical consequences of black holes in quadratic gravity is investigated, characterized by the parameters S_0, S_2, m_0 and m_2, in addition to the black hole mass M. To evaluate the physical validity of the fundamental quadratic gravity black hole like solutions, their gravitational lensing properties are analyzed in the strong field regime. Specifically, the shadows are examined and are constrained using observational data from the $M87^*$ and $SgrA^*$ supermassive black holes. Our analysis reveals that, within the 1σ confidence level, a significant portion of the parameter space for quadratic gravity black holes is consistent with the Event Horizon Telescope (EHT) observations of $M87^*$ and $SgrA^*$. As an additional observational test, a detailed investigation of the strong gravitational lensing properties of these black holes is performed. The fundamental strong lensing observables are explored in detail, including the angular positions and separations of the lensed images, the relative magnifications, the radius of the outermost Einstein ring and the relativistic time delay between images.

Chapter.7: This study aims to identify wormholes within newly derived wormhole solutions in the context of the Yukawa gravitational potential. This type of study may help to indicate the presence of a wormhole in a galactic region. The three newly calculated wormhole solutions satisfy all the required properties. In reasonable ranges, null energy conditions are violated to the requirement of wormhole structure. Further, the embedding surface and its revolution have been generated using numerical methods to investigate how

the length of the throat is influenced by the parameter β in the context of wormhole geometry under the effects of the Yukawa gravitational potential. The wormhole solutions for the wavelength λ are determined to be physically stable when we evaluate the stability of these wormhole solutions graphically. Since Yukawa-modified potential acts as a contribution of dark matter in the galactic region, it is concluded that wormhole solutions exist with viable physical properties in the galactic region comprising with the Yukawa gravitational potential. We investigate the shadow by the wormhole throat for all the three models. Here it is considered that the wormhole throat acts as a photon sphere. Keeping all other parameters fixed, it is observed that the parameters a for Model-I, γ for Model-II and β for Model-III with Yukawa gravitational potential significantly affect the wormhole shadow.

Chapter.8: The prospect of identifying wormholes by investigating their shadows constitutes a foremost source of insight into the evolution of compact objects and is considered one of the essential problems in contemporary astrophysics. The nature of the wormholes plays a crucial role in the shadow effect, which arises during strong gravitational lensing. Current EHT observations have inspired scientists to study and construct the shadow images of wormholes. In this work, the shadow cast by a certain class of rotating wormholes is explored. To achieve this, the null geodesics are first composed and the effects of various parameters on the photon orbit are studied. The form and size of the wormhole shadow are exposed, revealing that it is slanted and can be altered depending on different parameters present in the wormhole spacetime. The size and spin of the wormhole are also constrained using results from the $M87^*$ observation by investigating the average diameter of the wormhole and deviations from circularity with respect to the wormhole throat size.

9.2 Future Prospects

Future prospects of all the chapters are written below.

Chapter.2: Expanding on the chapter's results, future studies could further investigate exploring the broader implications of Bose-Einstein Condensate (BEC) compact stars for astrophysical observations and theoretical models are,

- **Further Observational Verification**: The theoretical model proposed can be tested against observational data from current and future astrophysical surveys.
- **Refinement of Theoretical Models**: The parameters and assumptions in the BEC compact star model could be refined. Further theoretical work may focus on exploring variations in the polytropic equation of state and density profiles, potentially expanding the range of possible compact star configurations and behaviors.
- **Implications for Gravitational Theories**: Insights gained from this research could inform modifications to general relativity or other gravitational theories, particularly in extreme conditions. This could contribute to a broader understanding of how exotic matter influences gravitational phenomena.
- **Exploration of Stellar Evolution**: Future research could investigate the formation and evolution of BEC compact stars in different astrophysical contexts.

Chapter.3: Based on the insights provided in this chapter, upcoming research may explore further investigation and development.

- **Extension to Other Metric Potentials**: Future work could explore solutions using different metric potentials beyond the Tolman-Kuchowicz (TK) type to examine how these choices impact the physical characteristics and stability of anisotropic quintessence compact stars.
- **Inclusion of Additional Physical Effects**: The impact of additional physical factors such as rotation, magnetic fields, or charge on the anisotropic quintessence compact stars could be investigated to provide a more comprehensive understanding of their behavior.
- **Observational Constraints and Comparisons**: The model predictions could be compared with observational data from astrophysical sources to test its validity.
- **Generalization to Different $f(T)$ Functions**: Future studies might generalize the findings by considering different forms of the $f(T)$ function to understand how varying the functional form affects the compact star solutions and their physical properties.

- **Impact of Quintessence Parameters**: Further investigation into how variations in the quintessence field parameter ω_q influence the model's results could provide deeper insights into the nature of dark energy and its effects on compact stars.

Chapter.4: In the context of this chapter, several important aspects of the complexity factor have been explored. The study of anisotropic models with vanishing complexity suggested a relationship between the metric functions, providing insights into the collapse dynamics. Based on these findings, the following future directions can be suggested

- **Extension to Other Metric Potentials**: Future work could explore solutions using different metric potentials.
- **Numerical Simulations**: Conducting simulations to assess the complexity factor in various astrophysical contexts, allowing for a deeper understanding of stellar dynamics and evolution.

Chapter.5: Building on the findings of this chapter, future research could delve deeper into how the interplay between charged black holes and the evolving universe in different cosmological models might reveal new insights.

- **Extension to Higher Dimensions**: Investigating the Reissner-Nordström+Λ black hole solutions in higher-dimensional spacetimes could reveal how extra dimensions affect the cosmological constant and the interaction between the black hole and the expanding universe.
- **Analyzing Physical Properties**: More physical properties can be calculated and shown.
- **Impact of Varying Cosmological Models**: Studying how different cosmological models (e.g., modified FRW models or alternative dark energy scenarios) influence the results could provide insights into the broader implications of the research.

Chapter.6: Building on the insights of this chapter, future investigations could explore these avenues as promising prospects.

- **Application to Additional Black Hole Candidates**: Apply the framework to other astrophysical black hole systems beyond $M87^*$ and $SgrA^*$.

- **Incorporation of Modified Gravity Theories**: One can compare the strong lensing predictions of quadratic gravity with other modified gravity theories.

- **Higher-Order Corrections**: One can include higher-order corrections to the strong lensing observables.

Chapter.7: Future research on integrating the Yukawa gravitational potential into wormhole models presents a rich avenue for exploration, with several key areas of focus.

- **Modeling Compact Stars and Gravaster Dynamics**: The Yukawa potential could help refine the description of compact stars and gravaster by incorporating modifications to the gravitational interactions at small scales.

Chapter.8: Following the conclusions of this chapter, subsequent investigations could examine.

- **Exploration of Different Wormhole Classes**: Future research could investigate shadows of various classes of wormholes beyond the rotating ones studied, including static or charged wormholes, to understand how different characteristics influence the observed shadows.

- **Impact of Additional Parameters**: Studies could incorporate additional parameters or modifications to wormhole models, such as those involving exotic matter or alternative theories of gravity, to explore how these factors affect the shadow's properties.

Somi Aktar
05.12.2024

Piyali Bhar
05/12/2024

DR. PIYALI BHAR
Assistant Professor
W.B.E.S. (Gr. 'A')
Department of Mathematics
Govt. General Degree College
Singur, Hooghly, WB-712409

Farook Rahaman
05.12.24

DR. FAROOK RAHAMAN
Professor
Department of Mathematics
JADAVPUR UNIVERSITY
Kolkata-700032, W.B., INDIA

Bibliography

Abbott, B. P., et al. (2016). Observation of Gravitational Waves from a Binary Black Hole Merger. *Phys. Rev. Lett.*, *116*(6), 061102.

Abbott, B. P., et al. (2018). GW170817: Measurements of neutron star radii and equation of state. *Phys. Rev. Lett.*, *121*(16), 161101.

Abbott, R., et al. (2020). GW190814: Gravitational Waves from the Coalescence of a 23 Solar Mass Black Hole with a 2.6 Solar Mass Compact Object. *Astrophys. J. Lett.*, *896*(2), L44.

Abdujabbarov, A., Amir, M., Ahmedov, B., & Ghosh, S. G. (2016a). Shadow of rotating regular black holes. *Phys. Rev. D*, *93*, 104004.

Abdujabbarov, A., Juraev, B., Ahmedov, B., & Stuchlík, Z. (2016b). Shadow of rotating wormhole in plasma environment. *Astrophys. Space Sci.*, *361*(7), 226.

Abdujabbarov, A., Toshmatov, B., Stuchlík, Z., & Ahmedov, B. (2017). Shadow of the rotating black hole with quintessential energy in the presence of plasma. *International Journal of Modern Physics D*, *26*(06), 1750051.

Abreu, H., Hernandez, H., & Nunez, L. A. (2007). Sound Speeds, Cracking and Stability of Self-Gravitating Anisotropic Compact Objects. *Class. Quant. Grav.*, *24*, 4631–4646.

Abubekerov, M. K., Antokhina, E. A., Cherepashchuk, A. M., & Shimanskii, V. V. (2008). The Mass of the Compact Object in the X-Ray Binary Her X-1/HZ Her. *Astron. Rep.*, *52*, 379–389.

Adler, S. L., & Virbhadra, K. S. (2022). Cosmological constant corrections to the photon sphere and black hole shadow radii. *Gen. Rel. Grav.*, *54*(8), 93.

Afrin, M., & Ghosh, S. G. (2023). EHT observables as a tool to estimate parameters of supermassive black holes. *Mon. Not. Roy. Astron. Soc.*, *524*(3), 3683–3691.

Afrin, M., Kumar, R., & Ghosh, S. G. (2021). Parameter estimation of hairy Kerr black holes from its shadow and constraints from $M87^*$. *Monthly Notices of the Royal Astronomical Society*, *504*(4), 5927–5940.

Aharony, O., & Banks, T. (1999). Note on the quantum mechanics of M theory. *Journal of High Energy Physics*, *1999*(03), 016–016.

Akiyama, K., et al. (2019). First M87 Event Horizon Telescope Results. I. The Shadow of the Supermassive Black Hole. *Astrophys. J. Lett.*, *875*, L1.

Akiyama, K., et al. (2022a). First Sagittarius A* Event Horizon Telescope Results. I. The Shadow of the Supermassive Black Hole in the Center of the Milky Way. *Astrophys. J. Lett.*, *930*(2), L12.

Akiyama, K., et al. (2022b). First $SagittariusA^*$ Event Horizon Telescope Results. II. EHT and Multiwavelength Observations, Data Processing, and Calibration. *Astrophys. J. Lett.*, *930*(2), L13.

Akiyama, K., et al. (2022c). First Sagittarius A* Event Horizon Telescope Results. IV. Variability, Morphology, and Black Hole Mass. *Astrophys. J. Lett.*, *930*(2), L15.

Akrami, Y., et al. (2021). *Modified Gravity and Cosmology. An Update by the CANTATA Network* (E. N. Saridakis, R. Lazkoz, V. Salzano, P. Vargas Moniz, S. Capozziello, J. Beltrán Jiménez, M. De Laurentis, & G. J. Olmo, Eds.). Springer.

Al-Badawi, A., Alloqulov, M., Shaymatov, S., & Ahmedov, B. (2024). Shadows and weak gravitational lensing for black holes within Einstein-Maxwell-scalar theory. *Chin. Phys. C*, *48*(9), 095105.

Aldrovandi, R., & Pereira, J. G. (2009). Is Physics Asking for a New Kinematics? *Int. J. Mod. Phys. D*, *17*, 2485–2493.

Alloqulov, M., Atamurotov, F., Abdujabbarov, A., Ahmedov, B., & Khamidov, V. (2024). Shadow and weak gravitational lensing for Ellis-Bronnikov wormhole. *Chinese Physics C*, *48*(2), 025104.

Almheiri, A., Hartman, T., Maldacena, J., Shaghoulian, E., & Tajdini, A. (2020). Replica wormholes and the entropy of Hawking radiation. *Journal of High Energy Physics*, *2020*(5), 1–42.

Amarilla, L., & Eiroa, E. F. (2012). Shadow of a rotating Braneworld black hole. *Phys. Rev. D*, *85*, 064019.

Amarilla, L., & Eiroa, E. F. (2013). Shadow of a Kaluza-Klein rotating dilaton black hole. *Phys. Rev. D*, *87*, 044057.

Amir, M., & Ghosh, S. G. (2016). Shapes of rotating nonsingular black hole shadows. *Phys. Rev. D*, *94*, 024054.

Amir, M., Jusufi, K., Banerjee, A., & Hansraj, S. (2019). Shadow images of Kerr-like wormholes. *Classical and Quantum Gravity*, *36*(21), 215007.

Anderson, M. H., Ensher, J. R., Matthews, M. R., Wieman, C. E., & Cornell, E. A. (1995). Observation of Bose-Einstein condensation in a dilute atomic vapor. *science*, *269*(5221), 198–201.

Anjum, A., Afrin, M., & Ghosh, S. G. (2023). Investigating effects of dark matter on photon orbits and black hole shadows. *Physics of the Dark Universe*, *40*, 101195.

Arora, D., Molla, N. U., Chaudhary, H., Debnath, U., Atamurotov, F., & Mustafa, G. (2023). Exploring tidal force effects and shadow constraints for Schwarzschild-like black hole in Starobinsky–Bel-Robinson gravity. *Eur. Phys. J. C*, *83*(11), 995.

Arvanitaki, A., Dimopoulos, S., Gorbenko, V., Huang, J., & Van Tilburg, K. (2017). A small weak scale from a small cosmological constant. *Journal of High Energy Physics*, *2017*(5), 1–57.

Astashenok, A. V., Capozziello, S., Odintsov, S. D., & Oikonomou, V. K. (2020). Extended gravity description for the GW190814 supermassive neutron star. *Physics Letters B*, *811*, 135910.

Astashenok, A. V., Capozziello, S., Odintsov, S. D., & Oikonomou, V. (2021). Causal limit of neutron star maximum mass in $f(R)$ gravity in view of GW190814. *Physics Letters B*, *816*, 136222.

Atamurotov, F., Abdujabbarov, A., & Ahmedov, B. (2013a). Shadow of rotating Hořava-Lifshitz black hole. *Astrophysics and Space Science*, *348*, 179–188.

Atamurotov, F., Abdujabbarov, A., & Ahmedov, B. (2013b). Shadow of rotating non-Kerr black hole. *Phys. Rev. D*, *88*, 064004.

Atamurotov, F., Ahmedov, B., & Abdujabbarov, A. (2015). Optical properties of black holes in the presence of a plasma: The shadow. *Phys. Rev. D*, *92*, 084005.

Atamurotov, F., Hussain, I., Mustafa, G., & Övgün, A. (2023). Weak deflection angle and shadow cast by the charged-Kiselev black hole with cloud of strings in plasma. *Chinese Physics C*, *47*(2), Article 025102, 025102.

Aygün, S, Aktaş, C, & Mishra, B. (2019). Quadratic equation of state solutions with Λ in $f(R,T)$ gravitation theory. *Indian Journal of Physics*, *93*, 407–414.

Azreg-Aïnou, M. (2015). Confined-exotic-matter wormholes with no gluing effects—imaging supermassive wormholes and black holes. *Journal of Cosmology and Astroparticle Physics*, *2015*(07), 037.

Bahamonde, S., Böhmer, C. G., & Wright, M. (2015). Modified teleparallel theories of gravity. *Physical review D*, *92*(10), 104042.

Bahamonde, S., Dialektopoulos, K. F., Escamilla-Rivera, C., Farrugia, G., Gakis, V., Hendry, M., Hohmann, M., Said, J. L., Mifsud, J., & Di Valentino, E. (2023). Teleparallel gravity: from theory to cosmology. *Reports on Progress in Physics*, *86*(2), 026901.

Bahamonde, S., Dialektopoulos, K. F., & Said, J. L. (2019). Can Horndeski theory be recast using teleparallel gravity? *Physical Review D*, *100*(6), 064018.

Bahcall, J. N., & Wolf, R. A. (1965). Neutron stars. II. Neutrino-cooling and observability. *Physical Review*, *140*(5B), B1452.

Bamba, K., Geng, C.-Q., Lee, C.-C., & Luo, L.-W. (2011). Equation of state for dark energy in $f(T)$ gravity. *Journal of Cosmology and Astroparticle Physics*, *2011*(01), 021.

Bambi, C. (2013). Can the supermassive objects at the centers of galaxies be traversable wormholes? The first test format of strong gravity for mm/sub-mm very long baseline interferometry facilities. *Physical Review D*, *87*(10), 107501.

Bambi, C., Freese, K., Vagnozzi, S., & Visinelli, L. (2019). Testing the rotational nature of the supermassive object $M87^*$ from the circularity and size of its first image. *Phys. Rev. D*, *100*(4), 044057.

Banados, M., Teitelboim, C., & Zanelli, J. (1992). Black hole in three-dimensional spacetime. *Physical review letters*, *69*(13), 1849.

Banerjee, A. (2013). Stability of charged thin-shell wormholes in (2+ 1) dimensions. *International Journal of Theoretical Physics*, *52*, 2943–2958.

Barcelo, C., Liberati, S., & Visser, M. (2001). Analogue gravity from Bose-Einstein condensates. *Classical and Quantum Gravity*, *18*(6), 1137.

Bartelmann, M., & Schneider, P. (2001). Weak gravitational lensing. *Phys. Rept.*, *340*, 291–472.

Bauswein, A., Just, O., Janka, H.-T., & Stergioulas, N. (2017). Neutron-star radius constraints from GW170817 and future detections. *The Astrophysical Journal Letters*, *850*(2), L34.

Bejarano, C., Eiroa, E. F., & Simeone, C. (2014). General formalism for the stability of thin-shell wormholes in 2+ 1 dimensions. *The European Physical Journal C*, *74*(8), 3015.

Bengochea, G. R., & Ferraro, R. (2009). Dark torsion as the cosmic speed-up. *Physical Review D*, *79*(12), 124019.

Berezhiani, Z., Nesti, F., Pilo, L., & Rossi, N. (2009). Gravity modification with Yukawa-type potential: dark matter and mirror gravity. *Journal of High Energy Physics*, *2009*(07), 083.

Bhadra, A. (2003). Gravitational lensing by a charged black hole of string theory. *Phys. Rev. D*, *67*, 103009.

Birrell, N. D., & Davies, P. C. W. (1982). *Quantum Fields in Curved Space*. Cambridge University Press.

Bisht, R. K., Gedela, S., Pant, N., & Tewari, N. (2021). A relativistic model of stellar objects with core-crust-envelope division. *Research in Astronomy and Astrophysics*, *21*(7), 162.

Blome, H. J., & Priester, W. (1984). Vacuum energy in a friedmann-lemaître cosmos. *Naturwissenschaften*, *71*, 528–531.

Boehmer, C. G., & Harko, T. (2006). Bounds on the basic physical parameters for anisotropic compact general relativistic objects. *Class. Quant. Grav.*, *23*, 6479–6491.

Boehmer, C., & Harko, T. (2007). Can dark matter be a Bose–Einstein condensate? *Journal of Cosmology and Astroparticle Physics*, *2007*(06), 025.

Boehmer, C. G., Harko, T., & Lobo, F. S. (2012). Wormhole geometries in modified teleparallel gravity and the energy conditions. *Physical Review D*, *85*(4), 044033.

Bogoliubov, N. (1947). On the theory of superfluidity. *J. Phys*, *11*(1), 23.

Böhmer, C. G., & Jensko, E. (2021). Modified gravity: A unified approach. *Physical Review D*, *104*(2), 024010.

Bondi, H. (1964). Massive spheres in general relativity. *Proceedings of the Royal Society of London. Series A. Mathematical and Physical Sciences*, *282*(1390), 303–317.

Bondi, H. (1999). The gravitational redshift from static spherical bodies., *302*(2), 337–340.

Borka, D., Jovanović, P., Jovanović, V. B., & Zakharov, A. F. (2013). Constraining the range of Yukawa gravity interaction from S2 star orbits. *Journal of Cosmology and Astroparticle Physics*, *2013*(11), 050.

Botta Cantcheff, M., Grandi, N. E., & Sturla, M. (2010). Wormhole solutions to Hořava gravity. *Phys. Rev. D*, *82*, 124034.

Bousso, R. (2011). The Cosmological Constant Problem, Dark Energy, and the Landscape of String Theory. *Pontif. Acad. Sci. Scr. Varia*, *119*, 129–151.

Bowers, R. L., & Liang, E. (1974). Anisotropic spheres in general relativity. *Astrophysical Journal, Vol. 188, p. 657 (1974)*, *188*, 657.

Bowyer, S., Byram, E. T., Chubb, T. A., & Friedman, H. (1964). Lunar Occultation of X-ray Emission from the Crab Nebula. *Science*, *146*(3646), 912–917.

Bozza, V. (2002). Gravitational lensing in the strong field limit. *Phys. Rev. D*, *66*, 103001.

Bozza, V. (2003). Quasiequatorial gravitational lensing by spinning black holes in the strong field limit. *Phys. Rev. D*, *67*, 103006.

Bozza, V. (2008). A Comparison of approximate gravitational lens equations and a proposal for an improved new one. *Phys. Rev. D*, *78*, 103005.

Bozza, V., Capozziello, S., Iovane, G., & Scarpetta, G. (2001). Strong field limit of black hole gravitational lensing. *Gen. Rel. Grav.*, *33*, 1535–1548.

Bozza, V., & Mancini, L. (2004). Time delay in black hole gravitational lensing as a distance estimator. *Gen. Rel. Grav.*, *36*, 435–450.

Bozza, V. (2010). Gravitational Lensing by Black Holes. *Gen. Rel. Grav.*, *42*, 2269–2300.

Brassel, B. P., Maharaj, S. D., & Goswami, R. (2021). Higher-dimensional inhomogeneous composite fluids: energy conditions. *Progress of Theoretical and Experimental Physics*, *2021*(10), 103E01.

Broderick, A. E., Johannsen, T., Loeb, A., & Psaltis, D. (2014). Testing the no-hair theorem with event horizon telescope observations of Sagittarius A. *The Astrophysical Journal*, *784*(1), 7.

Broderick, A. E., & Loeb, A. (2005). Frequency-dependent Shift in the Image Centroid of the Black Hole at the Galactic Center as a Test of General Relativity. *The Astrophysical Journal*, *636*(2), L109.

Bronnikov, K. A., & Baleevskikh, K. A. (2019). On gravitational lensing by symmetric and asymmetric wormholes. *Grav. Cosmol.*, *25*(1), 44–49.

Bronnikov, K. A., & Kim, S.-W. (2003). Possible wormholes in a brane world. *Phys. Rev. D*, *67*, 064027.

Bronzwaer, T., & Falcke, H. (2021). The Nature of Black Hole Shadows. *Astrophys. J.*, *920*(2), 155.

Buchdahl, H. A. (1959). General Relativistic Fluid Spheres. *Phys. Rev.*, *116*, 1027.

Buchdahl, H. A. (1970). Non-linear Lagrangians and cosmological theory. *Monthly Notices of the Royal Astronomical Society*, *150*(1), 1–8.

Cai, Y.-F., & Capozziello, S. (2016). Mariafelicia De Laurentis, and Emmanuel N. Saridakis. $f(T)$ teleparallel gravity and cosmology. *Rept. Prog. Phys*, *79*(10), 106901.

Cai, Y.-F., Chen, S.-H., Dent, J. B., Dutta, S., & Saridakis, E. N. (2011). Matter bounce cosmology with the $f(T)$ gravity. *Classical and Quantum Gravity*, *28*(21), 215011.

Calbet, X., & López-Ruiz, R. (2001). Tendency towards maximum complexity in a nonequilibrium isolated system. *Phys. Rev. E*, *63*, 066116.

Canuto, V. (1974). Equation of state at ultrahigh densities. I. *In: Annual review of astronomy and astrophysics. Volume 12.(A75-13476 03-90) Palo Alto, Calif., Annual Reviews, Inc., 1974, p. 167-214.*, *12*, 167–214.

Cao, L.-M., Wu, L.-B., Zhao, Y., & Zhou, Y.-S. (2023). Quasinormal modes of tensor perturbations of Kaluza-Klein black holes in Einstein-Gauss-Bonnet gravity. *Phys. Rev. D*, *108*(12), 124023.

Capano, C. D., Tews, I., Brown, S. M., Margalit, B., De, S., Kumar, S., Brown, D. A., Krishnan, B., & Reddy, S. (2020). Stringent constraints on neutron-star radii from multimessenger observations and nuclear theory. *Nature Astronomy*, *4*(6), 625–632.

Capozziello, S., & De Laurentis, M. (2011). Extended theories of gravity. *Physics Reports*, *509*(4-5), 167–321.

Cardall, C. Y., Prakash, M., & Lattimer, J. M. (2001). Effects of strong magnetic fields on neutron star structure. *The Astrophysical Journal*, *554*(1), 322.

Cardoso, V., & Pani, P. (2019). Testing the nature of dark compact objects: a status report. *Living Reviews in Relativity*, *22*(1), 4.

Cattoen, C., Faber, T., & Visser, M. (2005). Gravastars must have anisotropic pressures. *Classical and Quantum Gravity*, *22*(20), 4189.

Chan, K., & Mann, R. B. (1994). Static charged black holes in (2+ 1)-dimensional dilaton gravity. *Physical Review D*, *50*(10), 6385.

Chan, R, Herrera, L, & Santos, N. (1993). Dynamical instability for radiating anisotropic collapse. *Monthly Notices of the Royal Astronomical Society*, *265*(3), 533–544.

Chandrasekhar, S. (1964). Dynamical instability of gaseous masses approaching the Schwarzschild limit in general relativity. *Physical Review Letters*, *12*(4), 114.

Chandrasekhar, S. (1931). The maximum mass of ideal white dwarfs. *Astrophysical Journal, vol. 74, p. 81*, *74*, 81.

Chavanis, P.-H. (2017). Dissipative self-gravitating Bose-Einstein condensates with arbitrary nonlinearity as a model of dark matter halos. *Eur. Phys. J. Plus*, *132*(6), 248.

Chavanis, P.-H., & Harko, T. (2012). Bose-Einstein condensate general relativistic stars. *Physical Review D*, *86*(6), 064011.

Claudel, C.-M., Virbhadra, K. S., & Ellis, G. F. R. (2001). The Geometry of photon surfaces. *J. Math. Phys.*, *42*, 818–838.

Collaboration, E. H. T., et al. (2019). First $M87$ event horizon telescope results. IV. Imaging the central supermassive black hole. *arXiv preprint arXiv:1906.11241*.

Collas, P., & Klein, D. (2012). Embeddings and time evolution of the Schwarzschild wormhole. *American Journal of Physics*, *80*(3), 203–210.

Colpi, M., Shapiro, S. L., & Wasserman, I. (1986). Boson stars: Gravitational equilibria of self-interacting scalar fields. *Physical review letters*, *57*(20), 2485.

Cramer, J. G., Forward, R. L., Morris, M. S., Visser, M., Benford, G., & Landis, G. A. (1995). Natural wormholes as gravitational lenses. *Phys. Rev. D*, *51*, 3117–3120.

Cunha, P. V. P., Herdeiro, C. A. R., Radu, E., & Rúnarsson, H. F. (2015). Shadows of Kerr Black Holes with Scalar Hair. *Phys. Rev. Lett.*, *115*, 211102.

Cunha, P. V. P., Herdeiro, C. A. R., & Rodriguez, M. J. (2018). Does the black hole shadow probe the event horizon geometry? *Phys. Rev. D*, *97*, 084020.

Cunha, P. V., Herdeiro, C. A., Kleihaus, B., Kunz, J., & Radu, E. (2017). Shadows of Einstein–dilaton–Gauss–Bonnet black holes. *Physics Letters B*, *768*, 373–379.

Dalfovo, F., Giorgini, S., Pitaevskii, L. P., & Stringari, S. (1999). Theory of Bose-Einstein condensation in trapped gases. *Reviews of modern physics*, *71*(3), 463.

Daouda, M. H., Rodrigues, M. E., & Houndjo, M. (2012). Anisotropic fluid for a set of non-diagonal tetrads in $f(T)$ gravity. *Physics Letters B*, *715*(1-3), 241–245.

Darmois, G. (1927). Mémorial des sciences mathématiques. *Fascicule XXV*, 1927.

Darwin, C. G. (1959). The gravity field of a particle. *Proceedings of the Royal Society of London. Series A. Mathematical and Physical Sciences*, *249*(1257), 180–194.

Das, S., Govender, M., & Bogadi, R. S. (2024). Compact stellar model with vanishing complexity under Vaidya–Tikekar background geometry. *The European Physical Journal C*, *84*(1), 13.

Das, S., Rahaman, F., & Baskey, L. (2019). A new class of compact stellar model compatible with observational data. *Eur. Phys. J. C*, *79*(10), 853.

Dastan, S., Saffari, R., & Soroushfar, S. (2016). Shadow of a Kerr-Sen dilaton-axion Black Hole.

Davis, K. B., Mewes, M.-O., Andrews, M. R., van Druten, N. J., Durfee, D. S., Kurn, D., & Ketterle, W. (1995). Bose-Einstein condensation in a gas of sodium atoms. *Physical review letters*, *75*(22), 3969.

Davoudiasl, H., & Denton, P. B. (2019). Ultra Light Boson Dark Matter and Event Horizon Telescope Observations of $M87^*$. *Physical review letters*, *123*(2), 021102.

de Vries, A. (2000). The apparent shape of a rotating charged black hole, closed photon orbits and the bifurcation set A4. *Classical and Quantum Gravity*, *17*(1), 123.

Deb, D., Chowdhury, S. R., Ray, S., Rahaman, F., & Guha, B. (2017). Relativistic model for anisotropic strange stars. *Annals of Physics*, *387*, 239–252.

Dent, J. B., Dutta, S., & Saridakis, E. N. (2011). $f(T)$ gravity mimicking dynamical dark energy. Background and perturbation analysis. *Journal of Cosmology and Astroparticle Physics*, *2011*(01), 009.

Denz, T., Pawlowski, J. M., & Reichert, M. (2018). Towards apparent convergence in asymptotically safe quantum gravity. *The European Physical Journal C*, *78*, 1–24.

DeWitt-Morette, C., & DeWitt, B. S. (1973). *Black Holes* (Vol. 23). CRC Press.

Di Prisco, A, Herrera, L, Le Denmat, G., MacCallum, M. A., & Santos, N. O. (2007). Nonadiabatic charged spherical gravitational collapse. *Physical Review D*, *76*(6), 064017.

Ditta, A., Ahmad, M., Hussain, I., & Mustafa, G. (2021). Anisotropic stellar structures in the theory of gravity with quintessence via embedding approach. *Chin. Phys. C*, *45*(4), 045102.

Doeleman, S. S., Weintroub, J., Rogers, A. E., Plambeck, R., Freund, R., Tilanus, R. P., Friberg, P., Ziurys, L. M., Moran, J. M., Corey, B., et al. (2008). Event-horizon-scale structure in the supermassive black hole candidate at the Galactic Centre. *Nature*, *455*(7209), 78–80.

Eddington, A. (1925). Circulating currents in rotating stars. *The Observatory, Vol. 48, p. 73-75 (1925)*, *48*, 73–75.

Einstein, A. (1936). Lens-Like Action of a Star by the Deviation of Light in the Gravitational Field. *Science*, *84*, 506–507.

Einstein, A., & Rosen, N. (1935). The Particle Problem in the General Theory of Relativity. *Phys. Rev.*, *48*, 73–77.

Eiroa, E. F., Romero, G. E., & Torres, D. F. (2002). Reissner-Nordström black hole lensing. *Phys. Rev. D*, *66*, 024010.

Eiroa, E. F., & Sendra, C. M. (2011). Gravitational lensing by a regular black hole. *Class. Quant. Grav.*, *28*, 085008.

Eiroa, E. F., & Sendra, C. M. (2012). Gravitational lensing by massless braneworld black holes. *Phys. Rev. D*, *86*, 083009.

Eiroa, E. F., & Torres, D. F. (2004). Strong field limit analysis of gravitational retrolensing. *Phys. Rev. D*, *69*, 063004.

El Hanafy, W., & Nashed, G. G. L. (2016). Exact Teleparallel Gravity of Binary Black Holes. *Astrophys. Space Sci.*, *361*(2), 68.

Estrada, M., Tello-Ortiz, F., Singh, K. N., & Maurya, S. (2023). Representation of compact stars using the black string set-up. *Chinese Journal of Physics*, *81*, 92–103.

Falcke, H., Melia, F., & Agol, E. (1999). Viewing the Shadow of the Black Hole at the Galactic Center. *The Astrophysical Journal*, *528*(1), L13.

Ferraro, R., & Fiorini, F. (2007). Modified teleparallel gravity: Inflation without an inflaton. *Physical Review D*, *75*(8), 084031.

Flamm, L. (1916). Comments on Einstein's theory of gravity. *Physikalische Zeitschrift*, *17*, 448.

Frieben, J., & Rezzolla, L. (2012). Equilibrium models of relativistic stars with a toroidal magnetic field. *Monthly Notices of the Royal Astronomical Society*, *427*(4), 3406–3426.

Frittelli, S., Kling, T. P., & Newman, E. T. (2000). Space-time perspective of Schwarzschild lensing. *Phys. Rev. D*, *61*, 064021.

Frolov, V. P., & Zelnikov, A. (2011, September). *Introduction to Black Hole Physics*. Oxford University Press.

Galloway, G. J., Schleich, K, Witt, D., & Woolgar, E. (2001). The AdS/CFT correspondence and topological censorship. *Physics Letters B*, *505*(1-4), 255–262.

Galloway, G. J., Schleich, K., Witt, D. M., & Woolgar, E. (1999). Topological censorship and higher genus black holes. *Physical Review D*, *60*(10), 104039.

Gao, C. J., & Zhang, S. N. (2004). Reissner–Nordström metric in the Friedman–Robertson–Walker universe. *Physics Letters B*, *595*(1-4), 28–35.

Garattini, R., & Lobo, F. S. N. (2007). Self-sustained phantom wormholes in semi-classical gravity. *Classical and Quantum Gravity*, *24*(9), 2401–2413.

Garcia, N. M., & Lobo, F. S. N. (2010). Wormhole geometries supported by a nonminimal curvature-matter coupling. *Phys. Rev. D*, *82*, 104018.

Garcia, N. M., & Lobo, F. S. N. (2011). Nonminimal curvature–matter coupled wormholes with matter satisfying the null energy condition. *Classical and Quantum Gravity*, *28*(8), 085018.

Garny, M., Sandora, M., & Sloth, M. S. (2016). Planckian Interacting Massive Particles as Dark Matter. *Phys. Rev. Lett.*, *116*(10), 101302.

Gedela, S., Pant, N., Pant, R., & Upreti, J. (2019a). Relativistic anisotropic model of strange star SAX J1808. 4-3658 admitting quadratic equation of state. *International Journal of Modern Physics A*, *34*(29), 1950179.

Gedela, S., Pant, N., Upreti, J., & Pant, R. P. (2019b). Relativistic core-envelope anisotropic fluid model of super dense stars. *Eur. Phys. J. C*, *79*(7), 566.

Geng, C.-Q., Lee, C.-C., Saridakis, E. N., & Wu, Y.-P. (2011). "Teleparallel" dark energy. *Physics Letters B*, *704*(5), 384–387.

Ghasemi-Nodehi, M, Azreg-Aïnou, M., Jusufi, K., & Jamil, M. (2020). Shadow, quasinormal modes, and quasiperiodic oscillations of rotating Kaluza-Klein black holes. *Physical Review D*, *102*(10), 104032.

Ghorani, E., Puliçe, B., Atamurotov, F., Rayimbaev, J., Abdujabbarov, A., & Demir, D. (2023). Probing geometric proca in metric-palatini gravity with black hole shadow and photon motion. *Eur. Phys. J. C*, *83*(4), 318.

Giacconi, R., Gursky, H., Paolini, F. R., & Rossi, B. B. (1962). Evidence for x Rays From Sources Outside the Solar System. *Phys. Rev. Lett.*, *9*, 439–443.

Gillessen, S., Plewa, P., Eisenhauer, F., Sari, R., Waisberg, I., Habibi, M., Pfuhl, O., George, E., Dexter, J., von Fellenberg, S., et al. (2017). An update on monitoring stellar orbits in the galactic center. *The Astrophysical Journal*, *837*(1), 30.

Gonzalez, E., Jusufi, K., Leon, G., & Saridakis, E. N. (2023). Observational constraints on Yukawa cosmology and connection with black hole shadows. *Physics of the Dark Universe*, *42*, 101304.

Gonzalez-Caniulef, D., Guillot, S., & Reisenegger, A. (2019). Neutron star radius measurement from the ultraviolet and soft X-ray thermal emission of PSR J0437−4715. *Mon. Not. Roy. Astron. Soc.*, *490*(4), 5848–5859.

Govender, M., Govender, W., Govender, G., & Duffy, K. (2022). Complexity and the departure from spheroidicity. *The European Physical Journal C*, *82*(9), 832.

Gralla, S. E., Holz, D. E., & Wald, R. M. (2019). Black hole shadows, photon rings, and lensing rings. *Physical Review D*, *100*(2), 024018.

Green, R. F., Schmidt, M., & Liebert, J. (1986). The Palomar-Green catalog of ultraviolet-excess stellar objects. *Astrophysical Journal Supplement Series (ISSN 0067-0049), vol. 61, June 1986, p. 305-352. Research supported by the California Institute of Technology.*, *61*, 305–352.

Greenstein, J. L. (1986). The Frequency of Hydrogen White Dwarfs as Observed at High Signal to Noise., *304*, 334.

Grenzebach, A., Perlick, V., & Lämmerzahl, C. (2014). Photon regions and shadows of Kerr-Newman-NUT black holes with a cosmological constant. *Phys. Rev. D*, *89*, 124004.

Guo, H., Liu, H., Kuang, X.-M., & Wang, B. (2020). Acoustic black hole in Schwarzschild spacetime: Quasinormal modes, analogous Hawking radiation, and shadows. *Physical Review D*, *102*(12), 124019.

Guo, Y., & Miao, Y.-G. (2020). Null geodesics, quasinormal modes, and the correspondence with shadows in high-dimensional Einstein-Yang-Mills spacetimes. *Physical Review D*, *102*(8), 084057.

Gurtug, O, Mazharimousavi, S. H., & Halilsoy, M. (2012). 2+ 1-dimensional electrically charged black holes in Einstein-power-Maxwell theory. *Physical Review D*, *85*(10), 104004.

Guzik, J., Jain, B., & Takada, M. (2010). Tests of Gravity from Imaging and Spectroscopic Surveys. *Phys. Rev. D*, *81*, 023503.

Gyulchev, G., Nedkova, P., Tinchev, V., & Yazadjiev, S. (2018). On the shadow of rotating traversable wormholes. *Eur. Phys. J. C*, *78*(7), 544.

Habib Mazharimousavi, S., Amirabi, Z., & Halilsoy, M. (2017). Thin-shell wormholes in (2+1)-dimensional Einstein-scalar theory. *Mod. Phys. Lett. A*, *32*(10), 1750064.

Hamil, B., & Lütfüoğlu, B. (2023). Thermodynamics and Shadows of quantum-corrected Reissner–Nordström black hole surrounded by quintessence. *Physics of the Dark Universe*, *42*, 101293.

Harko, T., Lobo, F. S. N., Mak, M. K., & Sushkov, S. V. (2013). Modified-gravity wormholes without exotic matter. *Phys. Rev. D*, *87*, 067504.

Harrison, B. K., Wakano, M., & Wheeler, J. A. (1958). Matter-energy at high density: end point of thermonuclear evolution. *La structure et évolution de l'univers*, *124*.

Hawking, S. W. (1988). Wormholes in Space-Time (G. W. Gibbons & S. W. Hawking, Eds.). *Phys. Rev. D*, *37*, 904–910.

Hawking, S. W., & Ellis, G. F. R. (1973). *The Large Scale Structure of Space-Time*. Cambridge University Press.

Hayashi, K., & Shirafuji, T. (1979). New general relativity. *Physical Review D*, *19*(12), 3524.

Held, A., & Zhang, J. (2023). Instability of spherically symmetric black holes in quadratic gravity. *Phys. Rev. D*, *107*(6), 064060.

Herrera, L. (1992). Cracking of self-gravitating compact objects. *Phys. Lett. A*, *165*, 206–210.

Herrera, L. (2018). New definition of complexity for self-gravitating fluid distributions: The spherically symmetric, static case. *Phys. Rev. D*, *97*, 044010.

Herrera, L. (2020). Stability of the isotropic pressure condition. *Physical Review D*, *101*(10), 104024.

Herrera, L., Ospino, J., & Di Prisco, A. (2008). All static spherically symmetric anisotropic solutions of Einstein's equations. *Phys. Rev. D*, *77*, 027502.

Herrera, L., & Santos, N. O. (1995). Jeans Mass for Anisotropic Matter., *438*, 308.

Herrera, L., & Santos, N. O. (1997). Local anisotropy in self-gravitating systems. *Physics Reports*, *286*(2), 53–130.

Hewish, A. (1975). Pulsars and high density physics. *Rev. Mod. Phys.*, *47*, 567–572.

Hioki, K., & Maeda, K.-i. (2009). Measurement of the Kerr spin parameter by observation of a compact object's shadow. *Phys. Rev. D*, *80*, 024042.

Hioki, K., & Miyamoto, U. (2008). Hidden symmetries, null geodesics, and photon capture in the Sen black hole. *Phys. Rev. D*, *78*, 044007.

Hochberg, D. (1990). Lorentzian wormholes in higher order gravity theories. *Physics Letters B*, *251*(3), 349–354.

Hohmann, M., Järv, L., & Ualikhanova, U. (2018). Covariant formulation of scalar-torsion gravity. *Physical Review D*, *97*(10), 104011.

Hu, W., Barkana, R., & Gruzinov, A. (2000). Fuzzy cold dark matter: the wave properties of ultralight particles. *Physical Review Letters*, *85*(6), 1158.

Iorio, L., Radicella, N., & Ruggiero, M. L. (2015). Constraining $f(T)$ gravity in the Solar System. *Journal of Cosmology and Astroparticle Physics*, *2015*(08), 021.

Islam, S. U., & Ghosh, S. G. (2021). Strong field gravitational lensing by hairy Kerr black holes. *Phys. Rev. D*, *103*(12), 124052.

Islam, S. U., Ghosh, S. G., & Maharaj, S. D. (2024). Strong gravitational lensing by Bardeen black holes in 4D EGB gravity: Constraints from supermassive black holes. *Chin. J. Phys.*, *89*, 1710–1724.

Islam, S. U., Kumar, J., & Ghosh, S. G. (2021). Strong gravitational lensing by rotating Simpson-Visser black holes. *JCAP*, *10*, 013.

Islam, S. U., Kumar, R., & Ghosh, S. G. (2020). Gravitational lensing by black holes in the $4D$ Einstein-Gauss-Bonnet gravity. *JCAP*, *09*, 030.

Ivanov, B. V. (2002). Maximum bounds on the surface redshift of anisotropic stars. *Physical Review D*, *65*(10), 104011.

Ivanov, B. (2010). The importance of anisotropy for relativistic fluids with spherical symmetry. *International Journal of Theoretical Physics*, *49*, 1236–1243.

Jamil, M., Momeni, D., & Myrzakulov, R. (2012a). Attractor Solutions in $f(T)$ Cosmology. *Eur. Phys. J. C*, *72*, 1959.

Jamil, M., Momeni, D., & Myrzakulov, R. (2012b). Resolution of dark matter problem in $f(T)$ gravity. *Eur. Phys. J. C*, *72*, 2122.

Jamil, M., Momeni, D., & Myrzakulov, R. (2013). Wormholes in a viable $f(T)$ gravity. *Eur. Phys. J. C*, *73*, 2267.

Jamil, M., Momeni, D., & Myrzakulov, R. (2015). Warm Intermediate Inflation in $f(T)$ Gravity. *Int. J. Theor. Phys.*, *54*(4), 1098–1112.

Jasim, M., Singh, K. N., Errehymy, A., Maurya, S., & Mandke, M. (2023). Study of a Minimally Deformed Anisotropic Solution for Compact Objects with Massive Scalar Field in Brans–Dicke Gravity Admitting the Karmarkar Condition. *Universe*, *9*(5), 208.

Jochim, S., Bartenstein, M., Altmeyer, A., Hendl, G., Riedl, S., Chin, C., Denschlag, J. H., & Grimm, R. (2003). Bose-Einstein Condensation of Molecules. *Science*, *302*(5653), 2101–2103.

Jusufi, K., Leon, G., & Millano, A. D. (2023a). Dark Universe phenomenology from Yukawa potential? *Physics of the Dark Universe*, *42*, 101318.

Jusufi, K., & Sheykhi, A. (2023). Entropic corrections to Friedmann equations and bouncing universe due to the zero-point length. *Physics Letters B*, *836*, 137621.

Jusufi, K., Sheykhi, A., & Capozziello, S. (2023b). Apparent dark matter as a non-local manifestation of emergent gravity. *Physics of the Dark Universe*, *42*, 101270.

Kala, S., Saurabh, Nandan, H., & Sharma, P. (2020). Deflection of light and shadow cast by a dual-charged stringy black hole. *Int. J. Mod. Phys. A*, *35*(28), 2050177.

Kalam, M., Rahaman, F., Ray, S., Hossein, S. M., Karar, I., & Naskar, J. (2012). Anisotropic strange star with de Sitter spacetime. *The European Physical Journal C*, *72*, 1–7.

Kaloper, N., Kleban, M., & Martin, D. (2010). McVittie's legacy: Black holes in an expanding universe. *Physical Review D*, *81*(10), 104044.

Kanti, P., Kleihaus, B., & Kunz, J. (2012). Stable Lorentzian wormholes in dilatonic Einstein-Gauss-Bonnet theory. *Physical Review D*, *85*(4).

Kastor, D., & Traschen, J. (1993a). Cosmological multi-black-hole solutions. *Physical Review D*, *47*(12), 5370.

Kastor, D., & Traschen, J. (1993b). Linear instability of nonvacuum spacetimes. *Physical Review D*, *47*(2), 480.

Kerr, R. P. (1963). Gravitational Field of a Spinning Mass as an Example of Algebraically Special Metrics. *Phys. Rev. Lett.*, *11*, 237–238.

Khlebnikov, S. (2002). Strong acoustic turbulence and the speed of Bose-Einstein condensation. *Physical Review A*, *66*(6), 063606.

Kippenhahn, R., Weigert, A., & Weiss, A. (1990). *Stellar structure and evolution* (Vol. 192). Springer.

Koester, C. G., D. (1990). Physics of white dwarf stars. *Reports on Progress in Physics*, *53*(7), 837–915.

Kofinas, G., & Saridakis, E. N. (2014). Teleparallel equivalent of Gauss-Bonnet gravity and its modifications. *Physical Review D*, *90*(8), 084044.

Kolmogorov, A. N. (1965). Three approaches to the quantitative definition of information. *Problems of information transmission*, *1*(1), 1–7.

Konoplya, R. A., & Zhidenko, A. (2022). Traversable Wormholes in General Relativity. *Phys. Rev. Lett.*, *128*, 091104.

Konoplya, R., & Zhidenko, A. (2016). Wormholes versus black holes: quasinormal ringing at early and late times. *Journal of Cosmology and Astroparticle Physics*, *2016*(12), 043.

Kormendy, J., & Ho, L. C. (2013). Coevolution (Or Not) of Supermassive Black Holes and Host Galaxies. *Ann. Rev. Astron. Astrophys.*, *51*, 511–653.

Kruglov, S. (2020). The shadow of $M87^*$ black hole within rational nonlinear electrodynamics. *Modern Physics Letters A*, *35*(35), 2050291.

Kuhfittig, P. K. F. (2019). Spherically symmetric wormholes of embedding class one. *Pramana*, *92*(5).

Kuhfittig, P. K. F. (2021). On wormholes in spacetimes of embedding class one.

Kumar, J., Islam, S. U., & Ghosh, S. G. (2022a). Investigating strong gravitational lensing effects by supermassive black holes with Horndeski gravity. *Eur. Phys. J. C*, *82*(5), 443.

Kumar, J., Islam, S. U., & Ghosh, S. G. (2022b). Testing Strong Gravitational Lensing Effects of Supermassive Compact Objects with Regular Spacetimes. *Astrophys. J.*, *938*(2), 104.

Kumar, J., Islam, S. U., & Ghosh, S. G. (2023). Strong gravitational lensing by loop quantum gravity motivated rotating black holes and EHT observations. *Eur. Phys. J. C*, *83*(11), 1014.

Kumar, R., & Ghosh, S. G. (2020). Black Hole Parameter Estimation from Its Shadow. *The Astrophysical Journal*, *892*(2), 78.

Kumar, R., Ghosh, S. G., & Wang, A. (2020a). Gravitational deflection of light and shadow cast by rotating Kalb-Ramond black holes. *Phys. Rev. D*, *101*(10), 104001.

Kumar, R., Islam, S. U., & Ghosh, S. G. (2020b). Gravitational lensing by charged black hole in regularized 4*D* Einstein–Gauss–Bonnet gravity. *Eur. Phys. J. C*, *80*(12), 1128.

Lake, K. (1979). Reissner-Nordström-de Sitter metric, the third law, and cosmic censorship. *Physical Review D*, *19*(2), 421.

Lamy, F., Gourgoulhon, E., Paumard, T., & Vincent, F. H. (2018). Imaging a non-singular rotating black hole at the center of the Galaxy. *Classical and Quantum Gravity*, *35*(11), 115009.

Lanczos, C. (1932). Elektromagnetismus als natürliche eigenschaft der riemannschen geometrie. *Zeitschrift für Physik*, *73*, 147–168.

Lanczos, C. (1938). A remarkable property of the Riemann-Christoffel tensor in four dimensions. *Annals of Mathematics*, *39*(4), 842–850.

Lanczos, K. (1924). Flächenhafte verteilung der materie in der einsteinschen gravitationstheorie. *Annalen der Physik*, *379*(14), 518–540.

Landry, P., Abdelqader, M., & Lake, K. (2012). McVittie solution with a negative cosmological constant. *Physical Review D*, *86*(8), 084002.

Latifah, S, Sulaksono, A., & Mart, T. (2014). Bosons star at finite temperature. *Physical Review D*, *90*(12), 127501.

Lemos, J. P. S., Lobo, F. S. N., & Quinet de Oliveira, S. (2003). Morris-Thorne wormholes with a cosmological constant. *Phys. Rev. D*, *68*, 064004.

Lemos, J. P., & Zanchin, V. T. (2011). Regular black holes: Electrically charged solutions, Reissner-Nordström outside a de Sitter core. *Physical Review D*, *83*(12), 124005.

Letelier, P. S. (1980). Anisotropic fluids with two-perfect-fluid components. *Physical Review D*, *22*(4), 807.

Li, B., Sotiriou, T. P., & Barrow, J. D. (2011). $f(T)$ gravity and local Lorentz invariance. *Phys. Rev. D*, *83*, 064035.

Li, C., Cai, Y., Cai, Y.-F., & Saridakis, E. N. (2018). The effective field theory approach of teleparallel gravity, $f(T)$ gravity and beyond. *Journal of Cosmology and Astroparticle Physics*, *2018*(10), 001.

Li, J., Guo, L, & Zhang, B. (2007). The Chinese VLBI network and its astrometric role. *Proceedings of the International Astronomical Union*, *3*(S248), 182–185.

Li, P.-C., Guo, M., & Chen, B. (2020). Shadow of a spinning black hole in an expanding universe. *Phys. Rev. D*, *101*, 084041.

Li, Z., & Bambi, C. (2014). Measuring the Kerr spin parameter of regular black holes from their shadow. *Journal of Cosmology and Astroparticle Physics*, *2014*(01), 041.

Liebes, S. (1964). Gravitational Lenses. *Phys. Rev.*, *133*, B835–B844.

Lighuda, A., Maharaj, S., Sunzu, J., & Mureithi, E. (2021). A model of a three-layered relativistic star. *Astrophysics and Space Science*, *366*(8), 76.

Lin, K., Pavan, A. B., Flores-Hidalgo, G., & Abdalla, E. (2017). New Electrically Charged Black Hole in Higher Derivative Gravity. *Braz. J. Phys.*, *47*(4), 419–425.

Linder, E. V. (2010). Einstein's other gravity and the acceleration of the universe. *Physical Review D*, *81*(12), 127301.

Lloyd, S., & Pagels, H. (1988). Complexity as thermodynamic depth. *Annals of Physics*, *188*(1), 186–213.

Lobo, F. S. N., & Oliveira, M. A. (2009). Wormhole geometries in $f(R)$ modified theories of gravity. *Phys. Rev. D*, *80*, 104012.

London, F. (1938). The λ-phenomenon of liquid helium and the Bose-Einstein degeneracy. *Nature*, *141*(3571), 643–644.

Long, F., Chen, S., Wang, M., & Jing, J. (2020). Shadow of a disformal Kerr black hole in quadratic degenerate higher-order scalar–tensor theories. *Eur. Phys. J. C*, *80*(12), 1180.

Lovelock, D. (1970). Divergence-free tensorial concomitants. *Aequationes Mathematicae*, *4*, 127–138.

Lovelock, D. (1971). The Einstein tensor and its generalizations. *Journal of Mathematical Physics*, *12*(3), 498–501.

Luminet, J.-P. (1979). Image of a spherical black hole with thin accretion disk. *Astronomy and Astrophysics, vol. 75, no. 1-2, May 1979, p. 228-235.*, *75*, 228–235.

Luyten, W. J. (1970). *White dwarfs*. University of Minnesota Press.

Madelung, E. (1927). Quantum theory in hydrodynamical form. *z. Phys*, *40*, 322.

Maeda, K.-i., & Ohta, N. (2014). Cosmic acceleration with a negative cosmological constant in higher dimensions. *Journal of High Energy Physics*, *2014*(6), 1–33.

Maharaj, S., & Mafa Takisa, P. (2012). Regular models with quadratic equation of state. *General Relativity and Gravitation*, *44*, 1419–1432.

Mak, M. K., & Harko, T. (2003). Anisotropic stars in general relativity. *Proc. Roy. Soc. Lond. A*, *459*, 393–408.

Maki, T., & Shiraishi, K. (1993). Multi-black hole solutions in cosmological Einstein-Maxwell-dilaton theory. *Classical and Quantum Gravity*, *10*(10), 2171.

Maluf, J. W. (2013). The teleparallel equivalent of general relativity. *Annalen der Physik*, *525*(5), 339–357.

Marolf, D. (1999). Spacetime Embedding Diagrams for Black Holes. *General Relativity and Gravitation*, *31*(6), 919–944.

Martinez, C., Teitelboim, C., & Zanelli, J. (2000). Charged rotating black hole in three spacetime dimensions. *Physical Review D*, *61*(10), 104013.

Maurya, S. K., Gupta, Y. K., Ray, S., & Deb, D. (2016). Generalised model for anisotropic compact stars. *Eur. Phys. J. C*, *76*(12), 693.

Maurya, S., Deb, D., Ray, S., & Kuhfittig, P. (2019). A study of anisotropic compact stars based on embedding class 1 condition. *International Journal of Modern Physics D*, *28*(09), 1950116.

Maurya, S., Errehymy, A., Singh, K. N., Dayanandan, B, & Daoud, M. (2023). Self-gravitating electrically charged anisotropic strange star model. *New Astronomy*, *101*, 102000.

Mazharimousavi, S. H., & Halilsoy, M. (2016). Wormhole solutions in $f(R)$ gravity satisfying energy conditions. *Modern Physics Letters A*, *31*(34), 1650192.

McVittie, G. C. (1933). The mass-particle in an expanding universe. *Mon. Not. Roy. Astron. Soc.*, *93*, 325–339.

Mellier, Y. (1999). Probing the universe with weak lensing. *Ann. Rev. Astron. Astrophys.*, *37*, 127–189.

Millano, A. D., Jusufi, K., & Leon, G. (2023). Phase space analysis of the bouncing universe with stringy effects. *Physics Letters B*, *841*, 137916.

Mirzaev, T., Li, S., Narzilloev, B., Hussain, I., Abdujabbarov, A., & Ahmedov, B. (2023). Simulated image of the shadow of the Kerr–Newman–NUT–Kiselev black hole in the Rastall gravity with a thin accretion disk. *Eur. Phys. J. Plus*, *138*(1), 47.

Molla, N. U., & Debnath, U. (2022). Gravitational lensing for power-Maxwell charged quintessence black hole in Rastall gravity. *Int. J. Geom. Meth. Mod. Phys.*, *19*(12), 2250183.

Molla, N. U., & Debnath, U. (2023a). Gravitational Lensing of Acoustic Charged Black Holes. *Astrophys. J.*, *947*(1), 14.

Molla, N. U., & Debnath, U. (2023b). Shadows and strong gravitational lensing by Van der Waals black hole in homogeneous plasma. *Annals Phys.*, *453*, 169304.

Molla, N. U., Ghosh, S. G., & Debnath, U. (2024). Testing gravitational lensing effects by supermassive massive black holes with superstring theory metric: Astrophysical implications and EHT constraints. *Phys. Dark Univ.*, *44*, 101495.

Moraes, P. H. R. S., & Sahoo, P. K. (2017). Modeling wormholes in $f(R,T)$ gravity. *Phys. Rev. D*, *96*, 044038.

Morris, M. S., & Thorne, K. S. (1988). Wormholes in spacetime and their use for interstellar travel: A tool for teaching general relativity. *American Journal of Physics*, *56*(5), 395–412.

Narzilloev, B., Hussain, I., Abdujabbarov, A., Ahmedov, B., & Bambi, C. (2021a). Dynamics and fundamental frequencies of test particles orbiting Kerr–Newman–NUT–Kiselev black hole in Rastall gravity. *Eur. Phys. J. Plus*, *136*(10), 1032.

Narzilloev, B., Shaymatov, S., Hussain, I., Abdujabbarov, A., Ahmedov, B., & Bambi, C. (2021b). Motion of Particles and Gravitational Lensing Around (2+1)-dimensional BTZ black holes in Gauss-Bonnet Gravity. *Eur. Phys. J. C*, *81*, 849.

NASA. (2000). Crab Nebula. https://en.wikipedia.org/wiki/Crab_Nebula#/media/File:Crab_Nebula.jpg

Nashed, G., & Bamba, K. (2022). Realistic compact stars in conformal teleparallel gravity. *Progress of Theoretical and Experimental Physics*, *2022*(10), 103E01.

Nayak, K. R., MacCallum, M. A., & Vishveshwara, C. (2000). Black holes in nonflat backgrounds: The Schwarzschild black hole in the Einstein universe. *Physical Review D*, *63*(2), 024020.

Nayak, K., & Vishveshvara, C. (2000). Geometry of the Kerr Black Hole in the Einstein Cosmological Background. *Preprint to be submitted for publication.*

Nedkova, P. G., Tinchev, V. K., & Yazadjiev, S. S. (2013). Shadow of a rotating traversable wormhole. *Phys. Rev. D*, *88*, 124019.

Newman, E. T., Couch, E., Chinnapared, K., Exton, A., Prakash, A., & Torrence, R. (1965). Metric of a Rotating, Charged Mass. *Journal of Mathematical Physics*, *6*(6), 918–919.

Ngubelanga, S. A., Maharaj, S. D., & Ray, S. (2015). Compact stars with quadratic equation of state. *Astrophys. Space Sci.*, *357*(1), 74.

Nishiyama, M., Morita, M.-a., & Morikawa, M. (2004). Bose Einstein condensation as dark energy and dark matter. *arXiv preprint astro-ph/0403571.*

Nordström, G. (1918). On the Energy of the Gravitation field in Einstein's Theory. *Koninklijke Nederlandse Akademie van Wetenschappen Proceedings Series B Physical Sciences*, *20*, 1238–1245.

Ohgami, T., & Sakai, N. (2015). Wormhole shadows. *Physical Review D*, *91*(12), 124020.

Ohgami, T., & Sakai, N. (2016). Wormhole shadows in rotating dust. *Physical Review D*, *94*(6), 064071.

Oppenheimer, J. R., & Volkoff, G. M. (1939). On Massive Neutron Cores. *Phys. Rev.*, *55*, 374–381.

Övgün, A. (2019). Weak field deflection angle by regular black holes with cosmic strings using the Gauss-Bonnet theorem. *Phys. Rev. D*, *99*(10), 104075.

Övgün, A, & Sakalli, I. (2017). A particular thin-shell wormhole. *Theoretical and Mathematical Physics*, *190*, 120–129.

Ozel, F., Guver, T., & Psaltis, D. (2009). The Mass and Radius of the Neutron Star in EXO 1745-248. *Astrophys. J.*, *693*, 1775–1779.

Ozel, F., Psaltis, D., Guver, T., Baym, G., Heinke, C., & Guillot, S. (2016). The Dense Matter Equation of State from Neutron Star Radius and Mass Measurements. *Astrophys. J.*, *820*(1), 28.

Panos, C. P., Nikolaidis, N., Chatzisavvas, K. C., & Tsouros, C. (2009). A simple method for the evaluation of the information content and complexity in atoms. a proposal for scalability. *Physics Letters A*, *373*, 2343–2350.

Panpanich, S., Ponglertsakul, S., & Tannukij, L. (2019). Particle motions and Gravitational Lensing in de Rham-Gabadadze-Tolley Massive Gravity Theory. *Phys. Rev. D*, *100*(4), 044031.

Pant, R. P., Gedela, S., Bisht, R. K., & Pant, N. (2019). Core-envelope model of super dense star with distinct equation of states. *Eur. Phys. J. C*, *79*(7), 602.

Papapetrou, A, & Hamoui, A. Couches simples de matière en relativité générale. In: In *Annales de l'institut henri poincaré. section a, physique théorique. 9.* (2). 1968, 179–211.

Papnoi, U., Atamurotov, F., Ghosh, S. G., & Ahmedov, B. (2014). Shadow of five-dimensional rotating Myers-Perry black hole. *Phys. Rev. D*, *90*, 024073.

Pawlowski, J. M., & Tränkle, J. (2024). Effective action and black hole solutions in asymptotically safe quantum gravity. *Phys. Rev. D*, *110*(8), 086011.

Penington, G., Shenker, S. H., Stanford, D., & Yang, Z. (2022). Replica wormholes and the black hole interior. *Journal of High Energy Physics*, *2022*(3), 1–87.

Penrose, O. (1951). CXXXVI. On the Quantum mechanics of helium II. *The London, Edinburgh, and Dublin Philosophical Magazine and Journal of Science*, *42*(335), 1373–1377.

Perlick, V., & Tsupko, O. Y. (2022). Calculating black hole shadows: Review of analytical studies. *Phys. Rept.*, *947*, 1–39.

Perry, G., & Mann, R. B. (1992). Traversible wormholes in (2+ 1) dimensions. *General relativity and gravitation*, *24*, 305–321.

Pitaevskii, L., & Stringari, S. (2016). *Bose-Einstein condensation and superfluidity* (Vol. 164). Oxford University Press.

Podolský, J., Švarc, R., Pravda, V., & Pravdova, A. (2020). Black holes and other exact spherical solutions in Quadratic Gravity. *Phys. Rev. D*, *101*(2), 024027.

Pravda, V., Pravdova, A., Podolsky, J., & Svarc, R. (2017). Exact solutions to quadratic gravity. *Phys. Rev. D*, *95*(8), 084025.

Psaltis, D., Medeiros, L., Christian, P., Özel, F., Akiyama, K., Alberdi, A., Alef, W., Asada, K., Azulay, R., Ball, D., et al. (2020). Gravitational test beyond the first post-Newtonian order with the shadow of the M87 black hole. *Physical review letters*, *125*(14), 141104.

Quintero Angulo, G., Pérez Martínez, A., & Pérez Rojas, H. (2019). Magnetized Bose–Einstein condensate stars with boundary conditions depending on magnetic field. *Astronomische Nachrichten*, *340*(9-10), 909–913.

Rahaman, F., Banerjee, A, & Radinschi, I. (2012). A new class of stable (2+ 1) dimensional thin shell wormhole. *International Journal of Theoretical Physics*, *51*, 1680–1691.

Rahaman, F., Banerjee, S., & Islam, S. (2019). Wormholes with quadratic equation of state. *Phys. Astron. Int. J.*, *3*(1), 14–17.

Rahaman, F., Jamil, M., & Chakraborty, K. (2011a). Revisiting the classical electron model in general relativity. *Astrophysics and Space Science*, *331*, 191–197.

Rahaman, F., Jamil, M., Ghosh, A., & Chakraborty, K. (2010). On generating some known black hole solutions. *Modern Physics Letters A*, *25*(10), 835–842.

Rahaman, F., Kuhfittig, P., Kalam, M, Usmani, A., & Ray, S. (2011b). A comparison of Hořava–Lifshitz gravity and Einstein gravity through thin-shell wormhole construction. *Classical and Quantum Gravity*, *28*(15), 155021.

Randall, L., & Sundrum, R. (1999). Large mass hierarchy from a small extra dimension. *Physical review letters*, *83*(17), 3370.

Rawls, M. L., Orosz, J. A., McClintock, J. E., Torres, M. A. P., Bailyn, C. D., & Buxton, M. M. (2011). Refined Neutron-Star Mass Determinations for Six Eclipsing X-Ray Pulsar Binaries. *Astrophys. J.*, *730*, 25.

Raychaudhuri, A. (1955). Relativistic Cosmology. I. *Phys. Rev.*, *98*, 1123–1126.

Reissner, H. (1916). Über die Eigengravitation des elektrischen Feldes nach der Einsteinschen Theorie. *Annalen der Physik*, *355*(9), 106–120.

Riazuelo, A. (2019). Seeing relativity-I: Ray tracing in a Schwarzschild metric to explore the maximal analytic extension of the metric and making a proper rendering of the stars. *International Journal of Modern Physics D*, *28*(02), 1950042.

Richarte, M. G., & Simeone, C. (2007). Thin-shell wormholes supported by ordinary matter in Einstein-Gauss-Bonnet gravity. *Phys. Rev. D*, *76*, 087502.

Riess, A. G., Filippenko, A. V., Challis, P., Clocchiatti, A., Diercks, A., Garnavich, P. M., Gilliland, R. L., Hogan, C. J., Jha, S., Kirshner, R. P., et al. (1998). Observational evidence from supernovae for an accelerating universe and a cosmological constant. *The astronomical journal*, *116*(3), 1009.

Ror, A. K., Gupta, R., Aryan, A., Pandey, S. B., Oates, S. R., Castro-Tirado, A. J., & Kumar, S. (2024). Exploring the Origin of Ultralong Gamma-Ray Bursts: Lessons from GRB 221009A. *Astrophys. J.*, *971*(2), 163.

Roupas, Z., & Nashed, G. G. L. (2020). Anisotropic neutron stars modelling: constraints in Krori–Barua spacetime. *Eur. Phys. J. C*, *80*(10), 905.

Ruderman, M. (1972). Pulsars: structure and dynamics. *Annual Review of Astronomy and Astrophysics, vol. 10, p. 427*, *10*, 427.

Russell, H. N. Relations Between the Spectra and Other Characteristics of the Stars (from Popular Astronomy, 22, 275). In: In *The HR Diagram, In Memory of Henry Norris Russell. IAU Symposium No. 80, held November 2, 1977, at the National Academy of Sciences, Washington, DC. Report No. 13, edited by AG Davis Philip and David H. DeVorkin, December, 1977., p. 115. 80.* 1977, 115.

Rybicki, G. B., Heinke, C. O., Narayan, R., & Grindlay, J. E. (2006). A Hydrogen atmosphere spectral model applied to the neutron star X7 in the globular cluster 47 Tucanae. *Astrophys. J.*, *644*, 1090–1103.

Saha, A., Modumudi, S. M., & Gangopadhyay, S. (2018). Shadow of a noncommutative geometry inspired Ayón Beato García black hole. *General Relativity and Gravitation*, *50*(8).

Sarbach, O., & Zannias, T. The propagation of particles and fields in wormhole geometries. In: In *Aip conference proceedings. 1473*. (1). American Institute of Physics. 2012, 223–232.

Sarkar, S., Sarkar, N., Aktar, S., Sarkar, M., Rahaman, F., & Yadav, A. K. (2024). Dark matter supporting traversable wormholes in the Galactic halo., *109*, Article 102183, 102183.

Sarkar, S., Sarkar, N., Rudra, P., Rahaman, F., & Ghorui, T. (2023). Relativistic model of anisotropic star with Bose-Einstein density depiction. *The European Physical Journal C*, *83*(11), 1005.

Sawyer, R. F. (1972). Condensed π- phase in neutron-star matter. *Physical Review Letters*, *29*(6), 382.

Schmidt, F. (2008). Weak Lensing Probes of Modified Gravity. *Phys. Rev. D*, *78*, 043002.

Schunck, F. E., & Mielke, E. W. (2003). General relativistic Boson stars. *Classical and Quantum Gravity*, *20*(20), R301.

Schwarzschild, K. (1916). On the gravitational field of a mass point according to Einstein's theory. *Sitzungsber. Preuss. Akad. Wiss. Berlin (Math. Phys.)*, *1916*, 189–196.

Sekhmani, Y., Myrzakulov, R., Kaczmarek, A. Z., Rayimbaev, J., Szczśniak, D., et al. (2024). Dark matter effects of a black hole with nonsingular Yukawa-modified potential in Einstein-Gauss-Bonnet Gravity. *arXiv preprint arXiv:2402.05344*.

Sen, N. (1924). Über die grenzbedingungen des schwerefeldes an unstetigkeitsflächen. *Annalen der Physik*, *378*(5-6), 365–396.

Shaikh, R. (2018). Shadows of rotating wormholes. *Phys. Rev. D*, *98*, 024044.

Shaikh, R. (2019). Black hole shadow in a general rotating spacetime obtained through Newman-Janis algorithm. *Phys. Rev. D*, *100*, 024028.

Shaikh, R. Shadows cast by rotating wormholes. In: In *The fifteenth marcel grossmann meeting: On recent developments in theoretical and experimental general relativity, astrophysics, and relativistic field theories (in 3 volumes)*. World Scientific. 2022, 600–605.

Shaikh, R., Banerjee, P., Paul, S., & Sarkar, T. (2019a). A novel gravitational lensing feature by wormholes. *Physics Letters B*, *789*, 270–275.

Shaikh, R., Banerjee, P., Paul, S., & Sarkar, T. (2019b). Strong gravitational lensing by wormholes. *Journal of Cosmology and Astroparticle Physics*, *2019*(07), 028.

Sharif, M, & Iftikhar, S. (2016). Shadow of a charged rotating non-commutative black hole. *The European Physical Journal C*, *76*, 1–9.

Sharma, R., & Ratanpal, B. (2013). Relativistic stellar model admitting a quadratic equation of state. *International Journal of Modern Physics D*, *22*(13), 1350074.

Shipley, J. O., & Dolan, S. R. (2016). Binary black hole shadows, chaotic scattering and the Cantor set. *Classical and Quantum Gravity*, *33*(17), 175001.

Shirafuji, T., & Nashed, G. G. (1997). Energy and momentum in the tetrad theory of gravitation. *Progress of Theoretical Physics*, *98*(6), 1355–1370.

Shiromizu, T., & Gen, U. (2000). A Probe particle in Kerr-Newman-de Sitter cosmos. *Class. Quant. Grav.*, *17*, 1361–1368.

Singh, A., Raushan, R., Chaubey, R, & Singh, T. (2018). Aspects of nonflat FRW bouncing models with quadratic equation of state. *International Journal of Modern Physics A*, *33*(35), 1850213.

Singh, B. P. (2022). Rotating charged black hole shadow in quintessence. *Annals of Physics*, *441*, 168892.

Singh, G., Lalke, A. R., & Hulke, N. (2020). Study of particle creation with quadratic equation of state in higher derivative theory. *Brazilian Journal of Physics*, *50*, 725–743.

Sokolov, A. (1980). Phase transitions in a superfluid neutron liquid. *Sov. Phys. JETP*, *52*(4), 575.

Stelle, K. S. (1977). Renormalization of higher-derivative quantum gravity. *Physical Review D*, *16*(4), 953.

Sushkov, S. (2005). Wormholes supported by a phantom energy. *Phys. Rev. D*, *71*, 043520.

Synge, J. L. (1966). The Escape of Photons from Gravitationally Intense Stars. *Mon. Not. Roy. Astron. Soc.*, *131*(3), 463–466.

Takahashi, R. (2004). Shapes and Positions of Black Hole Shadows in Accretion Disks and Spin Parameters of Black Holes. *The Astrophysical Journal*, *611*(2), 996.

Takisa, P. M., Maharaj, S. D, & Mulangu, C. (2019). Compact relativistic star with quadratic envelope. *Pramana*, *92*(3), 40.

Tello-Ortiz, F., Maurya, S. K., & Gomez-Leyton, Y. (2020). Class I approach as MGD generator. *Eur. Phys. J. C*, *80*(4), 324.

Teo, E. (1998). Rotating traversable wormholes. *Physical Review D*, *58*(2), 024014.

Thejll, P., & Shipman, H. L. (1986). Temperature, radius, and rotational velocity of Sirius B. *Publications of the Astronomical Society of the Pacific*, *98*(608), 922.

Tsukamoto, N. (2016). Strong deflection limit analysis and gravitational lensing of an Ellis wormhole. *Physical Review D*, *94*(12), 124001.

Tsukamoto, N. (2017). Deflection angle in the strong deflection limit in a general asymptotically flat, static, spherically symmetric spacetime. *Physical Review D*, *95*(6), 064035.

Tsukamoto, N. (2021). Gravitational lensing by two photon spheres in a black-bounce spacetime in strong deflection limits. *Physical Review D*, *104*(6), 064022.

Tsukamoto, N., & Gong, Y. (2018). Extended source effect on microlensing light curves by an Ellis wormhole. *Phys. Rev. D*, *97*, 084051.

Ualikhanova, U., & Hohmann, M. (2019). Parametrized post-Newtonian limit of general teleparallel gravity theories. *Physical Review D*, *100*(10), 104011.

Unzicker, A., & Case, T. (2005). Translation of Einstein's attempt of a unified field theory with teleparallelism. *arXiv preprint physics/0503046*.

Usmani, A., Rahaman, F., Ray, S., Nandi, K., Kuhfittig, P. K., Rakib, S. A., & Hasan, Z. (2011). Charged gravastars admitting conformal motion. *Physics Letters B*, *701*(4), 388–392.

Usov, V. V. (2004). Electric fields at the quark surface of strange stars in the color-flavor locked phase. *Physical Review D*, *70*(6), 067301.

Vagnozzi, S., Roy, R., Tsai, Y.-D., Visinelli, L., Afrin, M., Allahyari, A., Bambhaniya, P., Dey, D., Ghosh, S. G., Joshi, P. S., et al. (2023). Horizon-scale tests of gravity theories and fundamental physics from the Event Horizon Telescope image of Sagittarius A. *Classical and Quantum Gravity*, *40*(16), 165007.

Vagnozzi, S., & Visinelli, L. (2019). Hunting for extra dimensions in the shadow of $M87^*$. *Phys. Rev. D*, *100*, 024020.

Van Maanen, A. (1917). Two faint stars with large proper motion. *Publications of the Astronomical Society of the Pacific*, *29*(172), 258–259.

Vazquez, S. E., & Esteban, E. P. (2004). Strong field gravitational lensing by a Kerr black hole. *Nuovo Cim. B*, *119*, 489–519.

Vincent, F., Wielgus, M, Abramowicz, M., Gourgoulhon, E, Lasota, J.-P., Paumard, T, & Perrin, G. (2021). Geometric modeling of $M87^*$ as a Kerr black hole or a non-Kerr compact object. *Astronomy & Astrophysics*, *646*, A37.

Virbhadra, K. S., & Ellis, G. F. R. (2002). Gravitational lensing by naked singularities. *Phys. Rev. D*, *65*, 103004.

Virbhadra, K. S., & Ellis, G. F. R. (2000). Schwarzschild black hole lensing. *Phys. Rev. D*, *62*, 084003.

Virbhadra, K. S., Narasimha, D., & Chitre, S. M. (1998). Role of the scalar field in gravitational lensing. *Astron. Astrophys.*, *337*, 1–8.

Visser, M. (1989). Traversable wormholes: Some simple examples. *Phys. Rev. D*, *39*, 3182–3184.

Visser, M. (1995). Lorentzian wormholes from einstein to hawking. *Woodbury*.

Wali, K. (2006). The Man Behind Bose Statistics. *Physics Today*, *59*(10), 46–52.

Wang, M., Chen, S., & Jing, J. (2017). Shadow casted by a Konoplya-Zhidenko rotating non-Kerr black hole. *Journal of Cosmology and Astroparticle Physics*, *2017*(10), 051.

Wang, X., Li, P.-C., Zhang, C.-Y., & Guo, M. (2020). Novel shadows from the asymmetric thin-shell wormhole. *Physics Letters B*, *811*, 135930.

Warner, D. J. (1968). Alvan Clark & Sons: Artist in Optics. *Bulletin of the United States National Museum*.

Webb, N. A., & Barret, D. (2007). Constraining the equation of state of supra-nuclear dense matter from XMM-Newton observations of neutron stars in globular clusters. *Astrophys. J.*, *671*, 727.

Weber, F. (1999). Quark matter in neutron stars. *Journal of Physics G: Nuclear and Particle Physics*, *25*(9), R195.

Wei, S.-W., & Liu, Y.-X. (2013). Observing the shadow of Einstein-Maxwell-Dilaton-Axion black hole. *Journal of Cosmology and Astroparticle Physics*, *2013*(11), 063.

Weyl, H. (1917). Zur Gravitationstheorie. *Annalen der Physik*, *359*(18), 117–145.

Weyl, H. (1919). Über die statischen kugelsymmetrischen Lösungen von Einsteins "kosmologischen" Gravitationsgleichungen. *Phys. Z*, *20*(31-34), 65.

Whisker, R. (2005). Strong gravitational lensing by Braneworld black holes. *Phys. Rev. D*, *71*, 064004.

Wielgus, M., Horák, J., Vincent, F., & Abramowicz, M. (2020). Reflection-asymmetric wormholes and their double shadows. *Physical Review D*, *102*(8), 084044.

Yan, S.-F., Zhang, P., Chen, J.-W., Zhang, X.-Z., Cai, Y.-F., & Saridakis, E. N. (2020). Interpreting cosmological tensions from the effective field theory of torsional gravity. *Physical Review D*, *101*(12), 121301.

Yerzhanov, K., Myrzakul, S. R., Kulnazarov, I., & Myrzakulov, R. (2010). Accelerating cosmology in $f(T)$ gravity with scalar field. *arXiv:1006.3879*.

Young, P. J. (1976). Capture of particles from plunge orbits by a black hole. *Phys. Rev. D*, *14*, 3281–3289.

Younsi, Z., Zhidenko, A., Rezzolla, L., Konoplya, R., & Mizuno, Y. (2016). New method for shadow calculations: Application to parametrized axisymmetric black holes. *Phys. Rev. D*, *94*, 084025.

Yukawa, H. (1935). On the interaction of elementary particles. I. *Proceedings of the Physico-Mathematical Society of Japan. 3rd Series*, *17*, 48–57.

Yumoto, A., Nitta, D., Chiba, T., & Sugiyama, N. (2012). Shadows of multi-black holes: Analytic exploration. *Phys. Rev. D*, *86*, 103001.

Zakharov, A., Nucita, A., DePaolis, F., & Ingrosso, G. (2005a). Measuring the black hole parameters in the galactic center with Radioastron. *New Astronomy*, *10*(6), 479–489.

Zakharov, A. F. (2014). Constraints on a charge in the Reissner-Nordström metric for the black hole at the Galactic Center. *Physical Review D*, *90*(6), 062007.

Zakharov, A. F., De Paolis, F., Ingrosso, G., & Nucita, A. (2005b). Direct measurements of black hole charge with future astrometrical missions. *Astronomy & Astrophysics*, *442*(3), 795–799.

Zanchin, V. T., Kleber, A., & Lemos, J. P. (2002). Four-dimensional anti-de Sitter toroidal black holes from a three-dimensional perspective: Full complexity. *Physical Review D*, *66*(6), 064022.

Zanchin, V. T., & Miranda, A. S. (2004). Spherical and planar three-dimensional anti-de Sitter black holes. *Classical and Quantum Gravity*, *21*(4), 875.

Zhao, S.-S., & Xie, Y. (2017). Strong deflection gravitational lensing by a modified Hayward black hole. *Eur. Phys. J. C*, *77*(5), 272.

Zhu, Y., & Wang, T. (2021). Shadow of the wormholelike static aether solution. *Phys. Rev. D*, *104*, 104052.

Zubair, M, & Abbas, G. (2016). Analytic models of anisotropic strange stars in $f(T)$ gravity with off-diagonal tetrad. *Astrophysics and Space Science*, *361*(1), 27.